

Université de Limoges

ED 609 - Sciences et Ingénierie des Matériaux, Mécanique, Énergétique (SIMME)
Institut de recherche sur les céramiques (IRCER)

Thèse pour obtenir le grade de
Docteur de l'Université de Limoges
Matériaux céramiques et traitements de surface

Présentée et soutenue par
Tuan NGUYEN VAN

le 7 Mai 2021

**Dual pulsed laser vaporization process dedicated to nanocomposite
Development of soft (Co, FeCo) in hard (NdFeB, FePt) magnetic
nanocomposites**

Thèse dirigée par Corinne CHAMPEAUX and Frédéric DUMAS-BOUCHIAT

JURY :

Président du jury

Rapporteurs

Professor, **Eric MILLON**, GREMI – UMR 7344 CNRS, Univ Orléans, France

Professor, **Viorel POP**, Facultatea de Fizica, Universitatea Babes-Bolyai, Cluj-Napoca, Romania

Examineurs

Nora M. DEMPSEY, Directrice de Recherches CNRS, Institut Néel, Grenoble, France

Professor, **Corinne CHAMPEAUX**, IRCER – UMR 7315 CNRS, Univ Limoges, France

Professor, **Frédéric DUMAS-BOUCHIAT**, IRCER – UMR 7315 CNRS, Univ Limoges, France



Abstract

The results of the thesis were carried out at the IRCER institute in Limoges, France over the past three years. It presents all the steps to synthesize ferromagnetic nanocomposites composed of hard magnetic matrix and soft magnetic nanoparticles (NPs). This work is a part of a joint project SHAMAN ANR-16-CE09-0019 on magnetic nanocomposites bringing collaboration between three laboratories Néel Institute in Grenoble, Lumière Matière Institute in Lyon and Institute of Research for Ceramics in Limoges, and the European Synchrotron Radiation Facility in Grenoble. All of the magnetic characterizations presented in this work were conducted at Néel Institute.

Thin films of NdFeB and FePt have been successfully developed by Pulsed Laser Deposition (PLD) on various substrates (Si/SiO₂, Al₂O₃, MgO) using single alloy targets. The control of the structure and microstructure of materials have led to achieve quite remarkable magnetic properties. 150 nm-thin films composed of Nd₂Fe₁₄B₁ grains decoupled by a secondary Nd-rich paramagnetic phase present values of magnetic coercivity and remanence close to the best macroscopic magnets on the market, e. g., $\mu_0 H_c \sim 1.3$ T, $\mu_0 M_r \sim 1.1$ T and a square loop shape with single magnetic phase behavior. Taking advantage of dewetting process induced by rapid thermal annealing process, 15 nm-FePt granular films possess also very good magnetic characteristics up to $\mu_0 H_c \sim 4.4$ T, $\mu_0 M_r \sim 1.3$ T, but with remaining secondary phase.

Moreover, a homemade nanoparticle generator entirely developed at IRCER and associated with the main PLD chamber allowed to fabricate ferromagnetic Co and Fe₆₅Co₃₅ nanoparticles. The diameters of NPs are well controlled in the range 2-5 nm, depending on the parameters in the nucleation cavity. All NPs are crystallized and magnetically soft.

Soft-hard magnetic nanocomposites with defined architectures and composed of FePt grains with 25% volume fraction of Fe₆₅Co₃₅ NPs, exhibit a significant increase of + 24% in remanence compared to that of conventional FePt thin film, while the coercivity remains constant at around 2 T. The challenge is about preserving simultaneously the properties of hard and soft magnetic phases, with the required high temperatures of 750°C and the associated diffusion phenomena. These results constitute an experimental evidence validating the theory about the enhancement of the magnetic properties in the composites, allowing exchange-coupling interaction between hard and soft phases. This work opens the way to micro/nanoscale architectures of model materials in order to augment their magnetic properties.

Keywords: Pulsed Laser Ablation, Soft-hard nanocomposites, Magnetic thin films, Nanoparticles.

Acknowledgement

The work presented in this thesis would not have been possible without the enthusiastic support from a large number of people, to whom I am immensely grateful. My last three years in France have been considerably colorful with all of you. I would like to take this opportunity to express my great attitude to you. Hope I can manage to do you all justice, thank you for all.

First of all, I would like to thank my thesis supervisors, Professor Corinne CHAMPEAUX and Professor Frédéric DUMAS-BOUCHIAT. Thank you for giving me the great chance to go outside Vietnam and work with you and many others in France, especially in the prosperous environment of IRCER and Néel. During my time working in France, you both shared with me the experience of doing good scientific work and encouraged me to do my very best by warmly smiling and saying that "you can do it, go". You are very patient to teach me to do everything well, e. g., writing a good scientific paper, being an independent researcher and preparing for my career and having joy in doing it. You are very kind to me with almost instant support right after I asked for, and willingly discussing with me even when we were in the car. Thank you for your time and all of many lessons that I have learnt. In the meantime, I would like to thank Professor Eric MILLON and Professor Viorel POP for attentively reviewing my thesis.

Thank you, Professor Nora DEMPSEY, for your kindness and advice, for your help with all the magnetic characterizations carried out at Néel Institute, and especially strong discussion relating to magnetism. I am much impressed and really appreciate your time, your support during the COVID19 national lockdown, and weekend.

Laurent RANNO, for your recommendation of applying to this fascinating SHAMAN project, for sharing your knowledge about magnetism, for interesting discussion in all aspects of physics and life, for your friendship and particularly the collaboration in the upcoming simulation. Thank you!

I gratefully acknowledge financial support from the SHAMAN ANR-16-CE09-0019 for funding this work and my Ph.D.

I would like to thank many IRCER members for your continuous help during my work in France. I would like to express my thanks to Philippe THOMAS – the director of IRCER. Special thanks to Pierre CARLES for impressive TEM characterizations and discussion. Many great thanks are extended to Etienne LABORDE for your enthusiasm and XPS investigation. Patrice DUPORT for all of your help on the FIB. Richard MAYET for all of the help with the XRD - you are incredibly helpful. I am highly indebted to Valérie COUDERT, for your non-stop support with plenty of AFM measurements. I thank other CARMALIM members for your support during my PhD.

I would like to thank colleagues and staff at Néel for your support with magnetic characterization. I am thankful to Isabelle DE MORAES for your support on magnetic hysteresis loops, and magnetic discussion together with the FORC measurements. You, Isabelle, was readily to stay at work late to help passing the samples with SQUID and willingly assist at any time. I am greatly indebted to you. Thank you so much Isabelle. Great thanks to Yuan HONG for all of your help with scanning MOKE. I thank Richard Haettel and Frederico Orlando Keller for the induction melted targets.

My sincere thanks to my colleagues at the Department of Physics, Le Quy Don Technical University, Vietnam. I am grateful to Dr. Thin NGUYEN VAN for your help and support in both person and work as well as upcoming project collaboration. A big thanks to Dr. Hue NGUYEN MINH, Dr. Tung

NGUYEN VU, Prof. Xuan NGUYEN NHU for your encouragement of persuading this Ph.D accompanied by valuable suggestions for post-Ph.D ideas.

It would be my great pleasure to express very special thanks to Prof. Duc NGUYEN HUU and Prof. Giang DO THI HUONG at the VNU - University of Engineering and Technology, for your help and support in a variety of ways, especially for your willing acceptance of serving as my major mentors for the upcoming postdoctoral fellowship.

Thanks to my friends outside work, Bercea ADRIAN IONUT, Alberto ION PUIU and Victor BADEA, who have made life here in France so much fun with nights out, and with travelling. Thank you guys.

Finally, to my family, who have always been there for me and sharing with me through everything. MOM, for always encouraging me though you have not known what I am doing. And my beloved - Hong DO THI, for sharing each single moment and encouraging me to do my very best. You are all amazing and you are the finest family I could ask for. Thank you!

Contents

Abstract	ii
Acknowledgement.....	iii
Contents.....	v
List of Abbreviations.....	vii
List of Figures	ix
List of Tables.....	xx
Thesis motivation	xxi
Chapter I. Theoretical background and revision	1
I.1. Magnetism fundamentals and soft-hard nanocomposites	1
I.1.1. Magnetic parameters	1
I.1.2. Characteristic lengths.....	5
I.1.3. What is spring magnet and how to augment magnetic energy product?.....	6
I.2. Hard magnetic NdFeB based films	10
I.2.1. Nd ₂ Fe ₁₄ B structure and its properties	10
I.2.2. Thin film growth	11
I.2.3. Development of hard magnetic NdFeB films	12
I.3. Hard magnetic FePt thin films	14
I.3.1. L1 ₀ -FePt structure and its properties.....	14
I.3.2. FePt phase transformation.....	15
I.3.3. Development of hard magnetic FePt films.....	16
I.4. Soft Magnetic Nanoparticles (NPs)	17
I.5. Chapter highlights	20
Chapter II. Fabrication and characterization techniques	21
II.1. Fabrication methods.....	21
II.1.1. Pulsed laser deposition (PLD)	21
II.1.2. The lasers	23
II.1.3. Home-made free cluster generator.....	25
II.1.4. Improvement in the setup, and depositing parameters in use	27
II.1.5. Rapid Thermal Processing (RTP)	30
II.2. Characterization methods	31
II.2.1. Transmission electron microscopy (TEM)	32
II.2.2. Magnetic force microscopy (MFM)	33
II.2.3. Vibrating sample magnetometer SQUID (VSM-SQUID).....	34
II.2.4. How to characterize soft in hard magnetic nanocomposites.....	35
II.3. Chapter highlights.....	37
Chapter III. Hard magnetic thin films (Nd ₂ Fe ₁₄ B and FePt)	39
III.1. NdFeB matrix without post-annealing	39
III.1.1. Effect of target compositions.....	39
III.1.2. Influence of deposition temperatures (<i>T_d</i>)	44
III.1.3. Al ₂ O ₃ versus Si/SiO ₂ substrates.....	48
III.2. NdFeB matrix with post-annealing	51
III.2.1. Atomic structure	52

III.2.2. Microstructure	53
III.2.3. Magnetic properties	55
III.3. FePt matrix without RTP annealing	58
III.3.1. Deposition repetition rates.....	59
III.3.2. Deposition temperatures (T_d).....	63
III.3.3. MgO versus Si/SiO ₂ substrates (towards to silicon compatibility)	67
III.4. As-deposited FePt matrix with RTP annealing	68
III.4.1. Annealing temperatures.....	69
III.4.2. Heating rate influence.....	73
III.4.3. Effect of annealing time	76
III.5. Chapter highlights	79
Chapter IV. Soft magnetic nanoparticles.....	81
IV.1. FeCo NPs properties	81
IV.1.1. Initial parameters for NPs fabrication	81
IV.1.2. Size distribution	82
IV.1.3. Composition	85
IV.1.4. Structure and microstructure	87
IV.1.5. Magnetic properties.....	92
IV.2. Chapter highlights	95
Chapter V. Nanocomposites-soft magnetic NPs assemblies embedded in hard matrices	97
V.1. Tri-layer FePt/FeCo (or Co)/FePt systems of continuous layers.....	97
V.1.1. Structural and microstructural characterizations	97
V.1.2. Magnetic characterizations	99
V.2. Does diffusion exist?	103
V.2.1. Theoretical estimation	103
V.2.2. Experimental confirmation	106
V.3. Nanocomposites based FePt matrix.....	110
V.3.1. Nanocomposites with various FeCo diluted percentage (NPs vol content).....	110
V.3.2. FeCo nanocomposites architecture (NPs size, layer-layer)	116
V.3.3. Effect of annealing time (FeCo NPs nanocomposites, 10s)	120
V.3.4. Difference between Co and FeCo NPs embedded NPs (10s).....	122
V.3.5. Effect of Ta spacer.....	124
V.4. Chapter highlights	128
Conclusions and Prospects	129
Appendix	133
List of Scientific Contribution.....	143
References	145

List of Abbreviations

$\mu_0 H_c$	Magnetic coercivity/coercive field/coercive force
$\mu_0 M_r$	Remanence/remanent magnetisation/remanent magnetization
$\mu_0 M_s$	Saturated magnetisation/Spontaneous magnetisation
M	Magnetisation/magnetization
μ_0	Magnetic permeability of free space
m	Magnetic moment
χ	Magnetic susceptibility
H_{app}	Applied magnetic field/external applied magnetic field
B	Induced magnetisation/ magnetic flux density/magnetic induction
T_C	Curie temperature
T_N	Néel temperature
K	Anisotropy constant
A	Exchange stiffness/strength
J_{ex}	Exchange integral
S	Spin angular momentum
l_{ex}	Exchange length
H_d	Demagnetizing field
H_a	Anisotropy field
N	Demagnetizing factor
$(BH)_{max}$	Magnetic energy product/energy product
δ_w^B	Bloch domain wall
δ_w^N	Néel domain wall
AFM	Atomic Force microscopy
EBN	Electron beam nanolithography
EDS/EDX	Energy Dispersive X-Ray Spectroscopy
FCG	Free Cluster Generator
FIB	Focused Ion Beam
MFM	Magnetic Force Microscopy
Ip	In-plane
Oop	Out-of-plane

PLD	Pulsed Laser Deposition
QCM	Quartz Crystal Microbalance
RTP	Rapid Thermal Annealing
SEM	Scanning Electron Microscopy
SQUID VSM	Superconducting QUantum Interference Device Vibrating Sample Magnetometer
TEM	Transmission Electron Microscopy
VSM	Vibrating Sample Magnetometer
XMCD	X-ray magnetic circular Dichroism
XRD	X-Ray Diffractometer

List of Figures

- Figure I.1: (a) The major hysteresis loop of a ferromagnet $M(H)$. The magnetisation mechanism of a ferromagnet is mostly governed by nucleation-type or pinning-type behavior; (b) An energy landscape as a function of applied field $\mu_0 H$ for a homogeneously magnetized single-domain particle; and Details in obtaining more information from $M(H)$ loop, e. g., corrected and normal curves, where the $(BH)_{\max}$ -magnetic energy product are implied [7]..... 2
- Figure I.2: Various micromagnetic spin manifestations adapted from [15]: (a) single-domain state in very small particles, (b) two-domain configuration in fairly small particles with uniaxial anisotropy, (c) flux-closure in cubic magnets, (d) complicated domain structure in a polycrystalline magnet, (e) Multiple domains and domains walls in a thin film (f) Bloch wall in a thin film with perpendicular anisotropy, (g) Néel wall in a thin film with ip anisotropy, (h) single-domain particle and (I) two-domain particle. 5
- Figure I.3: Schematic sketch of different types of domain walls (a) Bloch wall rotating in the xOz plane; (b) Rotated Néel wall (for two consecutive orthogonal magnetisation) rotating in yOz plane; (c) Néel wall (for two opposite magnetisation) rotating in yOz plane; (d) Cross-tie wall (top-view) with mixture of Bloch and Néel walls. The Bloch and Néel walls are commonly found in oop and ip anisotropy thin films respectively..... 5
- Figure I.4: Three manifestations of hysteresis loops of pure magnetic soft phase inclusions/nanoparticles (black line), hard magnetic phase (matrix, red line) and the resultant of the combination of the two phases- the exchange spring nanocomposite (blue line). 7
- Figure I.5: Schematic one-dimensional model of the micromagnetic structure of the magnetic exchange-coupled nanocomposites. The hard magnetic phase stiffness response of soft magnetic phase at different levels of the applied field in a composite material [14]. 7
- Figure I.6: Three main manifestations of possible nanostructured composites (blue) which are the combination of soft (black) and hard (red) phases and their corresponding hysteresis loops in (a) layered structure configuration, (b) soft nanoparticles in hard matrix and (c) hard inclusion in soft matrix..... 8
- Figure I.7: Schematic diagram illustrates the effect of interaction between different soft regions with various distances between the soft inclusions. (a) the magnetisation decreases exponentially in case of large distance while (b) small distance leads to reduction in coercivity [10]..... 8
- Figure I.8: A pictorial representation scheme for Soft in Hard magnetic nanocomposite presented in this work..... 10
- Figure I.9: Schematic representation of the unit cell of $\text{Nd}_2\text{Fe}_{14}\text{B}$ (P42/mnm space group). The c/a ratio in the figure is exaggerated to emphasize the puckering of the hexagonal iron nets (the lattice parameters $a = 8.80 \text{ \AA}$, $c = 12.19 \text{ \AA}$) [57]. 11
- Figure I.10: Plane views of the three primary thin film growth manifestations (a) Frank-van der Merwe (FM-layer-by layer), (b) Volmer-Weber (VW-island), and (c) Stranski-Krastanov (SK-layer plus island), (d) step flow which caused by a fast intralayer mass transport. The film morphology is determined by the balance between the free energies of film surface ϵ_F , substrate surface ϵ_S , and the interface between film and substrate ϵ_{FS} [79]. 12
- Figure I.11: (a) Phase diagram of binary FePt alloy in which the crystal structures of the phases coming along with various composition ranges and temperatures are shown. Schematic illustration of unit cells of

different FePt states corresponding to (b) disordered state $\gamma(A1-fcc)$, (c) ordered state $\gamma_2(L1_0-fct)$ and (d) ordered state $\gamma_3(L1_2-fcc)$ [105].	14
Figure I.12: The estimation of clusters/NPs diameter- $2R$ as a function of number of atoms- n for Fe, Cu and Au atoms based on equation $R=r_{w.s}.n^{1/3}$.	17
Figure I.13: A 561-atom cuboctahedral NPs from an <i>fcc</i> crystal. The atoms on the edges are shaded for visualization.	17
Figure I.14: Slater-Pauling curve of mean atomic moment as a function of atomic number and their composition for various binary nanoalloys [109].	19
Figure I.15: Phase diagram of the Fe–Co binary system [105].	19
Figure I.16: The schematic <i>bcc</i> FeCo unit cell of ordered CsCl-B2 (α') phase when annealed below 920 K [7].	19
Figure II.1: Schematic setup for a conventional PLD.	21
Figure II.2: The time resolved plasma imaging under 1×10^{-1} mbar of ambient Ar gas at different time scale while ablating the $La_{0.4}Ca_{0.6}MnO_3$ cylindrical target by a KrF excimer laser (pulse duration: 20 ns, $\lambda = 248$ nm, fluence: $3 J.cm^{-2}$, frequency: 4 Hz, distance between target and substrate: 4 cm) [176].	22
Figure II.3: Beam profile of excimer (KrF, left) and solid state (Nd: YAG, right) lasers with single shot at 10 Hz, in (a) 2D; (b) constructed 3D; (c) O_x direction; (d) O_y direction. The (excimer and solid state) lasers parameters are: wavelength (248 and 1064, 532, 355) nm, beam profile (rectangular $\sim 26 \times 12$ mm ² and circled $\Phi \sim 10$ mm), pulse duration (25 and 5-8) ns, pulse energy up to (750 and 450) mJ, pulsing frequency (1–25 and 4-20) Hz, respectively. These images are adapted from [180].	23
Figure II.4: (a) The KrF excimer laser LightMachinery IPEX 742 (violet arrow) and (b) solid state laser (Nd: YAG laser)-Quanta-Ray Spectra Physics (green arrow).	24
Figure II.5: The conventional PLD and home-made Free cluster generator setup at IRCER [99,181].	25
Figure II.6: The advanced augmentation of the PLD and FCG setups in ablating the materials from a target of (a) the representation of classically irradiated target with small amount percentage of ablated zone compared to the whole target surface; (b) the home-made double targets holder which helps reducing time in changing the target from 15 minutes (individually separated target) to 3 minutes in the conventional PLD setup. Moreover, the rotary target + reflected mirror movements permit a sufficiently large ablated zone; and (c) The hypocycloidal motion allows increasing effectively the ablated zone compared to classically rotary target surface. The target diameters are all about 2.5 cm (one inch).	28
Figure II.7: The routine used in identifying deposition rate or the thickness distribution as depositing a NdFeB thin film by conventional PLD at distance: 3.3 cm, fluence: $5 J.cm^{-2}$, frequency 10 Hz, base pressure: 1×10^{-7} mbar (a) Lithography pattern in use and later measured the step height of the deposited film with Veeco DEKTAK 6M profilometer operating in the range of 10 nm to 1 mm; and (b) the reconstructed normalized thickness distribution of the deposited sample with size of 1×1 cm ² .	29
Figure II.8: Various deposition modes can be deposited with the combined PLD+FCG system for (a) a few NPs deposited on a substrate (normally NPs on Cu/C-TEM grid); (b) stacks of NPs deposited on a substrate; (c) nanocomposites of NPs embedded inside a matrix, taken place when using co-deposition; and (d) nanocomposites of layer-stack structures of thin film-NPs, developed when using sandwich mode of PLD and FCG [181].	30

Figure II.9: The schematic diagram of the main part of the RTP system at IRCER.	31
Figure II.10: The configuration of the TEM adapted from [198].....	32
Figure II.11: The schematic diagram of two-pass technique in investigating magnetic properties by MFM.	33
Figure II.12: The VSM-SQUID Quantum Design MPMS 3 setup associated with its main core configuration including Josephson junctions [201]......	34
Figure II.13: A comparison for correction to diamagnetic contribution from the substrate.....	35
Figure II.14: The representative illustration of single particles with idealized square hysteresis loops (hysterons), where the easy axis of magnetization is aligned with the applied field. Such representative could be used to interpret FORC diagrams.	36
Figure II.15: The FORC analysis with various representations. (a) A conventional dependence of magnetization on the applied field $-\mu_0H$; (b) the re-drawn three dimensional data showing the dependence of magnetization on both reversal field $-\mu_0H_r$ and μ_0H ; (c) The two dimensional surface map re-plotted from (b); and (d) FORC diagram distribution obtained from such FORC data in (a).....	37
Figure III.1: Nd/Fe atomic ratios on targets versus Nd/Fe atomic ratio on films. Films deposited by PLD at $T_d = 600^\circ\text{C}$ and $\sim 6 \text{ J.cm}^{-2}$ in Ta/Nd-Fe-B/Ta configuration on Si/SiO ₂ substrates. Black dash-dotted line represents the perfect congruent transfer.....	39
Figure III.2: Characterizations of Ta/Nd-Fe-B (150 nm)/Ta films deposited at 600°C on Si/SiO ₂ substrates, made from the five different targets (a) XRD patterns; (b) SEM images of the fractured cross sections; (c) AFM rms surface roughness; (d) Out-of-plane magnetic hysteresis loops (uncorrected for demagnetization field and normalized); and (e) Normalized dM/dH plots.	40
Figure III.3: Characterizations of the film made from target #2 deposited at 600°C on Si/SiO ₂ . (a) FIB-EBS cross-sectional images in which the Nd ₂ Fe ₁₄ B grains elongated in the z direction (black regions, one of which is indicated by a white arrow) are found together with a Nd-rich phase (gray regions, one of which is identified by an orange arrow), and (b) In-plane (ip) and out-of-plane (oop) magnetic hysteresis loops (uncorrected for demagnetizing field).	42
Figure III.4: The evolution of magnetic energy product $-(BH)$ as a function of internal applied field, of Ta/Nd-Fe-B (150 nm)/Ta films deposited at 600°C on Si/SiO ₂ substrates from five distinct targets (#1 – #5) by taking the values in the second quadrant after correcting the out-of-plane magnetic hysteresis loops for demagnetization field with the demagnetizing factor of about 0.73. Note that the maximum magnetic energy product $-(BH)_{\text{max}}$ is technically picked the maxima of the presented parabolas (BH) curves and this product considerably depends on the correcting with demagnetizing factor.....	42
Figure III.5: The evolution in structural properties - the XRD diffractograms of Ta/Nd-Fe-B/Ta thin films on Si/SiO ₂ substrates made from target #2 as a function of deposition temperatures- T_d ranging from 500°C to 700°C	44
Figure III.6: Plane-view SEM images showing the distinct surface microstructures of Ta/Nd-Fe-B/Ta films deposited at T_d (a) 500°C ; (b) 630°C ; and (c) 650°C . The scale bar in all three images is $1 \mu\text{m}$. (d) The AFM rms surface roughness of Ta/Nd-Fe-B/Ta films from target #2 as a function of deposition temperatures- T_d	45
Figure III.7: The evolution in magnetic properties of Ta/Nd-Fe-B/Ta thin films on Si/SiO ₂ substrates made from target #2 as a function of deposition temperatures- T_d ranging from 500°C to 700°C . (a) Oop magnetic	

hysteresis loops (uncorrected for demagnetization field and normalized); (b) Coercivity ($\mu_0 H_c$), remanent magnetization ($\mu_0 M_r$) and $(BH)_{\max}$ product corrected for demagnetizing field with $N = 0.73$ together with curves representing guides to the eye; and (c) Normalized dM/dH plots for this set of films.	46
Figure III.8: Dependence of monolayer formation time on partial deposition pressure of O_2 at different deposition temperatures.....	47
Figure III.9: Characterizations of the film made from target #2 deposited at 630°C on Si/SiO ₂ and <i>c</i> -sapphire with (a) XRD patterns; (b) SEM image for top-view of the film deposited on <i>c</i> -sapphire; (c) cross-sectional SEM images; and (d) oop magnetic hysteresis loops with absolute magnetization scale.	49
Figure III.10: Characterizations of the two NdFeB based thin films deposited at 630°C , from target #2, on (a) Si/SiO ₂ substrate; and (b) On <i>c</i> -sapphire substrate, in terms of AFM topography and MFM magnetic contrast in virgin magnetic state, with hard magnetic probe of coercivity larger than 0.5 T.	50
Figure III.11: Oop hysteresis loops (Normalized and uncorrected for demagnetization field) of seven Si/SiO ₂ /Ta/NdFeB/Ta thin films deposited at arbitrary temperatures in the ideal zone to test the reproducibility, from target #2.	51
Figure III.12: The schematic RTP annealing representation of the annealing procedure used in this work.	52
Figure III.13: (a) the XRD diffraction patterns of the Si/SiO ₂ /Ta/NdFeB/Ta thin films deposited from target #2, at 450°C , then processed by RTP at different annealing temperatures T_a , with heating rate of 50°C/s , in 60 s and 1×10^{-1} mbar of Ar flow; and (b) the additional zooms for as-deposited and typical annealed films.....	52
Figure III.14: The evolution of microstructures (top-view AFM and SEM images) of the Si/SiO ₂ /Ta/NdFeB/Ta thin films deposited from target #2, at 450°C , then processed by RTP at different annealing temperatures T_a , with heating rate of 50°C/s , in 60s and 1×10^{-1} mbar of Ar flow corresponding to (a) no RTP applied; (b) 450°C ; (c) 500°C ; (d) 550°C ; (e) 600°C ; and (f) 650°C	54
Figure III.15: The rms roughness of the Si/SiO ₂ /Ta/NdFeB/Ta thin films deposited from target #2, at 450°C , then processed by RTP at different annealing temperatures T_a , with heating rate of 50°C/s , in 60s and 1×10^{-1} mbar of Ar flow.	54
Figure III.16: The representative FIB-EBS cross-sectional images of the Si/SiO ₂ /Ta/NdFeB/Ta thin films deposited from target #2 then processed by RTP at different annealing temperatures of (a) 600°C , (b) 500°C , with heating rate of 50°C/s , in 60s and 1×10^{-1} mbar of Ar flow, and (c) The 450°C -deposited film without RTP.	55
Figure III.17: The (left) – the uncorrected for demagnetizing field and normalized oop hysteresis loops; and the (right) – the dM/dH plots of the Si/SiO ₂ /Ta/NdFeB/Ta thin films deposited from target #2, at 450°C , then processed by RTP at different annealing temperatures T_a , with heating rate 50°C/s , in 60s and 1×10^{-1} mbar of Ar flow.	56
Figure III.18: In-plane (ip) and out-of-plane (oop) magnetic hysteresis loops (uncorrected for demagnetization field) of the sample deposited from target #2, at 450°C and then applied heat treatment by RTP at 500°C , with heating rate of 50°C/s , in 60s and 1×10^{-1} mbar of Ar flow.	57
Figure III.19: The evolution in (a) structure (XRD patterns); (b) the S parameter and the LOF parameter; (c) the c/a ratio and $FWHM$ extracted from (001) peak; and (d) Crystallite sizes obtained from Scherrer	

equation (XRD) and AFM rms surface roughness as a function of KrF laser deposition frequencies, of the MgO/FePt (50 nm) thin films deposited from Fe₅₀Pt₅₀ target, at 750°C, at laser fluence 5 J.cm⁻²..... 60

Figure III.20: Characterizations of the structure with high resolution XRD of the 50 nm FePt film deposited from Fe₅₀Pt₅₀ target, at 750°C, 2 Hz, on heated MgO (001) single crystal substrate, (a) Comparison between conventional and high resolution XRD showing the in-plane relationship for FePt film and MgO substrate; (b) The ϕ – scan measurement showing the out-of-plane relationship for FePt film and MgO substrate; and (c) the rocking curve recorded through the (001) reflection of grown FePt film showing the film quality. 61

Figure III.21: The evolution in microstructure observed by SEM as a function of KrF laser deposition repetition rates, of the MgO/FePt (50 nm) thin films deposited from Fe₅₀Pt₅₀ target, at 750°C. 62

Figure III.22: (a) The normalized and uncorrected with demagnetizing field oop hysteresis loops of the MgO/FePt (50 nm) thin films deposited from Fe₅₀Pt₅₀ target, at 750°C, at laser fluence 5 J.cm⁻², with respect to the KrF laser deposition frequencies; and (b) The normalized dM/dH plots of such oop hysteresis loops..... 63

Figure III.23: The evolution in (a) structure (XRD patterns); (b) the S parameter and the LOF parameter; (c) the c/a ratio and $FWHM$; and (d) Crystallite sizes obtained from Scherrer equation followed by XRD and AFM rms surface roughness as a function of deposition temperatures – T_d ranging from RT to 750°C, of the MgO/FePt (35 nm) thin films deposited from Fe₅₀Pt₅₀ target, at 2 Hz, at laser fluence 5 J.cm⁻². .. 64

Figure III.24: The evolution in microstructure observed from SEM plan-view as a function of deposition temperatures ranging from RT to 750°C, of the MgO/FePt (35 nm) thin films deposited from Fe₅₀Pt₅₀ target, at 2 Hz, at laser fluence 5 J.cm⁻²..... 65

Figure III.25: (a) The normalized and uncorrected with demagnetizing field oop hysteresis loops; (b) The normalized dM/dH plots of such oop hysteresis loops; and (c) a sum-up of magnetic properties of the MgO/FePt (35 nm) thin films deposited from Fe₅₀Pt₅₀ target, at 2 Hz, at laser fluence 5 J.cm⁻² as a function of deposition temperatures – T_d 66

Figure III.26: The structural, microstructural, and magnetic comparison between films deposited on MgO and Si/SiO₂ (100nm) substrate at 750°C, from Fe₅₀Pt₅₀ target, 2 Hz, at laser fluence 5 J.cm⁻² (a) The XRD patterns; (b) the plan-view microstructure of film deposited on Si/SiO₂; and (c) The normalized and uncorrected with demagnetizing field oop hysteresis loops. 68

Figure III.27: The evolution in (a) structure (XRD patterns); (b) the S parameter and the LOF parameter; (c) the c/a ratio and $FWHM$; and (d) AFM rms surface roughness of the as-deposited sample and annealed samples at 50 °C/s, in 60 s, and in 1×10^{-1} mbar of Ar flow as a function of annealing temperatures – T_a 69

Figure III.28: The evolution in microstructures of annealed samples (at 50 °C/s, in 60 s) as a function of T_a for two kinds of equivalent characterizations AFM and SEM. 71

Figure III.29: Characterizations of FePt films deposited on Si/SiO₂ substrates at RT and then processed by RTP (heating rate 50 °C/s, in 60 s) as a function of T_a (a) Histograms of grain size distribution of films annealed at 700 °C, 750 °C, and 800 °C extracted from plane-view SEM images; (b) Out-of-plane magnetic hysteresis loops (uncorrected for demagnetization field and normalized) of as deposited and annealed films; (c) The normalized dM/dH plots for this set of films; (d) Representative ip and oop magnetic hysteresis loops (uncorrected for demagnetization field) of samples annealed at 650°C, 700 °C,

and 750 °C; and (e) A classical representation of magnetic coercivity- μ_0H_c , remanent magnetisation- μ_0M_r , and remanence ratio- M_{0T}/M_{7T} of the annealed films.	72
Figure III.30: The evolution of (a) structure (XRD patterns); (b) the S parameter and the LOF parameter; (c) the c/a ratio and $FWHM$; and (d) rms roughness of the as-deposited sample and annealed samples at 750 °C, in 60 s, and in 1×10^{-1} mbar of Ar flow as a function of heating rates.	74
Figure III.31: The microstructures of annealed samples ($T_a = 750$ °C, in 60 s) as a function of heating rates, characterized by AFM and SEM. The scale bar in AFM images is 500 nm.	75
Figure III.32: Characterizations of FePt films deposited on Si/SiO ₂ substrates at RT and then processed by RTP (at $T_a = 750$ °C, in 60 s) as a function of heating rates (a) Out-of-plane magnetic hysteresis loops (uncorrected for demagnetization field and normalised) of as deposited and annealed films; (b) The normalized dM/dH plots for this series of annealed films; and (c) A representation of magnetic coercivity- μ_0H_c , remanent magnetisation- μ_0M_r , and remanence ratio- M_{0T}/M_{7T} of the annealed films.	76
Figure III.33: The evolution of (a) structure (XRD patterns); (b) the S parameter and the LOF parameter; (c) the c/a ratio and $FWHM$; and (d) rms roughness of the as-deposited sample and annealed samples at 750 °C, at 50 °C/s, and in 1×10^{-1} mbar of Ar flow as a function of annealing time.	76
Figure III.34: The surface evolution in microstructures of annealed samples (at 750°C/s, at 50°C/s) as a function of annealing time probed by AFM (above) and statistical grain size distribution extracted from SEM images (below). The scale bar in the AFM images is 500 nm.	77
Figure III.35: Characterizations of FePt films deposited on Si/SiO ₂ substrates at RT and then processed by RTP ($T_a=750$ °C, heating rate 50 °C/s) as a function of annealing time (a) Out-of-plane magnetic hysteresis loops (uncorrected for demagnetization field and normalised) of as deposited and annealed films; (b) The normalized dM/dH plots for this series of annealed films; and (c) A representation of magnetic coercivity- μ_0H_c , remanent magnetisation- μ_0M_r , and remanence ratio- M_{0T}/M_{7T} of the annealed films.	79
Figure IV.1: The experimentally normalized (per hour) deposition rate as a function of the opening t – time of the helium pulsed valve determined by AFM (from Fe ₆₅ Co ₃₅ alloy target). In each single measurement, a stack of NPs corresponding to 15 minutes of deposition, the helium pressure of 10 bar, the Nd:YAG laser fluence ~ 8 J.cm ⁻² , laser repetition of 4 Hz and the delay between the laser and the helium pulsed valve of 1.650 ms, PLD chamber base pressure of 1×10^{-6} mbar are applied.	81
Figure IV.2: TEM images for Fe-Co clusters/NPs and their corresponding size histogram together with lognormal/gaussian fitted curves with a variety of opening t – time of (a) 300 μ s; (b) 400 μ s; (c) 500 μ s and (d) 600 μ s. The number of nanoparticles in the histogram is about 400 NPs.	83
Figure IV.3: The calculated and normalized relative population of number of Ag metal NPs as a function NPs' diameter induced by changing τ – the degree of condensation. Note that τ will be again controlled by the opening t – time. The figure is partly adapted from [99,181].	84
Figure IV.4: The EDS spectrum for a Fe-Co clusters/NPs on TEM grid characterized by TEM JEOL 2100F.	85
Figure IV.5: The XPS compositional analysis for stacks of FeCo NPs deposited from Fe ₆₅ Co ₃₅ target, at various deposition temperatures – T_d of (a) RT; (b) 500°C; (c) 730°C. (d) The Co/Fe ratio from such sample is lately compiled in, the blue straight line at Co/Fe = 0.54 \sim 35/65 representing guide to the eye. Note that the XPS etching profile is of raster size of 16 mm ² , etched with 5 keV, 7 mA, and photoelectrons	

is at 1s, 2p, 2p, 1s, 2p level for C, Co, Fe, O, Si respectively. The gray region qualitatively presents for start of etching to the substrate.....	86
Figure IV.6: Characterizations of stacks of FeCo clusters/NPs deposited on TEM grid at RT with opening t – time, $t = 500 \mu\text{s}$ (a) TEM image with the inset of representative SAED pattern extracted from the whole TEM image; (b) Zooms (HRTEM images) of some NPs focused from TEM images and their corresponding Fast Fourier Transforms (FFTs), for which the (hkl) indices are indicated; (c) A precisely indirect approach to extract the inter-reticular distance from SAED patterns (averagely collected from all of the clusters/NPs in the image); (d) A precisely direct approach to obtain the inter-reticular distance from a single NPs; and (e) a HRTEM image consists of several NPs showing well crystallized NPs (orange arrows) and being crystallized in short range order (white arrows).....	88
Figure IV.7: The XRD diffractograms of stacks of FeCo clusters/NPs, with opening t – time, $500 \mu\text{s}$, as a function of deposition temperatures – T_d on Si/SiO ₂ substrate.....	89
Figure IV.8: The AFM cross-sectional analysis of lines crossing the middle images and the surface morphology of stacks of Fe-Co clusters/NPs deposited onto Si/SiO ₂ (100 nm) in one hours at various deposition temperatures – T_d , which are below and above the transition temperature of 647°C for Fe ₆₅ Co ₃₅ from ordered phase (B2) to disordered phase (A2).	90
Figure IV.9: Plane-view SEM images (Inlens mode) for stacks of NPs deposited at various deposition temperatures – T_d from RT to 730°C, on Si/SiO ₂ substrates.	91
Figure IV.10: The AFM rms surface roughness of stacks of FeCo NPs as a function of deposition temperatures – T_d	92
Figure IV.11: The magnetic response of 100 nm thickness of stacks of FeCo NPs (averaged diameter of around 4 nm) measured as the applied field is perpendicular (<i>oop</i>) and parallel (<i>ip</i>) with the substrate at RT in (left) large range of applied field (± 3 T) and (right) a zoom (± 10 mT).	92
Figure IV.12: The magnetic response of 100 nm thickness of stacks of FeCo NPs at different deposition temperatures – T_d (averaged diameter of around 4 nm) measured as the applied field is perpendicular (<i>oop</i>) with the substrate in (a) large range of applied field (± 3 T) and (b) a zoom (± 100 mT).	93
Figure IV.13: The magnetic response of 100 nm thickness of stacks of FeCo NPs (averaged diameter of around 4 nm) measured as the applied field is perpendicular (<i>oop</i>) and parallel (<i>ip</i>) with the substrate in (a) large range of applied field (± 3 T) and (b) a zoom (± 40 mT) for sample annealed at 750°C by RTP, 60s.	95
Figure V.1: The schematic diagram of FePt-FeCo/Co sandwich structured continuous film.	97
Figure V.2: The evolution in structure of the as-deposited sample and annealed samples with RTP at 750°C, 50°C/s, in 60 s, and in 1×10^{-1} mbar of Ar flow as a function of the Fe ₆₅ Co ₃₅ volume content. ..	97
Figure V.3: Plane-view SE – SEM images of the tri-layer FePt/Fe ₆₅ Co ₃₅ (or Co)/FePt films as a function of Fe ₆₅ Co ₃₅ (or Co) volume content, deposited at RT on Si/SiO ₂ and then applied RTP heat treatment at 750°C, 50°C/s, 60s, 1×10^{-1} mbar of Argon flow. (a) 15% Co; (b) 15% Fe ₆₅ Co ₃₅ ; (c) 30% Fe ₆₅ Co ₃₅ ; and (d) 40% Fe ₆₅ Co ₃₅ . Inset of figure (b) displays a high resolution plane-view Inlens SEM image of the film. Note that the contrast (black and white parts) is reserved between the SE and Inlens images.	99
Figure V.4: The collection of normalized and uncorrected with demagnetizing field <i>oop</i> hysteresis loops; (b) The normalized dM/dH plots of such <i>oop</i> hysteresis loops; and (c) a sum-up of magnetic properties of the FePt/FeCo (and Co) trilayers as a function of hard-phase FePt percentage. The trilayer-structured	

samples were deposited at RT and then subjected to RTP in 1×10^{-1} mbar of Argon flow, at 750°C , at 50°C/s , and in 60s.....	100
Figure V.5: Magnetic characterizations of the tri-layer FePt/Fe ₆₅ Co ₃₅ /FePt film with 15% Fe ₆₅ Co ₃₅ content, deposited at RT on Si/SiO ₂ and then applied RTP heat treatment at 750°C , 50°C/s , 60s, 1×10^{-1} mbar of Argon flow. (a) in-plane (ip) and out-of-plane (oop) magnetic hysteresis loops; (b) oop FORC raw data; and (c) the respective FORC diagram. All the data shown here are subtracted from substrate diamagnetic contribution and uncorrected for demagnetization field.	101
Figure V.6: Model of interdiffusion calculation for concentration – C of the materials with different concentration corresponding to $C_0 > C_1$ (left), and the concentration profile obtained from Fick's second law of diffusion (right).	103
Figure V.7: The calculated diffusion profiles for Fe diffusion to L1 ₀ -FePt (a) and Pt (in L1 ₀ -FePt) diffusion to Fe (b) during the annealing 10s and 60s at 750°C . The position distance $x = 0$ is originated the side edges between Fe layer (left side of graph/Figure V.6-left) and FePt layer (right side of graph/Figure V.6-left).	104
Figure V.8: The calculated diffusion length followed by the Arrhenius equation at various annealing conditions as a function of (a) annealing time; and (b) annealing temperatures.	105
Figure V.9: TEM cross-sectional images of the tri-layer heterogeneous structured sample of FePt/Co (stacks of NPs)/FePt before annealing. (a) the TEM overview image with the inset of HRTEM images for the interface between the SiO ₂ and FePt layers; (b) The HRTEM image for the three layers; (c) The dark field (HAADF) STEM image of the tri-layer system; and (d) The SAED pattern of a region crossing through the three layers with the indicated (hkl) indices.....	107
Figure V.10: TEM cross-sectional images of the tri-layer heterogeneous structured sample of FePt/Co (stacks of NPs)/FePt after annealing by RTP at 750°C , 50°C/s , 30s. (a) The TEM overview image; (b) The HAADF image with high magnification; (c) The HAADF image with low magnification for the three layers; (d), (e), (f) A collection of soft magnetic Co-NPs inside the hard magnetic FePt matrix – HRTEM images; (g) The SAED pattern of the area without NPs in (f) image – red dashed square; (h) The SAED pattern of the area with both NPs and several hard magnetic FePt grains in the (h) image – red dashed square; and (i) the HRTEM image focusing on the intermixing region between the NPs and the matrix of image (f). Note that the white arrows in (a), (b) and (c) indicate the NPs; and the (hkl) indices are indicated in (g) and (h).....	108
Figure V.11: The schematic diagram of FePt-FeCo/Co nanocomposite structure.	110
Figure V.12: The XRD diffraction patterns as a function of 4 nm – Fe ₆₅ Co ₃₅ ($t = 480 \mu\text{s}$) soft magnetic NPs' percentage, embedded in 15 nm FePt matrix, at RT on Si/SiO ₂ and then processed by RTP, at annealing temperature of 750°C , heating rate of 50°C/s , annealing time of 60s, and in 1×10^{-1} mbar of Ar flow.....	110
Figure V.13: The AFM morphological and SEM (SE mode) microstructural evolution of as-deposited and annealed nanocomposites as a function of 4 nm – Fe ₆₅ Co ₃₅ NPs volume content, embedded in 15 nm FePt matrix, at RT on Si/SiO ₂ and then processed by RTP, at annealing temperature of 750°C , heating rate of 50°C/s , annealing time of 60s, and in 1×10^{-1} mbar of Ar flow. Size of each AFM image is $2 \times 2 \mu\text{m}^2$	112
Figure V.14: The plane-view SEM (Inlens mode) and EDS maps observed with (FIB-SEM) for the two annealed samples of only FePt matrix (upper) and nanocomposites with 25% volume content of 4 nm –	

Fe ₆₅ Co ₃₅ NPs, embedded in 15 nm FePt matrix (under). All were deposited at RT on Si/SiO ₂ and then processed by RTP (750°C, 50°C/s, 60s, and in 1 × 10 ⁻¹ mbar of Ar flow).	113
Figure V.15: The magnetic characterizations of nanocomposites based FePt deposited on Si/SiO ₂ substrates at RT and then processed by RTP (750°C, 50 °C/s, 60 s) as a function of of 4 nm – Fe ₆₅ Co ₃₅ NPs volume content (left) Out-of-plane magnetic hysteresis loops (uncorrected for demagnetization field and normalized) of as deposited and annealed films; (right) A classical representation of magnetic coercivity- μ_0H_c , remanent magnetisation- μ_0M_r , remanence ratio- M_{0T}/M_{7T} , and calculated saturation magnetisation- μ_0M_s corresponding to the Fe ₆₅ Co ₃₅ volume content of the annealed films. Note that the μ_0M_s of L1 ₀ -FePt and Fe ₆₅ Co ₃₅ are 1.43 T and 2.45 T are applied to the calculated estimation.	114
Figure V.16: Advanced magnetic characterizations (oop FORC raw data, ip $M(H)$ loops, and the respective oop FORC diagrams) of the nanocomposites with different volume content of 4 nm – Fe ₆₅ Co ₃₅ NPs, after annealing at 750°C, 50°C/s, 60s. All the data has been subtracted from substrate diamagnetic contribution and uncorrected for demagnetization field.....	115
Figure V.17: The dependence of XRD diffraction patterns on the structured nanocomposites with different configurations in terms of NPs sizes (2.7 nm and 4 nm) deposited by FCG and layer deposited from PLD. Note that the case study is dedicated to 15% of Fe ₆₅ Co ₃₅ , in 15 nm FePt matrices. Samples were deposited at RT on Si/SiO ₂ and then processed by RTP, at annealing temperature of 750°C, heating rate of 50°C/s, annealing time of 60s, and in 1 × 10 ⁻¹ mbar of Ar flow.	117
Figure V.18: The dependence of microstructure (SEM images, Inlens mode) on the structured nanocomposites with different configurations in terms of NPs sizes (2.7 nm and 4 nm) deposited by FCG, layer deposited from PLD, and 100% FePt film. Note that the case study is dedicated to 15% of Fe ₆₅ Co ₃₅ with fixed 15 nm FePt matrices, all compared to the 100% FePt film. Samples were deposited at RT on Si/SiO ₂ and then processed by RTP, at annealing temperature of 750°C, heating rate of 50°C/s, annealing time of 60s, and in 1 × 10 ⁻¹ mbar of Ar flow.	117
Figure V.19: Magnetic characterizations (oop FORC raw data, ip $M(H)$ loops, and the respective oop FORC diagrams) of the nanocomposites with different configurations (size of NPs embedded and continuous soft layer), after annealing at 750°C, 50°C/s, 60s. All the data has been subtracted from substrate diamagnetic contribution and uncorrected for demagnetization field.	118
Figure V.20: The microstructural evolution SEM (Inlens mode) of annealed nanocomposites as a function of 4 nm – Fe ₆₅ Co ₃₅ NPs volume content embedded in 15 nm FePt matrix. Nanocomposites was initially deposited at RT on Si/SiO ₂ and then processed by RTP, at annealing temperature of 750°C, heating rate of 50°C/s, annealing time of 10s, and in 1 × 10 ⁻¹ mbar of Ar flow.....	120
Figure V.21: The magnetic characterizations of nanocomposites based FePt deposited on Si/SiO ₂ substrates at RT and then processed by RTP (750°C, 50 °C/s, 10 s) as a function of of 4 nm – Fe ₆₅ Co ₃₅ volume content (left) Out-of-plane magnetic hysteresis loops (uncorrected for demagnetization field and normalized) of annealed films; (right) A classical representation of magnetic coercivity- μ_0H_c , remanent magnetisation- μ_0M_r , remanence ratio- M_{0T}/M_{7T} , and calculated saturation magnetisation- μ_0M_s corresponding to the Fe ₆₅ Co ₃₅ volume content of the annealed films. The μ_0M_s of L1 ₀ -FePt and Fe ₆₅ Co ₃₅ are 1.43 T and 2.45 T are applied to the calculated estimation, respectively.	121
Figure V.22: The microstructural evolution SEM (Inlens mode) of annealed nanocomposites as a function of 4 nm – Co NPs volume content embedded in 15 nm FePt matrix. Nanocomposites was initially deposited at RT on Si/SiO ₂ and then processed by RTP, at annealing temperature of 750°C, heating rate of 50°C/s, annealing time of 10s, and in 1 × 10 ⁻¹ mbar of Ar flow.....	122

Figure V.23: (a) The Out-of-plane magnetic hysteresis loops (uncorrected for demagnetization field and normalized) of annealed nanocomposites based FePt deposited on Si/SiO₂ substrates at RT and then processed by RTP (750°C, 50 °C/s, 10 s) as a function of of 4 nm – Co NPs vol content. The ip and oop $M(H)$ loops of the annealed nanocomposites with different soft Co NPs concentrations (b) 0%; (c) 7%; (d) 15%; (e) 22%; and (f) 25 %..... 123

Figure V.24: A summary of magnetic coercivity- μ_0H_c , remanent magnetisation- μ_0M_r , remanence ratio- M_{0T}/M_{7T} , and calculated saturation magnetisation- μ_0M_s corresponding to the 4 nm Co NPs volume content of the annealed films. The μ_0M_s of L10-FePt and Co are 1.43 T and 1.7 T are applied to the calculated estimation, respectively..... 124

Figure V.25: (left) The schematic diagram of FePt (3.75nm)/Ta (0.5 nm)/Co nanocomposite with multi-layer system. The thickness of stack of 4 nm Co NPs depends on how much dilution of the nanocomposite is. (right) The XRD diffraction patterns as a function of 4 nm – Co ($t = 480 \mu s$) soft magnetic NPs' percentage, embedded in 15 nm FePt matrix, at RT on Si/SiO₂ and then processed by RTP, at annealing temperature of 750°C, heating rate of 50°C/s, annealing time of 10s, and in 1×10^{-1} mbar of Ar flow. 125

Figure V.26: The evolution of microstructure as a function of 4 nm Co NPs vol content in nanocomposited performed by plane-view SEM (Inlens mode), 1st row. The microstructures and EDS maps observed with FIB-SE mode for the two annealed nanocomposites with 15% (2nd and 3rd rows) and 22% (4th and 5th rows) volume content of 4 nm – Co NPs, embedded in 15 nm FePt matrices, respectively. All were deposited at RT on Si/SiO₂ and then processed by RTP (750°C, 50°C/s, 10s, and in 1×10^{-1} mbar of Ar flow). 126

Figure V.27: The magnetic characterizations of nanocomposites based FePt deposited on Si/SiO₂ substrates at RT and then processed by RTP (750°C, 50 °C/s, 10 s) as a function of of 4 nm – Co NPs volume content (top-left) Out-of-plane magnetic hysteresis loops (uncorrected for demagnetization field and normalized) of annealed samples; (bottom-left) The in-plane and out-of-plane hysteresis loops of the nanocomposites with Ta spacer and 15% Co volume content; (right) A sum-up of magnetic coercivity- μ_0H_c , remanent magnetisation- μ_0M_r , remanence ratio- M_{0T}/M_{7T} , and calculated saturation magnetisation- μ_0M_s corresponding to the Co volume content of the annealed samples. Note that the μ_0M_s of L10-FePt and Co are 1.43 T and 1.7 T are applied to the calculated estimation..... 127

Figure A. 1: Energy levels diagram in the (a) Excimer Laser-KrF and (b) Nd-YAG Laser [256]. 133

Figure A. 2: The schematic diagram of synchronizing between the two lasers and pulsed He valve/IOTA ONE to deposit nanocomposites, in which a representation (a) showing how to trigger the signal of pulsed valve (CCD high-speed camera) and Nd:YAG laser and (b) the PLD+FCG system is all triggered and synchronized by the digital pulse generator. 134

Figure A. 3: The schematic diagram of a SEM [258]. 136

Figure A. 4: Illustration of observation chamber of the FIB-ZEISS CROSSBEAM 550 at IRCER 137

Figure A. 5: The schematic diagram of a contact AFM mode [259]..... 137

Figure A. 6: Magnetic hysteresis loops of the PrCo_x-Co nanocomposite at different temperatures. The arrows indicate the switching points [261]..... 138

Figure A. 7: The easy axis demagnetizing curve and recoil loops measured at 300 K of Sm-Co/Fe nanocomposite deposited at (a) 100°C and (b) 400°C. The inset in (b) shows normalized remanence curves of sample deposited at 100°C and 400°C respectively [263]. 139

Figure A. 8: The Henkel plots of FePt–Fe₃Pt composite systems revealing the magnetic interactions between compacted nanoparticles. Here, x denotes for the weight fraction of Fe₃O₄ NPs of the precursor of the soft phase added into FePt NPs in the soft and hard magnetic phases, respectively, before a heat treatment [253]. 139

Figure A. 9: The high resolution XPS phase compositional analysis for stacks of FeCo NPs deposited from Fe₆₅Co₃₅ target, at 730°C for 2p spectra corresponding to (a) Co element core-level band; and (b) Fe element core-level band..... 140

Figure A. 10: The TEM prepared sample representation soldered by FIB, in which (a) SEM images of FIB cut slide readily to be transferred to the TEM holder; (b) and (c) Procedure to place and fix the TEM sample to the pin..... 142

List of Tables

Table I.1: Intrinsic properties and derived properties at room temperature for several typical hard magnetic materials [15,18–20].	4
Table I.2: Domain wall parameters for several ferromagnetic materials adapted from [7,25,26]. Note that the δ_w , σ_w , and I_{ex} are all recalculated by the formulas given in this thesis.	6
Table I.3: Theoretically predicted magnetic properties for some nanocomposites [10,52–56].	9
Table I.4: Positional parameters and standard deviations of each single element in the $Nd_2Fe_{14}B$ crystal structure. [57,58].	11
Table I.5: The magnitude of the magnetic moments in μ_B /atom calculated for three ordered Fe-Pt alloys with stoichiometric concentrations [110].	15
Table II.1: The deposition parameters used in depositing thin films, NPs and nanocomposites.	30
Table III.1: Magnetic properties of the Si/SiO ₂ /Ta/NdFeB/Ta thin films deposited from target #2, at 450°C, then processed by RTP at different annealing temperatures T_a , with heating rate 50°C/s, in 60s and 1×10^{-1} mbar of Ar flow.	56
Table III.2: Parameters used to estimate the ordering parameter S of the FePt thin films [122,214,215].	59
Table IV.1: The mean diameter and size dispersion of the clusters/NPs deposited on TEM grid with various opening t – time ranging from 300 μs to 600 μs .	84
Table IV.2: The extracted structural parameters of stacks of NPs deposited on TEM grid at RT employed by the indirect approach from XRD/SAED patterns.	88
Table IV.3: Crystallite sizes obtained from Scherrer equation based on by XRD spectrum.	90
Table IV.4: The experimental magnetic properties of stacks of Fe ₆₅ Co ₃₅ NPs deposited at various temperatures ranging from RT to 730°C.	94
Table V.1: The diffusing activation parameters for the diffusion in the Fe/FePt system [241–243].	104
Table V.2: Nanocomposites crystallite sizes obtained from Scherrer equation based on XRD patterns.	111
Table V.3: The effective anisotropy constant and anisotropy field of the nanocomposites based FePt as a function of 4 nm NPs Co volume content.	124

Thesis motivation

1. General introduction

Magnetic materials have so far contributed considerably to the development of science and technology as well as all aspects of our modern lives. At macroscale, electric power generators, electric vehicles, and actuators are among the applications that are visible to our eyes. Vice versa at microscale, magnetic nanoparticles enhance the magnetic contrast while they are used magnetic resonance imaging to diagnose illnesses of a patient in medical operation, etc. Traditionally, the magnetic materials can be manifested into three distinct categories regarding their coercivity, which is one of the characteristic parameters of a magnetic material: soft, semi-hard, and hard magnetic material [1]. The soft magnetic materials whose coercivities are smaller than 1×10^{-3} T (1 mT), high permeability, low magnetic losses, and are widely exploited in today's applications such as magnetic cores in electric transformers [2], NPs for drug delivery [3,4] and magnetic sensors [5]. A less glamorous, but no less important set of materials provide modest coercive force for applications such as brakes, clutches, tensioners and being machined with standard metalworking tools. Those are semi-hard magnetic materials possessing the intermediate coercive field ranging from 1×10^{-3} T to 1×10^{-2} T. Most of these materials are some kinds of malleable alloys like FeCrCo, remalloy, vicalloy, cunife, cunico, etc, that they are easily extruded into wire, rods and stamped into other forms. The last in the magnetic catalog is hard magnetic materials or permanent magnets with coercivity exceeding more than 1×10^{-2} T (10 mT), and they can keep the remanence in the absence of imposed magnetic field. Currently, the permanent magnets have been extensively attracted from researches and practical applications. For instance, they have registered irreplaceable potential for wide range of demands such as electric generator (wind turbine), transport (electric vehicles, robotics), electronics devices (mobile phones), Micro-electro-mechanical systems (MEMS) [6] and the Internet of Things (IoT) reflected in terms of magnetic data storage.

Owing to the enormous importance of permanent magnets, efforts to enhance the magnet performance are stunningly attractive. For comparing between magnets, a key figure of merit often used is magnetic energy product $(BH)_{\max}$, which evaluates the potential energy stored in the magnets. The $(BH)_{\max}$ product doubled in value every 12-year period in 20th century [7], and presently it is stagnant with the discovery of rare earth (RE) transition metal magnet with $\text{Nd}_2\text{Fe}_{14}\text{B}$ phase [8,9]. The RE element based magnets prove crucial weight in the strategic value chains, however, they are facing challenging problems, such as RE metal crisis in 2011 of ten-fold prices increased, environment pollution owing to the RE mining, emergence of energy transformation from classical agenda into clean and renewable them, etc. A compromise resolution to significantly enhance the $(BH)_{\max}$ without adding an additional amount of RE element is to develop two-phase/or soft-hard nanocomposites, at which the soft and hard magnetic phases co-exist and are exchanged couple to each other [10]. The exchanged couple combination between the high coercivity of the hard magnetic phase and the high magnetisation of soft phase, results in exceptional properties in soft-hard nanocomposites (expressed by high values of remanence, $(BH)_{\max}$). Therefore, the objective of the thesis is to fabricate and examine the potential of soft-hard nanocomposites with magnetic properties that those of today's high performance magnets.

2. Soft in HArD MAgnetic Nanocomposite (SHAMAN ANR-16-CE09-0019)

Since the last independent and simultaneous discovery in Japan and the United States of the most famous permanent magnet based on $\text{Nd}_2\text{Fe}_{14}\text{B}$, an iron-rich tetragonal phase in 1984 [8,9], there has been no major development in maximum magnetic energy product $(BH)_{\text{max}}$ of permanent magnets, meanwhile the room temperature (RT) energy product for such NdFeB-based magnets approaches (~87%) closely to the theoretical limit of $516 \text{ kJ}\cdot\text{m}^{-3}$ [11]-thick film $400 \text{ kJ}\cdot\text{m}^{-3}$; [12]-sintered magnet $474 \text{ kJ}\cdot\text{m}^{-3}$. Therefore it has a huge motivation for people to look for a magnetic material that retains $(BH)_{\text{max}}$ surpassing the best theoretical limit of $\text{Nd}_2\text{Fe}_{14}\text{B}$ single phase.

Back to the past, as Coehoorn and his colleagues initially discovered in 1989 [13] the exchanged coupling effect between a hard magnetic phase and a high magnetisation soft phase in the rapidly quenched Fe_3B - $\text{Nd}_2\text{Fe}_{14}\text{B}$ nano-structured composite ribbons that significantly increase the magnetisation and hence augment the $(BH)_{\text{max}}$ to $95 \text{ kJ}\cdot\text{m}^{-3}$. A couple of years later, the concept of nano-structured composites was proposed by Kneller and Hawig [14] by suggesting a 1D simulation model of an exchange coupled soft in hard magnetic nanocomposite based on the experimental finding from Coehoorn. The simulation presents that such nanocomposites with a desired nano-structured could be an elegant approach to considerably escalate the $(BH)_{\text{max}}$ in permanent magnets. Once the soft phase is sufficiently thin enough, due to the interphase exchange coupling effect, magnetic moments of both soft and hard magnetic phases will be shifted coherently.

Another two years later, Skomski and Coey [10] drew their attention and investigated a geometrical configuration of the oriented nanostructured two-phase nanocomposite by examining free energy terms given in a ferromagnetic nanocomposite system. They show that without losing the coercive field required for high $(BH)_{\text{max}}$, the soft phase volume might be as high as 91% of the nanocomposites [10]. Additionally in a well-defined soft-hard nanocomposite, the $(BH)_{\text{max}}$ could go up to $1 \text{ MJ}\cdot\text{m}^{-3}$, and this attracts a wide range of interest due to a low weight percentage of RE element demanded.

On the way to searching for such superior magnetic materials, if that material is not available in nature, an artificially structured material could be a right approach (layer-layer, nano-inclusion inside a matrix, etc). Over the last few years, advances in metallurgical processing approaches have developed a variety of soft-hard nanocomposites fabrications. However, the current nanocomposites are of practically poor magnetic properties owing to the degradation of coercivity for high $(BH)_{\text{max}}$ value, which is attributed to simple combination of soft and hard phases, or insufficient control the dimensions of the soft phase less than twice the domain wall width of the hard phase [10]. For this purpose, the thesis will use modern nanoscience tools based on a dual pulsed laser ablation system consisting of a conventional Pulsed Laser Deposition coupled with a specific Free Cluster Generator to produce model soft-hard nanocomposites with various architectures. The soft-hard nanocomposites will be investigated and correlated the physical properties to comprehend the many interested aspects of the superior nanocomposites.

3. Outline

This thesis includes five chapters and is structured as follows:

Chapter I encloses briefly the main magnetic background including some important physical magnetic quantities and then passes through overviews about hard, soft and nanocomposites magnetic materials. The main emphases are on the spring magnets, whose magnetic property possesses the highest $(BH)_{\max}$, and on why this thesis should start from NdFeB, FePt, FeCo, Co magnetic materials.

In the next part, Chapter II shows the preparation in each single stage of fabrication of hard magnetic matrices, soft magnetic nanoparticles and especially the magnetic nanocomposites. In addition, some of the modern nanoscience tools available are introduced and explained why they are well adapted to characterize the fabricated samples.

Following the two previous sections, Chapter III reveals some very first initial results of NdFeB and FePt based thin films. For NdFeB based thin films, the dependence of magnetic properties of the deposited films on thin films' compositions, deposition temperatures, substrates and two-step annealing is demonstrated explicitly, while for FePt based thin films, the influence of deposition frequencies, deposition temperatures, substrates and two-step annealing conditions on structures, microstructures and thin films' magnetic properties is described adequately. These originally important results determine the optimal factors which are responsible for processing the consecutively deposited and fabricated soft-hard nanocomposites.

In Chapter IV, by synthesizing nanoparticles in the gas phase, the impacts of free cluster generator's parameters, deposition conditions on structures, morphologies, size distribution and magnetic properties of nanoparticles are identified positively. These investigations contribute to the further understanding of the nanoparticles and the upcoming deposited nanocomposites.

Chapter V deals with embedding soft magnetic nanoparticles into hard magnetic matrices to form magnetic nanocomposites and characterizing the fabricated nanocomposites. The theoretical calculation and TEM imaging are coherent with diffusion, which is associated with Ostwald ripening mechanism, dewetting process and Kirkendall effect, for which the soft and hard magnetic phases are both coexisted and with limited intermixing region between the two phases. It is shown that the magnetic properties of such nanocomposites are all dependent on soft phase volume content, nanoparticles' diameters, architecture of nanocomposites, the nature of soft nanoparticles, and the capping Ta layer for better preventing diffusion. For deeper comprehension, additional First Order Reversal Curves are performed, that confirm the magnetic contribution of each individual phase to the total magnetic properties together with the coupling effect of hard and soft magnetic phases in the nanocomposites.

Chapter I. Theoretical background and revision

This part intends to present the most fundamental magnetic parameters and characteristic lengths, which do a favor in justifying the experimental outcomes on ferromagnetic materials of hard magnetic thin films ($\text{Nd}_2\text{Fe}_{14}\text{B}$, FePt), soft magnetic nanoparticles-NPs (Co , $\text{Fe}_{65}\text{Co}_{35}$) and the promising soft-hard magnetic nanocomposites. Owing to the nanocomposites based on the combinations of both hard magnetic matrices and soft magnetic NPs, the overviews concerning each single component of the nanocomposites are therefore described. While the general overview on magnetic nanocomposites provides comprehensive ideas in estimating their compositions, structures and magnetic properties, the other constituent ingredients deal with the prerequisite parameters to obtain individually good magnetic properties and thus contribute to the phenomenal properties of the combined nanocomposites.

I.1. Magnetism fundamentals and soft-hard nanocomposites

The following fundamental backgrounds presented in this thesis already discussed in many other textbooks in details [7,15]. Here they are just briefly listed.

I.1.1. Magnetic parameters

Essential practical characteristics when examining the ferromagnetic soft-hard nanocomposites are to understand the response of *magnetisation* $-\mu_o M$ to an *applied magnetic field* $-\mu_o H$, accompanied with the constituent magnetic materials of soft and hard ones. In the absence of $\mu_o H$, while the hard materials (permanent magnets) show high value of *coercivity* $-\mu_o H_c$ and can keep their $\mu_o M$, in contrast, the soft materials (temporary magnets) depict low value of $\mu_o H_c$ and can not maintain their $\mu_o M$. The responding behaviors of $\mu_o M$ to $\mu_o H$ are usually nonlinear and can be plotted to a graph, which is often-called the *hysteresis loop* (Figure I.1a). μ_o is the magnetic permeability of free space.

In the unmagnetized state, the material is divided into microscopic regions represented by *magnetic moments* (or *domains*), which are randomly oriented leading to zero resultant magnetization. As the ferromagnet is imposed in $\mu_o H$, $\mu_o M$ starts appearing, modifying and eventually erasing the microstructures of the ferromagnetic domains, in which they are magnetized in distinct directions. The ferromagnet will be saturated with the *spontaneous/saturated magnetisation* $\mu_o M_s$, for which all of the domains are in the same direction. There will be a certain value of magnetisation left behind in the ferromagnet after $\mu_o H$ is removed, which is so-called *remanence* $-\mu_o M_r$. Further increasing $\mu_o H$ in the opposite direction to the coercivity value $\mu_o H_c$ leads the $\mu_o M$ equal to zero. Different kinds of the virgin curves could suggest type of magnets of nucleation-type or pinning-type behavior (Figure I.1a).

Depending on time, temperature and the history of the magnetic materials, the magnetisation can be at distinct states. Therefore, the hysteresis arises in the applied field, from which the stable and metastable energy minima are present. Figure I.1b illustrates the energy landscape when considering the *Stoner-Wohlfarth* model (coherent rotation) of a single-domain particle. The two metastable minima are at either $\theta = 0$ (up) or $\theta = \pi$ (down) of equal energy at $\mu_o H = 0$. θ is the angle between the magnetisation and applied field. This energy is no longer equivalent when the applied field goes beyond. Namely, at $\mu_o H \leq \mu_o H_c$, the up state becomes unstable and readily to lose their states, at $\mu_o H > \mu_o H_c$ the up state is unstable and switches to the down state. In short, the energy of the system always tends to find its minimum energy configuration.

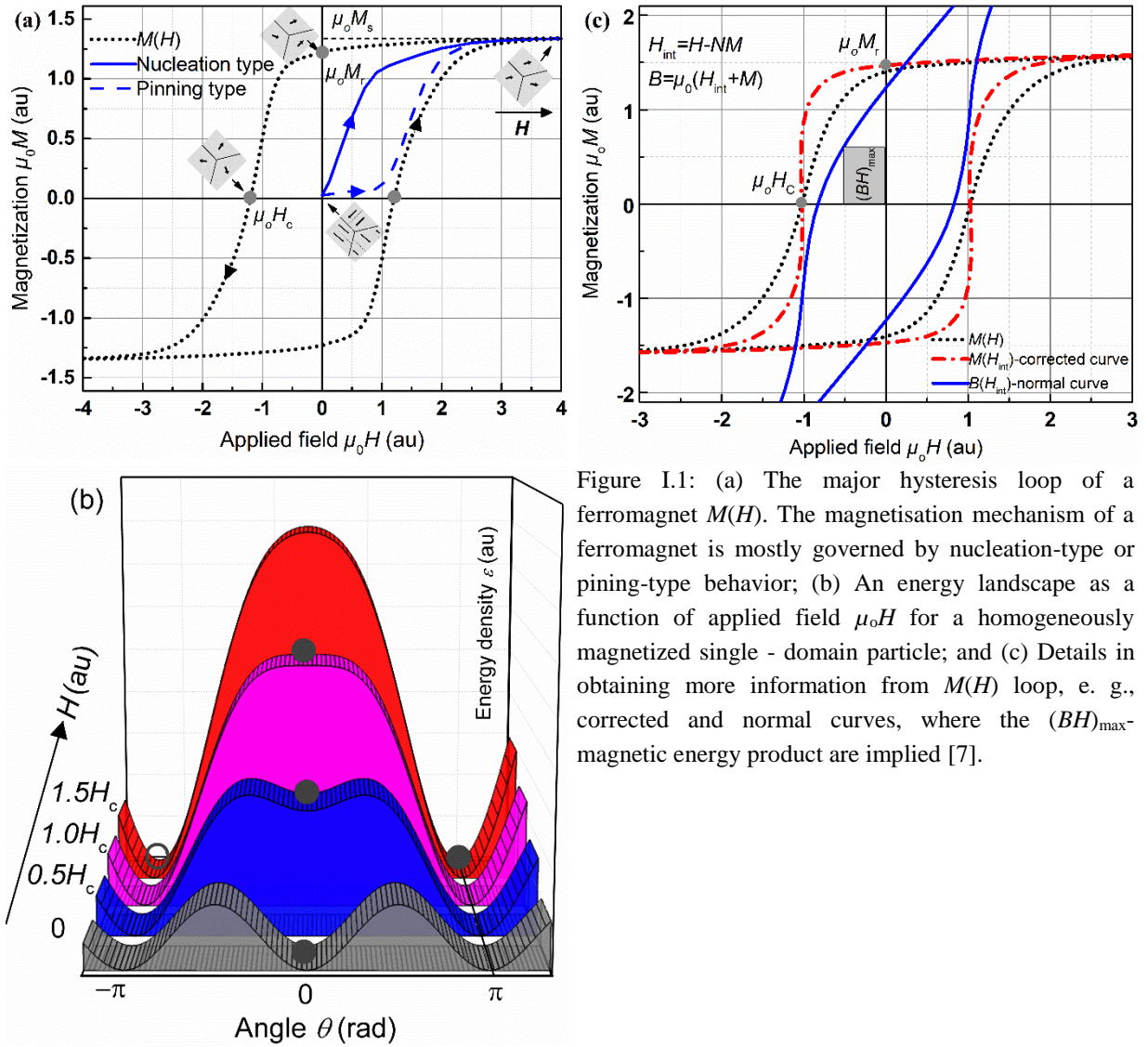


Figure I.1: (a) The major hysteresis loop of a ferromagnet $M(H)$. The magnetisation mechanism of a ferromagnet is mostly governed by nucleation-type or pinning-type behavior; (b) An energy landscape as a function of applied field $\mu_0 H$ for a homogeneously magnetized single - domain particle; and (c) Details in obtaining more information from $M(H)$ loop, e. g., corrected and normal curves, where the $(BH)_{max}$ -magnetic energy product are implied [7].

From Maxwell's partial differential equations, the complex relation between \mathbf{H} and \mathbf{M} is obtained and the *induced magnetisation* $\mathbf{B} = \mu_0(\mathbf{H}_{int} + \mathbf{M})$ could be figured out. The dependence of M on H could be presented in a well-known and formal equation as: $M = \chi H_{int}$, where χ and H_{int} are the *magnetic susceptibility* and *internal applied field* inside the material respectively. Based on χ , one can classify the magnetic materials. For examples $\chi \sim 10^{-5} - 10^{-2} > 0$ for paramagnets such as aluminum, magnesium; $\chi \sim 10^{-5}$, < 0 for diamagnets like bismuth, copper, etc.; $\chi \sim 10^2$ for superparamagnets; $\chi > 10^4$ for ferromagnets.

In regard to hysteresis loop, the extrinsic properties are the magnetic remanence $-\mu_0 M_r$, the magnetic coercivity $-\mu_0 H_c$ and the magnetic energy product $-(BH)_{max}$ (or $(BH_{int})_{max}$). Figure I.1c demonstrates the three typical major hysteresis behaviors. Note that these hysteresis loops depend on the metallurgical of the magnetic samples such as their shapes of horseshoe or cylinder. The raw loop shows the variation of M as a function of H (also known as extrinsic loop) while the corrected curve reflects the M with respect to H_{int} , at which $H_{int} = H_{app} - NM$ and N is *demagnetizing factor*. Experimentally, the last mentioned loop is $B(H_{int})$ normal curve, which allows to estimate the $(BH)_{max}$ (usually has an upper limit of $\mu_0 M_r^2 / 4$), which is twice the maximum magnetostatic energy stored in free space ($\frac{1}{2} \int_V |BH| dV$) by a magnetic material of unit volume. Moreover, due to the direct tie of B and H_{int} , the induced magnetisation replies on the demagnetizing field.

As concisely mentioned, the exceptional properties obtained in well-nanostructured soft-hard nanocomposites come from solving the free energy terms, (Equation I.1), given in a micromagnetism system by Skomski and Coey [10] as follows:

$$E = \int \left\{ A \left[\nabla \left(\frac{\mathbf{M}}{M_s} \right) \right]^2 - K_1 \frac{(n\mathbf{M})^2}{M_s^2} - \mu_o \mathbf{M}\mathbf{H} \right\} dV \quad (\text{Equation I.1})$$

Where the first, second and last terms show magnetic exchange interaction energy, anisotropy energy and Zeeman energy. Obviously, those sources of magnetic energy involve the magnetisation reversal, which refines the various energy landscapes. Such magnetic energy will be shortly expressed below.

A magnetized object is characterized by the magnetic moment (dipole) $\mathbf{m}=\mathbf{M}.V$ (\mathbf{M} is the averaged magnetisation in the volume V of a magnetic sample). When this dipole is exposed into an applied field \mathbf{H} , the magnetic moment will rotate so that the energy of the system reaches the minimum. This interaction can be described by the term of energy, which is later named as **Zeeman energy** and given as follows:

$$E_{Zeeman} = -\mu_o \int_V \mathbf{M}\mathbf{H} dV \quad (\text{Equation I.2})$$

The interaction between these magnetic moments is administered by a coupling between the magnetic dipoles, from which the wave functions of neighboring particles overlap. This coupling effect is the so-called exchange interaction and the **exchange energy** is represented by:

$$E_{exchange} = \int_V A \left(\nabla \frac{\mathbf{M}}{M_s} \right)^2 dV \quad (\text{Equation I.3})$$

where $A = \frac{J_{ex} \langle S \rangle^2}{a} c$ is exchange stiffness/strength, a is lattice constant or interatomic distance, c is a constant J_{ex} is exchange integral, S is the spin angular momentum measured in multiples of $\hbar/2\pi$.

The magnetic orderings in magnetic samples are only in existence under certain temperatures. For instance, **Curie temperature** (T_C) for ferromagnetic order which is usually determined by Curie–Weiss law, **Néel temperature** (T_N) for ferrimagnetic and antiferromagnetic orders. Going beyond these critical temperatures leading to thermal fluctuation energy comparable to $E_{exchange}$, the original microscopic magnetic orders will be destroyed and switched to a new state of paramagnetism, at which the moments are randomly oriented or not coupled.

As viewed from an individual magnetic moment, which is placed somewhere in space, this moment will generate a stray field at a distance r and $H_d \sim 1/r^3$. Thus, inside a magnetic object, there will be a stray field generated by the object itself which is the so-called self-interaction field or **demagnetizing field** $H_d = -NM$. The magnetic object reacts to its H_d by means of **dipolar interaction**. This **demagnetization/dipolar energy** is so-called **magnetostatic energy**. The demagnetization energy for the whole material is equal to:

$$E_{demagnetization} = -\frac{1}{2} \mu_o \int_V \mathbf{M}\mathbf{H}_d dV \quad (\text{Equation I.4})$$

where the factor 1/2 is responsible for the double-counting of dipolar interaction bonds. The demagnetizing factor is basically dependent on the shape of the investigated magnetic objects. The analytical solution for N is only given for general ellipsoids [16] while the others are based on numerical calculation or experimental observation.

Once material is crystallized which means the material's crystal is of an ordered arrangement of atoms in a 3D lattice. This leads to specific translational and rotational symmetries of magnetic moments. On the contrary to the exchange interaction, which is rotationally invariant, the magnetic dipoles might possess preferred orientations in space. This preferred orientation is often-called as **anisotropy** and the field influence in this circumstance is known as **anisotropy field**. Thus, the magnetic properties of the studied materials strongly depend on which directions they are measured. One of the primary origins of anisotropy is **magnetocrystalline anisotropy**, on which the competition between the electrostatic crystal-field interaction and spin-orbit coupling takes place [17]. Magnetocrystalline anisotropy is an intrinsic property of a ferrimagnet, independent of grain size and shape.

A magnetic material with a single **easy axis** (when the sample is magnetized, an easy axis is an energetically preferential direction of spontaneous magnetisation and vice versa for the hard axis) perpendicular to the **hard axes**, the energy associated with the magnetic anisotropy is the so-called **uniaxial anisotropy** can be written as:

$$E_{anisotropy}^{uniaxial} = \int_V \left(\sum_{i=1}^n K_i \sin^{2i} \theta \right) dV \quad (\text{Equation I.5})$$

where K_i are anisotropy constants and independent of θ , θ is the angle between M and the easy axis.

A material with a three easy axes such as simple cubic structure (i.e., iron), the anisotropy energy or sometimes called **cubic anisotropy** is given by:

$$E_{anisotropy}^{cubic} = \int_V \left[K_1 (\alpha_1^2 \alpha_2^2 + \alpha_2^2 \alpha_3^2 + \alpha_3^2 \alpha_1^2) + K_2 \alpha_1^2 \alpha_2^2 \alpha_3^2 + \dots \right] dV \quad (\text{Equation I.6})$$

where α_i are the direction cosines relative to cube edges. Take into account the dimensional analysis, the term $K_1 / \mu_o M_s$ is of dimension as magnetic field. It is a useful parameter which helps to define another physical quantity-anisotropy field and given as:

$$H_a = 2 \sum_{i=1}^n K_i / (\mu_o M_s) \quad (\text{Equation I.7})$$

The factor of 2 allows a direct comparison of H_a with H_c . The sum of high-order anisotropies gives rise to distinct non-equivalent definitions of anisotropy field. For example, anisotropy field of uniaxial materials with second-order anisotropy is $H_a = 2K_1 / \mu_o M_s$ while comparing $\theta = 0$ and $\theta = \pi / 2$ causes to $H_a = 2(K_1 + K_2 + K_3) / \mu_o M_s$.

Table I.1: Intrinsic properties and derived properties at room temperature for several typical hard magnetic materials [15,18–20].

Material	T_c (K)	$\mu_o M_s$ (T)	K_1 (MJm ⁻³)	$\mu_o H_a$ (T)	$(BH)_{max}^{theoretical}$ (kJm ⁻³)
Nd ₂ Fe ₁₄ B	585	1.61	4.9	7.6	516
L1 ₀ -FePt	750	1.43	6.6	11.6	407 [18]
L1 ₀ -FePd	760	1.37	1.8	3.3	373 [19]
NdCo ₅	910	1.23	0.7	N/a	301
Sm ₂ Co ₁₇	1190	1.20	3.5	7.0	286
SmCo ₅	1003	1.07	17.0	40	228
L1 ₀ -CoPt	840	1.00	4.9	12.3	199
Sm ₂ Co ₇	693	0.80	6.3	20	127 [20]
BaFe ₁₂ O ₁₉	723	0.48	0.33	1.8	46

Table I.1 compares the intrinsic values and typical derived parameters of hard magnetic materials.

I.1.2. Characteristic lengths

All the systems in nature always prefer to remain in the lowest energy state or the fundamental level, so do the magnetic systems. In the ferromagnetic system, the magnetostatic or demagnetization energy promotes magnetic domain formation with partial/complete flux closure structure as shown in Figure I.2. This leads to the whole magnetized materials not being in an ordered state or the ordered arrangement of moments, and just existing in a limited size of uniformly magnetized region of **domain**.

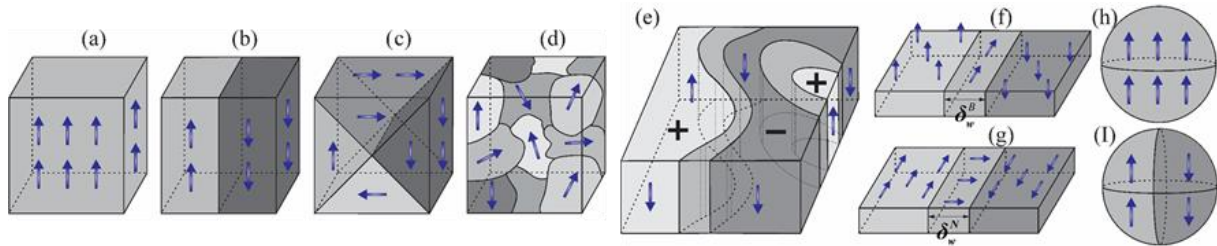


Figure I.2: Various micromagnetic spin manifestations adapted from [15]: (a) single-domain state in very small particles, (b) two-domain configuration in fairly small particles with uniaxial anisotropy, (c) flux-closure in cubic magnets, (d) complicated domain structure in a polycrystalline magnet, (e) Multiple domains and domains walls in a thin film (f) Bloch wall in a thin film with perpendicular anisotropy, (g) Néel wall in a thin film with ip anisotropy, (h) single-domain particle and (I) two-domain particle.

Due to the minimizing energy, the magnetisation of the two adjacent domains should be different and they are separated by a planar transition layer which is the so-called **domain wall**-where the magnetisation rotates from one easy axis to another. There are a variety of domain walls such as **Bloch**, **rotated Néel/Néel**, **Cross-tie**, **transverse** walls, etc (Figure I.3), that are sorted out by their characteristics.

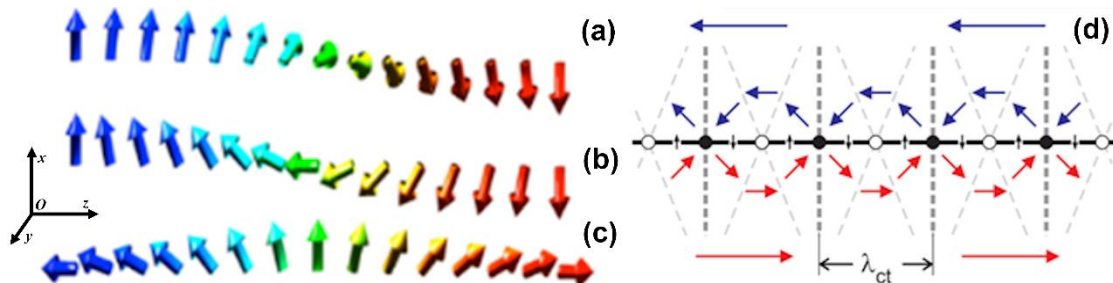


Figure I.3: Schematic sketch of different types of domain walls (a) Bloch wall rotating in the xOz plane; (b) Rotated Néel wall (for two consecutive orthogonal magnetisation) rotating in yOz plane; (c) Néel wall (for two opposite magnetisation) rotating in yOz plane; (d) Cross-tie wall (top-view) with mixture of Bloch and Néel walls. The Bloch and Néel walls are commonly found in oop and ip anisotropy thin films respectively.

The name **Bloch wall** denotes the transition layer after Bloch [21] first studied the nature of the transition layer (Figure I.3a). The vital assumption of the Bloch wall is that the change in magnetisation between two domains magnetized in opposite directions could take place gradually over the **domain wall width** in lieu of occurring abruptly. The reason behind this deduces logically from lower required exchange energy for gradual change distributing over many moments in comparison with discontinuous jump [22,23]. Consider the commonest 180° - π Bloch wall with two domains magnetized antiparallel to each other (Figure I.3a), from which the magnetisation flips in the plane of the wall. By minimizing the total magnetic energy of the system (involving exchange and anisotropy energies) in this circumstance, The Bloch domain wall width δ_w and total wall energy per unit area σ_w are given as follows [7,15,23]:

$$\delta_w^B = Na = \pi \sqrt{\frac{J \langle S \rangle^2}{K_1 a}} = \pi \sqrt{\frac{A}{K_1}} \text{ and } \sigma_w^B = \pi \sqrt{J_{ex} K_1 \langle S \rangle^2 / a} = \pi \sqrt{AK_1} \quad (\text{Equation I.8})$$

The critical domain size – r_c [22] also given as:

$$r_c = 9\sigma_w^B / (2\mu_o M_s^2) \quad (\text{Equation I.9})$$

Note that the maximum domain size is strongly dependent on the shape of the magnetic object [15] such as cylindrical, spherical, needle-like particles, etc.

By minimizing the energy of system when considering exchange energy and dipolar energy, the range, for which the exchange interaction is effective, is characterized by **exchange length** – l_{ex} :

$$l_{ex} = \sqrt{\frac{2A}{\mu_o M_s^2}} \quad (\text{Equation I.10})$$

Note that the l_{ex} for most ferromagnetic materials is in the same order of magnitude (~5 nm for permalloy [24]) and l_{ex} is an important parameter involving the discussion of spring magnets presented in the following section.

Table I.2: Domain wall parameters for several ferromagnetic materials adapted from [7,25,26]. Note that the δ_w , σ_w , and l_{ex} are all recalculated by the formulas given in this thesis.

Material	M_s (MAm ⁻¹)	A (pJm ⁻¹)	K_1 (kJm ⁻³)	δ_w (nm)	σ_w (mJm ⁻²)	l_{ex} (nm)
Ni ₈₀ Fe ₂₀	0.84	10	0.15	811	0.1	4.7
Fe	1.71	21	48	65.7	3.2	3.4
Co	1.44	31	410	27.3	11.2	4.9
Fe ₆₅ Co ₃₅	1.95	26 [25]	20	113	2.3	3.3
CoPt	0.81	10	4900	4.5	22.0	4.9
Li ₀ -FePt	1.14	27	6600	[26] 6.4	41.9	5.8
Nd ₂ Fe ₁₄ B	1.28	8	4900	4.0	19.7	2.8
SmCo ₅	0.86	12	17200	2.6	45.1	5.1
CrO ₂	0.39	4	25	39.7	1.0	6.5
Fe ₃ O ₄	0.48	7	-13	72.9	0.9	7.0
BaFe ₁₂ O ₁₉	0.38	6	330	13.4	4.4	8.1

Table I.2 presents domain wall-related parameters of some ferromagnetic materials.

I.1.3. What is spring magnet and how to augment magnetic energy product?

High values of H_c and M_r (or M_s) are simultaneously exhibited in an excellent hard magnetic material, thus, a larger value of $(BH)_{max}$ is obtained. In several simple cases, a mixture of hard and soft magnetic powder is of a lateral rectangular hysteresis behavior and therefore it causes unanticipated $(BH)_{max}$. The **spring magnet/exchange spring magnets/soft-hard composites** have been initially proposed and changed the game of achieving excellent hard magnetic material.

Spring magnet is one kind of permanent composite magnets, at which it is constituent of a soft magnetic phase being inter-exchanged coupled with a hard magnetic phase and was first quoted in 1991 [14]. A representation for magnetic properties of such materials is graphically described in Figure I.4. The winning combination of the two magnetic phases in the nanocomposites, where the size of soft nano-inclusions in a hard magnetic matrix can be restricted to below two times of domain wall width of the hard phase, augment the magnetic properties ($(BH)_{max}$) [10,13,14,27]. These nanocomposites have been just far practically obtained in thin films with granular or continuous layer-by-layer structures [28–35].

The additional advantage in having a soft phase in a magnet is about to reduce the larger proportion of rare earth elements which can be up to 91% of such magnet [10,14,28]. In these nanocomposites, a striking feature is that the soft phase is relatively pinned to the hard matrix grains, which are induced by exchange interaction at the interfaces, and the centre of the soft grains can revolve in a reverse field (shown in Figure I.5).

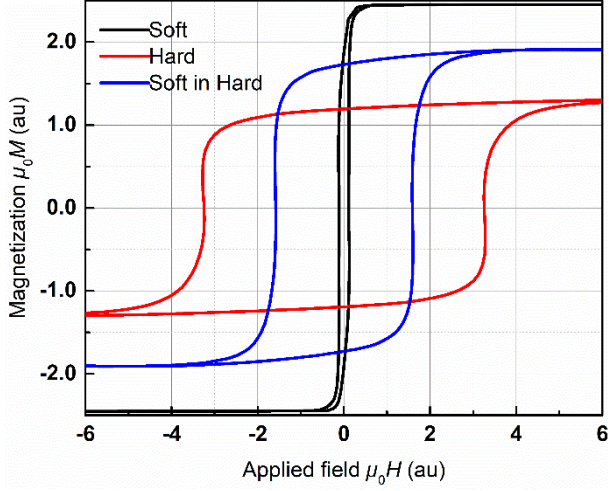


Figure I.4: Three manifestations of hysteresis loops of pure magnetic soft phase inclusions/nanoparticles (black line), hard magnetic phase (matrix, red line) and the resultant of the combination of the two phases-the exchange spring nanocomposite (blue line).

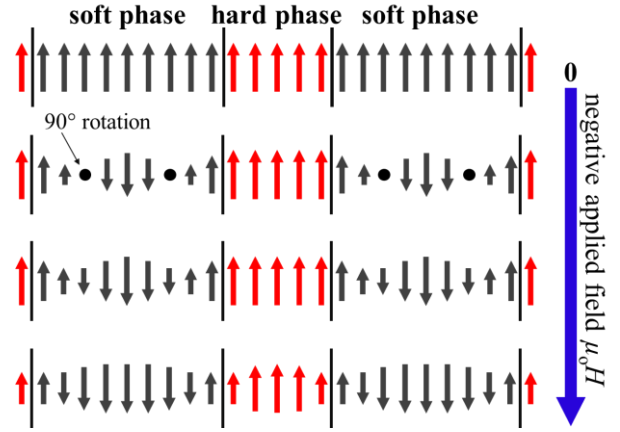


Figure I.5: Schematic one-dimensional model of the micromagnetic structure of the magnetic exchange-coupled nanocomposites. The hard magnetic phase stiffness response of soft magnetic phase at different levels of the applied field in a composite material [14].

In these nanostructured composites which are the mixture of both soft and hard magnetic phases, the total remanent magnetisation is approximately calculated as [10,14]:

$$M_r^{total} = f_{soft} M_r^{soft} + f_{hard} M_r^{hard} \quad (\text{Equation I.11})$$

where $f_{soft}, f_{hard} = (1 - f_{soft})$, M_r^{soft} and M_r^{hard} are the volume fractions, remanence of soft and hard magnetic phases respectively. In a similar way, the effective anisotropy constant is given by [10]:

$$K_1^{eff} = f_{soft} K_1^{soft} + f_{hard} K_1^{hard} \quad (\text{Equation I.12})$$

Neglecting the pinning of the nucleus, the rectangular hysteresis loop is obtained with $H_c = H_a$ and $M_r = M_s$ (as in Stoner-Wohlfarth model), the maximum attainable theoretical anisotropy field/coercivity is given analogously as in (Equation I.7) by:

$$\mu_0 H_c = 2 \left(f_{soft} K_1^{soft} + f_{hard} K_1^{hard} \right) / \left(f_{soft} M_s^{soft} + f_{hard} M_s^{hard} \right) \quad (\text{Equation I.13})$$

The optimal magnetic energy product $-(BH)_{max}$ (which depends on shape/demagnetizing correction) of the nanocomposites is then yielded by (Equation I.14) [10]. Note that K_1^{soft} is relatively small as compared to K_1^{hard} (Table I.2) and $(BH)_{max} = \mu_0 M_r^2 / 4$ for $H_c > M_r / 2$ or $(BH)_{max} = \mu_0 H_c M_r / 4$ for $H_c < M_r / 2$, corresponding to hard/soft ferromagnets.

$$(BH)_{\max} \approx \frac{\mu_o (M_s^{\text{soft}})^2}{4} \left[1 - \frac{\mu_o (M_s^{\text{soft}} - M_s^{\text{hard}}) M_s^{\text{soft}}}{2K_1^{\text{hard}}} \right] \quad (\text{Equation I.14})$$

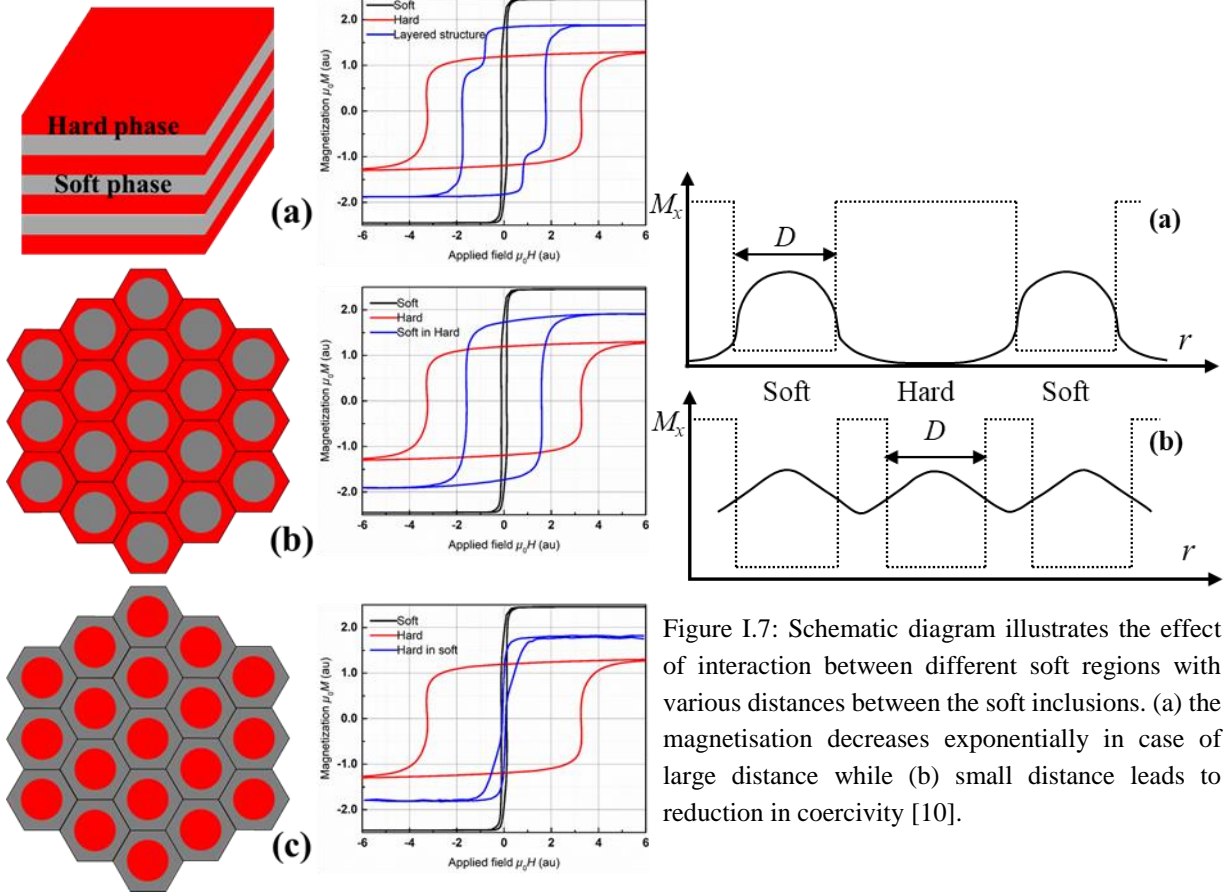


Figure I.6: Three main manifestations of possible nanostructured composites (blue) which are the combination of soft (black) and hard (red) phases and their corresponding hysteresis loops in (a) layered structure configuration, (b) soft nanoparticles in hard matrix and (c) hard inclusion in soft matrix.

Figure I.7: Schematic diagram illustrates the effect of interaction between different soft regions with various distances between the soft inclusions. (a) the magnetisation decreases exponentially in case of large distance while (b) small distance leads to reduction in coercivity [10].

In order to achieve high performance magnetic nanocomposites, one has to manage precisely the spacing, size of the inclusions, the coupling between the two phases [10] and the volume ratio between them [36]. It is also a must to better comprehend the various possible architectures of the soft and hard phases. Among different possible structures, three typical architectures of **layered structure**, **soft nanoparticles in hard matrix** and **hard inclusion in soft matrix** are presently attracted intensive attention (Figure I.6). In the first configuration of layered structure, the soft and the hard phases are only exchange-coupled at their interface. The coercivity is theoretically predicted and it varies $(1/L^2)$ as a function of soft layer thickness L . As L increases, the soft phase is dominant and therefore strongly induced by the external applied field (reduction in coercivity). It initiates the magnetisation and contributes unfavorably to the shoulder in hysteresis loop [14]. While in the second type of nanostructured composites, the magnetisation of the two both phases is initially supposed to be lined up. Under a certain degree of external applied field, the magnetisation state of the soft phase starts changing with step $D \sim \delta_w$ of the hard matrix (normally, it is Bloch wall). For instance, in $\text{Sm}_2\text{Fe}_{17}\text{N}_3$ composites, the coercivity is about 20 T (anisotropy field) with the soft phase diameter of $D \sim 3\text{nm}$ while H_c downs to 7 T at $D \sim 7\text{nm}$. The coercivity should be $1/D^2$

dependence [10]. The higher remanent magnetisation is in the composite, the larger volume of soft phase is required. In addition, the coercivity will be destroyed by exchange interaction in case the space between soft neighboring zones approaching too close ($D < \delta_w$) that means the magnetisation of soft phases easily tunnels one to each other through the hard phase as shown in Figure I.7b. Hence, *the challenge to synthesizing this composite is to obtain a smaller size of the soft phase in the order of δ_w of the hard phase* to prevent nucleation at a narrow field. Finally, the hard inclusions in soft matrix, the average anisotropy in a volume V ($\sim l_{ex}^3 = (A / \langle K \rangle)^{3/2}$ [37]) with hypothesis of randomly oriented, ferromagnetically coupled grains and following the random anisotropy model [38], is given by $\langle K \rangle = K_1^4 D^6 / A^3$ where $D \ll l_{ex}$. The grain size is comparable or exceeds l_{ex} , however, it leads to the magnetocrystalline anisotropy of the system is K_1 . Thus, the H_c reaches maxima at $D \sim l_{ex}$ and is of $1/D$ dependence as $D > \pi l_{ex}$ (normally, it is Néel wall).

One of the very first spring magnets was first assembled [13,39] by melt-spun technique, and later by mechanical milling [40,41] for which the size of the soft phase is close to δ_w [14,40,41]. Recently, just few studies have been conducted on the nanocomposite multilayers/hybrid systems [42–47], from which they investigated the properties at high temperatures on the thickness of the soft/hard layer or figured out the magnetisation reversal processes. In addition, there is insufficient work illustrating the enhancement of remanent magnetisation/ $(BH)_{max}$ [29,34,48–51] that the $(BH)_{max}$ does not go beyond a half of the $Nd_2Fe_{14}B$ single phase value (given in Table I.1) and of course the achievable $(BH)_{max}$ in reality for the composites is still far from the values predicted [10]. The reasons behind these unsuccessful attempts might be attributed to the diameter of soft phase not being satisfied, the critical size limited as high as two times of the domain wall width of the hard phase in the nanocomposites [10,14]. The Table I.3 depicts some theoretical/simulated predictions for magnetic properties of several magnetic nanocomposites.

Here, in this thesis, we propose an outstanding method based on laser ablation, on which the diameter of the NPs could be controlled precisely around the δ_w of the hard phase and then the soft in hard nanocomposite is feasible. It is convenient to positively comprehend the magnetic properties of hard matrix and soft inclusions so that one could manage to fabricate the desirable magnetic nanocomposites. Follow what have been given in Table I.1 and Table I.2, we deliberately decide to work on the nanocomposites, at which the hard matrices can be either NdFeB or FePt based thin films while the soft inclusions will come from $Fe_{65}Co_{35}$, or Co.

Table I.3: Theoretically predicted magnetic properties for some nanocomposites [10,52–56].

Magnetic nanocomposites	$\mu_0 M_s$ of hard/soft phase (T)	Volume fraction of soft phase (%)	Grain/layer sizes of hard/soft phase (nm)	$(BH)_{max}$ (kJm^{-3})
$Sm_2Fe_{17}N_3/Fe_{65}Co_{65}$	1.55/2.43	91	2.4/ 9	1090 [10]
$Sm_2Fe_{17}N_3/Fe$	1.55/2.15	93	<10 /10	880 [10]
$Nd_2Fe_{14}B /Fe$	1.61/2.15	50	< 4.2/ 4.2	716 [52]
$Nd_2Fe_{14}B /Fe$	1.61/2.15	50	N/a / 5	692 [53]
FePt /Fe	1.43/2.15	61.5	N/a	716 [54]
$SmCo_5 /FeCo_3$	1.05/1.80	72.2	5.0/13	517 [55]
MnBi / $Fe_{65}Co_{65}$	0.78/2.43	14	20 /20	199 [56]

Figure I.8 gives an inspired pictorial representation scheme for Soft in Hard magnetic nanocomposite presented in the manuscript. Following each single branch, it allows to conceptualize the routes to unearth the soft in hard magnetic nanocomposites.

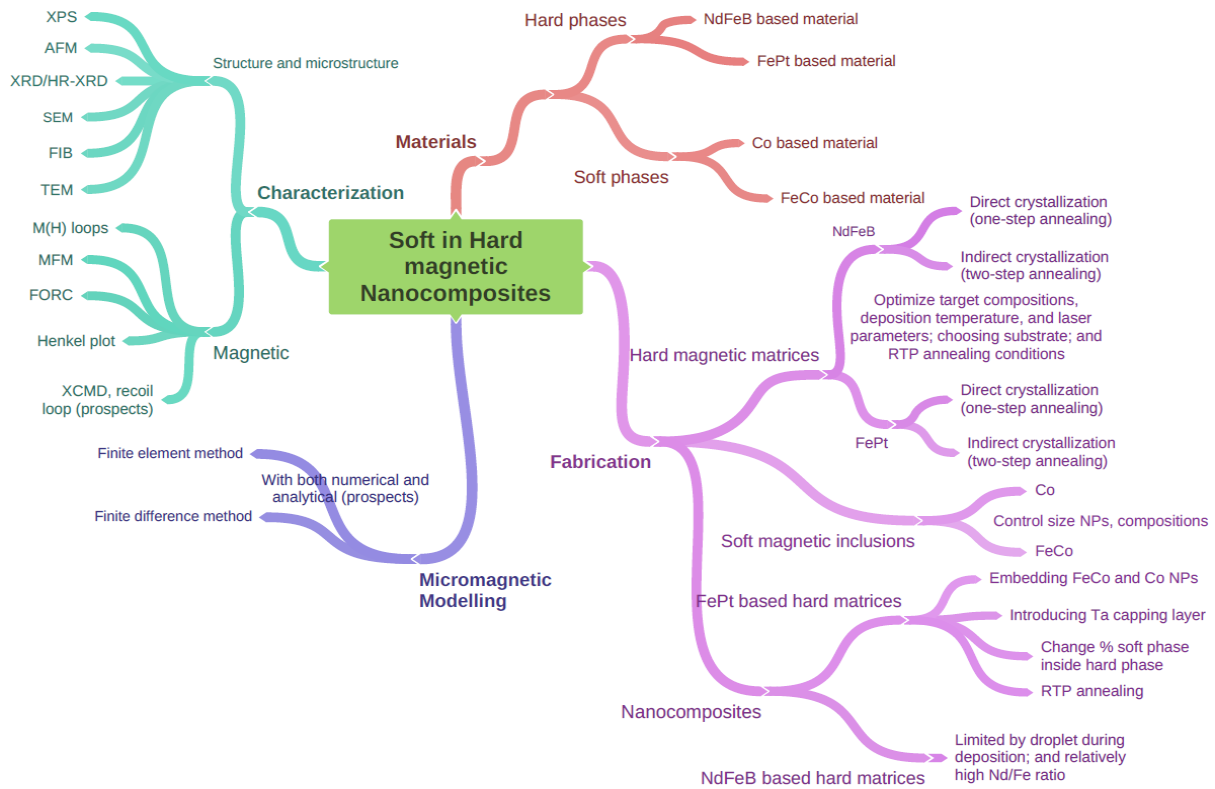


Figure I.8: A pictorial representation scheme for Soft in Hard magnetic nanocomposite presented in this work.

I.2. Hard magnetic NdFeB based films

I.2.1. Nd₂Fe₁₄B structure and its properties

The highest $(BH)_{\max}$ of a single phase permanent magnet is accomplished in a well-known Nd₂Fe₁₄B compound thanks to its tetragonal crystallographic structure (Figure I.9) [57]. This specific structure is related to the typical structure for other rare earth transition compounds of hexagonal CaCu₅-type structure [58]. In this structural configuration, there are four Nd₂Fe₁₄B units of 68 atoms per unit cell with the lattice constants $a = 8.8 \text{ \AA}$ and $c = 12.19 \text{ \AA}$.

There are all Nd, B and four of the 56 Fe atoms residing in the $z = 0$ and $z = 0.5$ mirror planes in which they fall into three groups of two distinct Nd sites, one Boron position and six different Fe locations (Table I.4). While the B atom preserves in the centers of trigonal prisms composed by the three nearest neighboring Fe atoms above and the three below the mirror plane, all the rest of Fe atoms occupy in a puckered hexagonal nets between the basal and $z = 0.5$ planes [57].

The magnetic properties of the compounds originate from the magnetic moment of each single atom and their interactions arranged in the crystallographic structure. Nd is a rare-earth metal and reveals ferromagnetic/antiferromagnetic properties (these properties only exist below the T_C of 19 K) [59] while Fe shows weak ferromagnetic properties at room-temperature (RT) with high $T_C = 1044 \text{ K}$ [7]. Additionally, the B itself exhibits the diamagnetic properties [60] which do not make a direct contribution to the magnetism of the Nd₂Fe₁₄B compound. Nonetheless, boron atoms enhance cohesion by strong covalent bonding [61]. The percentage of rare-earth element in Nd₂Fe₁₄B is sufficiently low in comparison with the others (SmCo) which leads the price of neodymium magnets less expensive than SmCo magnets [61]. Within the lattice, Fe is of various magnetic moments replying upon its occupancy in the net, at which the moments could be either indicated from neutron diffraction [62,63] and Mössbauer

spectroscopy [64] or computed from band-structure calculations [65–68]. It is shown that the moment of Fe ranges from $2.1 \mu_B/\text{atom}$ to $2.9 \mu_B/\text{atom}$ [66] where 1 Bohr magneton, $1\mu_B = |e|\hbar / (2m_e) = 0.9274 \times 10^{-23} JT^{-1}$. In contrast to Fe, the localized $4f$ states of Nd are of strong spin-orbital coupling which are not allowed to supply the bonding, yet contribute to the local exchange field of parallel coupling Nd^{3+} with the moment of $3.3 \mu_B/\text{atom}$ [66]. Nd is responsible for a total moment of $38.1 \mu_B/\text{formula unit}$ of $\text{Nd}_2\text{Fe}_{14}\text{B}$ [66] and a bit higher than experimental value of $37.9 \mu_B/\text{formula unit}$ [62]. It is however all Nd atoms add a less amount of spontaneous magnetisation as compared to Fe atoms due to 1/3 atomic fractional volume contribution.

Table I.4: Positional parameters and standard deviations of each single element in the $\text{Nd}_2\text{Fe}_{14}\text{B}$ crystal structure. [57,58].

Atom	Site	Occupancy	Coordinates		
			<i>x</i>	<i>y</i>	<i>z</i>
Nd	<i>f</i>	4	0.266	0.266	0.0
Nd	<i>g</i>	4	0.139	-0.14	0.0
Fe	<i>k</i> ₁	16	0.224	0.568	0.128
Fe	<i>k</i> ₂	16	0.039	0.359	0.176
Fe	<i>j</i> ₁	8	0.097	0.097	0.205
Fe	<i>j</i> ₂	8	0.318	0.318	0.247
Fe	<i>e</i>	4	0.5	0.5	0.113
Fe	<i>c</i>	4	0.0	0.5	0.0
B	<i>g</i>	4	0.368	-0.37	0.0

The excellent magnetic property of $\text{Nd}_2\text{Fe}_{14}\text{B}$ magnet ($\mu_0 H_a = 7.6 \text{ T}$, $\mu_0 M_s = 1.61 \text{ T}$, $(BH)_{\text{max}} = 516 \text{ kJm}^{-3}$, $T_C = 588 \text{ K}$) is able to be well explained because of several parameters. Among those factors, the tetragonal $\text{Nd}_2\text{Fe}_{14}\text{B}$ crystal structure plays a crucial role, i. e., this structure acquires exceptionally high uniaxial magnetocrystalline anisotropy of 7.6 T [15] thanks to the preferentially magnetized along a specific crystal axis of the compound. Moreover, the $\text{Nd}_2\text{Fe}_{14}\text{B}$ magnet displays both itinerant ($3d$ -Fe) and localized ($4f$ -Nd) features [15] sustained by a crystal

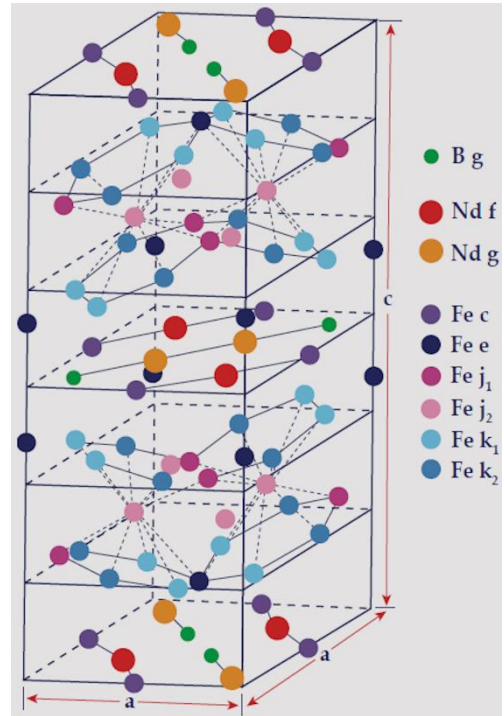


Figure I.9: Schematic representation of the unit cell of $\text{Nd}_2\text{Fe}_{14}\text{B}$ ($P42/mmm$ space group). The c/a ratio in the figure is exaggerated to emphasize the puckering of the hexagonal iron nets (the lattice parameters $a = 8.80 \text{ \AA}$, $c = 12.19 \text{ \AA}$) [57].

electric field. In its crystallographic arrangement, Nd obtains predominant magnetic moment as a consequence of Nd owning four unpaired electrons in its electron shell structure which is slightly larger than three on average in Fe [7,62,66]. This higher moment of Nd could be indicated by considering the intervention of possible $5d$ electron configuration. The comprehensive coupling includes interaction of $4f$ - $5d$ in Nd (usually induces ferromagnetic properties) and hybridization of $5d$ leading to $3d$ - $5d$ pairing (usually causes antiferromagnetic properties) [62]. These overall couplings lead to a strong exchange interaction $3d$ - $4f$, favoring ferromagnetic alignment of the Nd moments along the Fe magnetisation, with a moment close to $3.27 \mu_B$ [62]. Thus, the unpaired electrons, aligning up in order to their spins point to the direction (c -axis in tetragonal structure), that supports a spontaneous magnetisation of 1.61 T at RT.

I.2.2. Thin film growth

The magnetic thin/thick films are mostly prepared by physical vapor deposition (magnetron sputtering [11,69–71], PLD [72–74], molecular beam epitaxy [75] or thermal evaporation [76]).

fundamental physical mechanism behind this method is known as vacuum deposition, for which the atoms/molecules from the target reach the substrate with/without collisions with certain amount of residual gas molecules in the deposition chamber requiring good vacuum. After reaching the substrate, the film growth will take place at atomic level as a result of the condensation of adatoms-the atoms are mobile on the surface of the substrate [77]. The film growth is of various stages including condensation and nucleation of the adatoms, nuclei growth, interface formation, nucleation and reaction with previously deposited material, post-deposition treatments...[77]. These steps are all essential in regulating the properties of the deposited film [78].

The thermodynamic equilibrium, including the free energies of film surface ϵ_F , substrate surface ϵ_S , and the interface between film and substrate ϵ_{FS} , allows determining the growth modes of the films and their morphologies. Three primary growth modes are schematically demonstrated in Figure I.10. In the FM-layer-by-layer mode or 2D growth (Figure I.10a), the overall energy of the wetted substrate, $\epsilon_F + \epsilon_{FS}$, is lower than ϵ_S of bare substrate (strong bonding between film and substrate reduces ϵ_{FS}). While 3D islands are promoted to form in the VM-island formation (Figure I.10b), because the film does not wet the substrate (no bonding between film and substrate) leads to the total ϵ_S not increasing. In the SK-layer plus island mode, the growth

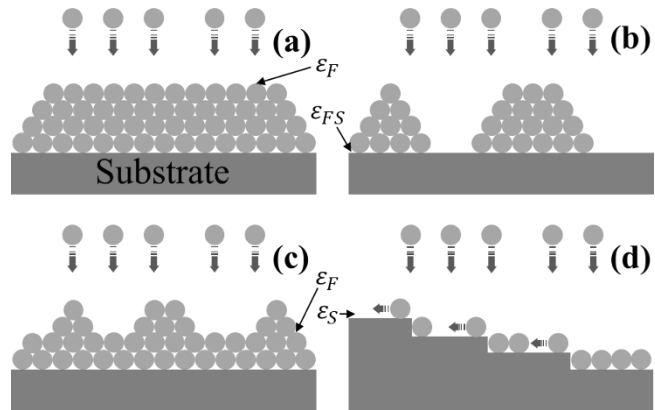


Figure I.10: Plane views of the three primary thin film growth manifestations (a) Frank-van der Merwe (FM-layer-by layer), (b) Volmer-Weber (VW-island), and (c) Stranski-Krastanov (SK-layer plus island), (d) step flow which caused by a fast intralayer mass transport. The film morphology is determined by the balance between the free energies of film surface ϵ_F , substrate surface ϵ_S , and the interface between film and substrate ϵ_{FS} [79].

changes from 2D to 3D (Figure I.10c). It is due to biaxial strain caused by the lattice mismatch between the substrate and the film. This misfit dislocation is responsible for elastic energy which is proportional to the film thickness. If the thickness exceeds a critical thickness, the elastic energy is equivalent to the addition in interfacial energy and therefore leads to equilibrium defects [79]. The final case mentioned here relating to homoepitaxial growth, which the film and the substrate are the same, and the substrate crystallite is preferentially prolonged into the film, thus the misfit and thermal expansion is no longer the case. This usually induces 2D growth of the film [80]. A fast intralayer mass transport will drive the step flow growth on a vicinal surface (Figure I.10c) if one took into account the surface diffusion coefficient of adatoms and the sticking probability of adatoms coming to the edge of a terrace.

I.2.3. Development of hard magnetic NdFeB films

In regard to PLD, just few papers have been truly dedicated to magnetic NdFeB based materials deposited from one single target [81–86] or multiple targets [72–74] that are all still far from the best experimental values of a 5 μ m thick film obtained by triode sputtering with $\mu_0 H_c \sim 1.6$ T, $\mu_0 M_r \sim 1.4$ T, $(BH)_{\max} \sim 400$ kJm $^{-3}$ [11]. It turns out to be that the specific phase of Nd $_2$ Fe $_{14}$ B with an improvement of magnetic properties could be reached by adjusting through processing techniques, i. e., one [72–74,85,87] or two steps of annealing [11,88]. Practically, the high demand in excellent magnetic films requires both high coercivity and remanent magnetisation [6,89]. These properties are counted on several parameter

such as chemical composition of the films [72,82], anisotropy (textured)/isotropy films [72–74,90], microstructure [72,74], deposition temperature [74,84], ambient gas [85].

In one-step annealing method (direct crystallization), the $\text{Nd}_2\text{Fe}_{14}\text{B}$ can crystallize at elevated above 400°C [91], and well crystallized at around 600°C [72–74], from which the films normally shows out-of-plane (oop) textured. It is, however, the degree of textured films depends on the deposition temperature and the substrate in use. For examples, films deposited on Ta/Si substrates at around 600°C [81,84] or annealed by pulsed annealing at 700°C [82,83,92] lead to isotropic crystallization and thus the coercivity, magnetisation and $(BH)_{\text{max}}$ are all limited ($(BH)_{\text{max}}=118 \text{ kJm}^{-3}$). In contrast with deposition on Ta/Si substrate, other authors did successful attempts in promoting NdFeB based thin films with *c*-textured and therefore a high ratio of M_r/M_s and μ_0H_c were both obtained [72–74,85,90]. Namely, in lieu of using "inexpensive" substrates (Ta, Si), the authors use more expensive single crystal substrates such as MgO or Al_2O_3 (*c*-sapphire) accompanied by deposition at 650°C , the epitaxial growth of NdFeB thin films on *c*-sapphire has been preferentially promoted with the help of Ta layer. Note that the purpose of the buffer layer is to prevent oxygen diffusion from the substrate into the films which will cause the oxidation, and frequently promote the epitaxial growth of $\text{Nd}_2\text{Fe}_{14}\text{B}$ phase. This *c* axis growth gives rise to almost complete alignment of all magnetic moments perpendicular to the substrate/film plane, hence, high values of coercivity, magnetisation and M_r/M_s of 2.0 T, 0.9 T and 0.97 respectively have been achieved [90].

Within these works, the authors sought a good composition of deposited films by tuning different types of single target (sintered/alloy targets with various mass density) [82] or adjusting the number of pulses on the different elemental/binary targets [72]. Unfortunately, these efforts were still limited by magnetisation of ~ 0.7 T and still lack of comprehensive explanation for obtained properties of such films. In addition, the effect of deposition temperatures ranging from 545°C to 745°C on the microstructure and magnetic properties was revealed [74] with a coercivity of 1.9 T whereas remanent magnetisation being as high as 0.6 T. These properties restrict the enormous potential for use at the microscale such as micro-systems dedicated to telecommunications, internet of connected things and bio-technology [6,89].

On the other hand of post-annealing method (crystallized during a post-deposition anneal process), there is a lack of research linked to PLD followed by this route. Literature about NdFeB based films shows that there are a few studies related to this route with magnetron sputtering [11,88,93–95]. The films are commonly either deposited directly on Si/glass substrates at RT [95–97] or at intermediate temperature [11,98] and then proceeded by heat treatment with the help of buffer layers. The films initially interpret both kinds of amorphous and *c*-textured $\text{Nd}_2\text{Fe}_{14}\text{B}$ phase (which frequently induces isotropic films), accordingly a second step of annealing up to 750°C in 10 minutes is necessary to complete the crystallization. One of the notable results was obtained with $(BH)_{\text{max}}$ up to 400 kJm^{-3} which is comparable to the best available sintered NdFeB magnets [11].

In general, the isotropic films are of poorer magnetic properties as compared to anisotropic films that normally come up with *c*-axis textured growth. Although the NdFeB based films sputtered by magnetron sputtering possess much better magnetic properties, it is true that PLD is more flexible about developing NdFeB based films in general and magnetic nanocomposites in particularly owing to the following reasons: (i)-The target in PLD is sufficiently small (around 3 cm) which is effortless to be produced; (ii)-The PLD system is well adapted to deposit at different conditions (in terms of ambient gas pressure 10^{-9} to 10^{-1} mbar); and (iii)- in situ embedding soft magnetic nanoparticles to the hard magnetic matrix to synthesize magnetic nanocomposites by dual laser ablation [99–101].

I.3. Hard magnetic FePt thin films

I.3.1. L1₀-FePt structure and its properties

The second candidate in the list possessing the highest theoretical $(BH)_{\max}=407 \text{ kJm}^{-3}$ is L1₀-FePt phase [15,102]. One of the very first systematic works on the properties of FePt binary alloys was initiated in 1907 [103]. Depending on the compositional ratio between Fe and Pt, temperature, some possible intermediate crystal configurations have been established such as FePt₃, FePt, Fe₃Pt [104] which are shown from the phase diagram given in Figure I.11a. Our interested structure is L1₀ phase which normally exists at elevated temperatures with the Fe/Pt ratio ranging from 0.49 to 1.22 in the alloy (Figure I.11a)

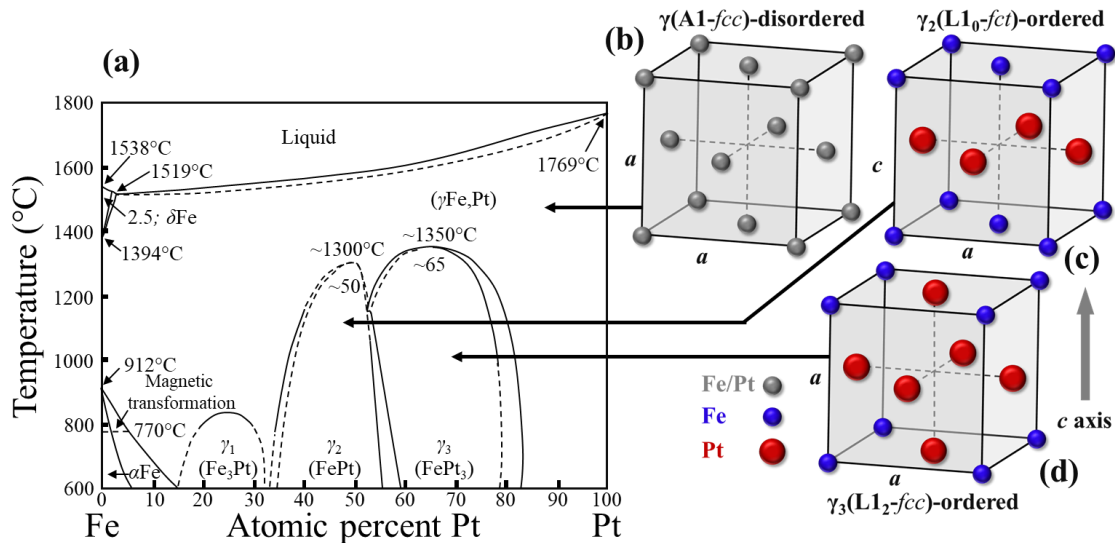


Figure I.11: (a) Phase diagram of binary FePt alloy in which the crystal structures of the phases coming along with various composition ranges and temperatures are shown. Schematic illustration of unit cells of different FePt states corresponding to (b) disordered state $\gamma(A1-fcc)$, (c) ordered state $\gamma_2(L1_0-fct)$ and (d) ordered state $\gamma_3(L1_2-fcc)$ [105].

Among all the possible structures, the γ or frequently denoted in Strukturbericht symbols as A1 phase is of a face-centered cubic (*fcc*) structure in disordered state with lattice parameter of unit cell is 3.878 \AA , on which Fe and Pt atoms randomly reside the crystallographic sites (Figure I.11b) [106,107]. Meanwhile in the ordered states, there are two crystallographic arrangements denoted as γ_2 with face-centered tetragonal (*fct*-Figure I.11c) and γ_3 with face-centered cubic structures (Figure I.11d) depending on the compositional fraction of Pt in the alloys. In the interested γ_2 phase, the Fe and Pt atoms are specifically occupied in stacked planes (Fe atoms at $(\frac{1}{2} 0 \frac{1}{2})$ and $(0 \frac{1}{2} \frac{1}{2})$ sites while Pt atoms at $(0 0 0)$ and $(\frac{1}{2} \frac{1}{2} 0)$) in an AuCu-type structure with the P4/mmm space group with $a=3.852 \text{ \AA}$ and $c=3.713 \text{ \AA}$ [108].

The phase diagram of the Fe-Pt system also reveals several types of magnetic orders such as ferromagnetism in Fe₃Pt, FePt and FePt₃ and antiferromagnetism in FePt₃ [109,110]. In the alloys, the magnetic moments of Fe in the FePt alloy ranges from 2.8 to $3.5 \mu_B/\text{atom}$ [111–114]. The different chemical composition and fabricating temperature of the alloys lead to different magnetic states and thus there is dependence of T_C or T_N on composition of Fe-Pt system. With composition ranging from 24 to 36 % at Fe, a variation in antiferromagnetic order takes place from parallel iron moments in the (110) planes to parallel moments in the (100)/(010) planes. In addition, an iron moment of about $3.3 \mu_B/\text{atom}$ had been observed [115], this value is just slightly lower than that of a value $3.325 \mu_B/\text{atom}$ calculated from first

principle calculation [110]. If the portion of Fe exceeds more than 32 %at, the ferromagnetic phase becomes majority [115].

The ordered equiatomic FePt alloy is ferromagnetic with T_C of about 670 K and hard to magnetize [116]. By disordering the bulk alloy, magnetisation is enhanced markedly and neutron diffraction depicts that iron moments at 300 K is about $2.8 \mu_B/\text{atom}$, parallel to the c axis [109]. Another calculation reveals the magnetic moments of Fe and Pt are about 2.966 and $0.354 \mu_B/\text{atom}$ respectively [110]; these moments are varied as compared to other computed moments of 2.92 and $0.33 \mu_B/\text{atom}$ [117] or experimental moments of 2.9 and $0.34 \mu_B/\text{atom}$ [118]. Magnetic moments of various unit cells are given in Table I.5.

Table I.5: The magnitude of the magnetic moments in μ_B/atom calculated for three ordered Fe-Pt alloys with stoichiometric concentrations [110].

Atom	Fe ₃ Pt (FM)	FePt (FM)	FePt ₃ (FM)	FePt ₃ (AFM)
Fe	2.711	2.966	3.258	3.325
Pt	0.349	0.354	0.359	0.000

As the disordered-ordered transformation occurs normally from γ to γ_2 phases, a spontaneous re-alignment of the magnetisation parallel to the c -axis will be induced. This results in an anisotropy constant of $K_1 = 6.6\text{-}7.0 \times 10^7 \text{ erg.cm}^{-3}$ (or $6.6\text{-}7.0 \text{ MJ.m}^{-3}$) which is about 100 times higher than that of in the γ (fcc) structure [119]. The origin of this re-alignment originates from the strong perpendicular anisotropy in γ_2 ($L1_0$) phases and the strong spin-orbit coupling which lead to the Fe moment of $2.9 \mu_B/\text{atom}$ while Pt moment is about $0.3 \mu_B/\text{atom}$ [120,121].

I.3.2. FePt phase transformation

When the transition from A1 to $L1_0$ occurs, there is a compression along the a -axis and c -axis of about 0.67% and 4.3% respectively [106–108]. This slight distortion induces a shift of (111) reflection to higher diffraction θ - 2θ angle due to lower energy level or smaller interplanar distance d of (111) reflection compared to other reflections. Supposing the long-range order is S and given by [122]:

$$S = f_{Fe}^r - f_{Pt}^w = f_{Pt}^r - f_{Fe}^w = \frac{f_{Fe}^r - x_{Fe}}{x_{Pt}} = \frac{f_{Pt}^r - x_{Pt}}{x_{Fe}} \quad (\text{Equation I.15})$$

where $f_{Fe/Pt}^r, f_{Fe/Pt}^w, x_{Fe/Pt}$ are the fraction of Fe or Pt sites occupied by the right (r), wrong (w) atoms and the alloy stoichiometry respectively. $S=1$ represents an ideal atom distribution of equiatomic composition, whereas $S=0$ suggests a random distribution and $S<1$ depicts non-stoichiometric structure even with a perfectly ordered arrangement. The intensities of the superstructure reflections are experimentally proportional to S^2 , thus the S along the c -axis can be implied by comparing the integration of (001) and (002) intensities.

The equiatomic A1 phase is normally obtained as deposited the alloy onto single substrates at either RT or low temperatures ($<400^\circ\text{C}$), thus, it requires another heat treatment to complete the ordering of $L1_0$ phase [123–127]. Owing to this, the volume fraction transformed from A1 to $L1_0$ is followed by the Johnson-Mehl-Avrami-Kolmogorov model and expressed as [128,129]:

$$f_V = 1 - e \left[-v^n \exp \left(\frac{-nQ}{k_B T} \right) t^n \right] \text{ where } v = k_2(T) \exp \left(\frac{-Q}{k_B T} \right) \quad (\text{Equation I.16})$$

where n can run from 1.17 to 1.71 depending on the ratio of Fe/Pt, Q is the effective activation energy for the transformation, k_B is the Boltzmann's constant, T is the temperature in Kelvin, t is the transformation time, $k_2(T)$ is a pre-exponential rate constant [129].

Based on Time Temperature Transformation diagrams, the FePt alloy composition plays a crucial role in the phase transformation kinetics [129]. For instance, at 300°C, the phase transformation in thin film (10 nm) with Fe-rich initiated earlier than in case of Pt-rich sample and the time to achieve 95% transformed volume fraction is about 10^3 s and 10^5 s for Fe-rich and Pt-rich samples respectively. In contrast, with bulk specimens, this time increases considerably (10^6 s and 10^8 s) [129].

On the other hand, as deposited at high temperature ($>700^\circ\text{C}$), the films have already obtained some degree of long-range order (S parameter). There are two possible cases. If the deposition time is sufficiently large enough, the film obtains high S and f_V values [125]. Whereas in case of deposition time is too short, the ordering and phase transformation stages are not completely finished, thus it still requires a second step of heat treatment to attain high S and f_V values [123,127].

1.3.3. Development of hard magnetic FePt films

There currently exists several available methods for fabricating $L1_0$ -FePt thin films such as magnetron sputtering [124–126,130–132], PLD [123,127,133–136], Molecular beam epitaxy (MBE) [137] and electrodeposition [138–140]. The ordered phase can be achieved by employing appropriate processing and deposition techniques. On the one hand, films are either deposited by sequential monolayer deposition or prepared by co-deposition from elemental or alloy targets onto heated substrates, thus the films obtain ordered phase directly. On the other hand, the second step of annealing is required to attain the ordered phase in case of initial films being of either disordered phase or Fe/Pt multilayers.

The dependence of S on the deposition temperatures (T_d) in epitaxial FePt (001) films deposited on single crystal MgO (001) substrate was initially investigated in the range from 100°C to 600°C. At low T_d of 100°C, the films shows $S=0$, while S gradually increases with T_d and reaches maximum of 0.93 at $T_d=500^\circ\text{C}$ [137]. The effect of T_d on S was further carried out on both kinds of single crystal substrates of MgO (001) and (110). It has been found that $S_{(001)} > S_{(110)}$ and a nearly perfect S factor and a huge perpendicular anisotropy have been achieved in FePt (001) grown at $T_d \geq 450^\circ\text{C}$ [123,126,131,141]. While the polycrystalline FePt films usually grows on amorphous or Ta or thermally oxidized layer on Si substrates [133,134,142,143]. Second step of annealing is required to complete the $L1_0$ phase transformation of the films up to 700°C depending on both the annealing time and thickness of the films [123,142–144].

The atomic or chemical composition acts as an intrinsic parameter affecting the $L1_0$ of the FePt films [133,137,145]. Polycrystalline $\text{Fe}_{100-x}\text{Pt}_x$ thin films ($x=25\text{--}67$ at.%) were sputtered onto natural-oxidized silicon substrates. The post-annealing in vacuum induced the optimum ip squareness and coercivity for 200 nm equiatomic film at 600°C in 30 min but no $L1_0$ phase was correlated [146]. Meanwhile other authors investigated films ($x=19\text{--}68$ at.%) at low deposition temperature of 300°C and observed epitaxial growth of (001) peaks indicating the $L1_0$ phase and exhibiting perpendicular magnetisation, high K_1 of 1.8×10^7 erg.cm⁻³ for $\text{Fe}_{38}\text{Pt}_{62}$ film [147]. It is reasonable that the equilibrium temperature for disorder-order transition is lower in Fe-rich films as compared to Pt-rich alloys. Moreover, in thick films up to 1 μm ($x=42.4\text{--}54.0$ at.%), the films exhibited the dependence of $L1_0$ phase on both stoichiometry and annealing method (i. e., with and without post-annealing) [148].

Regarding nanocrystalline materials, the films thickness associated with grain size are of strong effect on crystallographic, microstructure and magnetic properties of fabricated films [123,126,130–132,136]. By increasing the film's thickness, this induced the addition in volume average of long-order range and the volume fraction of the ordered phase, while the S remained almost constant of 0.95 [130–132,149]. This result indicates that not all the $L1_0$ phase exists in the film owing to inhomogeneous

nucleation sites of the expected phase, e. g., grain boundary. However, exceeding critical films' thickness leads to poorer magnetic properties of the films, e. g. 45 nm for sputtered films on to MgO (001) [131,132]. This resulted in changing microstructure from isolated like-islands to percolation of transition between discontinuous and continuous morphology, when the films are smaller and exceed than the critical thickness respectively. It is also fascinating to see that the S dramatically drops as the size of particles below ~ 3 nm, and approaches 0 as the size ≤ 2 nm [150,151]. Hence, miserable magnetic properties were observed as a result [123,130].

It is widely-known that the substrates have major influence on properties of the FePt films ranging from atomic structure, microstructure to magnetic properties owing to the variation in nature properties, interfacial energy, film stress, adhesion [134,136,152]. One can imply that the lattice mismatch, then the misfit strain between the substrates (single crystal-MgO, SrTiO₃, amorphous substrate-glass, Si/SiO₂) and the films affected the ordering of the expected L₁₀ phase. As mentioned previously, it is also possible that the difference in the surface morphologies of the substrates are of significant impact on the atomic mobility of the distinct adatoms of either Fe or Pt during the deposition process. Thus, this leads to differences in microstructure and then the magnetic properties of the deposited films.

In conclusion, the magnetic properties of FePt based thin films are strongly dependent on various parameters during the deposition process such as deposition temperatures [123,125,127,131,132], the stoichiometry of the alloy [133,145], the film thickness [123,130–132], the crystallographic structure of the substrates [134,136,152] and the deposition or annealing conditions [123,135,153] or even the grain size [123,127,130–132,136].

I.4. Soft Magnetic Nanoparticles (NPs)

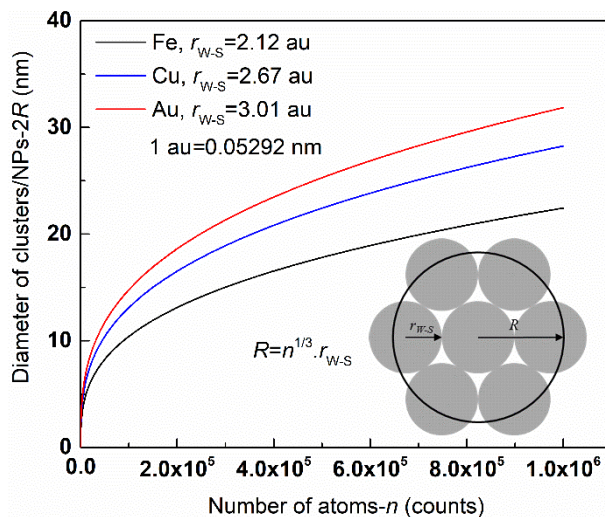


Figure I.12: The estimation of clusters/NPs diameter- $2R$ as a function of number of atoms- n for Fe, Cu and Au atoms based on equation $R=r_{w-s}.n^{1/3}$.

Difference from covalent elements (carbon, sulfur, etc.), clusters/NPs of a metal have a delocalized bond, which involves a tremendous number of bonds. The clusters/NPs geometries are somewhat governed by maximizing degree of compactness of the configuration and therefore adopt the dense sphere structure. It is instructive to estimate the size of the clusters/NPs by using the liquid drop model, which simply neglect their the internal configuration and present them as a unique sphere with

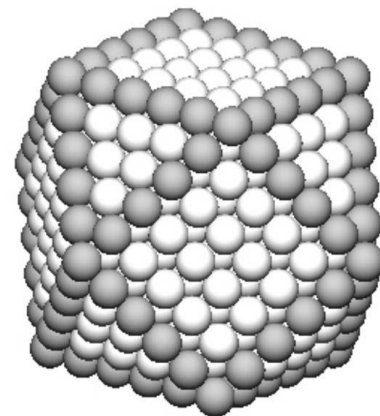


Figure I.13: A 561-atom cuboctahedral NPs from an fcc crystal. The atoms on the edges are shaded for visualization.

radius R . Considering building block of atoms as a dense sphere, the approximate clusters/NPs radius as a function of number of atoms n given by $R=r_{w.s}.n^{1/3}$ where the $r_{w.s}$ is the Wigner–Seitz radius coming from solid state physics and expressed in atomic units (au, 1 au = 0.05292 nm – the Bohr radius) [154]. The dependence of diameter of the clusters/NPs on the number of atoms is presented in Figure I.12. Though the use of this approach is approximation, it has the advantage of being simple and estimating the size of clusters/NPs which has dimension close to a real value.

Another feature of clusters/NPs that make them distinguishable from bulk materials is the fraction of atoms on the surface. In order to estimate this, one can cut out a regular NPs, i. e *fcc* lattice, and count the surface atoms of various size NPs. A 561-atom cuboctahedral NPs from an *fcc* crystal will form six square and eight triangular facets as indicated in Figure I.13. This fraction approaches 0 when a number of atoms in a particle reach to infinity (or cluster is close to solid material), and vice versa, the smaller cluster is, the higher fraction of atoms on surface is. In general, clusters/NPs are of size effect, which favors outstanding properties of electron confinement, phase transition, thermodynamic, magnetic, optical, and electrical features.

The aim of production of NPs is to control their sizes and other parameters like structure (with/without core-shell), chemical compositions. Thus, a variety of approaches has been used to achieve this aim and the four basic generic techniques is listed as follows:

- Depositing and self-assembling on surfaces: In this technique, vapor material is collected on substrates, which possess low surface energy. Thanks to Volmer-Weber growth, optimizing the substrate temperature, coverage and deposition rate promote island growth of the materials with natural pattern.

- Wet chemist: The purpose of this technique is first to reduce the precursor salts and then collect the aggregation of the desired NPs in terms of a suspension in a surrounding solvent. Under a specific condition of evaporation, such suspension is condensed into an ordered flat layer of a base-substrate. Another similar practice, which is often called Langmuir–Blodgett deposition, can be exploited to obtain analogous ordered monolayer.

- The gas phase: The super-saturated NPs' component vapor is condensed into NPs, which could be then mass-filter selected and assembled in an ion trap, or accumulated on a substrate, or co-deposited with other vapor to create nanocomposite. This method will be discussed in details in Chapter II.

- Top-down: The above mentioned approaches are all bottom-up ones, by which atoms are accumulated into NPs. In striking contrast, NPs are formed from a larger configuration in the top-down approach, which is mostly available in either electron beam nanolithography (EBN) or FIB milling. In the EBN, the prior substrate is initially spun-coated with an electron resist substance, usually polymethyl methacrylate (PMMA), and finally exposed to an electron beam with spot diameter of around 5 nm to capture desired pattern through the resist. Note that the PMMA can be either positive or negative resist. The patterned resist can be now used as a nanoscale mask, in which the material can be deposited to form the nano islands and the rest of the resist could be further rinsed off by an applicable solvent. While in the FIB, layer of material is prior to deposition onto a specific substrate and the spare areas will be milled away by using a FIB of common Ga⁺ ions (spot size of about 5 nm). The EBN and FIB are of resolution limitation of ~20 nm owing to presence of available electron/ion beam but they are more adaptable to control the shape of NPs artificially not naturally as in bottom-up approaches.

FeCo alloys are an important soft magnetic material because of their unique magnetic properties including large permeability and very high saturation magnetization as evidenced from the Slater-Pauling curve [109] in Figure I.14. FeCo nanoparticles are ideal building blocks for nanostructured thin film or

bulk magnetic materials [1-3] and are also suitable for biomedical applications [4]. However, synthesis of monodisperse FeCo nanoparticles remains a challenging task due to the poor chemical stability of the nanoparticles.

Based on these methods, various types of NPs have been fabricated, which show extraordinary properties distinguishing from bulk materials. In regard to FeCo materials, owing to the cubic structure leading to the symmetry in its crystallographic structures, it obtains relatively low magnetocrystalline anisotropy H_a and is hence listed as one of soft magnetic materials [155] with the unique magnetic properties such as large permeability, high saturation magnetization. The FeCo NPs are one of the most promising candidates for building blocks of nanostructured

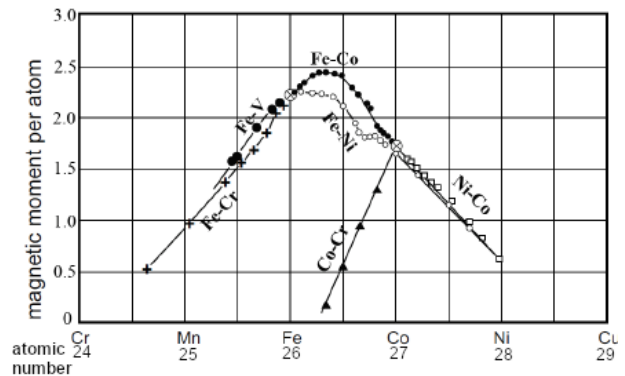


Figure I.14: Slater-Pauling curve of mean atomic moment as a function of atomic number and their composition for various binary nanoalloys [109].

films/composites [155,156]. The FeCo phase diagram of this binary system is presented in Figure I.15. Literature shows that the meeting point and T_C of Co alone is around 1495°C and between 1109°C and 1134°C respectively. The *fcc* γCo and *hcp* ϵCo are established when the temperatures go near and far below melting point [157]. While 1536°C —the melting point of Fe alone is slightly higher as compared to Co. Below the melting point, it is possible to find three distinct allotropes of Fe such as *bcc* δFe (1536°C – 1392°C), *fcc* γFe (1392°C – 911°C), and *bcc* αFe (911°C and below) [157]. Nevertheless, the T_C ranging from 767°C to 771°C is relatively lower than that of Co. In the binary compound of FeCo, at relatively high temperature ($1000^\circ\text{C} < T < 1500^\circ\text{C}$, the compound is apparently stable in (αCo , γFe) state with 30–70 at. % Fe [157]. The interesting B2 (α')-CsCl *bcc* structure is displayed in Figure I.16 and exists at temperature below 647°C , which possesses a high T_C up to 1210 K [7].

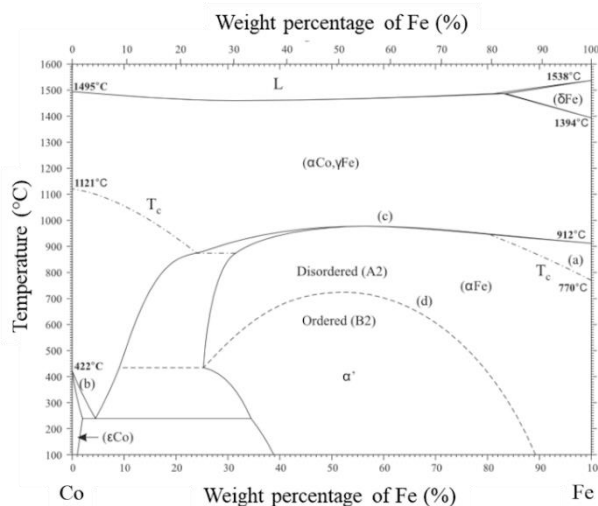


Figure I.15: Phase diagram of the Fe–Co binary system [105].

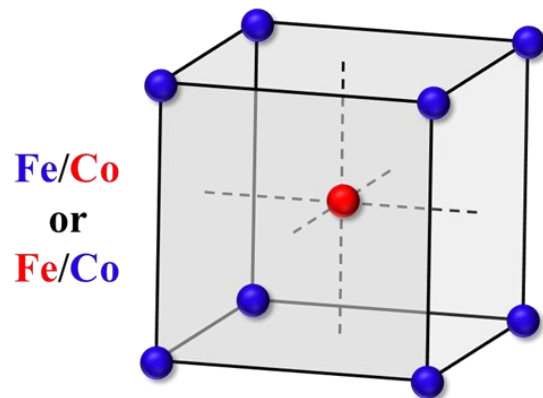


Figure I.16: The schematic *bcc* FeCo unit cell of ordered CsCl-B2 (α') phase when annealed below 920 K [7].

Permendur is of the highest RT spontaneous magnetisation of any bulk material up to 2.45 T ($\text{Fe}_{0.65}\text{Co}_{0.35}$) [7]. In the bulk type, the magnetisation and T_C remain almost constant in $\text{Fe}_x\text{Co}_{1-x}$ ($0.5 < x < 0.65$) [7], while magnetisation is enhanced with x ($0.65 < x < 1.0$) (as evidenced in Figure I.14) because

the magnetic moment of Co keeps relatively unchanged whereas that of Fe increases [158–160]. In *bcc* structure, at 0 K, the maximum average magnetic moment of $2.457 \mu_B/\text{atom}$ (or $\mu_o M_s = 2.49 \text{ T}$) has been observed with $x = 0.72$ [159], and these values are slightly lower in the equiatomic composition of $2.425 \mu_B/\text{atom}$ (or $\mu_o M_s = 2.40 \text{ T}$) [161].

A significant number of fabrication methods has been employed in synthesizing FeCo magnetic nanoparticles (NPs). These approaches are, however, generally categorized into two primary groups, e. g., either *top-down* or *bottom-up* approach [162]. Depending on various parameters such as condition, operation, protocol, etc, these techniques can be further divided into different subclasses. In the first top-down approach, early started from large molecules or small pieces of materials, which is broken into small-scale objects and are later decomposed into expected NPs. Typical processes of this method are chemical/physical vapor deposition, grinding or milling [163–168], etc. The bottom-up approach is also known as the building up method, at which the NPs are made up from elemental substances. Regular techniques of this approach are sol gel, spinning, green synthesis, and chemical synthesis [169–175].

The chemical approach is usually employed in fabrication of FeCo NPs. A spontaneous magnetisation- $\mu_o M_s = 2.12 \text{ T}$ was reported on a 20 nm NPs of $\text{Fe}_{0.7}\text{Co}_{0.3}$ nanocrystallite by using co-precipitation [173]. With increasing the NPs size, a reduction down to $\mu_o M_s = 1.52 \text{ T}$ was later observed with equiatomic composition of 35 nm NPs [171]. Employing other chemical methods, however, led to different observations in $\mu_o M_s$ [170,172,174]. For instance, FeCo NPs assembled by decomposition of organometallic precursors under presence of surfactant exhibited $\mu_o M_s = 2.15 \text{ T}$ and 1.33 T for 20 nm and 10 nm NPs systems respectively. A variation ranging from $\mu_o M_s = 1.63 \text{ T}$ to 1.88 T was also realized in equiatomic NPs [170,174]. Moreover, one of the highest values of $\mu_o M_s = 2.37 \text{ T}$ was measured in a system of core-shell $\text{Fe}_{0.6}\text{Co}_{0.4}$ NPs with a diameter of 7 nm prepared by a hydrothermal process [175].

The second of less popular approach of chemical/physical evaporation method is used in synthesis FeCo magnetic NPs as well. In the PLD process, it has been found that the increase in the NPs' size is proportional to the gas pressure due to higher collision probability in the growth stage [167]. The morphology of the NPs changed from interconnected chains caused by diffusion process, to compact fibrous structures as a result of increasing number of laser pulses [166]. Additionally, 10 nm mass-filtered of either Fe or FeCo NPs synthesized by arc cluster ion source in UHV chamber reveals a uniaxial magnetic anisotropy with the magnetic hard axis being perpendicular to the metallic W(110) surface [165]. Due to just few studies dedicated to Fe or Co or FeCo NPs, it is thus worth to devote more in comprehending the properties of magnetic NPs prepared by laser ablation.

I.5. Chapter highlights

Different magnetic energies dedicated to soft-hard nanocomposites were briefly described together with the associated key/derived magnetic parameters such as coercivity, remanence, demagnetizing field, anisotropy field, anisotropy constant, domains, domain wall width, characteristic lengths, etc. A short overview on two-phase magnets were clearly interpreted, at which it demonstrated what routes should be the best to obtain high performance soft-hard nanocomposites.

The origin of magnetic properties for the best hard and soft magnetic materials in literature was explained. While additional driving forces in thin film growth and processing techniques were also included, the development review of soft, hard materials helps figuring out how to achieve good hard magnetic thin films based NdFeB and FePt materials; and soft magnetic materials/NPs. All gave rise to understand more about the synthesis approach and properties of the systems.

Chapter II. Fabrication and characterization techniques

This chapter will be shortly discussed about fabrication and characterization approaches employed during this work. On the one hand, the hard magnetic thin film and soft magnetic nanoparticles are synthesized independently and further combined to form magnetic nanocomposites. The method in fabricating such thin films (PLD) and NPs (FCG) is all based on the laser ablation process. The laser-matter interaction will be also included to comprehend the phenomena involving the formation of the plasma plume whose expansion under a controlled atmosphere necessary for the formation of thin film and NPs. The deposition parameters, various nanocomposite configurations are listed. On the other hand, a sum-up of the characterizing approaches will be then listed and briefly described to reveal how the characterizations work and which features of the samples can be suggested (RTP, TEM, MFM, VSM-SQUID). Regarding the magnetic samples, specific characterizing method is detailed explicitly based on First Order Reversal Curves (FORCs).

II.1. Fabrication methods

II.1.1. Pulsed laser deposition (PLD)

Laser ablation deposition or more specific **PLD** is a physical vapor deposition conducted mostly in either vacuum or low-pressure gas atmosphere, in which PLD relies on the high-pulsed laser beam (from either excimer or solid state laser)-target surface interaction and create a plasma plume (under sufficiently high laser energy density). During the laser ablation process, the plasma plume is a complex phenomenon and can be roughly described into three distinct stages [79,176]: (i)-the interaction of incoming laser beam with the target surface resulting in the vaporization of the target; (ii)-the ejection of ablated material and high possibility of interaction between such evaporated material favoring the plasma plume and the incident laser beam; (iii)-the expansion of the ejected plasma plume in a vacuum or in a controlled atmosphere and thin film growth. Note that the mathematical-physical role models for

PLD (i. e., laser beam-target surface interaction, plasma formations, plasma plume expansion, etc.) have been discussed in many textbooks and other publications such as references [79,176].

In the initial stage with the laser fluence exceeding the ablation threshold of the target, energy of the laser beam is absorbed by the target surface promoting electronic excitation. In addition, the solid target thermal conductivity is usually far below as compared to the energy

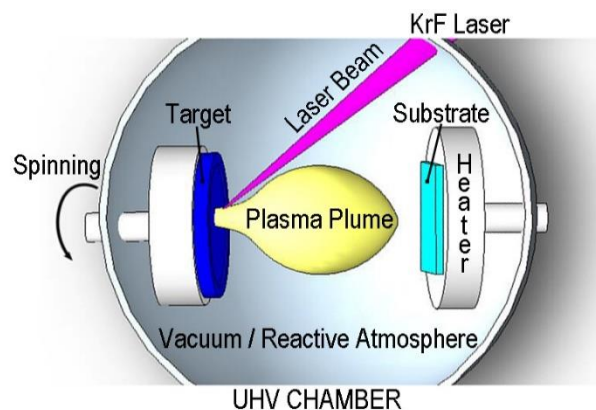


Figure II.1: Schematic setup for a conventional PLD.

dissipation rate in a short time interval of pulsed laser, the photon energy is thereby converted into thermal and chemical energy. Subsequently, a high temperature up to 3500°C is reachable in a small volume in the target and causes an instant evaporation, ionization and decomposition of the target components. The moving direction of such collection of particles constituting the plasma plume, which expands symmetrically along the axis of the plume. These plasma plumes are of direction perpendicular to the target surface no matter what direction of laser beam approaches with respect to the target surface, and will be collected on the substrate located in front of the target for film growth (see Figure II.1) [176].

The plasma plume starts travelling inside the deposition chamber. A significant variation in the species velocities ejecting from the target ranging up to 10 km/s has been observed, which strongly depend on present pressure, atomic number Z [176–178]. Regarding the interaction between the incoming beam and the plume, the class of laser plays a crucial role [177–179]. For instance, nanosecond pulse duration is normally considerably longer than the electron cooling (\sim femtosecond) or lattice heating time (\sim picosecond) and thus the energy absorbed by the surface electrons of the target has sufficient time to be transferred to the lattice. The lattice and surface electrons both later reach a thermal equilibrium. The significant energy loss is just heat conduction transferred to the target. Subsequently, the ejected plasma will absorb a notable amount of energy from the incoming laser ray, and thus contribute to the heating up of the plume. However, in case of ultrafast laser ablation (at least 1-10 picosecond laser), there no longer exists the interaction between the plume and the incoming ray because the ejected constituents of the plume is governed by the Coulomb explosion, which is the dominant ejection mechanism of the plume [179].

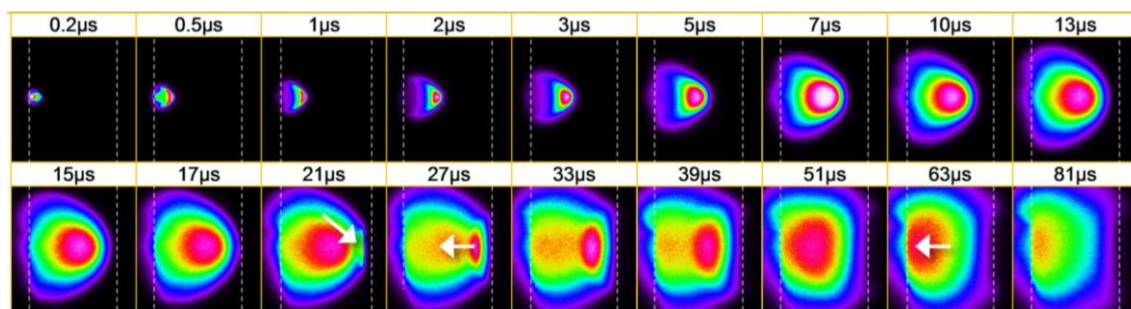


Figure II.2: The time resolved plasma imaging under 1×10^{-1} mbar of ambient Ar gas at different time scale while ablating the $\text{La}_{0.4}\text{Ca}_{0.6}\text{MnO}_3$ cylindrical target by a KrF excimer laser (pulse duration: 20 ns, $\lambda = 248$ nm, fluence: 3 J.cm^{-2} , frequency: 4 Hz, distance between target and substrate: 4 cm) [176].

In the final stage of approaching the in front substrate, the plasma plume is either controlled by residual pressure, ambient gases, or reactive atmosphere such as Ar, O_2 , N_2 . The higher pressure of the ambient gases, the more the plume is confined. The effect of ambient gases at different pressure has been observed clearly [176]. Figure II.2 demonstrates the evolution of the confined plasma plume with respect to time under ambient Ar gas. The experimental analysis shows that the constituents in the plume are all confined and reached the same velocity accompanied by a sluggish plume expansion, which creates a transient added local pressure. After reaching the substrate, it appears as an additional rebounding wave as a secondary source of plasma plume that sails backwards to the target. This effect is called as re-sputtering or recoating effect, which leads to the enrichment up to 30 % of the ablated material per pulse [176], of specific elements if the target is a compound material of binary, ternary or quaternary system. The current target composition due to the re-sputtering effect is therefore no longer the same as in the original target. In other words, the target surface is migrated and slightly changed in its composition. This recoating effect would slightly change the target composition, and the film composition as a result (details presented in section III.1.1). Note that the variation in composition of the target surface depends on numerous parameters such as background gas, materials, distance between the target and substrate, etc.

The deposited samples are of either the same (stoichiometric transfer) or different composition as compared to the target content. This fluctuation originates from multiplex sources of ambient gas or vacuum, laser fluence, laser wavelength, laser frequency, etc. Furthermore, the fabricated thin films or nanocomposites could be crystallized or amorphous, which exhibit tunable and novel properties that are inaccessible in case of bulk state. If the films are crystallized, their preferential orientation can be identified by multiple known variables such as the substrate nature (amorphous like glass, SiO_2 ; or single

Tuan NGUYEN VAN | Thèse de doctorat | Université de Limoges | 7 Mai 2021 22
Licence CC BY-NC-ND 3.0

crystals like MgO, sapphire), deposition temperature, ambient gas pressure, laser fluence, the laser properties, etc.

In conclusion, though involving various number of experimental variables influencing both plasma plume and later thin film growth makes PLD challenging to master, the PLD technique is itself actually simple and versatile. The specialized upsides in PLD approach as compared other fabrication techniques, make this technique to be employed in work, which can be listed as follows [79]:

- It allows achieving stoichiometric transfer from ablated bulk target (either single or compound target) into thin film mounted on the in front substrate holder and is well adapted with a wide range of target materials, especially with the complex ones.

- The energetic species in the plasma plume could bring benefits to the thin film growth and make the film crystallized even at RT, e. g. it tolerates decreasing deposition temperature, and frequently no further heat treatments are required (i. e., crystallized with A1 phase of FePt film).

- The compatibility in wide range pressure conditions ranging from ultrahigh vacuum up to 1 mbar, and the residual of ambient gas as well that open possibility in depositing heterostructures by adjusting the surrounding deposition media.

- The source of the laser beam is external to the deposition chamber, thus it quite easily isolates the deposition parameter involved and makes the reactor clean with respect to other methods.

- The incident laser beam can be focused and create various impacted spots on the target, which leads to high efficiency, controllable and flexible process.

II.1.2. The lasers

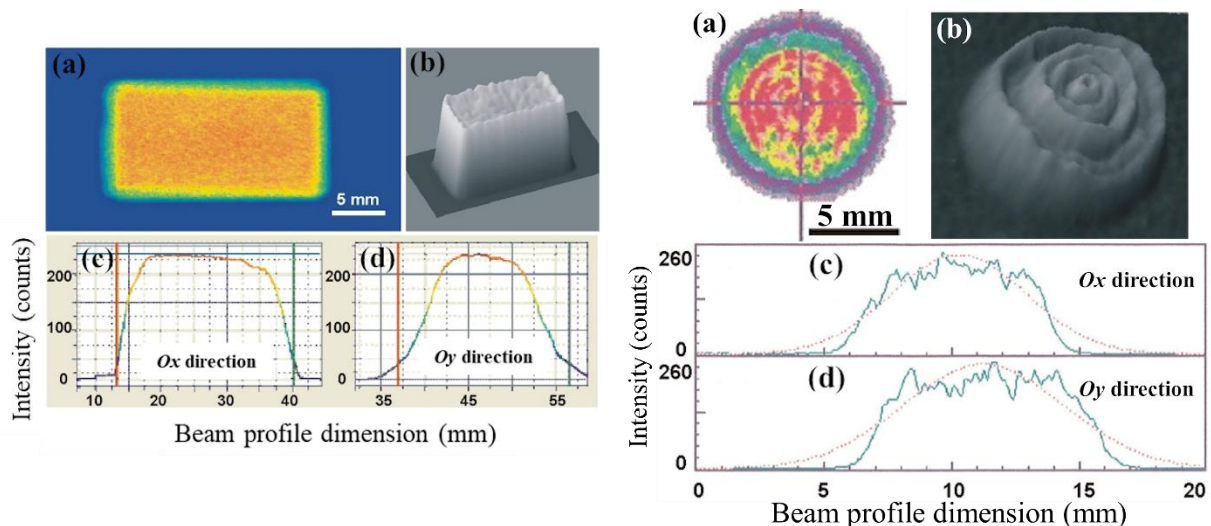


Figure II.3: Beam profile of excimer (KrF, left) and solid state (Nd: YAG, right) lasers with single shot at 10 Hz, in (a) 2D; (b) constructed 3D; (c) O_x direction; (d) O_y direction. The (excimer and solid state) lasers parameters are: wavelength (248 and 1064, 532, 355) nm, beam profile (rectangular $\sim 26 \times 12 \text{ mm}^2$ and circled $\Phi \sim 10 \text{ mm}$), pulse duration (25 and 5-8) ns, pulse energy up to (750 and 450) mJ, pulsing frequency (1–25 and 4–20) Hz, respectively. These images are adapted from [180].

Due to the specific purpose of depositing both thin films and nanoparticles, the two lasers of excimer and solid-state with distinct properties will be used during this thesis. While the excimer laser is used in depositing the thin films in the main chamber, the solid-state laser is used for synthesizing the nanoparticles in the cluster generators owing to the relatively small nucleation chamber. Details about these lasers and why they will be employed will be discussed below.

The laser used during this thesis is excimer KrF LightMachinery IPEX-742 with the properties as follows: wavelength $\lambda = 248$ nm, pulse duration of 25 ns, a maximum achievable energy of 475 mJ per pulse, the repetition rates ranging from 1-25 Hz, the beam dimension of 26×12 mm² at the exit, nominal beam divergence of vertical \times horizontal = 1×3 mrad and the energy fluctuation of around 3 %, the beam profile and model being found with explicit in Figure II.3 and Figure II.4a. In order to select the most homogeneous beam region, the KrF laser beam passes through a rectangular diaphragm with dimension 15×10 mm² located in front of the exit. The filtered laser beam then goes to the reflected dichroic mirrors with dielectric multilayers of 50 mm in diameter, whose reflection coefficient is 0.95 at $\lambda = 248$ nm under an incident angle of $45^\circ \pm 5^\circ$. The laser beam is then focused by a plano-convex lens with a diameter of 25.4 mm and a focal length of 30 cm, which helps to modify the impacted area on the target when changing the position of the lens (Figure II.5).

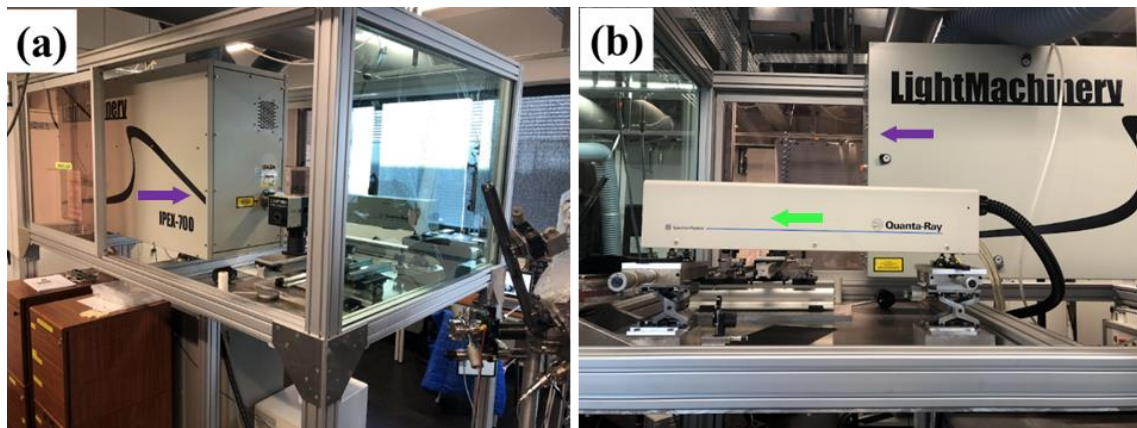


Figure II.4: (a) The KrF excimer laser LightMachinery IPEX 742 (violet arrow) and (b) solid state laser (Nd: YAG laser)-Quanta-Ray Spectra Physics (green arrow).

In comparison with the excimer laser, the performing principle of the solid-state (Nd:YAG) laser is different, at which the laserable substance is excited to a semi-stable by optical pumping. And in this case of Nd:YAG, the laserable matrix is a solid crystal, which is the so-called Nd:YAG rod (in lieu of gas in the excimer laser), whose their ends are polished flat shiny together with being coated with reflectors (mirrors) to make the cavity.

The solid state laser used during this thesis is an Nd: YAG laser of the INDI type from QUANTA RAY (Figure II.4b). It can operate at distinct wavelengths, with the use of a harmonic generation system, in the ultraviolet (UV 355 nm- 3ω), the visible (green 532 nm- 2ω) and the infrared (the fundamental 1064 nm). At the interested wavelength of 532 nm, the INDI Nd:YAG laser delivers, for a repetition rate of 4 Hz, a maximum energy of 100 mJ per pulse of duration 7 ns, while the output energy at 10 Hz can be up to ~ 180 mJ. In addition, the beam divergence is around < 0.5 mrad and the pulsed-pulsed energy fluctuation is less than 3%. At the output, the laser carries a circular beam with a diameter < 10 mm, i. e., a spot area < 80 mm² (Figure II.3 and and Figure II.4b). The laser beam is focused on the target by a focusing plano-convex lens (Figure II.5) with a diameter of 2.5 cm and a 25 cm focal length. Due to its outstanding beam profile (low divergence, small spot and sufficiently high delivery energy), this Nd:YAG laser is perfectly suited to the small cavity of the home-made free cluster generator (which will be discussed below). Details about the excimer laser and solid-state laser can be found in Appendix, A.1.

II.1.3. Home-made free cluster generator

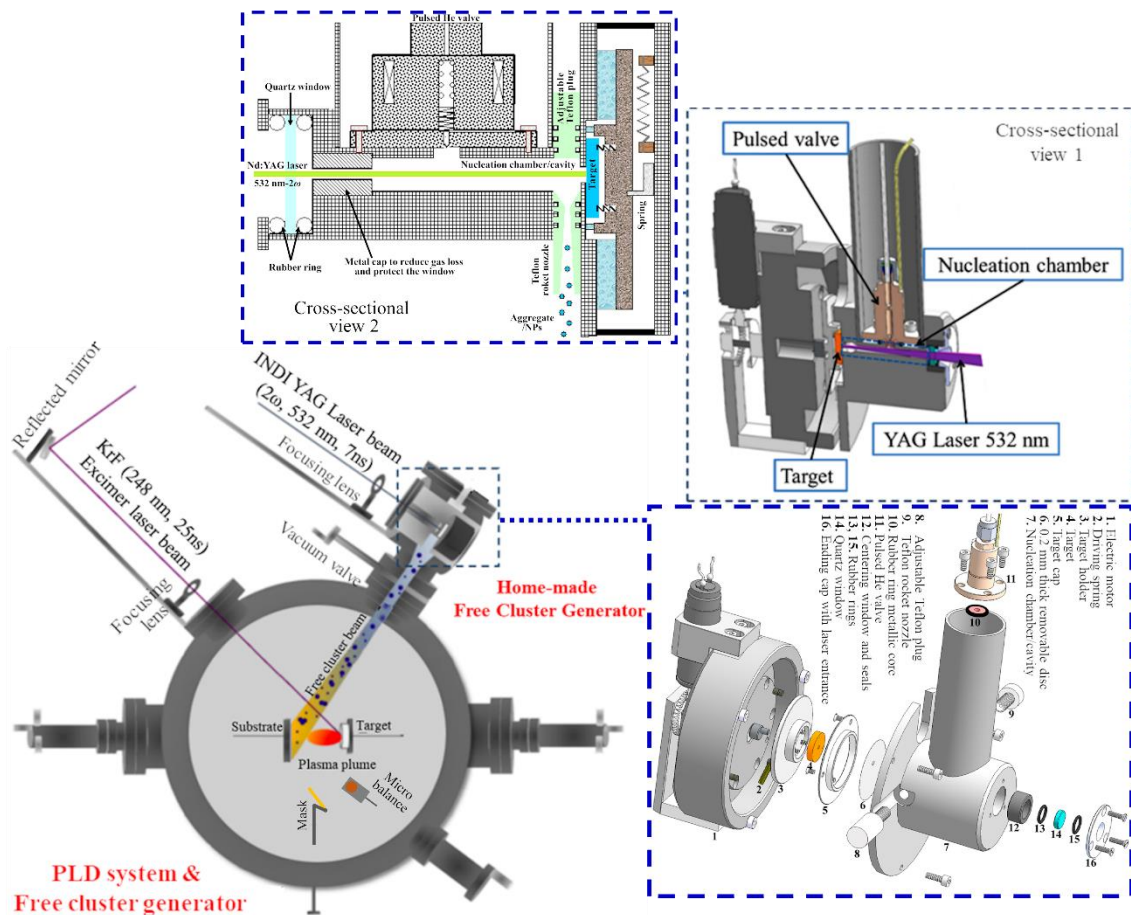


Figure II.5: The conventional PLD and home-made Free cluster generator setup at IRCER [99,181].

The home-made *free cluster generator (FCG)* presented in this thesis was entirely redesigned and manufactured at IRCER laboratory by Alain Catherinot, Frédéric Dumas-Bouchiat, and Nicolas Lory [181]. The principle and the concept of this FCG had been initially proposed and developed in the pioneering work of Richard Errett Smalley and his group in 1981 [182], which latter helped him to win the shared Chemistry Nobel prize in 1996 for the discovery of new form carbon of buckyballs-C₆₀ [182–184]. Following this concept, the NPs developed during this thesis were synthesized in the gas phase using the laser ablation from a metal/alloy target. The vaporized species generated from the interaction between a pulsed laser and the target are abruptly cooled by a high pressurized Helium flows. Thanks to this design, the NPs composed of a few *n*-atoms (*n* ranges from 2 to 100 atoms) are possible to be synthesized with wide range of materials like Iron (*n* ≤ 25), Silicon (*n* ≤ 50), Carbon (*n* ≤ 100) Nickel, Tungsten, and Molybdenum. The combination of PLD + FCG is displayed in Figure II.5.

Nevertheless, the original setup does not allow to synthesize of larger clusters/NPs of size of ~8–10 nm. Note that in the FCG configuration, the quenching rate of the plasma plume controlled by the pressurized helium gas can reach up to $dT/dt \sim 10^8\text{--}10^9 \text{ Ks}^{-1}$ [182]. In order to achieve larger NPs size, a small thermalization chamber (cavity, often called nucleation chamber) was added with respect to the original setup [182]. The small cavity helped to lengthen the residence time of the species and thus increase the number of collisions between them. Therefore larger nanoclusters are produced [185]. In the setup (Figure II.5), this cavity includes two coaxial cylinders of 4 mm and 5 mm in diameters, 42 mm and 10 mm in length respectively. Owing to the relatively small dimension, the FCG obligates a limited laser

beam ($<1 \text{ cm}^2$) being concentrated into such narrow cavity, obtained from the Nd:YAG laser with Q-switched mode (section II.1.2). The Nd:YAG laser is synchronized with an electrical pulsed valve delivering a pulsed pressurized pure helium gas (up to 10 bars), which quenches and thermalizes the vaporized constituents in the mixture. The opening t -time of the pulsed valve, defined as the interval between opening and closing moment, is of the order of hundreds of μs altering directly to the NPs diameter [99]. Namely, the opening t -time enables to fine-tune the resident time of the plume in the small cavity and thus, the vapor attains the supersaturated equilibrium inducing condensation of nuclei evolution and thereafter the coagulated assemblages of tiny species, i. e., NPs [99,182].

The cluster formation mechanism can be explained in terms of thermodynamics with the assumption of ignoring evaporation with sufficiently high supersaturation effect. The free Gibbs energy describing the surface free energy with respect to the volume one, approve the critical nucleus size n^* and given in reference [99]. In order to initiate the nucleation growth to form the NPs, the existing nozzle configuration is an important parameter affecting directly the adiabatic, supersonic expansion processes, the cooling rate, cluster beam profile and thus the deposition rate [186,187]. In the experimental setup as in Figure II.5, a typical Teflon converging diverging nozzle is manufactured with the diameters of 5.9 mm, 2 mm and 7.6 mm of the inlet, throat and exit respectively. Due to the curved or unaligned gas channel, there is no support for a high supersonic expansion. Therefore, in this process, the gas speed at the exit of the nozzle is given by Richard Nakka's equation (Equation II.1). However in our setup, the helium gas associated with NPs in drift motion makes the speed complicated to calculate theoretically. A profound estimation showed that the actual speed of the mixture (could be identified as NPs) at the nozzle exit is more than 500 m.s^{-1} [188]. This is responsible for the kinetic energy per atom is lower up to two orders of magnitudes than that of the NPs cohesive energy. For instance, kinetic energies of atom with speed of 500 m.s^{-1} are about 0.13 eV/atom for Mo and 0.24 eV/atom for W in comparison with cohesive energies of 4.25, 5.64 for Mo and 6.42, 8.20 eV/atom for W with 3 and 30 nm NPs respectively [189]. This is in agreement with a well-known fact that the cohesive energy is theoretically and experimentally proportional to the diameter of the NPs [189–191]. The low kinetic energy permits the fabricated NPs landing on the substrate to remain their shape after the direct impact on the substrate, that is why the FCG is sometimes referred as Low Energy Cluster Beam Deposition [100].

$$v_{He} = \sqrt{\frac{2R}{m_{He}} \left(\frac{\gamma}{\gamma-1} \right) T \left[1 - \left(\frac{P_e}{P_c} \right)^{\frac{\gamma-1}{\gamma}} \right]} \quad (\text{Equation II.1})$$

where k_B , T , γ , R , m_{He} , P_e , P_c are the Boltzmann's constant, the estimated temperature of the species before the nozzle expansion, the effective ratio of specific heat of exhaust gas-He, the universal gas constant, He molecular mass, the nozzle exit and the cavity pressure respectively.

Unlike the high energetic ions in the plasma plume of up to 100 eV [192] in the PLD, the low kinetic energy NPs travel and land on the substrate gently, which induce a certain porosity in the stacks of NPs. Experiments confirm the porosity of such stacks systems as high as 62 % [100,101,191], which is coherent with the simulations for Mo and Cu NPs [191,193]. A MAXTEC-Quartz Crystal Microbalance (QCM) (Figure II.5) with high reliability and high accurate resolution of about 0.1 \AA.s^{-1} at working frequency of 6 MHz is used to detect the cluster beam and later determine the deposition rate of the NPs deposition.

II.1.4. Improvement in the setup, and depositing parameters in use

The setup used during this work consists of conventional PLD coupled with FCG to develop nano-inclusions inside matrices. While the thin films are somewhat simpler to fabricate, the NPs become a little complicated to synthesize. In order to well control the properties of the NPs, various parameters need checking, such as the synchronization process between the He pulsed valve with Nd: YAG laser, the opening t -time, pressure, etc. Based on the previous work [218], the synchronization procedure was successfully established with this thesis's conditions (details are displayed in Appendix A.2). In addition, the opening t -time has an influence on the size of NPs but it will be discussed in section IV.1.2. In this part, the thesis just mainly focuses on supplementary components which make this combined setup more elegant and favorable as compared to others. Depositing parameters used during the deposition will be listed afterward.

The improvement in the setup

The substrate temperature is an important variable, which influences directly on the atomic organization and microstructure of the fabricated films/NPs/nanocomposites. In the PLD setup, a substrate will be heated up from the back side by a halogen lamp ranging from RT up to 750°C, with a homogeneity in temperature > 90 % for the 1 × 1 cm² substrate. The heating system is supplied by a power source from ALIMENTATION SODILEC SDL G3 36 V 30 A.

As demonstrated in Figure II.5 with conventional PLD setup, the KrF laser beam is directed to the deposition chamber with the use of a reflecting mirror, which can be oscillated around the pinned axis where it is hanged. Thanks to the mirror oscillation, the refreshed ablated zone is significantly improved compared to the virgin area. A comparison between the ablated zone in the simple rotary target and system used in this work, is demonstrated in Figure II.6a and b. In this setup, the reflecting mirror oscillates in a trajectory so that the laser fluence on the target is almost constant, thus it induces a relatively high homogeneity of the deposited films compared to the initial setup of rotary target (Figure II.7, note that the plasma plumes is purposely set out of the substrate center), i. e., a homogeneity > 75 % has been observed with scanning on rotary target against > 60 % without scanning, at laser fluence: 5 J.cm⁻², target-substrate distance: 3.3 cm, deposition pressure: 5 × 10⁻⁷ mbar, wavelength 248 nm, frequency: 10 Hz on NdFeB target and 1 × 1 cm² substrate. However, the distribution in thickness will be in the elliptic shape due to the PLD deposition characteristic of the pressure gradients in the plasma along the axes of the ellipse forming the laser impact, accompanied by the motion of the plasma plume induced from mirror oscillation. While this PLD setup is adopted for only one target holder, the rare-earth element of neodymium likely interacts with oxygen (relative high of partial resident oxygen still exist at even UHV condition), and thus a home-made double targets holder is introduced to optimize the time changing between the targets (either NdFeB/FePt target for the matrix or Ta/C for buffer/protective layers). The home-made holder can help to reduce the changing time from 15 minutes to 3 minutes in the classical setup and the double targets holder setup, respectively (Figure II.6b).

In the FCG, to refresh the irradiated surface for each single laser shot on the target, the target is under a hypocycloidal motion (Figure II.5, cross-sectional view 2). With the Nd:YAG laser beam remaining fixed, as a result of such motion, the ablated zone becomes significant in comparison with the virgin area (Figure II.6c).

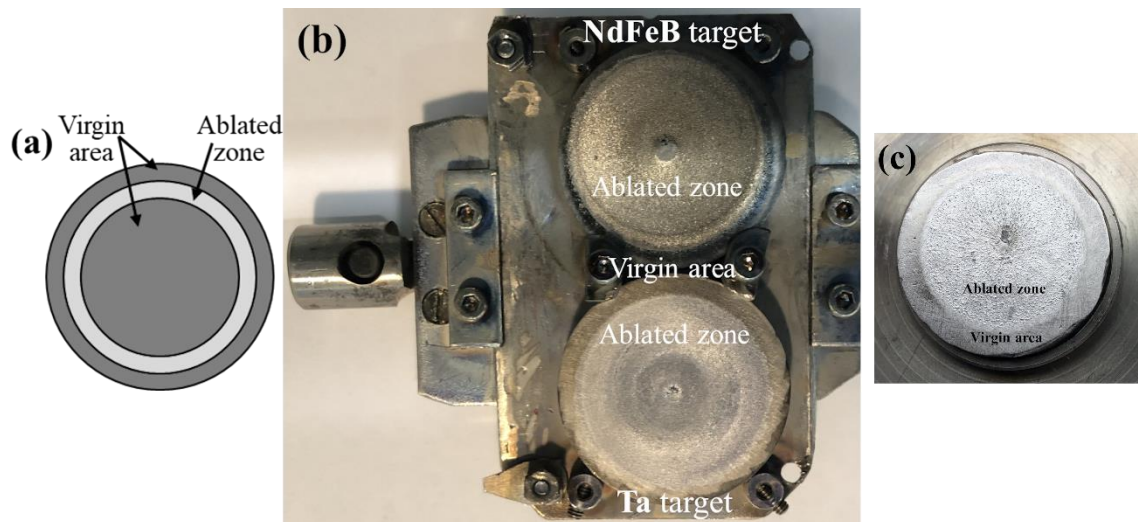


Figure II.6: The advanced augmentation of the PLD and FCG setups in ablating the materials from a target of (a) the representation of classically irradiated target with small amount percentage of ablated zone compared to the whole target surface; (b) the home-made double targets holder which helps reducing time in changing the target from 15 minutes (individually separated target) to 3 minutes in the conventional PLD setup. Moreover, the rotary target + reflected mirror movements permit a sufficiently large ablated zone; and (c) The hypocycloidal motion allows increasing effectively the ablated zone compared to classically rotary target surface. The target diameters are all about 2.5 cm (one inch).

Regarding the metal or the alloy compound target and the laser beam profile (beam homogeneity, pulse length, wavelength and fluence), after being bombarded/etched by the laser incident beam at a fixed angle to the target surface normal direction, it is found that there is a gradual development of cone-like surface structures tending to point back toward the incident laser beam, which induces the target roughening [79]. When the target roughness increases, it spreads the beam energy out over a broader range, the fluence and deposition rate are therefore reduced as a must. The deposited film from the rough target, on the front substrate will also bear a significant number of droplets. In order to reduce the droplet formation, target roughness and avoiding a reduction in the etch rate by shadowing of the cones, the target rotation and later laser plume (induced by mirror oscillation in the PLD) or hypocycloidal motion (in FCG) are used [194]. Furthermore, one should take care of the incident laser entrance windows because a thin metal film of about ~5 nm stuck on the entrance, will absorb considerable laser radiation and reduce the fluence and deposition rate. Fortunately, the nonmetallic materials can be effectively removed from the windows by intensifying the laser fluence on the windows, in contrast to the high ablation thresholds of metals, they require sufficiently high fluence and thus this causes windows to be damaged in some senses. Hence, a periodic removal cleaning the windows is an alternative solution (basically, cleaning up every averaged 30 hours of depositing time).

In this thesis setup, the features of this combination lie in the presence of the PLD and FCG, which allow using the two devices in independent, simultaneous and sequential ways. This flexibility opens new ways to produce distinct kinds of nanostructured materials varying to the choices of the target ablated by laser ablation (Figure II.8), and these structures will be listed in details as follows:

- Using only conventional PLD, the thin films/matrices (NdFeB, FePt) will be deposited on various substrates at various deposition conditions. Figure II.7 presents a route to identify the thickness (Figure II.7a) and homogeneity (Figure II.7b) of the deposited films. Note that the lithography pattern was obtained by using a mask that will be used to fabricate electrodes for other purposes, but in this thesis,

the mask helps to identify the thickness (and/or deposition rate) and the homogeneity distribution of fabricated samples.

- Using only FCG, since the deposition rate of the clusters/NPs beam is varied with respect to the materials (usually <100 nm/hour), the exact deposition rate will be indicated by measuring with the QCM. A few NPs can be deposited on a copper based carbon TEM grid to investigate the intrinsic properties of individual NPs such as their crystallinity, size distribution, shape, composition (Figure II.8a). Increasing deposition time or increasing the number of NPs deposited will produce another type of structure, called "stacking" structure, where the NPs are distributed and dispersed in a random fashion (Figure II.8b). This stacking of NPs, however, has a momentous porosity percentage of up to 62 % for Fe_{150} NPs [195] or $53 \pm 5\%$ in this setup for Co-NPs [101]. Therefore, the first two modes of deposition for NPs involve nanometric particles and the substrate, in a very well controlled manner and the use of these techniques will be carried out further to investigate the properties of Fe, Co, $\text{Fe}_{65}\text{Co}_{35}$ NPs in this thesis.

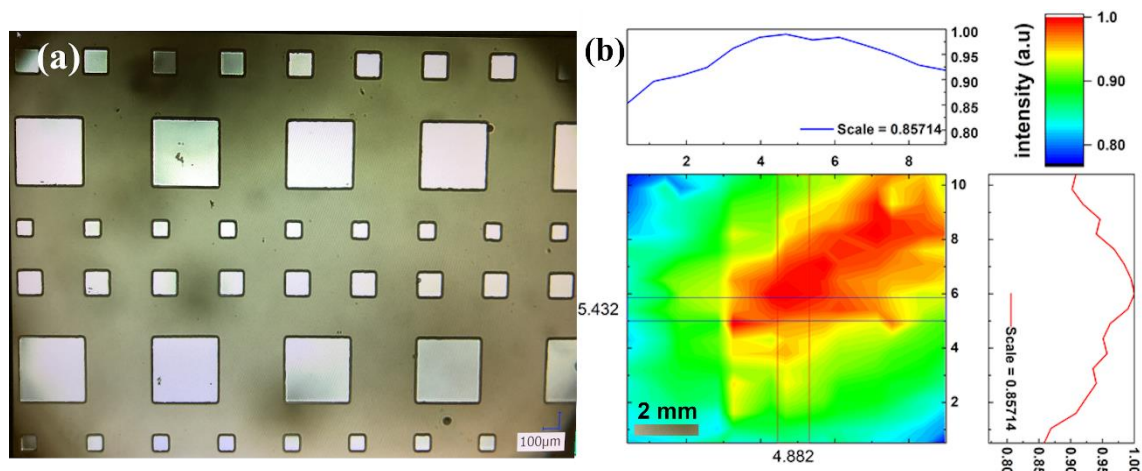


Figure II.7: The routine used in identifying deposition rate or the thickness distribution as depositing a NdFeB thin film by conventional PLD at distance: 3.3 cm, fluence: $5 \text{ J}\cdot\text{cm}^{-2}$, frequency 10 Hz, base pressure: 1×10^{-7} mbar (a) Lithography pattern in use and later measured the step height of the deposited film with Veeco DEKTAK 6M profilometer operating in the range of 10 nm to 1 mm; and (b) the reconstructed normalized thickness distribution of the deposited sample with size of $1 \times 1 \text{ cm}^2$.

- Using the combined setup of PLD + FCG, two other deposition modes (thin film by PLD + NPs by FCG) can be achieved either simultaneously or sequentially. In the case of simultaneous co-deposition, the conventional PLD permits forming a matrix, on which the NPs will be embedded to construct a well-mixed nanocomposite. Here it is capable to conceive a wide interest of either matrix or NPs (Figure II.8c). In using the PLD and FCG sequentially, it is possible to produce materials of the super-networks or layer by layer of thin film and stacks of NPs, alternatively (Figure II.8d). Additionally, estimating precisely the time flight of NPs and the expansion speed of the plasma plume (induced by the conventional PLD), interactions between the plasma plume and NPs can lead to the synthesis of new structures such as potential core-shell NPs. In this thesis, the nanocomposites will be deposited sequentially, in which the film matrices of hard magnetic phases (FePt or $\text{Nd}_2\text{Fe}_{14}\text{B}$) will act as a frame to reinforce the magnetisation of the soft phase of the embedded NPs (Co , $\text{Fe}_{65}\text{Co}_{35}$).

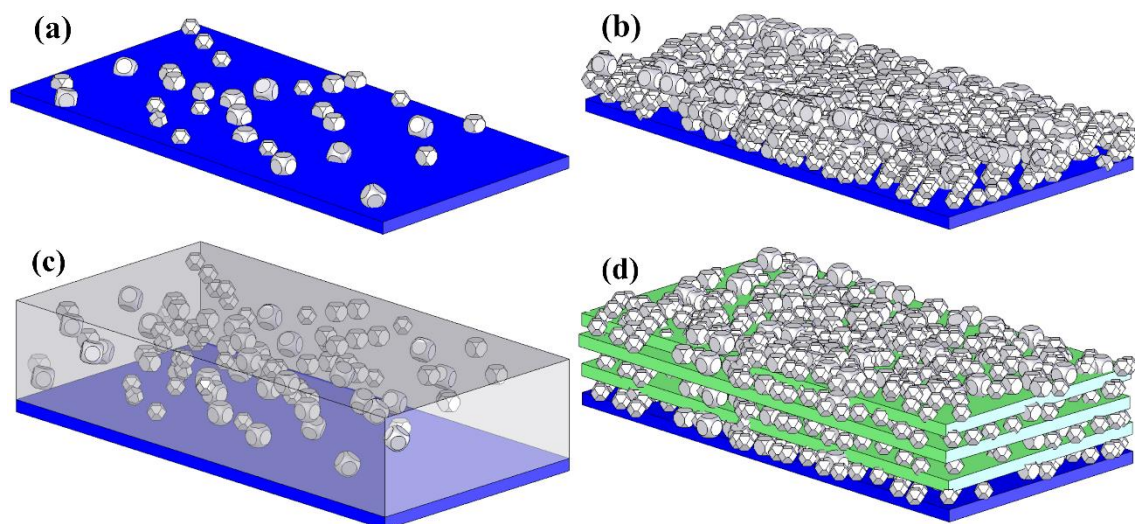


Figure II.8: Various deposition modes can be deposited with the combined PLD+FCG system for (a) a few NPs deposited on a substrate (normally NPs on Cu/C-TEM grid); (b) stacks of NPs deposited on a substrate; (c) nanocomposites of NPs embedded inside a matrix, taken place when using co-deposition; and (d) nanocomposites of layer-stack structures of thin film-NPs, developed when using sandwich mode of PLD and FCG [181].

Parameters in use during this work

The process itself involves in large number of parameters, thus these parameters need taking into account with care to deposit good thin films, NPs and nanocomposites. Table II.1 provides several useful fabricating parameters employed in this thesis.

Table II.1: The deposition parameters used in depositing thin films, NPs and nanocomposites.

	Thin films (NdFeB and FePt)	NPs (Fe, Co, FeCo)	Nanocomposites (thin films and NPs)
Based pressure (mbar)	1.0×10^{-7}	1.0×10^{-6}	1.0×10^{-6}
Depositing pressure (mbar)	$5.0-10.0 \times 10^{-7}$	5.0×10^{-4}	5.0×10^{-4}
Ambient gas	Vacuum	Vacuum + Helium	Vacuum + Helium
Substrate	Si(001)/SiO ₂ (100nm); Al ₂ O ₃ (0001); MgO (001)		
Laser type	Excimer KrF	Nd:YAG	KrF and Nd:YAG
Laser fluence (J.cm ⁻²)	6 and 5	8	5 and 8
Repetition rate (Hz)	10 and 2	4	(2 and 4)
Laser wavelength (nm)	248	532	248 and 532
Pulse duration (ns)	25	7	25 and 7
Target-substrate distance (cm)	3.3	45	3.3
Pulsed valve duration (μs)	Not in use	280 - 600	300, 480
Temperature (°C)	From RT to 750		
Annealing procedure	With and without RTP (up to 900°C, modular ramp)		

II.1.5. Rapid Thermal Processing (RTP)

The development of magnetic materials requires advanced processing techniques. The magnetic properties of samples usually relate to both intrinsic and extrinsic parameters, and thus the heat treatments are often applied to obtain the desired phase transformations and sometimes appropriate microstructures. In this work, besides the direct crystallization during the deposition used in the PLD chamber, another approach of two-step heat treatment process is also exploited. In order to apply heat treatment with post-annealing, the *Rapid Thermal Processing (RTP)* system is used, which is dedicated to low-dimensional magnetic materials (thin films, NPs, nanocomposites). RTP favors the crystallization from amorphous phases, the phase transitions, the grain size depletion, the grain isolation, the atomic structure [196,197].

Basically, the annealing process will induce the unexpected diffusion process in samples and it is really harmful to the nanocomposites with distinct soft and hard phases. Details about the diffusion process will be discussed in section V.2. Therefore, by well-controlling the RTP parameters, one can be able to obtain desired properties of magnetic materials as well as effectively prevent diffusion process with short annealing time.

The RTP system at IRCER is an AS-ONE 100, ANNEALSYS, which is mainly divided into two main parts of the reactor and associated circuits resided in the upper part. The reactor is composed of two parts. The first is the bedplate, which supports the substrate and is kept on a base plate, while the second is in a pivot allowing the introduction and removal of the substrate and sample. The annealing sample will be placed closely to the surface of a quartz window and is heated up by an array of lamp. This series of lamp is specifically developed for rapid thermal processes. Below the quartz windows is a

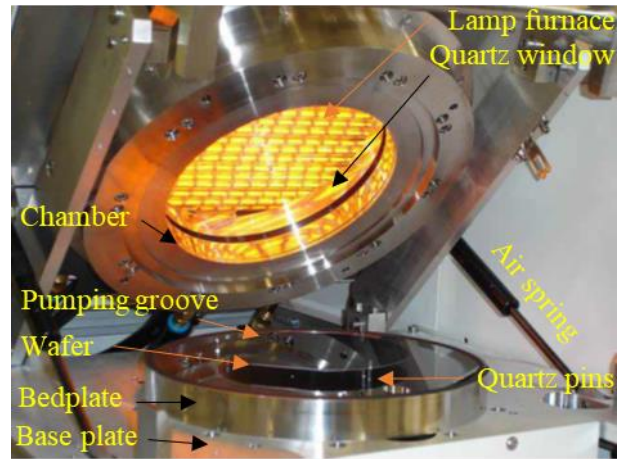


Figure II.9: The schematic diagram of the main part of the RTP system at IRCER.

collection of gas inlets. There are multiple purposes in using gases such as ambient environment, gas flows and cooling. The gas is evacuated by the vacuum pumps through pumping grooves located on the backside of the bedplate, in which the chamber can be performed from vacuum of (1 to) 5×10^{-2} mbar to atmospheric pressure. In order to control the exact temperature, a series of thermocouples and pyrometers is equipped with the bedplate. Three quartz pins with specific design prevent the thermal transfer from the sample holder (Si wafer) to the system, on which the sample is placed on Figure II.9. After reaching the desired temperature and maintained at a certain temperature during annealing process, the furnace/lamp is cooled down slowly by tangential air fans/gas/water to prevent dislocations and wafer breakage because of thermal shock. The proportional integral derivative (PID) controller entirely controls the whole system so that the control loop feedback mechanism manages the process parameters accurately and stably.

The RTP system can reach a ramp rate up to $200^\circ\text{C}/\text{s}$ in a larger homogeneous temperature surface area of up to 100 mm diameters, and temperature up to 1300°C . The specimens (normally, size of $5 \times 5 \text{ mm}^2$) are annealed at various annealing conditions of heating rate, annealing time, pressure, ambient gas of Ar flows to investigate their influences on structure, microstructure and magnetic properties of the magnetic samples.

II.2. Characterization methods

This part will mainly discuss about the characterization techniques that will be used to investigate structure, microstructure and magnetic properties of samples developed in this thesis. Some of conventional characterizing approaches will be in the Appendix, i. e., **XRD** (Appendix A.3), **SEM** (Appendix A.4), **FIB** (Appendix A.5), **AFM** (Appendix A.6). The other techniques that is more "specific" to dedicate to the fabricated samples will be presented below.

II.2.1. Transmission electron microscopy (TEM)

Transmission electron microscopy (TEM) is one of the most powerful characterization techniques, which benefit for deeper understanding at atomic scale. The discovery of wave-particle duality of electron, i. e., wave behavior, allows to use the the electron wave properties in electronic microscopy relating to the de Broglie's equation, which correlates the wavelength and energy. For instance, the wavelength of about 4 pm induced by typical electron beam energy of 100 keV in TEM, is sufficient good enough to observe the characteristics of atoms such as distances, diffraction patterns, etc. TEM characterization requires great careful sample preparation (discussed in section V.2.2) so that the specimen is thin enough to be transparent for the accelerated electrons and ready for measurement.

The NPs deposited on a carbon TEM grid or the nanocomposites, presented in this thesis, right after being cut from FIB, will be placed inside the TEM and ready for observation with high resolution analysis from TEM JEOL 2100F. A typical TEM configuration is presented in Figure II.10. In the TEM, various kinds of TEM images presented throughout this thesis that can be extracted to obtain more information about the structure, microstructure of the NPs and the thin films, will be briefly described as follows:

- **The Bright-field (BF) imaging:** Scattered electrons in which they pass through the specimen are elastically/inelastically (no energy loss/energy loss), and travel at an angle to the axis

of the beamline [198]. Additionally, they could be banned by an objective aperture located at the rear focal plane of the objective lens. Consequently, only unscattered electrons form a BF image. However, the areas of the sample having fewer electrons lead to darker contrast in the BF images. Based on the BF images, a lot of microstructural characteristics can be indicated such as regions with high Z and dislocations (inelastic scattering) or variation in crystal orientation of grain boundaries (elastic scattering).

- **The dark-field (DF) imaging:** In striking contrast to the BF imaging, the scattered electrons can be selected for constructing DF images. The DF image is frequently employed to track the regions

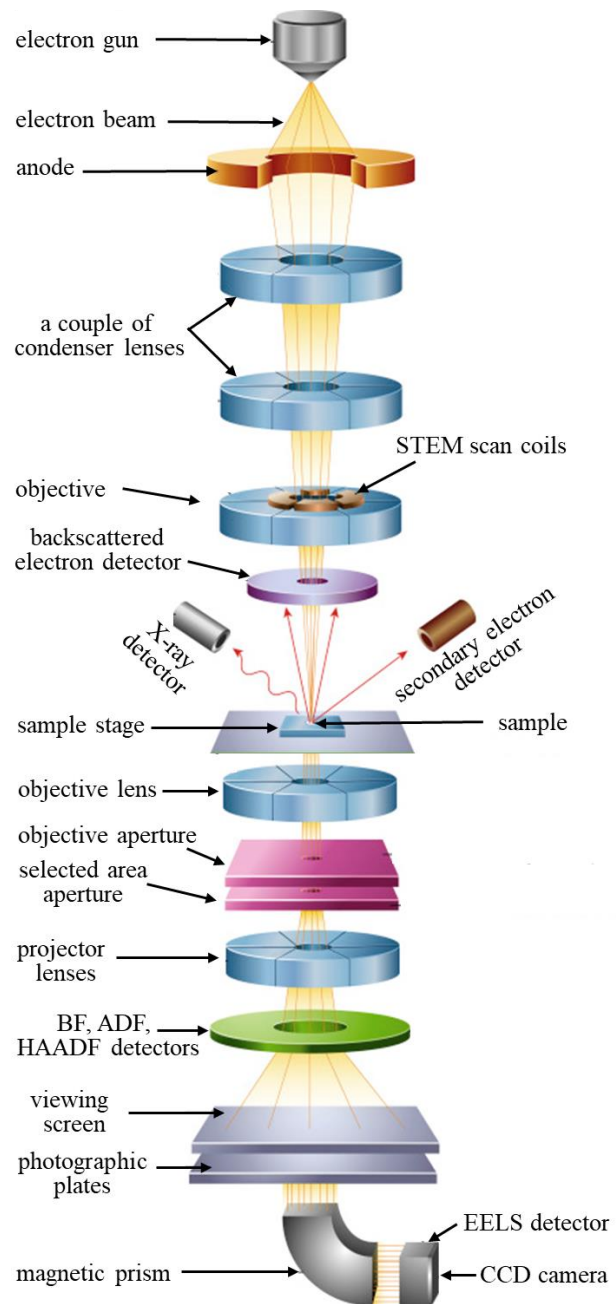


Figure II.10: The configuration of the TEM adapted from [198].

appearing brightly in the DF image or darker in BF image, for which the variation in chemical composition in the images could be revealed.

- **Electron diffraction**: In the elastic scattering effect, the scattered electrons keep their wavelength while their moving direction can be affected. Either crystal structure or sample orientation will define the constructive or destructive interference of such strong scattered beams of transmitted electrons, which is the so-called Bragg scattering/electron diffraction [198]. As a consequence, an electron diffraction pattern will be created if the sample structure favors the electron beams. This type of pattern is one of the key features in TEM because it allows to correlate the lattice parameters (or type), local crystal orientation and phase compositions/relations with the BF and EDS imaging.

- **High-resolution TEM (HRTEM)**: This imaging technique is well adapted to maximum 100 nm thick film and it is constituted of the elastic over inelastic scattering electrons. The electron waves diffract with the sample's lattice and establish sophisticated patterns under certain conditions, which are visible at high magnifications of ~ 400k and thus HRTEM is called to as high-resolution TEM.

- **Scanning TEM (STEM)**: In the sequential chemical investigation, the scan coils are used to identify the focused electron across the sample. Note that the focused spot can be as small as 0.05 nm in radius, it is thereby able to accurately reveal the positions of the atoms' arrangement.

- **High angle annular dark field (HAADF)**: The incoherent scattered electron at high angle can be gathered and this collection of electrons will depict a significant in contrast relating to local changes of Z, thus this imaging technique will be exploited in chemistry analysis. The images obtained from HAADF are complementary to the BF.

II.2.2. Magnetic force microscopy (MFM)

Magnetic force microscopy (MFM) is a scanning approach correlated with AFM (Details provided in Appendix A.6), which traces the interplay between a magnetic sample and a magnetic tip in terms of magnetic interaction (since a ferromagnetic magnetic sample creates a stray magnetic field above its surface) [199,200]. The MFM allows to investigate the fundamental properties of magnetic materials by imaging magnetic structures such as magnetic domains, magnetic/non-magnetic area on a sample.

In the MFM measurement, a double-stage progress is commonly used. While the first stage is dedicated to topography analysis, which can be operated by a standard of AFM mode, the second pass has been exploited to investigate the magnetic properties of the sample at specific distances of short-range or long-range interactions depending on what scan approach will employed in the second scan of MFM (normally a few tens nm above the previous scan of AFM/topography). The representation for the two

pass procedures measured with MFM is shown in Figure II.11. Practically, the second stage can be carried out in two distinct routes with either linear scan or lift scan. The linear scanning mode is usually applied to examine the small roughness sample with the tip being driven away from the surface and MFM analysis being conducted at a certain constant altitude, given frequency, but the fluctuation in amplitude and phase will be recorded. In contrast, the very rough specimens

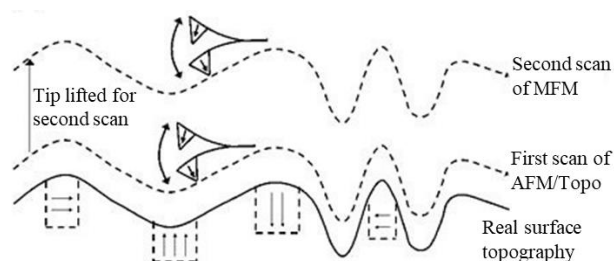


Figure II.11: The schematic diagram of two-pass technique in investigating magnetic properties by MFM.

frequently have overwhelming influence in damage to the scanning probe. The lift scan is therefore managed to avoid such damages of tip-specimen contact, specimen and probe ruin. To do that, the tip-sample distance remains unchanged based on the first scan of topography (Figure II.11).

In this work the probe is developed by our partner at Néel institut based in Grenoble, France (Force microscopy (AFM/MFM) measurements were performed using a ND-MDT/NTEGRA microscope. The microcantilever used was from Oxford Instruments Asylum Research (reference AC240TN, $C = 2 \text{ N/m}$ and $f = 70 \text{ Hz}$) and it was coated with SiO/Ta/FePt/Pt/SiO multilayer stack and annealed so as to have a hard magnetic coating (coercivity $\sim 0.5 \text{ T}$) suitable for MFM imaging). The relatively high coercivity of the tip is to mainly prevent reversing magnetization of the tip inducing by the stray field of hard magnetic sample. Furthermore, it is also possible to quantify the magnetic domain in a grain as low as $\sim 10^1 - 10^2 \text{ nm}$, which obviously gain potential use to comprehend either hard/soft magnetic samples or magnetic nanocomposites.

II.2.3. Vibrating sample magnetometer SQUID (VSM-SQUID)

The magnetic thin films/stack of NPs/nanocomposites reported in this work are basically deposited with a small amount of ferromagnetic materials on substrates, which are usually diamagnetic materials (Si/SiO₂, *c*-sapphire, MgO). The magnetic signal induced from such limited volume of those materials is thereby extremely small. Hence, the *Vibrating Sample Magnetometer (VSM)-Superconductive Quantum Interference Device (SQUID)* has been used as a well-established device to detect such low magnetic signals of the small specimens with high sensitivity and high accuracy.

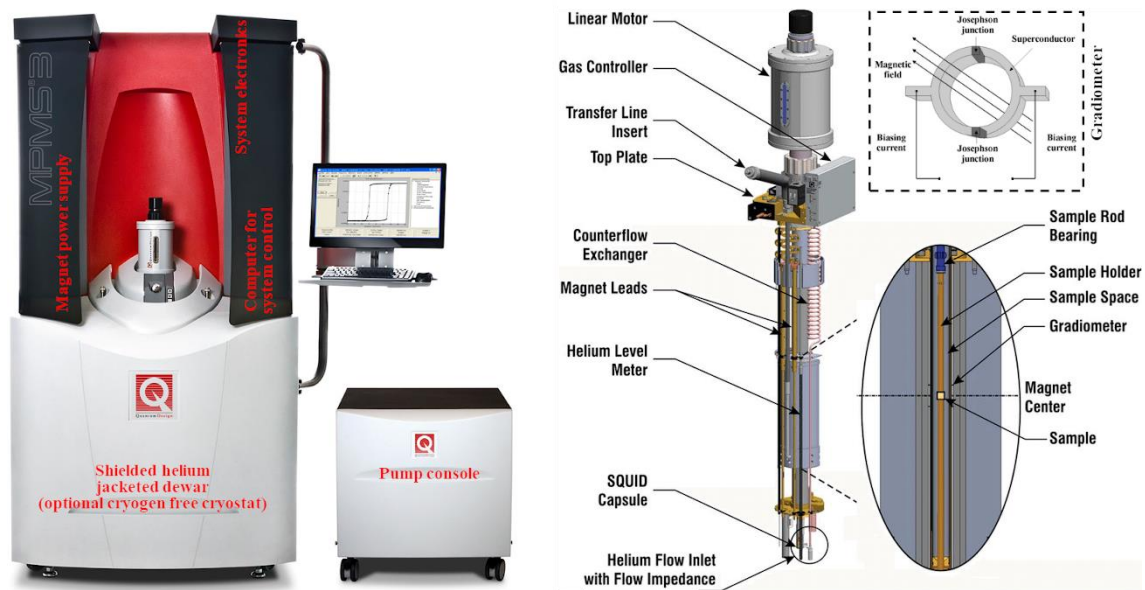


Figure II.12: The VSM-SQUID Quantum Design MPMS 3 setup associated with its main core configuration including Josephson junctions [201].

The fundamental principle of this equipment is based on integrating Faraday's induction law with respect to Stokes theorem, which yields the voltage of $V = -\partial\Phi/\partial t$ (Φ is the magnetic flux). This magnetic flux is sensed by the most elemental part of the VSM-SQUID, which is the so-called Josephson junctions, includes two distinct superconductors separated by thin layers of insulating materials. Thanks to this configuration, a high resolution of magnetic moment up to $\sim 10^{-8} \text{ emu}$ can be detected. A variety of measurements are possible from the basic magnetic analysis by hysteresis loops- $M(H)$ curves to advanced characterizations such as First Order Reversal Curves (FORCs), recoil/open recoil loops, etc. The magnetometer used in this work is the helium filled VSM-SQUID Quantum Design MPMS 3 in a

minimum/maximum applied field of -6.0/6.0 T (can be extended up to -7.0/7.0 T), with temperature ranging from 0.42 K to 400 K. This VSM-SQUID system is at Néel institut based in Grenoble, France. The representative of the system is displayed in Figure II.12, where the magnetic specimen is mounted at the ending of a rigid non-magnetic rod attached to a mechanical resonator, which oscillates the sample at a fixed frequency. The applied magnetic field is generated by a couple of "superconducting" coils so that the applied field is parallel to the rod.

By measuring the $M(H)$ loops at RT, the magnetic properties will enter into discussion in terms of magnetic coercivity, remanent magnetisation, spontaneous magnetisation, squareness ratio denoted as $\mu_0 H_c$, $\mu_0 M_r$, $\mu_0 M_s$, $S_q = M_r/M_s$ respectively [202]. Regarding the thin films (NdFeB, FePt), the observable (001) preferential orientation will contribute significantly to the degree of the hard magnetisation axis alignment to the film's surface, thus the reduction in the ip S_q is an useful parameter to quantifying the degree of the oriented films. Note that the ip and oop measurements are carried out when the applied magnetic field $\mu_0 H$ is parallel and perpendicular to the thin films' surface or the film substrate.

Moreover, in case of hard ferromagnetic materials, the first measurement (virgin curve, or initial curve) can be used as an indicator to discuss the magnetisation reversal dynamics of the magnets, which can be either pinning-type magnet or nucleation-type magnet.

When the thin films were deposited on the substrate, which can be Si substrates with thermally oxidized SiO_2 to a depth of 100 nm, or single sapphire c -cut – Al_2O_3 (0001), or MgO (001). The substrate could make a considerably diamagnetic contribution to the total magnetic recorded signal. Hence, it is essential to correct the magnetic signal by subtracting the effect of

substrate given by the following equation:

$$M_{\text{corrected}} = M_{\text{raw}} - M_{\text{substrate}} = M_{\text{raw}} - \chi_{m_s} mH \quad (\text{Equation II.2})$$

where $M_{\text{corrected}}$, M_{raw} , χ_{m_s} , m , and H are the corrected magnetization (in emu or T), the raw data read by VSM-SQUID (in emu or T), the mass susceptibility (in $\text{emu} \cdot \text{g}^{-1} \cdot \text{Oe}^{-1}$ or $\text{emu} \cdot \text{g}^{-1} \cdot \text{T}^{-1}$), the mass ($m = \text{surface area} \times \text{thickness} \times \text{density}$, in g), and the applied field (in Oe or T), respectively. The mass susceptibility and mass of the substrate will be experimentally verified and these values depend on what kind of substrates will be used. Figure II.13 compares the magnetic hysteresis loops of a nanocomposites deposited on Si/SiO₂ before and after correcting to diamagnetic contribution from the Si/SiO₂ substrate. Hereafter, all the $M(H)$ loops presented in this work will be shown in the forms after eliminating the diamagnetic contribution from the substrates.

II.2.4. How to characterize soft in hard magnetic nanocomposites

The hysteresis loop is actually one of the key informative characteristics of magnetic materials in general. The magnetic behavior at distinct conditions allows to quantify the inter-phase exchanged couple in a complex magnetic nanocomposite. In case of soft-hard nanocomposites (two-phase magnets), if the nanocomposite is decoupling between the soft and hard components, there should exist a kink on the

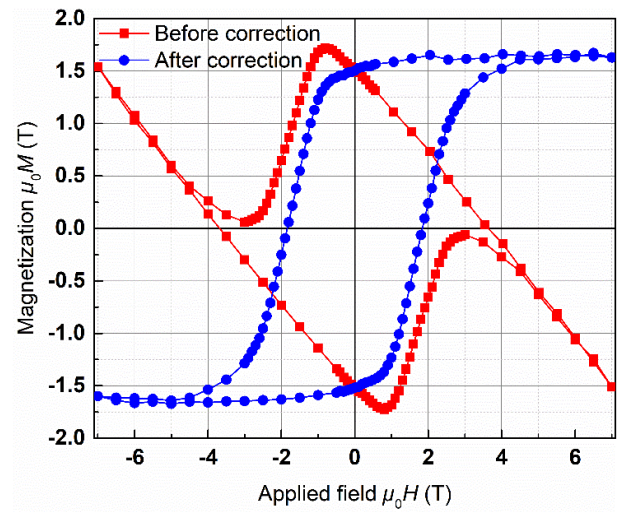


Figure II.13: A comparison for correction to diamagnetic contribution from the substrate.

hysteresis loop in the vicinity of zero applied field. It is common that the overall magnetic behavior of the two-phase magnets is the superposition of the two constituent loops of the soft and hard phases of such nanocomposites. While the combination of ip and oop measurement might display the major difference behaviors in soft-hard nanocomposites, however it is undistinguishable to specify the difference contribution of each phase in the soft-hard composite with single-phase behavior (revealed in the major hysteresis loop) or well exchanged couple nanocomposites. Hence, a variety of approaches has been derived to express the contribution of each single phase inside the nanocomposites such as *low-temperature measurements*, *recoil/open recoil loops*, *Henkel plot* or *δM method*, *X-ray magnetic circular Dichroism (XMCD)*, and *First Order Reversal Curves (FORCs)*. In the framework of this thesis, the soft-hard nanocomposites will be characterized by VSM-SQUID to obtain major hysteresis loops (ip and oop measurements) as well as the FORC. The other techniques might be conducted as post-PhD, which are about to be presented in the Appendix, section A.7.

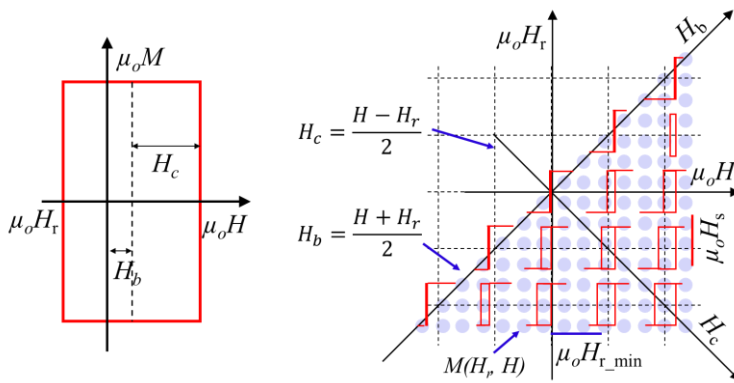


Figure II.14: The representative illustration of single particles with idealized square hysteresis loops (hysterons), where the easy axis of magnetization is aligned with the applied field. Such representative could be used to interpret FORC diagrams.

In the **FORCs** approach, the interaction between the soft and hard phases could be revealed by means of subtleties at various applied magnetic fields. The FORCs technique was employed from Preisach diagram and initially presented by Pike [203]. In the Preisach model, the major hysteresis loop is assumed that contains a summation response from each individual idealized hysteresis loop, as shown in Figure II.14. The magnetic parameters are expressed in terms of the mathematical hysterons together with the definition of the axis in the FORC distribution. The FORC protocol first begins by applying a large positive applied field of $\mu_0 H_s$ to saturate the specimen (Figure II.14). This saturated field value $-\mu_0 H_s$ will practically identify the maximum applied field used when measuring with FORC (Figure II.14). The applied field is later ramped down to a certain value of reversal field $-\mu_0 H_r$, which allows to determine the minimum reversal field. The magnetisation is then recorded from the $\mu_0 H_r$ along the FORCs by rising up the field back to saturation $\mu_0 H_s$, producing the data collection of $M(H_r, H)$ (Figure II.14). Note that $\mu_0 H_r < \mu_0 H_s$. Ultimately, this measurement can be done automatically, thanks to the FORC software. A thousands of magnetization data points obtained from the above recipe can be interpreted in various routes, i. e., the conventional illustration in Figure II.15a; more time-consuming 3D plots and 2D maps of magnetization as a function of both $\mu_0 H_r$ and $\mu_0 H$ in Figure II.15b and Figure II.15c, respectively. Though the structure for a typical set of FORC presented in Figure II.14 and Figure II.15a-c, is not readily obvious, it can be usually drawn accompanied by second derivatives to form a fashion of contour plot (Figure II.15d), referred to as FORC diagram.

$$\rho(H_r, H) = -\frac{1}{2} \frac{\partial^2 M(H_r, H)}{\partial H_r \partial H} = -\frac{1}{2} \frac{\partial M(H_r, H)}{\partial H_r} \frac{\partial M(H_r, H)}{\partial H} \quad (\text{Equation II.3})$$

Analyzing the FORC distribution, based on (Equation II.3), allows to extract more fruitful information about irreversible switching processes and switching fields. Thus, in the effectively

exchanged couple magnetic nanocomposites, the collective switching field of soft and hard components can be discovered by FORC distribution.

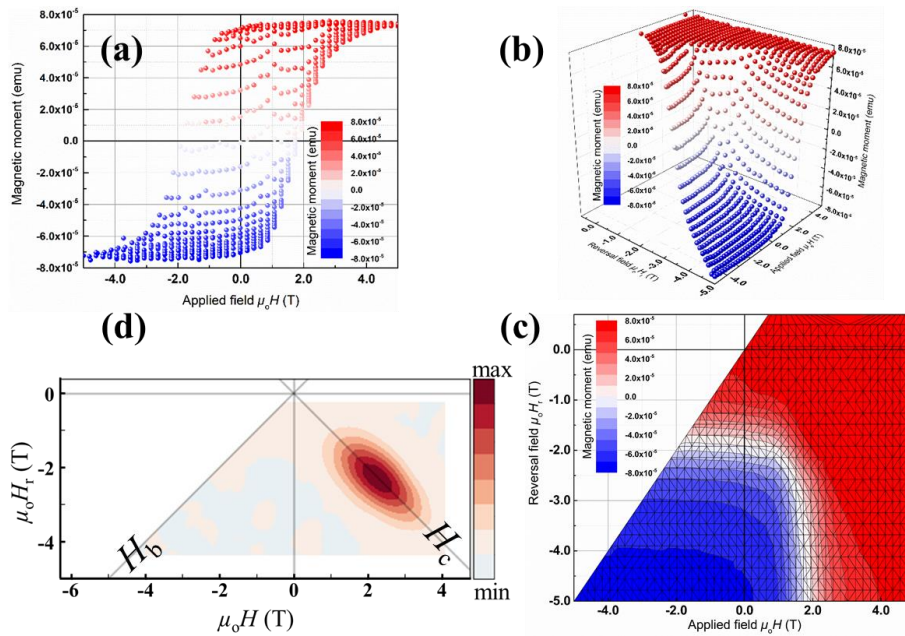


Figure II.15: The FORC analysis with various representations. (a) A conventional dependence of magnetization on the applied field – $\mu_0 H$; (b) the re-drawn three dimensional data showing the dependence of magnetization on both reversal field – $\mu_0 H_r$ and $\mu_0 H$; (c) The two dimensional surface map re-plotted from (b); and (d) FORC diagram distribution obtained from such FORC data in (a).

The typical FORC diagram distribution, presented Figure II.15d, is usually used in the context of this thesis inspiring by the approach developed in reference [204], in which exchanged couple soft-hard nanocomposite shows single magnetic phase behavior with one peak at around 2.2 T, and a symmetrical ridge. In case of decoupled or partially coupled nanocomposites the FORC diagram should display two or more peaks in the H_c axis. One of those peaks will be at around 0 T demonstrating the signature of the soft phases. The shape of the ridge, contour, etc, will reflect different magnetic behaviors of the nanocomposites. These differences will be discussed in details in Chapter V.

II.3. Chapter highlights

The dual pulsed laser ablation system consisting a conventional PLD coupled with FCG that allows to synthesize the thin films, NPs, and nanocomposites simultaneously and independently was described. The associated parameters came along with the system were also included that benefit in mastering fabrication of samples developed during this work. A brief description of RTP would help to fabricate magnetic sample with two step-annealing, at which the good magnetic soft-hard nanocomposites can be obtained with limited diffusion.

The approaches dedicated to fabricate/characterize samples from structure, microstructure to magnetic properties were illustrated. Especially, some useful techniques such as TEM, VSM-SQUID were labelled clearly, which will contribute to express the measured results in the thesis.

Chapter III. Hard magnetic thin films (Nd₂Fe₁₄B and FePt)

Literature presented in Chapter I shows that NdFeB and FePt are among the two best hard magnetic materials. In this chapter, the NdFeB and FePt based thin films will be fabricated and characterized independently under various fabrication conditions. The deposition parameters for fabrication of NdFeB and FePt thin films are provided in Table II.1.

Part of the work of this chapter has been published in "Textured Nd-Fe-B hard magnetic thin films prepared by pulsed laser deposition with single alloy targets" in Journal of Magnetism and Magnetic Materials 520, (2021), 167584 (accepted in October 2020).

Part A: NdFeB thin films

III.1. NdFeB matrix without post-annealing

In this approach, the NdFeB hard magnetic thin films deposited by conventional pulsed laser deposition (PLD), the effect of Nd/Fe ratio from a single ternary alloy target, deposition temperatures (T_d) and substrates on phase formation, microstructure and magnetic properties of trilayers substrate/Ta (nominal 50nm)/NdFeB (150nm)/Ta (50nm) will be examined. While the choices of target composition and T_d provide optimal conditions to obtain good magnetic properties, the use of different substrates contributes to the flexibility to both single crystal and amorphous substrates for various purposes.

III.1.1. Effect of target compositions

It is well-known that Nd₂Fe₁₄B phase is of complex structure [8,57] and Nd in excess encourages extrinsic magnetic property of coercivity of both bulk material and thin film due to the decoupling effect from Nd₂Fe₁₄B grains [205,206]. Taking into account the PLD specificities, and the required Nd-rich content in deposited thin films, five distinct NdFeB compound targets with different Nd/Fe atomic ratios - 0.47 (target #1), 0.45 (#2), 0.42 (#3), 0.33 (#4), 0.18 (#5) with approximately constant B/Nd (boron/neodymium) atomic ratio – were used to fabricate thin films on Si/SiO₂ at 600°C. This deposition temperature was chosen in good agreement with several studies pointing out that the optimum deposition temperature to directly crystallize good NdFeB thin films fluctuates around 600°C

[72–74]. Figure III.1 displays the Nd/Fe average value resulting from the EDS analysis of about 10 thin films deposited from each single target with the counterpart on compound targets. The proportion of the compound targets results in reduction of Nd/Fe in the deposited films. Indeed, the experimental Nd/Fe ratio in the thin films reduces from 0.44 to 0.11 in accordance to value from 0.47 to 0.18 on the targets.

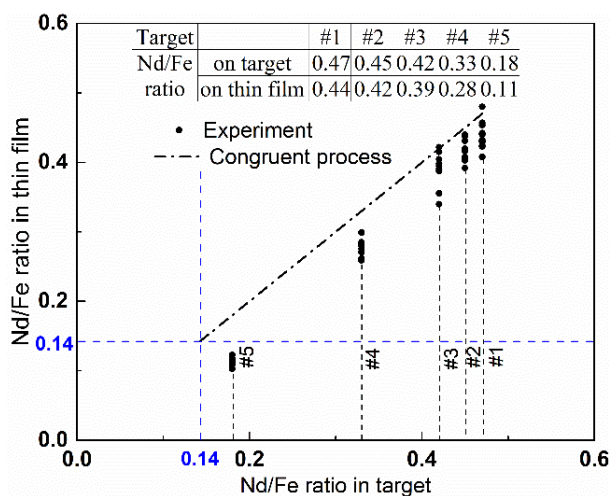


Figure III.1: Nd/Fe atomic ratios on targets versus Nd/Fe atomic ratio on films. Films deposited by PLD at $T_d = 600^\circ\text{C}$ and $\sim 6 \text{ J}\cdot\text{cm}^{-2}$ in Ta/Nd-Fe-B/Ta configuration on Si/SiO₂ substrates. Black dash-dotted line represents the perfect congruent transfer.

The Nd/Fe values in the thin films are lower than expected for a direct congruent transfer of 1:1 from target to substrate (dashed line in Figure III.1) of about 6 % (#1) to 38% (#5). At lower Nd/Fe ratio (targets #4, #5) near the natural Nd/Fe stoichiometry of $\text{Nd}_2\text{Fe}_{14}\text{B}$ phase of 0.14, the failure in following the trend increases.

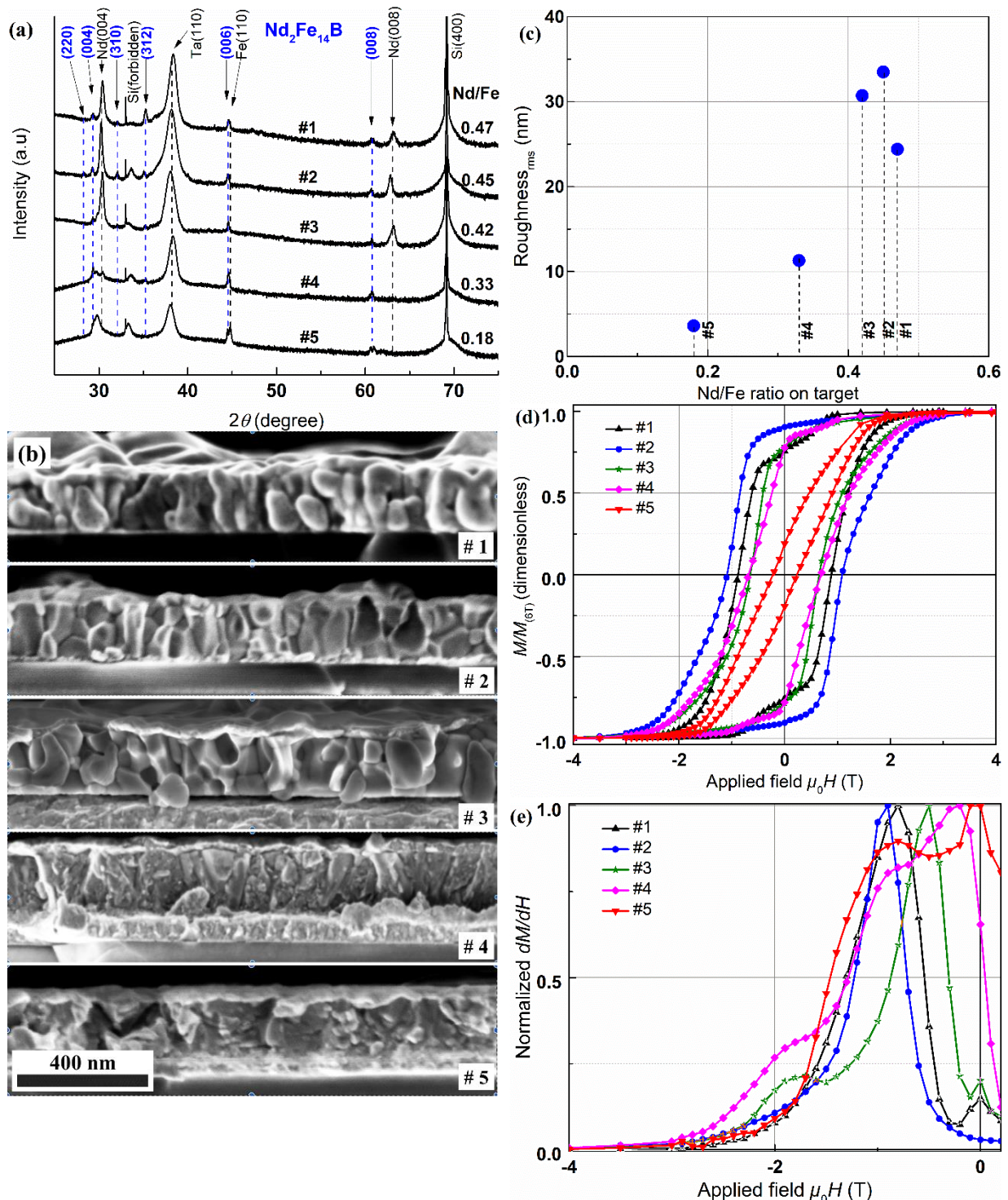


Figure III.2: Characterizations of Ta/Nd-Fe-B (150 nm)/Ta films deposited at 600°C on Si/SiO₂ substrates, made from the five different targets (a) XRD patterns; (b) SEM images of the fractured cross sections; (c) AFM rms surface roughness; (d) Out-of-plane magnetic hysteresis loops (uncorrected for demagnetization field and normalized); and (e) Normalized dM/dH plots.

The shortage of Nd/Fe ratio transferred from the target to thin film could be owing to the wide range of both melting point and atomic mass of concerned elements of Nd and Fe. The melting point of Nd (1016°C) is far lower from melting point of Fe (1538°C) and even much lower from the one of volatile boron (2076°C), while the atomic mass of Nd (144.24 u) is far higher ~250% from atomic mass of Fe (55.85 u) and much higher than B (10.811 u). These differences affect the compositional distribution of each element inside the plasma plume and may lead to a redistribution of elements at both surfaces of the target and thus the thin film. During the laser-target interaction (excimer laser beam interacts with compound target, and re-sputtering effect might occur, more details presented in section II.1.1), the constituent elements on the target might be somewhat migrated and thus induces local change in composition [207].

Figure III.2a presents XRD patterns of five thin films deposited at 600°C corresponding to the five different targets. In all patterns, the peaks of Si (400) at 69.25°, Si (forbidden) at 33.10° from substrate and Ta (110) at 38.40° from buffer/protective layers are displayed. Five diffractograms depict the major magnetic phases of Nd₂Fe₁₄B with (00*l*) reflections at 29.27°, 44.54° and 60.70° that point out a texturation. However, there exists minor orientations beside the main phase of (00*l*) reflections such as (220), (310), (312) at 28.17°, 32.11°, 35.24° respectively, for most of thin films except the sample from target #5. As the Nd/Fe in the target reduces to natural stoichiometry of 0.14, the intensity of the diffracted (00*l*) orientations is strengthened and reaches maximum for film from target #4 (see (006) reflection). In low Nd content films, the (00*l*) reflections are overlapped by the broaden peaks at low diffraction angle resulting in difficulty in observation of (004) reflection. Furthermore, it is visible to detect diffraction lines identified as elemental Nd corresponding to the overall Nd in excess (not target #5) accompanied by Nd₂Fe₁₄B reflections. With high Nd content thin film (from target #1 to #3), the Nd (00*l*) peaks are well defined. This Nd rich phase starts to disappear for films deposited from target of low Nd content in target #4 and obviously in target #5 (see (008) peak at a higher diffraction angle of 63°). Additionally, film with the lowest Nd content reveals a reflection which can be indexed as pure α -bcc Fe (110) at 44.67°. These diffraction patterns are well agreed with results obtained in EDS analyses in which the films obtained major phase of Nd₂Fe₁₄B tetragonal structure and surplus of Nd for higher content Nd films (from target #1, #2, #3) or an additional amount of pure iron in the film with the lowest Nd content. It is also worth noting that the relatively higher intensities of the (00*l*) orientations in comparison with other reflections of Nd₂Fe₁₄B phase depicts preferential out of plane orientation.

The cross-sectional microstructures of the deposited films are presented in Figure III.2b. Each layer of the Si/SiO₂/Ta/NdFeB/Ta heterostructures thin films obtained from all targets #1, #2, #3, #4 and #5 is clearly visible. The film with the lowest Nd/Fe ratio of 0.11 below the natural stoichiometry of 0.14 is predominantly composed of very fine grains or compact one with no valid grain shape. Increasing the Nd/Fe ratio leads to bigger grains with random shape for film from target #4 to more and more elongated in films made from targets #4 and #3, and finally reaches columnar grain structure for film grown from target #2 and #1. These big columnar grains apparently traverse through the film thickness and are separated by some smaller equiaxed grains with arbitrary shape. This medium of NdFeB layer is constituted of Nd, Fe, B mixture in which the contribution of Nd₂Fe₁₄B cannot be clearly distinguished by conventional SEM. AFM analysis performed at the surface of films, made from five target #1 – #5, confirms data obtained by SEM concerning the variation in grain size. Figure III.2c compares the root mean square (rms) surface roughness values (performed on the areas without droplets) increasing by a factor of ~8 globally, and following the Nd/Fe atomic ratio from about 4 nm to 33 nm for films with Nd/Fe = 0.11 – 0.42, respectively. These results are in good agreement with the fact that the grain size also increases with Nd content.

Out-of-plane (oop) $M(H)$ loops of all representative thin films deposited at 600°C from five distinct targets are compared in Figure III.2d. A good rectangular hysteresis loop of single magnetic phase behavior together with the highest values in all remanent magnetization- $\mu_0 M_r$, coercivity- $\mu_0 H_c$, and remanence ratio- M_{0T}/M_{6T} of about ~1.2 T, 1.1 T, and 0.9, respectively, is achieved for sample of thin film grown from target #2 compared to the other samples' properties. While films made from target #1, #3, and #4 illustrate little variation in coercivity around ~0.8 T and comparable remanence ratio M_{0T}/M_{6T} about 0.75, film made from target #5 drops significantly in magnetic properties with $\mu_0 H_c \sim 0.2$ T and $M_{0T}/M_{6T} = 0.19$. All of the other films depict obvious two or multiple magnetic phase behaviors pointed out by shoulders at an applied field around $\mu_0 H \sim 0$ T and long tails at high applied field ($\mu_0 H_c$), which are attributed to a secondary phase [14] of ferromagnetic phases such as Fe, Fe-B or Nd-Fe that lead magnetisation reversal occur at small negative fields. The properties of single or multi-phase magnetic behavior of the deposited from all five targets could be clearly observed by drawing the dM/dH plots, shown in Figure III.2e, which were done by taking the first derivative of magnetization with respect to the applied field after correcting to the diamagnetic contribution from Si/SiO₂ substrate (correcting details presented in section II.2.3). The film from target #2 depicts just one peak near the coercive field, while other films from the other targets demonstrate multiple peaks, especially the peak near $\mu_0 H \sim 0$ T showing the contribution of the soft phase. Thus, film from target #2 with Nd/Fe = 0.45 has been selected to carry out in details as presented in Figure III.3.

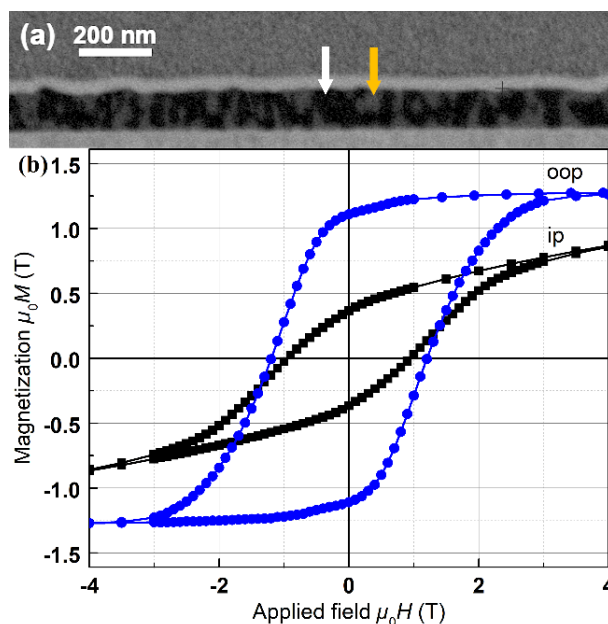


Figure III.3: Characterizations of the film made from target #2 deposited at 600°C on Si/SiO₂. (a) FIB-EBS cross-sectional images in which the Nd₂Fe₁₄B grains elongated in the z direction (black regions, one of which is indicated by a white arrow) are found together with a Nd-rich phase (gray regions, one of which is identified by an orange arrow), and (b) In-plane (ip) and out-of-plane (oop) magnetic hysteresis loops (uncorrected for demagnetizing field).

Figure III.3a exhibits a cross-sectional SEM image of a film made from target #2 using FIB in Energy Selective Backscattered – ESB mode, which is suitable for clear compositional contrast. The tri-layer microstructure of the films is certainly shown with the NdFeB layer being capped by two bright

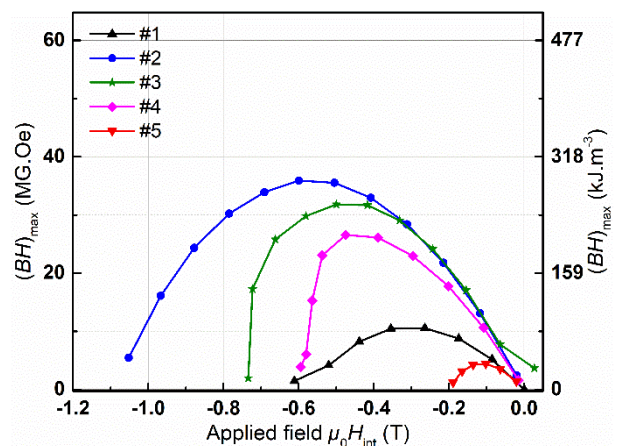


Figure III.4: The evolution of magnetic energy product – $(BH)_{max}$ as a function of internal applied field, of Ta/Nd-Fe-B (150 nm)/Ta films deposited at 600°C on Si/SiO₂ substrates from five distinct targets (#1 – #5) by taking the values in the second quadrant after correcting the out-of-plane magnetic hysteresis loops for demagnetization field with the demagnetizing factor of about 0.73. Note that the maximum magnetic energy product – $(BH)_{max}$ is technically picked the maxima of the presented parabolas (BH) curves and this product considerably depends on the correcting with demagnetizing factor.

layers of Ta, one buffer at the bottom and the other of the protective layer on the top. Inside the NdFeB layer, the chemical contrasts clearly revealed the phase structural distribution, i. e., the bright pillars surrounded by dark neighbors. Such bright zones are preferentially perpendicular to the Ta buffer layer with unique structure traversing through NdFeB layer and have discontinuous columnar structures, which are isolated from their surroundings of columnar dark parts. The EDS analysis on this NdFeB layer shows that the Nd/Fe ratio for gray region is about ~ 0.68 , while a lower ratio of about ~ 0.32 is observed for black region. Bright zones in the NdFeB layer, one of them indicated by an orange arrow, are referred to the Nd-rich paramagnetic phase, while the dark zones, representatively illustrated by a white arrow, are attributed to $\text{Nd}_2\text{Fe}_{14}\text{B}$ phase. The value of 0.32 is about two times higher than the Nd/Fe ratio for natural stoichiometry of ~ 0.14 ($= 2/14$) for pure $\text{Nd}_2\text{Fe}_{14}\text{B}$ phase. This variation could be attributed to a relatively high analyzed volume of $\sim 1 \mu\text{m}^3$, at a working voltage of 20 kV in EDS analysis, which contains simultaneously both many dark and bright zones while analyzing either Nd-rich phase zones or $\text{Nd}_2\text{Fe}_{14}\text{B}$ phase zones. Thanks to image analysis of a number of such FIB-ESB images, the statistical volume content of the $\text{Nd}_2\text{Fe}_{14}\text{B}$ phase (dark zone) is evaluated to be about $\sim 70\%$. This value is very close and in good agreement with a value of $\sim 67\%$, which is deduced from the average Nd/Fe atomic ratio (shown in Figure III.1). Note that in this circumstance, the film is considered for composing of two distinct phases of $\text{Nd}_2\text{Fe}_{14}\text{B}$ and pure Nd.

A comparison between an out-of-plane (oop) magnetic hysteresis loop and an in-plane (ip) loop measured on the same sample, which has the microstructure presented in Figure III.3a, is compiled in Figure III.3b. The $M(H)$ magnetic hysteresis loop is displayed in absolute value of magnetization, for which the sample volume was estimated by considering the surface area, thickness, and a coarse evaluation of the volume of droplets (which are characteristic of metallic films made by PLD [84,194]). Based on a number of conventional SEM images taken at low magnification mode ($\sim 5 \text{ kX}$), a statistically estimated droplets' volume of up to $\sim 25 \text{ vol}\%$ is accounted for overall deposited film volume. Extrapolating the ip and oop $M(H)$ loops results in an intercept at about $\sim 8 \text{ T}$ (in applied field, x -axis), which is comparable to the magnetocrystalline anisotropy of the $\text{Nd}_2\text{Fe}_{14}\text{B}$ pure phase ($\sim 7.6 \text{ T}$). Without losing generality, from the (Equation I.7), the anisotropy field can be rewritten as $H_a = 2K_{\text{eff}} / \mu_0 M_{6T}$, thus the effective anisotropy constant is estimated about 4.14 MJ.m^{-3} , which is gently lower than the value of 4.87 MJ.m^{-3} of $\text{Nd}_2\text{Fe}_{14}\text{B}$ phase [7]. A relative lower value of remanent magnetization and higher value of high field slope of the ip measurement compared to oop measurement reflect the oop texture induced during film growth at deposition temperature of 600°C . It is worth noting that the error in calculating magnetization is dominated by the error in volume estimation of up to $\sim 27\%$. Indeed, an oop saturation magnetization value closer to 1 T ($1.61 \text{ T} \times 70\% = 1.13 \text{ T}$) can be expected for a well textured NdFeB film in which the hard magnetic $\text{Nd}_2\text{Fe}_{14}\text{B}$ phase accounts for $70 \text{ vol}\%$.

In comparison between magnets, a key parameter of a magnet is usually applied, often called $(BH)_{\text{max}}$ product. The $(BH)_{\text{max}}$ representing the work can be done by the magnet. A further estimate of maximum energy product $(BH)_{\text{max}}$ for this set of films from five distinct targets, without considering the droplets' contribution, is shown in Figure III.4. Prior to extracting the $(BH)_{\text{max}}$, oop $M(H)$ loops ought to be corrected with demagnetizing field. A sample procedure of correcting $M(H)$ loop with demagnetization field is given in section I.1. Correcting with demagnetizing factor of $N = 1$ in hard magnetic thin films could lead to over-skewing of corrected loops, owing to the magnetization reversal occurring by discrete switching in these materials. Thus a value of demagnetizing factor of ~ 0.73 [208] is applied in correcting the $M(H)$ loops throughout this work, in which the overestimated $(BH)_{\text{max}}$ (induced by over-skewing loops) might be eliminated. Note that demagnetizing factor is greater than > 0.73 usually resulting in

higher values of $(BH)_{\max}$. In Figure III.4, though the coercivity and remanent magnetization in these films vary slightly, the $(BH)_{\max}$ corresponding to maxima of the presented parabolas vary greatly, e. g., it rises from $\sim 80 \text{ kJ.m}^{-3}$ in film from target #1 to a maximum value of $\sim 280 \text{ kJ.m}^{-3}$ in film made from target #2, and it reduces further in films made from target #3 & #4 and further again in the Nd-poorest film made from target #5 ($\sim 30 \text{ kJ.m}^{-3}$). As the best magnetic properties were obtained for films produced with target #2, further investigations will be conducted on films produced from this target.

III.1.2. Influence of deposition temperatures (T_d)

In order to obtain the optimal deposition temperatures (T_d), a set of thin films, from target #2 with Nd/Fe = 0.45 at different T_d in the range of 500°C - 700°C , was made to find out the effect of deposition temperatures on structures, microstructures and magnetic properties of the produced films. An EDS estimate of the Nd/Fe ratio for this series of thin films indicated a little variation in the Nd/Fe ratio of about 0.42 ± 0.01 between the films. This suggests that the compositional ratio between elements inside the films does not depend on T_d .

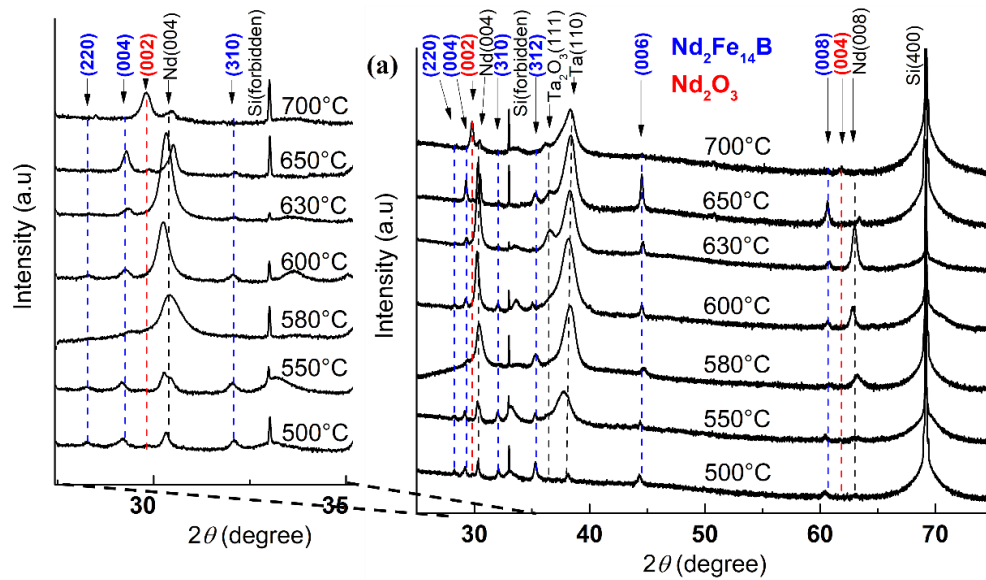


Figure III.5: The evolution in structural properties - the XRD diffractograms of Ta/Nd-Fe-B/Ta thin films on Si/SiO₂ substrates made from target #2 as a function of deposition temperatures- T_d ranging from 500°C to 700°C .

Figure III.5 compares the XRD patterns of films deposited at various T_d . The high degree of oop orientation NdFeB layer, reflected by the relatively high intensity of (00 l) reflections of primary phase of Nd₂Fe₁₄B compared to other peaks, is observed on the Ta buffer layer. The Ta layer is not well crystallized at low T_d ($<550^\circ\text{C}$), while at higher T_d this layer is well (110) oriented and partly oxidized (properly due to the monolayer formation time of O₂ effect). Orientations attributed to Ta₂O₃ are identified in films deposited at 630°C and above. The dominant Nd₂Fe₁₄B magnetic phase is obviously approved for T_d up to 650°C , e. g., the intensity of (00 l) Nd₂Fe₁₄B reflections gradually grows with T_d and reaches maximum at 650°C (see (006) orientation). The peaks attributed to Nd-rich phase are clearly promoted from 580°C to 630°C and moderately clear at 550°C (see Nd (004) reflection). Nonetheless, the Nd₂Fe₁₄B and Nd-rich phases drastically disappear beside the considerable contribution of Nd₂O₃ phase in the film deposited at 700°C . To sum-up, at low T_d ($<550^\circ\text{C}$), the Nd₂Fe₁₄B and Nd-rich phases are not completely crystallized while at T_d (550°C - 630°C) they are fully crystallized. However, owing to the high reaction of Nd and O₂, higher T_d (700°C) leads to significant formation of Nd₂O₃ phase because of the small amount of residual oxygen in the deposition chamber.

Distinctive surface morphologies of fabricated films at various T_d inspected by SEM plane-view is illustrated in Figure III.6. At 500°C, the morphology presents minor round "islands" of diameter up to ~200 nm on an underlying layer characterized by major surroundings smaller grains of diameter <100 nm (Figure III.6a). At 630°C, the microstructure displays predominant matrix to densely larger grains of

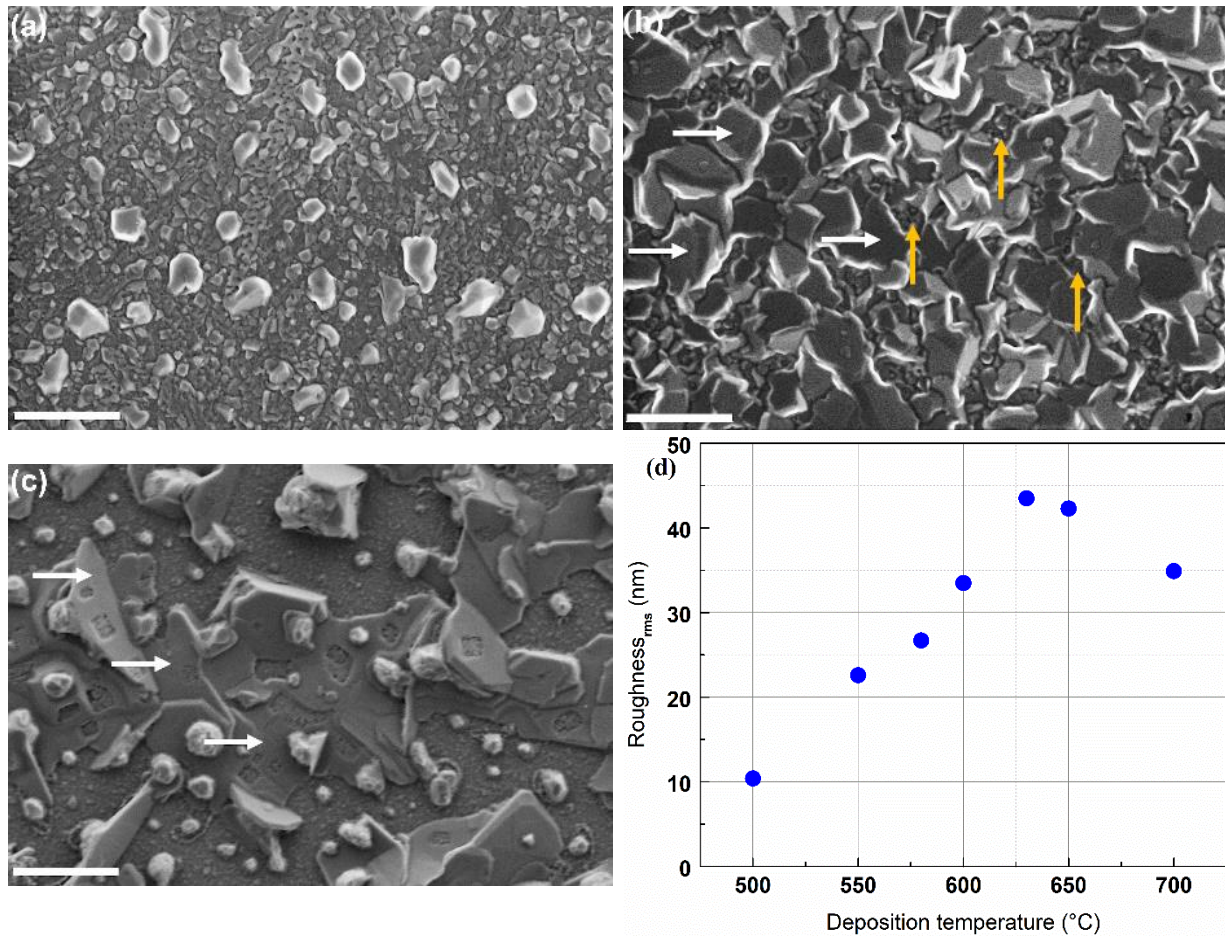


Figure III.6: Plane-view SEM images showing the distinct surface microstructures of Ta/Nd-Fe-B-Ta films deposited at T_d (a) 500°C; (b) 630°C; and (c) 650°C. The scale bar in all three images is 1 μm . (d) The AFM rms surface roughness of Ta/Nd-Fe-B-Ta films from target #2 as a function of deposition temperatures- T_d .

nearly 1 μm (indicated by white arrows) which are separated by much smaller grains from 50 to 100 nm (indicated by orange arrows-Figure III.6b). The surface of the film deposited at 650°C is governed entirely by separately connected platelet-like grains of size approaching up to 10 μm , with the platelets' planes frequently tilted with respect to that of the Si substrate, are identified, together with smaller grains of size close to 200 nm and an under-layer of grains of size 50–100 nm (Figure III.6c). A detailed EDS analysis in compositional elements reveals a difference between the big grains (white arrows) and smaller ones (orange arrows) in which Nd/Fe ratios are about ~0.3 and 0.7 for the big grains and smaller ones respectively.

Variation in grain size is validated by AFM analysis carried out at the films surfaces. The rms surface roughness, presented in Figure III.6d, develops from ~10 nm, for films deposited at 500°C, to a maximum ~45 nm at 630°C, and later slightly decreases to about 35 nm at higher deposition temperature of 700°C. The maximum in rms roughness for the film deposited at 630°C followed by a drop at higher deposition temperatures agrees well with the densely packed isolated grains and inter-connected islands (leading to a flatter surface in the same area of measurement) microstructures, respectively. The formation of connected platelet-like grains and smaller grains at 650°C could be attributed to Ostwald ripening

[209], in which larger grains become larger and smaller grains becomes smaller. The effect of Ostwald ripening concerning the formation of bigger grains presented in this work will be well described in section IV.1.4.

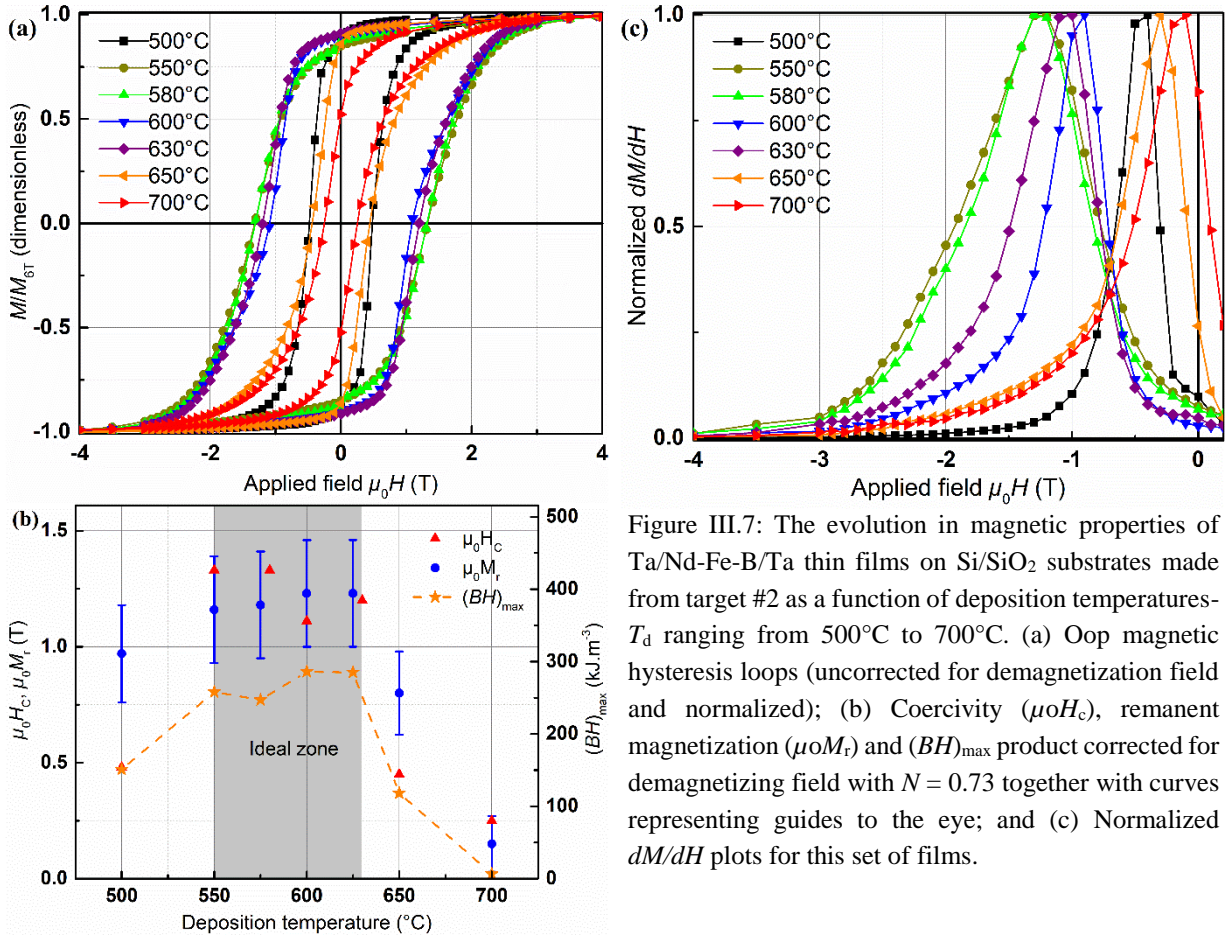


Figure III.7: The evolution in magnetic properties of Ta/Nd-Fe-B/Ta thin films on Si/SiO₂ substrates made from target #2 as a function of deposition temperatures- T_d ranging from 500°C to 700°C. (a) Oop magnetic hysteresis loops (uncorrected for demagnetization field and normalized); (b) Coercivity (μ_0H_c), remanent magnetization (μ_0M_r) and $(BH)_{max}$ product corrected for demagnetizing field with $N = 0.73$ together with curves representing guides to the eye; and (c) Normalized dM/dH plots for this set of films.

Normalized and uncorrected for demagnetizing field oop hysteresis loops of this series of fabricated films are illustrated in Figure III.7a. In all the cases with $500^\circ\text{C} < T_d < 650^\circ\text{C}$, the films represent nice rectangular loop shapes, comparable overall loop shape, and achieve a maximum M_{OT}/M_{6T} ratio of 0.91. The films show poorer rectangular loop shapes with M_{OT}/M_{6T} ratios approaching to lower values of up to 0.55 at higher T_d of 700°C. The oop $M(H)$ loops of all films in this set show fairly single magnetic phase behaviors, which are clearly demonstrated by plotting the dM/dH plots shown in Figure III.7c. In Figure III.7c, all films in this set exhibit somewhat one single peak near the coercivity.

The variations of magnetic coercivity, remanence, and $(BH)_{max}$ product with T_d are plotted in Figure III.7b. As can be observed that the magnetic coercivity, remanence, and $(BH)_{max}$ are all limited at low deposition temperature of $T_d < 550^\circ\text{C}$, and attain higher values of above 1 T as well as maximum value of $286 \text{ kJ}\cdot\text{m}^{-3}$ at intermediate T_d from 550°C to 630°C. Nonetheless, a further decline in all coercivity, remanence, and $(BH)_{max}$ is observed as T_d goes beyond, i. e., while not only μ_0H_c drops to about 0.25 T but also μ_0M_r falls down below 0.2 T, the magnetic energy product – $(BH)_{max}$ is downward to $6.5 \text{ kJ}\cdot\text{m}^{-3}$ when $T_d = 700^\circ\text{C}$. Note that the $(BH)_{max}$ is estimated without droplets' contribution and a proper value of demagnetizing factor $N = 0.73$ avoids over-skewing corrected $M(H)$ loops, which results in over-estimated $(BH)_{max}$ values. The substantially lower value of coercivity of 0.5 T of the film deposited at 500°C is due to poor distribution of the Nd-rich paramagnetic grain boundary phase, resulting in poor decoupling of the Nd₂Fe₁₄B grains, while the shortage in coercivity for films deposited at above 630°C is

due to a combination of both the degradation of the film through oxidation (see Figure III.5) and evolution of interconnected islands (~10 μm) in microstructure promoting magnetization reversal through domain wall motion. Initiation of oxidation at 650°C may not be visible using conventional XRD if it takes place over a very short range. The loop shape of the film deposited at 700°C is poorer than that deposited at 650°C, because of the greater extent of oxidation, as evidenced in the XRD patterns in Figure III.5. This suggests that the base oxygen pressure (sometimes called oxygen partial pressure) of the PLD chamber used is not sufficiently good enough to grow high quality NdFeB based thin films at 650°C and above, as explained previously in section III.1.1. Relatively large error bars associated with the $\mu_o M_r$ values is attributed to the notable error in evaluating the volume of these films, which was discussed above due to the unavoidable droplet formation. The ideal zone, in which both coercivity and remanence are achieved with the highest values, is obtained by roughly fitting the dependence of coercivity and remanence on T_d . These fitted lines admit that the optimized T_d to achieve the good magnetic thin film are in the range from 550°C to 630°C.

To qualitatively see the challenges when depositing the complex NdFeB material, which is sensitive to oxidation, the so-called monolayer formation time is considered. This monolayer formation time is given by $t = \frac{10^{15}}{sP} \sqrt{2\pi m k_B T}$, where t is monolayer formation time, 10^{15} is average surface site density, s is the sticking coefficient and supposed to be 1, P is partial pressure of molecular mass m in the deposition chamber, m is molecular mass, k_B is Boltzman's constant, T is deposition temperature. The dependence of monolayer formation time of O₂ with respect to deposition pressures at different temperatures could be graphically found in Figure III.8.

Supposing the gas inside the deposition chamber is of the same compositional element as the air with 20 % in volume of oxygen. While the base pressure was about 5×10^{-7} mbar, the oxygen partial pressure is about $20\% \times 5 \times 10^{-7}$ mbar. Therefore, the monolayer formation time of oxygen at 600°C is about 100s, which means that the film surface will be covered by one monolayer of oxygen (oxidized layer) in each single 100s. The deposition of 150 nm NdFeB film during the deposition at 600°C will normally cost at least 30 oxide monolayers. Noticeably, this monolayer formation time does not vary much as deposition temperatures increase from 300°C to 800°C. However, owing to the likely reaction of Nd and

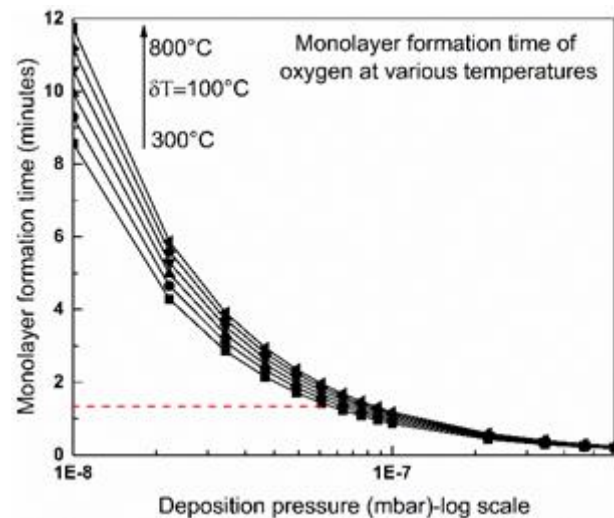


Figure III.8: Dependence of monolayer formation time on partial deposition pressure of O₂ at different deposition temperatures.

O₂ at high temperature, oxidation problem occurs as a result, and this oxidation phenomena is unavoidable for vacuum deposition. Hence, it is also possible that the Nd bounded in Nd₂Fe₁₄B phase is also oxidized even at not so high T_d due to monolayer formation time effect, which was the case of film deposited at 650°C, in which the oxygen partial pressure goes down compared at 600°C.

Based on the above results, target #2 with Nd/Fe=0.45 giving the best magnetic thin film with Nd/Fe = 0.42, this value is about three folds higher than natural stoichiometry of 0.14 of Nd₂Fe₁₄B phase. The answer to the question "Where does Nd go?" may be thus now available. Such high content of Nd in

the fabricated film guarantees to maintain sufficient Nd content to compensate Nd_xO_y formation (oxide monolayers), then form $\text{Nd}_2\text{Fe}_{14}\text{B}$ phase, and later surplus of Nd-rich paramagnetic phase to decouple $\text{Nd}_2\text{Fe}_{14}\text{B}$ ferromagnetic grains to achieve high coercivity film. Note that too much Nd content (the case of target #1) will dilute $\text{Nd}_2\text{Fe}_{14}\text{B}$ phase to form secondary phase of Nd-Fe, as indicated previously in section III.1.1. A T_d in the optimal range from 550°C to 630°C facilitates high quality NdFeB thin film of both large μ_0H_c and high μ_0M_r . The largest values of coercivity and remanence obtained in NdFeB based thin films in this work ($\mu_0H_c = 1.3$ T and $\mu_0M_r > 1$ T) are in the range of the optimal values reported for either thin films or thick films (e. g., Nd-Fe-B thick films deposited by high deposition rate (18 $\mu\text{m}/\text{h}$) triode sputtering ($\mu_0H_c = 1.6$ T and $\mu_0M_r = 1.4$ T [11], $\mu_0H_c = 2.7$ T and $\mu_0M_r = 1.15$ T [206] at 10^{-6} mbar). The μ_0H_c is intermediate while the μ_0M_r is relatively greater in comparison with films fabricated by PLD with multiple targets ($\mu_0H_c = 2$ T and $\mu_0M_r = 0.9$ T, at 10^{-9} mbar [90]) and compound targets with high deposition rate of 40 $\mu\text{m}/\text{h}$ ($\mu_0H_c = 0.72$ T and $\mu_0M_r = 0.9$ T, at 10^{-6} mbar [81,82,210]). NdFeB thin films are susceptible to oxidation and thus high deposition rates help to suppress oxidation of films deposited by triode sputtering [11,206] and high deposition rate in PLD [81,82,210]. Note that though the prior deposition pressure of the PLD chamber used in this work is superior ($\sim 10^{-7}$ mbar), the deposition rate of 0.5 $\mu\text{m}/\text{h}$ falls far short from the above values.

III.1.3. Al_2O_3 versus Si/SiO₂ substrates

In this part, a comparison in structural, microstructural, and magnetic properties of NdFeB thin films deposited on both kinds of substrates on *c*-sapphire- Al_2O_3 , which has been known as well adapted to $\text{Nd}_2\text{Fe}_{14}\text{B}$ structure [73,74], and on silicon-Si/SiO₂ (100nm) will be made. Thanks to the previous analysis for optimal deposition temperatures ranging from 550°C to 630°C (section III.1.2), the films were deposited at an arbitrary temperature in the ideal zone, e. g., at $T_d = 630^\circ\text{C}$. The XRD patterns on both kinds of substrates are depicted in Figure III.9a. The (00*l*) reflections of $\text{Nd}_2\text{Fe}_{14}\text{B}$ phase are both visible on two kinds of substrates, and there is no major distinction between films deposited onto the two substrates with the orientations indexed as $\text{Nd}_2\text{Fe}_{14}\text{B}$ and Nd rich phases, and even with Ta peaks. Films deposited on both kinds of substrates demonstrate oop texture of $\text{Nd}_2\text{Fe}_{14}\text{B}$ and Nd-rich phases reflected by the intensities of (00*l*) being relatively higher than those of other reflections. The microstructures of deposited film on *c*-sapphire and/or on Si/SiO₂ are exhibited in Figure III.9b (plane-view) and Figure III.9c (cross-sectional view). The high density of grains microstructure with arbitrary shapes on *c*-sapphire are compact and somewhat comparable with film deposited on Si/SiO₂ (Figure III.6b) with the smaller ones of ~50 – 100 nm (a few of such grains indicated by orange arrows) in the surrounding media of bigger grains of up to ~1 μm (indicated by white arrows Figure III.9b). The EDS analysis indicates that the bigger grains correspond to $\text{Nd}_2\text{Fe}_{14}\text{B}$ phase grains, while smaller ones are attributed to Nd-rich phase grains. Both of these grains are well mixed throughout the film surface. Figure III.9c presents SEM cross-sectional view of the two films. The films are predominantly composed of columnar grains traversing through the films' thickness and sometimes separated by some round, smaller equiaxed grains. Probably, those successive big (columnar) grains could be either $\text{Nd}_2\text{Fe}_{14}\text{B}$ or Nd-rich intergranular phases. The columnar grains are freely admitted to the XRD data for both $\text{Nd}_2\text{Fe}_{14}\text{B}$ and Nd-rich phase reflections. These similar structures and microstructures lead to almost identical magnetic properties of the two films deposited on both *c*-sapphire and Si/SiO₂ substrates, e. g., single magnetic phase behavior (proved in section III.1.2), $\mu_0H_c \sim 1.2$ T, $\mu_0M_r \sim 1.2$ T (without taking into account the droplet contribution to the total volume), and the remanence M_{0T}/M_{6T} ratio ~ 0.91 , as indicated in Figure III.9d. These advantageous properties accompanied by good rectangular overall loop shape, and elevated $(BH)_{\text{max}} \sim 285 \text{ kJ}\cdot\text{m}^{-3}$ which are the characteristics of an ideal hard magnetic material.

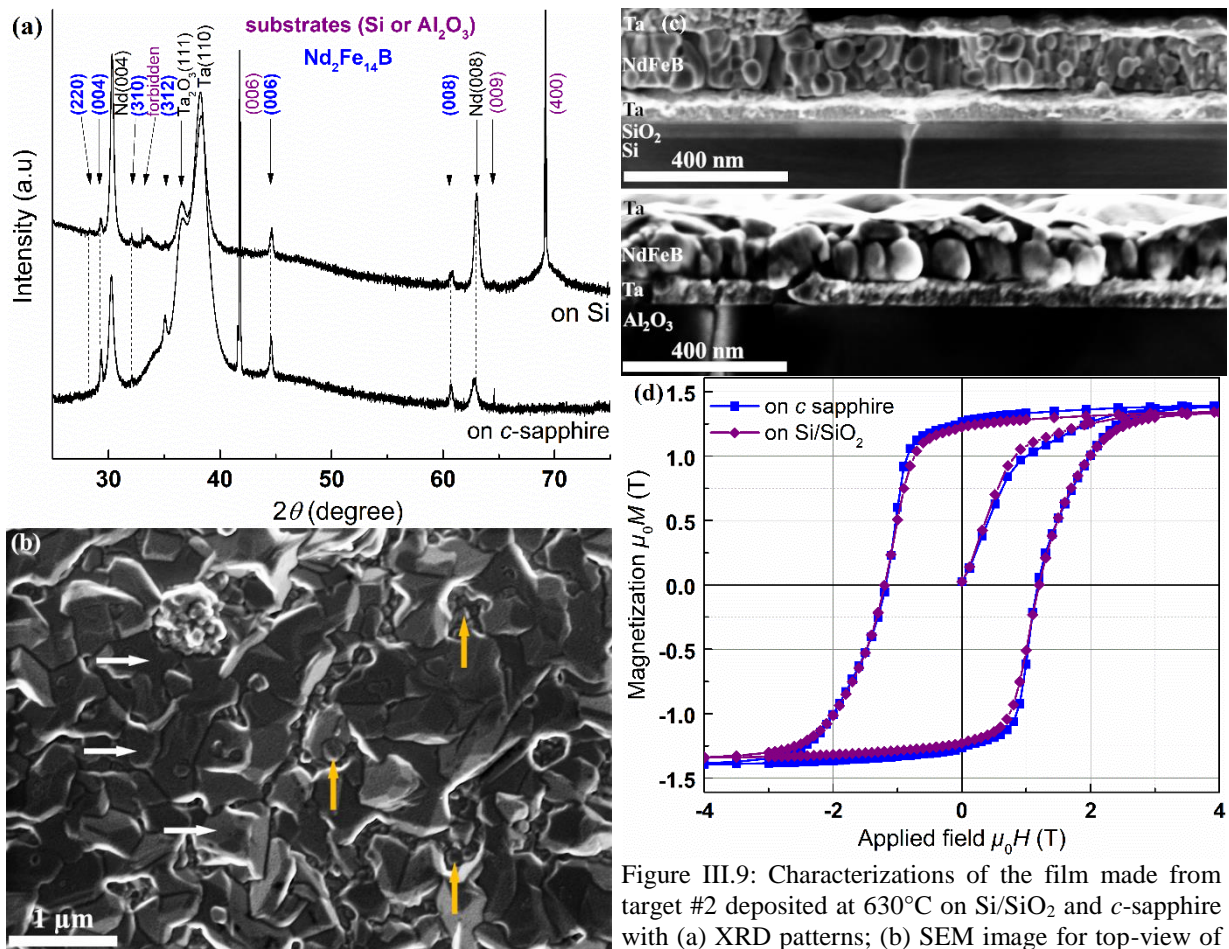


Figure III.9: Characterizations of the film made from target #2 deposited at 630°C on Si/SiO₂ and *c*-sapphire with (a) XRD patterns; (b) SEM image for top-view of the film deposited on *c*-sapphire; (c) cross-sectional SEM images; and (d) oop magnetic hysteresis loops with absolute magnetization scale.

Hard magnetic thin films whose magnetisation mechanism is dominated by pinning or nucleation that are distinguishable based on the virgin curves (see section I.1). The virgin curves for both kinds of thin films on *c*-sapphire and Si/SiO₂ are demonstrated to confirm the magnetic reversal feature, as shown in Figure III.9d. The films are increasingly magnetized as the applied field less than 1 T (high susceptibility), then change to another stage of gradually magnetized as applied field from 1 T to 3 T (low susceptibility) and finally reach the saturation where almost all the magnetic moments are parallel to the applied field. On the other hand, the initial magnetisation curves are of high initial susceptibility, which leads to the domain walls freely to move through the material. Such behaviors of initial curves express the nucleation-type magnet behavior [7]. The equivalence ranging from atomic to microscopic scale and magnetic properties has pointed out that NdFeB based thin films are well adapted on both single crystal and Si/SiO₂ substrates.

To better comprehend about the magnetic properties of fabricated films, this part was conducted toward the MFM measurement. The magnetic patterns were ascertained with home-made FePt hard magnetic probe (fabricated at Néel Institute), which is supposed of $\mu_0 H_c \sim 0.5$ T. Note that large coercivity of the probe making sure the stray field of the thin films would not magnetically reverse the probe. AFM and MFM images made on pieces of films deposited at 630°C using target #2, deposited on Si/SiO₂ (Figure III.10a) and *c*-sapphire (Figure III.10b) in the virgin magnetic state, are shown in Figure III.10. The two images of AFM and MFM were performed on exactly the same position of the samples. The AFM images present surface structures similar to that seen in the SEM plan-view images (Figure III.6b,

and Figure III.9b), i. e., grains with in-plane dimensions approaching 1 μm . The high peak to peak intensity value of 300 nm, agrees with the high roughness of these films, as evidenced for sample

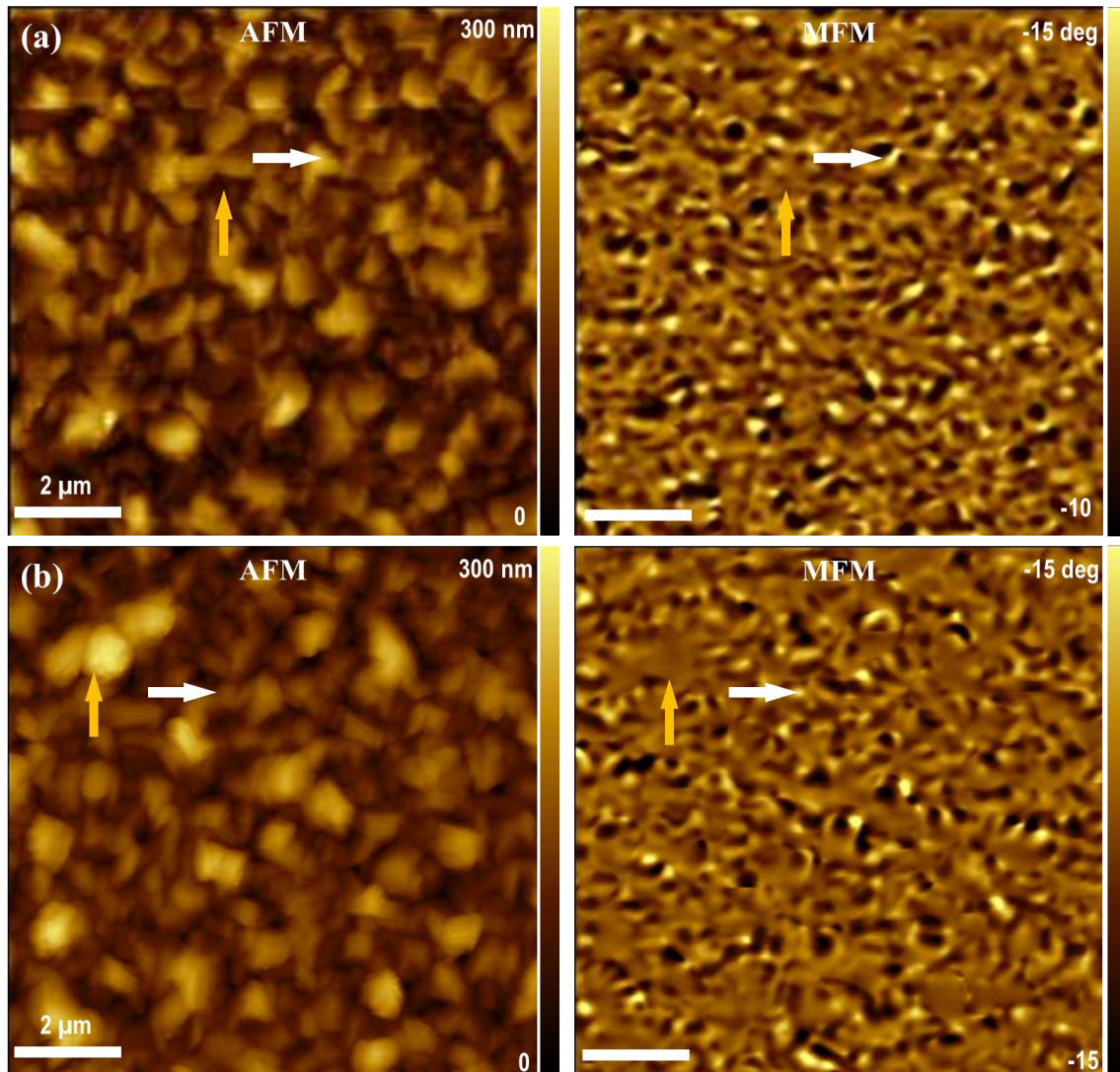


Figure III.10: Characterizations of the two NdFeB based thin films deposited at 630°C, from target #2, on (a) Si/SiO₂ substrate; and (b) On *c*-sapphire substrate, in terms of AFM topography and MFM magnetic contrast in virgin magnetic state, with hard magnetic probe of coercivity larger than 0.5 T.

deposited on Si/SiO₂ in SEM images cross section (Figure III.9c). In the MFM graphs, the negative phase shift corresponds to dark contrast while the positive one is responsible for bright contrast. The MFM images are characterized by regions of high contrast (one such region is identified by a white arrow) and regions of much lower contrast (e. g., the region identified by an orange arrow). The mixture of the high and low contrast suggests that these samples, in virgin magnetic state, present stripes magnetic domains. The size of the high contrast regions is comparable to the in-plane dimensions of the Nd₂Fe₁₄B grains. The high contrast is attributed to the stray field produced by these grains. The low contrast regions are attributed to paramagnetic Nd-rich regions. It is noting that the critical volume of single domain particle for NdFeB is about 300 nm [211]. Regarding the topology analysis, these big grain sizes rise up to 1 μm . It suggests that the bigger grains may contain a single domain of multiple domain particles of Nd₂Fe₁₄B. The AFM and MFM measurements reconfirm the decoupling effect of Nd paramagnetic phase to Nd₂Fe₁₄B magnetic grains which previously approved by, SEM plan-view images (shown in Figure III.6b,

and Figure III.9b), SEM image of the FIB-cut cross section (shown in Figure III.3a) and macroscopic magnetic measurement throughout these sections.

As mentioned earlier, one of the goal of this work is to dedicate to Soft in HARD Magnetic Nanocomposites (ANR SHAMAN-project). Thus the fabrication of thin films, often called matrices, could be reliable and producible before embedding soft magnetic nano-inclusions inside such matrices so that it is possible to quantify the contribution of each phase of soft and hard in the fabricated nanocomposite. The testing reproducibility of the fabrication for such matrices is crucial. Previous sections announce that the optimal deposition temperatures range from 550°C to 630°C for good magnetic properties of the thin films form target #2 (section III.1.1 and section III.1.2). Seven NdFeB based thin films were deposited on Si/SiO₂ substrate, from

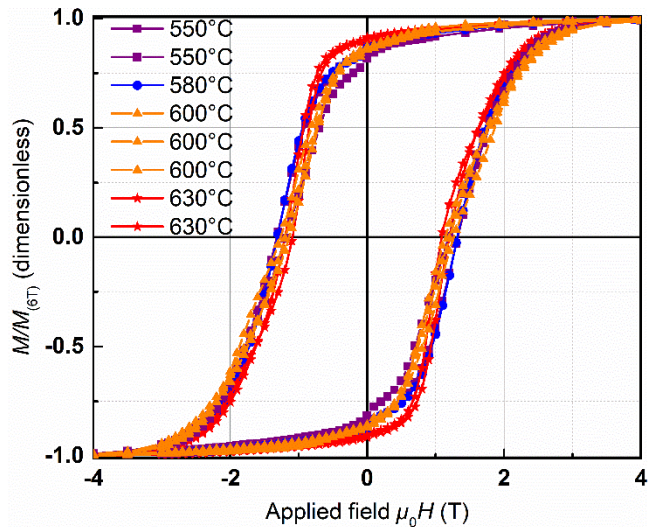


Figure III.11: Oop hysteresis loops (Normalized and uncorrected for demagnetization field) of seven Si/SiO₂/Ta/NdFeB/Ta thin films deposited at arbitrary temperatures in the ideal zone to test the reproducibility, from target #2.

target #2, and at temperatures in the ideal zone. The overall magnetic hysteresis loops of these samples are all compared in Figure III.11. While the magnetic coercivity and remanence M_{0T}/M_{6T} ratio are equivalent in all presented samples, e. g., $\mu_0H_c > 1.2$ T, $M_{0T}/M_{6T} > 0.90$, all films show single magnetic phase behaviors. These observed magnetic results demonstrate that the hard magnetic matrices of NdFeB thin films are of high quality and reproducible.

This work has investigated the chemical, structural and microstructural-magnetic properties relations of NdFeB thin films by examining the influence of target (thin films) elemental compositions, deposition temperatures and substrates. The compositional ratio strongly impacts magnetic properties of fabricated films. Good magnetic thin films require Nd₂Fe₁₄B structure, surplus of paramagnetic Nd-rich phase to decouple the Nd₂Fe₁₄B ferromagnetic grains and sufficient microstructure arrangement of compact grains to augment the magnetic coercivity of deposited films. The best magnetic properties of $\mu_0H_c = 1.3$ T, $\mu_0M_r > 1$ T, $M_{0T}/M_{6T} = 0.91$, nice rectangular loop shape, and single magnetic phase behavior are achieved for optimized films deposited inside the optimal deposition range (550°C – 630°C), from target #2 with Nd/Fe = 0.45. High quality, textured, and reproducible NdFeB magnetic thin films deposited from single alloy target with similar magnetic properties are achieved as grown on both inexpensive Si/SiO₂ (100 nm) and *c*-sapphire (Al₂O₃) single crystal substrates. Hence, deposition of the NdFeB based thin films is a favorable route to conduct further investigations.

III.2. NdFeB matrix with post-annealing

As indicated in section III.1, in order to effectively promote the Nd₂Fe₁₄B phase with good magnetic properties, textured NdFeB films require direct heating during the deposition elevated temperatures in the range 550°C – 630°C. This moderately high temperature process is unfavorable in several specific circumstances, which needs fabrication of NdFeB based thin films at lower temperatures. For example, RT or well below 500°C deposition is required to embed soft magnetic NPs (Co, FeCo) into

the matrices without losing NPs' integrity and preventing diffusion of the NPs into the matrices. If diffusion occurs, the anisotropy field of the skeleton hard matrices will be reduced, thus Soft in HARD Magnetic Nanocomposites will not stand. This part will therefore explore a two-step annealing approach allowing synthesis of such hard magnetic thin films that are deposited at lower deposition temperatures by conventional PLD.

150 nm NdFeB based thin films will be initially prepared by PLD on Si/SiO₂(100 nm) with Ta buffer layer of 50 nm nominal thickness, at 450°C (far below the transition temperature of FeCo alloy of 650°C), and then latter processed by RTP at various annealing temperatures. The RTP parameters (heating rate, annealing time) will be chosen based on the thorough studies presented in section III.4, in which the best value of coercivity was achieved. The schematic representation of annealing procedure by RTP for series of thin films used in this work is presented in Figure III.12. Note that in all the cases, the vacuum pressure was kept constant at 1×10^{-1} mbar of Ar flow. First, the heat treatment at various annealing temperatures, T_a , has been carried out on initially 450°C-deposited films from target #2, at other fixed

conditions, i. e., heating rate of 50°C/s, annealing time of 60s, and cooling down was control by the system itself, for which the cooling rate in the first five seconds is approximately same as heating rate. This section contains structural, microstructural characterizations (XRD, AFM, SEM, and FIB) and magnetic measurements (VSM-SQUID).

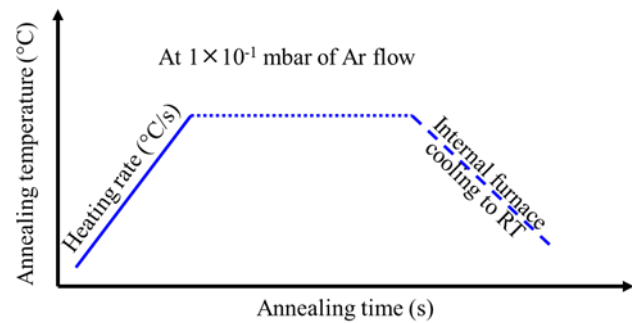


Figure III.12: The schematic RTP representation of the annealing procedure used in this work.

III.2.1. Atomic structure

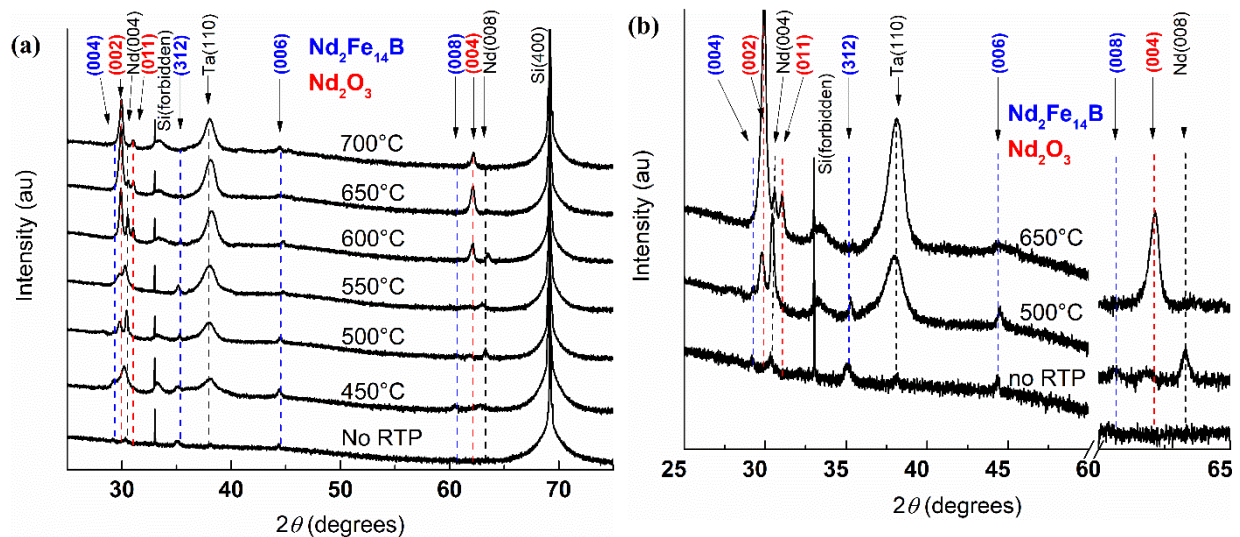


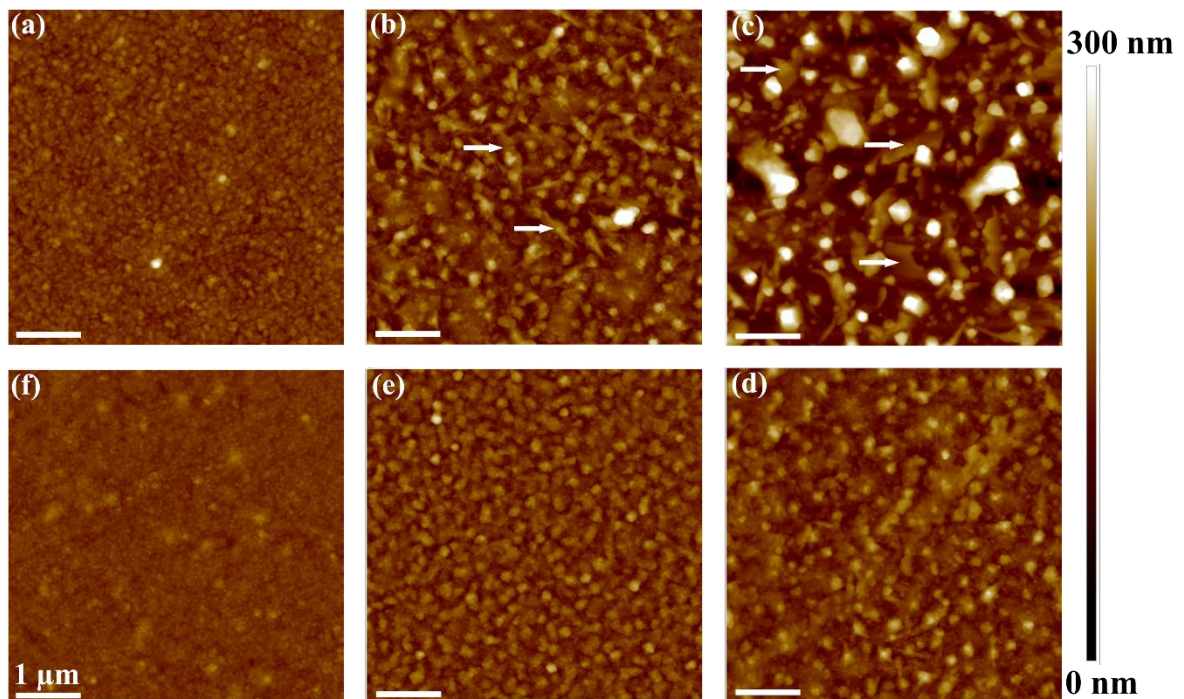
Figure III.13: (a) the XRD diffraction patterns of the Si/SiO₂/Ta/NdFeB/Ta thin films deposited from target #2, at 450°C, then processed by RTP at different annealing temperatures T_a , with heating rate of 50°C/s, in 60 s and 1×10^{-1} mbar of Ar flow; and (b) the additional zooms for as-deposited and typical annealed films.

Figure III.13 presents the evolution of atomic structure of all seven annealed thin films as a function of T_a . From Figure III.13a, the as-deposited film (deposited at 450°C and no second step of RTP heat treatment applied) is partly amorphous with only diffraction peaks identified as Nd (004), Nd₂Fe₁₄B

(312), $\text{Nd}_2\text{Fe}_{14}\text{B}$ (006), Ta (110) with relatively weak intensities. With RTP heat treatment at 450°C , the films is crystallized reflected by additional (00 l) reflections of $\text{Nd}_2\text{Fe}_{14}\text{B}$ phase, the broadened orientation of Nd (004) and the strong appearance of Ta (110). Predominant orientation of (00 l) reflections of $\text{Nd}_2\text{Fe}_{14}\text{B}$ phase indicated the strongly oriented perpendicular to the film plane of the annealed films, at 500°C . The $\text{Nd}_2\text{Fe}_{14}\text{B}$ is confirmed up to annealing temperature of 600°C , and the unique (00 l) Nd pure phase indicates preferential out-of-plane orientation and is confirmed up to 650°C .

Along with the expected phases attributed to paramagnetic Nd and ferromagnetic $\text{Nd}_2\text{Fe}_{14}\text{B}$ phases, the diffraction peaks identified as Nd_2O_3 phase is formed from $T_a=500^\circ\text{C}$ and above. The ratio of Nd_2O_3 phase in the layer, which is reflected in the intensities of the Nd_2O_3 ((002), (011), (004)) compared to other reflections of either Nd or $\text{Nd}_2\text{Fe}_{14}\text{B}$ reflections, increases with T_a . The signature of Nd_2O_3 phase are strongly visible at higher T_a ($\geq 600^\circ\text{C}$), in stark contrast, the signatures of Nd and $\text{Nd}_2\text{Fe}_{14}\text{B}$ phases are almost vanished starting from 650°C , respectively. A better magnification to see the evolution of the Nd_2O_3 phase is introduced in Figure III.13b. At 700°C , the sample is completely oxidized. Peaks indexed as Ta (110) appears in all the annealed films and no major change was observed. Though the film is protected by capping (avoid the inter-diffusion from SiO_2 layer) and protective (avoid the oxidation from exposing film to the environment) Ta layers, the oxidation problem still takes place. This might be attributed to the fact that the resident oxygen had contaminated the NdFeB film during the as-deposition (deposited at 450°C). Such resident oxygen promotes the oxidation reaction of reactive rare-earth element of Nd in excess inside the film (Nd/Fe inside the film ~ 0.42) to form Nd_2O_3 phase. The other probable contribution might come from the nominal 50 nm Ta protective layer, which was not thick enough, or might be cracked during RTP allowing oxygen from the RTP chamber to migrate to the films.

III.2.2. Microstructure



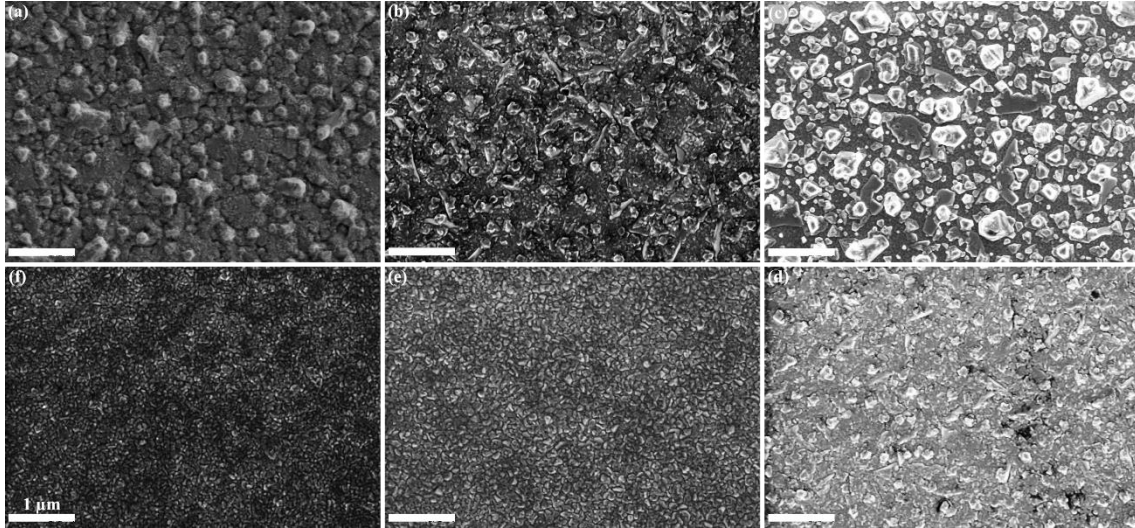


Figure III.14: The evolution of microstructures (top-view AFM and SEM images) of the Si/SiO₂/Ta/NdFeB/Ta thin films deposited from target #2, at 450°C, then processed by RTP at different annealing temperatures T_a , with heating rate of 50°C/s, in 60s and 1×10^{-1} mbar of Ar flow corresponding to (a) no RTP applied; (b) 450°C; (c) 500°C; (d) 550°C; (e) 600°C; and (f) 650°C.

The annealing temperatures, T_a , affect the surface morphologies of the annealed thin films together with the crystallization of the phases (as evidenced from XRD diffraction patterns). Two series of AFM and SEM images of annealed films at various T_a showing distinct surface morphologies are compared in Figure III.14. The as-deposited state film (deposited by PLD at 450°C) is composed of densely packed islands of diameter around 100 nm – 150 nm on top of a continuously underlying layer.

The surface of the RTP annealed films at 450°C is characterized by loosely bigger islands with diameter of about 200 nm on an underlying layer with grains of size approaching 1 μm , the plane of such grains frequently tilted slightly compared to that of the Si substrate (indicated by white arrow). Additionally, the film is more discontinuous represented by such loose grains. It is noticeable that these underlying grains start disappearing at $T_a = 550^\circ\text{C}$, and to be completely vanished at $T_a = 600^\circ\text{C}$, at which the film presents a less isolated grain microstructure. At $T_a = 650^\circ\text{C}$, the films is defined by very fine grains with dimensions of less than 50 nm.

The root-mean-square (rms) roughness of all the films as a function

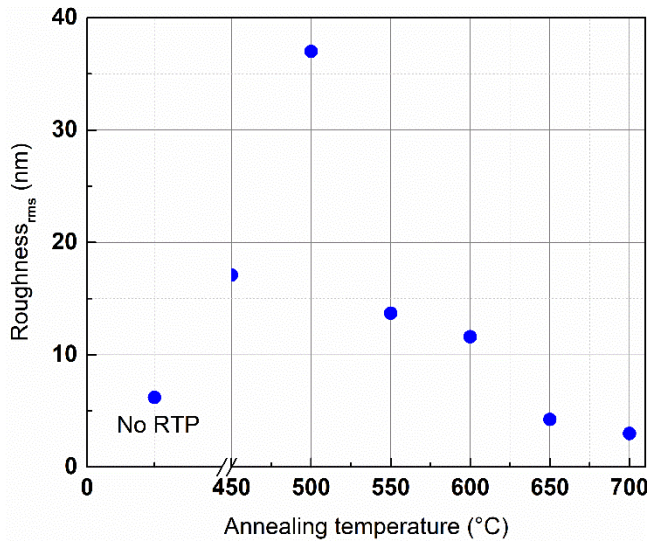


Figure III.15: The rms roughness of the Si/SiO₂/Ta/NdFeB/Ta thin films deposited from target #2, at 450°C, then processed by RTP at different annealing temperatures T_a , with heating rate of 50°C/s, in 60s and 1×10^{-1} mbar of Ar flow.

annealing temperatures, T_a , is demonstrated in Figure III.15. The rms roughness approaches the maximum value of about 37 nm at $T_a = 500^\circ\text{C}$. This highest rms roughness compared to others is coherent with the peak-to-peak intensity value of 300 nm for thin film, which exhibits a bimodal height distribution and is

characterized by distinctively isolated grain microstructure. Increasing further T_a significantly reduces the rms roughness.

Representative cross-sectional SEM images of the FIB-cut (FIB-ESB) of as-deposited and annealed films are compared in Figure III.16. The heterostructures Ta/NdFeB/Ta of the films are clearly visible. A Pt layer was deposited using FIB in order to protect the film during the ion milling process. The NdFeB layer shows distinct parts. One of gray/bright zones is attributed to the Nd-rich phase and the second of the dark zones is mostly Nd₂Fe₁₄B phase. Here the Nd/Fe ratios for the gray and dark regions are identified as ~ 0.67 and ~ 0.32 respectively. The as-deposited film reveals a mixture of the two gray and dark zones, which are scarcely distinguishable. This agrees with the observation in the XRD pattern that the as-deposited film is not fully crystallized. After being annealed at 500°C, the two zones become

easily distinguishable, and are well-defined. Obviously, the annealing process promotes the crystallization of the film from the amorphous/partly amorphous state of the as-deposited film. This is in good agreement with results from XRD showing the Nd and Nd₂Fe₁₄B reflections and agrees with the highest rms roughness estimated from AFM (see Figure III.15), where the grains (Nd and Nd₂Fe₁₄B) are well separated. As can be clearly seen in Figure III.16b, the the gray regions are somewhat equiaxed of diameter ~ 200 nm, while the dark regions are elongated

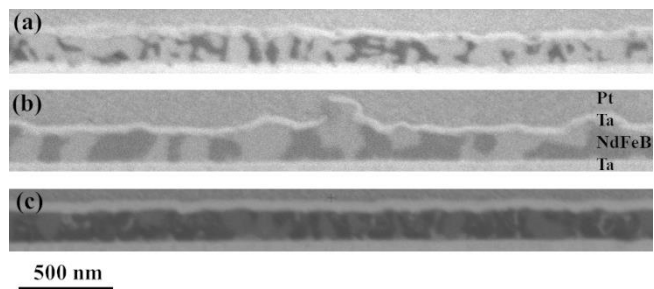


Figure III.16: The representative FIB-EBS cross-sectional images of the Si/SiO₂/Ta/NdFeB/Ta thin films deposited from target #2 then processed by RTP at different annealing temperatures of (a) 600°C, (b) 500°C, with heating rate of 50°C/s, in 60s and 1×10^{-1} mbar of Ar flow, and (c) The 450°C-deposited film without RTP.

in the ip direction with dimension of ~ 0.5 μm . Thus, the underlying and floating grains in Figure III.14 might be attributed to both Nd₂Fe₁₄B and Nd-rich grains. Going beyond in T_a , i. e., 600°C, the annealed film is mainly composed of brighter regions traversing through the film thickness. These brighter regions are attributed to the Nd₂O₃ oxidized phase, which is in agreement with results from XRD with strong signature of Nd₂O₃, very fine grains (Figure III.14) and lower rms roughness (Figure III.15).

Recently, other authors indicated that Nd₂Fe₁₄B grain boundaries in the NdFeB-based magnets may contain Nd₂O₃ oxide layers, which make positive contribution to magnetically decoupling Nd₂Fe₁₄B grains because they hinder the migration of domain walls from one Nd₂Fe₁₄B grain to another as the case of metallic Nd or intermetallic phases [212]. The authors demonstrated that thin layer of Nd₂O₃ may play the same role as metallic Nd or intermetallic phases.

III.2.3. Magnetic properties

Uncorrected for demagnetizing field and normalized out-of-plane (oop) hysteresis loops of the annealed films at various annealing temperatures, T_a are compared in Figure III.17-left. The film annealed at 500°C shows practically single phase magnetic behavior. It has the highest remanence ratio M_{OT}/M_{6T} (~ 0.92), while the coercivity value (~ 1 T) is among the highest and comparable with other annealed films at 450°C, 550°C, and 600°C. All these films show obvious two-phase or multi-phase behavior that is demonstrated with a representative kink in the hysteresis loop at applied field $\mu_0 H = 0$ T or a long tail at high applied field ($\mu_0 H > 2$ T for films annealed at 450°C and 550°C). One-magnetic-phase or multi-magnetic-phase characteristic can be seen in the dM/dH plots in Figure III.17-right. All films display a

vigorous peak near the coercive field $\mu_0 H_c$ being characterized by the highest normalized dM/dH values. While film annealed at 500°C exhibits arguably single magnetic phase behavior, owing to less visible peak near $\mu_0 H \sim 0.2$ T, the other films illustrate additional peaks at $\mu_0 H \sim 0$ T and sometimes long tails in dM/dH values at $\mu_0 H > 2$ T. Note that though film annealed at 650°C show single magnetic phase characteristic, due to poor values in both coercivity and remanence ratio M_{0T}/M_{6T} , it is considered as soft ferromagnetic material. While the sharpness of the hysteresis curves in the vicinity of the coercivity is comparable for films annealed at 450°C, 500°C, and 550°C, it is higher in the films annealed at 600°C, and higher again in the films annealed at 650°C. Details about magnetic properties at various annealing temperatures is compiled in Table III.1. Films annealed at different T_a and as-deposited film have the remanence ratio M_{0T}/M_{6T} falling far short from the best value (0.92) obtained for film annealed at 500°C. The magnetic properties in terms of coercivity, remanence, and $(BH)_{\max}$ are improved from the as-deposited one to the best values at 500°C, and reduces significantly when increasing T_a .

Table III.1: Magnetic properties of the Si/SiO₂/Ta/NdFeB/Ta thin films deposited from target #2, at 450°C, then processed by RTP at different annealing temperatures T_a , with heating rate 50°C/s, in 60s and 1×10^{-1} mbar of Ar flow.

RTP temperature (°C)	Magnetic properties of the annealed films			
	$\mu_0 H_c$ (T)	$\mu_0 M_r$ (T)	M_{0T}/M_{6T}	$(BH)_{\max}$ (kJ.m ⁻³)
No RTP	0.42	0.30	0.55	26
450	1.02	0.55	0.78	62
500	0.97	0.96	0.92	176
550	0.90	0.42	0.64	39
600	0.74	0.40	0.60	40
650	0.02	0.01	0.05	1

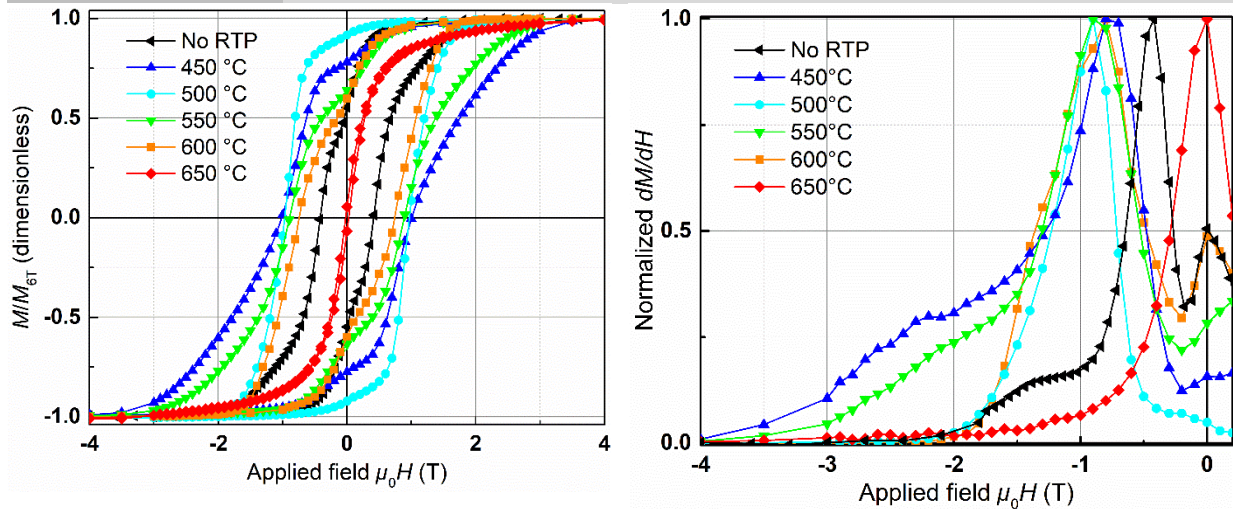


Figure III.17: The (left) – the uncorrected for demagnetizing field and normalized oop hysteresis loops; and the (right) – the dM/dH plots of the Si/SiO₂/Ta/NdFeB/Ta thin films deposited from target #2, at 450°C, then processed by RTP at different annealing temperatures T_a , with heating rate 50°C/s, in 60s and 1×10^{-1} mbar of Ar flow.

The augmentation in magnetic properties, as indicated in Table III.1, in the annealed films (e. g., 500°C) is tentatively attributed to (i) the annealing procedure assisting to complete crystallization of the Nd pure phase and Nd₂Fe₁₂B phase from the amorphous/partly amorphous state in the as-deposited film (as indicated in Figure III.13); (ii) the presence and redistribution of the paramagnetic Nd-rich intergranular phase inducing better magnetically decoupling of the ferromagnetic Nd₂Fe₁₄B grains. In contrast, the decrease in coercivity, remanence, remanence ratio associated with $(BH)_{\max}$ for films annealed at higher temperatures $T_a \geq 650^\circ\text{C}$ reflects the presence of Nd₂O₃ phase, obviously shown by XRD patterns, morphologies by AFM+SEM, cross-sectional FIB-cut image (see Figure III.16a).

An ip magnetic behavior of the film deposited at 450°C and later annealed at 500°C is compared with an oop loop of the same specimen in Figure III.18. The absolute value of the magnetization, which was estimated from the volume of the film, free of droplets' contribution, is given. From the two loops, extrapolation provides an intercept at about 7 T, which is slightly lower than that of the magnetocrystalline anisotropy of the Nd₂Fe₁₄B phase (7.6 T). Similarly, the effective anisotropy constant – $K_{\text{eff}} \sim 3.07 \text{ MJ.m}^{-3}$, according to (Equation I.7), is roughly determined lower compared to 4.87 MJ.m^{-3} of Nd₂Fe₁₄B phase [7]. Furthermore, a high value of oop remanent magnetization of about 1 T is approximate four folds larger than the ip one, and high ip value of magnetization

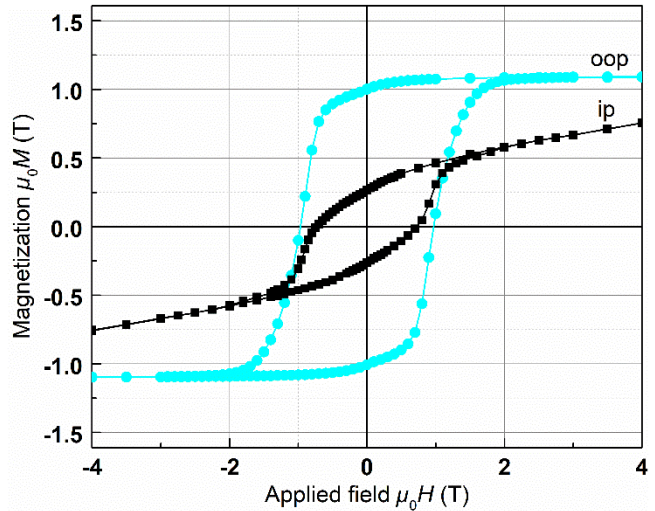


Figure III.18: In-plane (ip) and out-of-plane (oop) magnetic hysteresis loops (uncorrected for demagnetization field) of the sample deposited from target #2, at 450°C and then applied heat treatment by RTP at 500°C, with heating rate of 50°C/s, in 60s and 1×10^{-1} mbar of Ar flow.

at high applied field expresses the induced oop texture for film annealed at 500°C. The remanent value closing to the remanence obtained by one-step of direct crystallization during the NdFeB growth as shown in previous section of III.1 indicates that the textured films with good magnetic properties could be achieved by both one-step and two-step approaches.

Part B: FePt thin films

III.3. FePt matrix without RTP

Taking the advantage of congruent transfer process of PLD, a series of single layer FePt thin films will be deposited directly from an equiatomic alloy FePt target prepared by induction melting. Like magnetic thin film based NdFeB material, this section is going to demonstrate one of the main PLD parameters directly influence the properties of the deposited FePt films, i. e., the deposition repetition rate. The effect of deposition temperatures and substrates will be also carefully investigated.

In order to correlate more information from XRD, several structural parameters will be exploited. The first one is the degree of orientation, which is a semi-quantitative parameter – often called Lotgering

orientation factor (*LOF*). The *LOF* is defined as [213] $LOF = \frac{p - p_o}{1 - p_o}$ where $p = \frac{\sum I_{sample}^{(00l)}}{\sum_{all} I_{sample}^{(hkl)}}$ and

$p_o = \frac{\sum I_{powder}^{(00l)}}{\sum_{all} I_{powder}^{(hkl)}}$, where *I* is for intensity of the XRD reflection, (*hkl*) are Miller indices of the reflections. The *LOF* describing the degree of (00*l*) orientation can vary from a negative value to maximum of 1. Negative value stands for other preferential orientation rather than (00*l*) reflection. 0 represents non-oriented sample, and 1 assigns perfectly oriented sample. The second one, which is so-called the chemical order parameter, *S*, relating to the integral intensities of fundamental and superlattice peaks. In the nonstoichiometric composition, the long range chemical ordering parameter *S* is usually smaller than unity, thus the *S* parameter should be obtained experimentally. The *S* parameter is defined as

$$[122] S = \sqrt{\frac{I_{(001)}^{experiment} I_{(002)}^{theory}}{I_{(002)}^{experiment} I_{(001)}^{theory}}} = \sqrt{\frac{I_{(001)}^{experiment} K_o F_{(002)}^2 A(\theta)_{(002)} LP_{(002)} e^{\frac{B_{(002)}^{D-W} \sin^2 \theta_{(002)}}{\lambda^2}}}{I_{(002)}^{experiment} K_o F_{(001)}^2 A(\theta)_{(001)} LP_{(001)} e^{\frac{B_{(001)}^{D-W} \sin^2 \theta_{(001)}}{\lambda^2}}}}, \text{ where } I, K_o, F^2 = F \times F^*,$$

A(θ), *LP*, B^{D-W} , θ , and λ denote for the integrated intensity, a correction constant (relating to textured degree, normally it is *FWHM*), the structure factor/complex conjugate (F/F^*), the absorption factor, the Lorentz-polarization factor, Debye-Waller factor, Bragg diffraction angle for *hkl* planes, and diffraction wavelength ($\lambda_{Cu-K\alpha} = 0.15406$ nm). The integrated intensity *I* can be expressed as a product of a constant *C*, multiplicity *m*, *LP* and F^2 . Additionally, the F^2 values are varied for different peaks and calculated as follows:

$$\text{- Super-lattice reflections: } F_{(001)}^2 = 4S^2 \left\{ \left(f_{Pt} e^{-M_{Pt}} - f_{Fe} e^{-M_{Fe}} \right)^2 + \left(\Delta_{Pt} e^{-M_{Pt}} - \Delta_{Fe} e^{-M_{Fe}} \right)^2 \right\}$$

$$\text{- Fundamental reflections: } F_{(002)}^2 = 16 \left\{ \left(x_{Pt} f_{Pt} e^{-M_{Pt}} + x_{Fe} f_{Fe} e^{-M_{Fe}} \right)^2 + \left(x_{Pt} \Delta_{Pt} e^{-M_{Pt}} + x_{Fe} \Delta_{Fe} e^{-M_{Fe}} \right)^2 \right\}$$

The so-called Debye-Waller correction/temperature factor is estimated about 1.13. *f* and Δ are the real and imaginary parts of the atomic scattering factor, while x_{Pt} , x_{Fe} are the atomic percentage of each individual element in $Fe_{x_{Fe}}Pt_{x_{Pt}}$ compound. Since the mosaicity of these samples was found to be around 3° and the beam divergence was (0.9 ± 0.4) mrad, the Lorentz-polarization factor *LP* can be approximated

by using the expression for powder samples of $LP = \frac{1 + \cos^2 2\theta}{\sin^2 \theta \cos \theta}$, where the Lorentz factor

$L = \frac{1}{4 \sin^2 \theta \cos \theta}$, the polarization factor $P = \frac{1 + \cos^2 2\theta}{2}$, omitting constant of 1/8 factor to obtain

Lorentz-polarization factor [122]. Table III.2 shows the parameters in this work to calculate the S parameters. Note that $S = 0$ for a completely disordered sample and $S = 1$ for a fully ordered sample.

Table III.2: Parameters used to estimate the ordering parameter S of the FePt thin films [122,214,215].

Peak	2θ	LP	M_{Fe}	f_{Fe}	Δ_{Fe}	M_{Pt}	f_{Pt}	Δ_{Pt}	m	$A(\theta)$
$(001)_{sup}$	24.019	2.26	0.005	21.01	3.4	0.005	64.43	8	2	1
$(002)_{fun}$	49.184	0.94	0.019	16.93	3.3	0.018	55.12	7	2	1

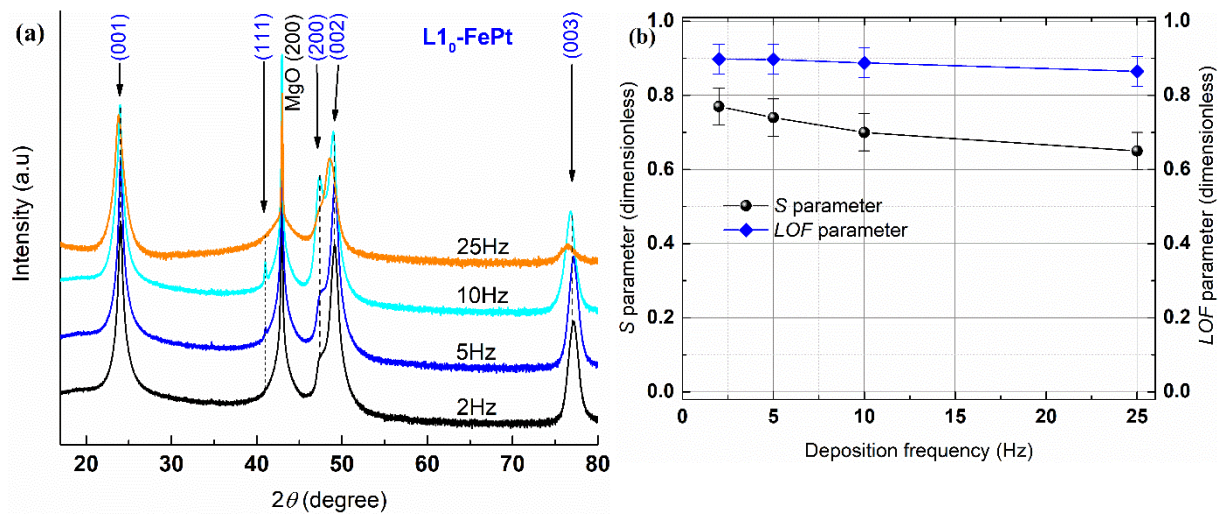
Sometimes, owing to the simplicity and near equiatomic binary thin film ($Fe_{46.5}Pt_{53.5}$), the S frequently calculated from [216] $S \sim 0.58 \sqrt{\frac{I_{(001)}^{experiment}}{I_{(002)}^{experiment}}}$ for films deposited on Si substrate or

$S \sim 0.82 \sqrt{\frac{I_{(001)}^{experiment}}{I_{(002)}^{experiment}}}$ for films deposited on MgO substrate (extracted from [123] with the hypothesis of only different from the diffraction wavelength being used). The last one is the c/a ratio, which is defined as [122,217] $S^2 = \frac{1 - (c/a)_{experiment}}{1 - (c/a)_{theory}}$, where c and a are the lattice parameters of fully tetragonal $L1_0$ -FePt

structure. In the fully ordered FePt bulk material (theory), this ratio $(c/a)_{theory}$ is about 0.956 [218]. Note that the calculation for c/a ratio estimated from S does not taken into account the strain induced by deposition method.

III.3.1. Deposition repetition rates

Regarding equiatomic FePt thin films, it is well known that the thin film are well-crystallized at high deposition temperatures of about 800°C [123] and the *in situ* annealing after growth can significantly augment the ordering and magnetic properties of the deposited films [219]. A set of near stoichiometry 50 nm thin films ($Fe_{46}Pt_{54}$) was deposited at various laser frequencies (2 Hz - 25 Hz), on single crystal MgO (001) substrates, at fixed deposition temperature of 750°C (maximum in this work), at laser fluence 5 J.cm⁻². As pointed out in the Chapter I, owing to the different lattice mismatch between the MgO substrate and $L1_0$ -FePt (~10 %), the microstructures of the FePt thin films on single crystal MgO substrate should follow the Volmer-Weber island growth mode of metallic materials on insulators [79,220].



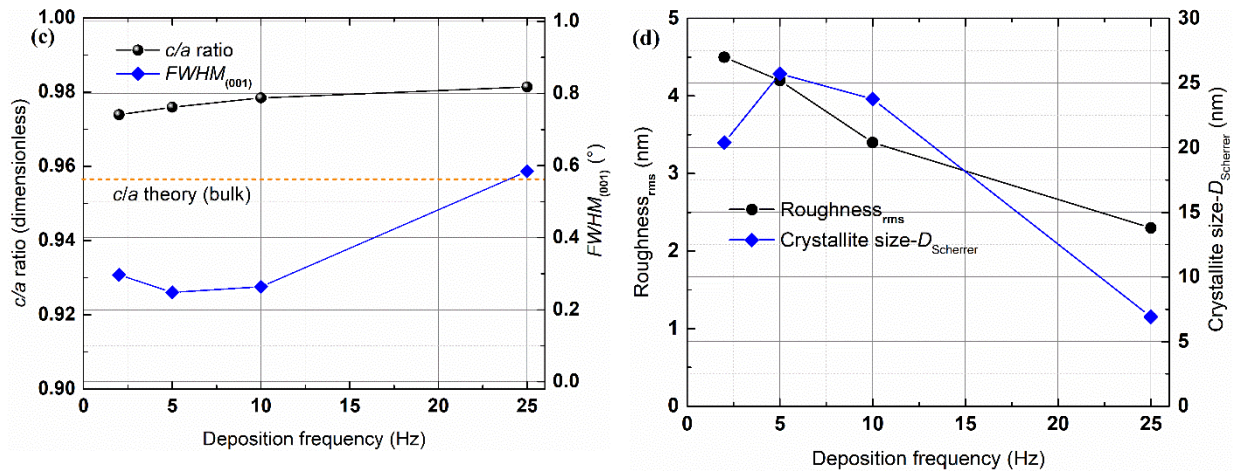


Figure III.19: The evolution in (a) structure (XRD patterns); (b) the S parameter and the LOF parameter; (c) the c/a ratio and $FWHM$ extracted from (001) peak; and (d) Crystallite sizes obtained from Scherrer equation (XRD) and AFM rms surface roughness as a function of KrF laser deposition frequencies, of the MgO/FePt (50 nm) thin films deposited from Fe₅₀Pt₅₀ target, at 750°C, at laser fluence 5 J.cm⁻².

The evolution of the crystallographic structure as a function of repetition rates from 2 Hz to 25 Hz are compared in Figure III.19a. The XRD patterns indicate the fundamental L1₀ (002) orientation together with the L1₀ (001) and L1₀ (003) superlattice peaks of the ordered *fcc*-L1₀-FePt phase. All remaining peaks in these patterns are due to the MgO substrate and the other orientations of L1₀-FePt. The appearance and increasing intensity of the L1₀ (200) (or maybe A1 phase) reflection at higher repetition rates (≥ 5 Hz) demonstrate a minor fraction of A1 phases presented, depicting a mixture of both A1 and L1₀-FePt phases. Higher repetition rates induce a decrease of pronounced c -axis, which are also observed in S and LOF evolutions in Figure III.19b. It is obvious that both S and LOF calculated from XRD patterns gradually decrease with increasing deposition frequency. Namely, the S and LOF values are about 0.77 and 0.89 for films deposited at 2 Hz and reduce to 0.65 and 0.86 for films deposited at 25 Hz respectively. Both S and LOF parameters do not achieve unity indicating the non-optimized fully c -pronounced texture of the deposited films. In a little contrast to S and LOF parameters, the c/a ratio and $FWHM$ of the L1₀ (001) peak increases with increasing deposition repetition rates, as evidenced in Figure III.19c. While the c/a ratio is well all above the nominal theoretical bulk value (0.956), the $FWHM$ becomes broadened, which suggest that the deposited films start transforming to disordered phase of A1 phase ($c/a = 1$) and a major fraction of such disordered phase existed in the films. These results strongly agree about the slight shift in the peak's position of the L1₀ (002) to L1₀ (200) or A1 phase, directly observed from XRD patterns. The crystallite sizes obtained from the Scherrer equation followed by XRD patterns are summarized in Figure III.19d (Details Appendix A.3. The crystallite size measured in the out-of-plane direction reaches a maximum value of ~ 25.7 nm at 5 Hz, and gradually reduces to about ~ 6.9 nm at 25 Hz. This estimate demonstrates the deposited films at high deposition frequency possessing a multiple crystallite in the film thickness (out-of-plane) direction.

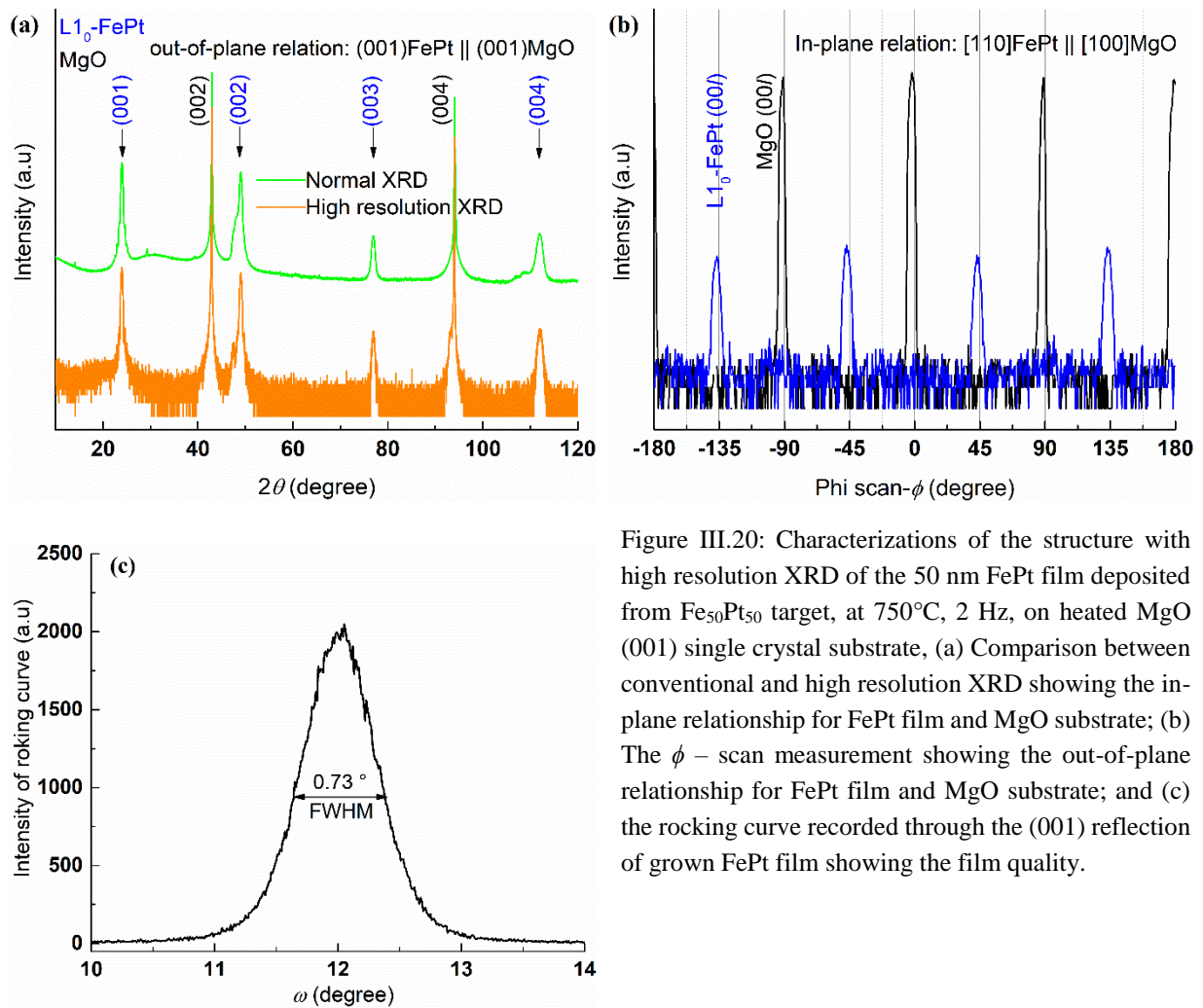


Figure III.20: Characterizations of the structure with high resolution XRD of the 50 nm FePt film deposited from Fe₅₀Pt₅₀ target, at 750°C, 2 Hz, on heated MgO (001) single crystal substrate, (a) Comparison between conventional and high resolution XRD showing the in-plane relationship for FePt film and MgO substrate; (b) The ϕ – scan measurement showing the out-of-plane relationship for FePt film and MgO substrate; and (c) the rocking curve recorded through the (001) reflection of grown FePt film showing the film quality.

The epitaxial relationships of the 50 nm FePt thin film, deposited at 750°C, 2 Hz, onto MgO substrate was examined by a high resolution XRD (Bruker D8 Discover diffractometer, equipped with Cu target – Cu_{K α 1} = 1.5406 Å, and a parabolic mirror associated with a two-reflection Ge monochromator). Figure III.20a compares the XRD patterns obtained by conventional (normal) XRD and the high resolution XRD. Only L1₀ (00l) reflections of the deposited FePt are visible, accompanied by the (00l) reflections from single crystal MgO substrate, which indicate the (001) planes of FePt film parallel to the (001) planes of MgO. The results obtained from $\theta - 2\theta$ suggest the out-of-plane orientation between the substrate and the FePt film of (001) FePt || (001) MgO relationship. The in-plane orientation was determined by ϕ – scan measurement using the (001) reflection plane from both MgO substrate and FePt film, as indicated in Figure III.20b. The reflections (as shown in XRD patterns, in Figure III.20b) arise at ~45° difference in azimuthal angle illustrating that the [110] direction of FePt is parallel to the [001] of the MgO. The MgO (001) has cubic structure, thus MgO (100) is equivalent to MgO (001). The eight symmetric orientations obtained from the ϕ – scan indicate that the FePt film grows epitaxially cube-on-cube in a granular fashion and rotated ~45° onto the MgO substrate with epitaxial relationship to MgO(100), exhibiting [110] FePt || [001] MgO. Thus, the epitaxial relationships of the FePt film grown onto the MgO substrate can be expressed as (001) FePt || (001) MgO for out-of-plane orientation and [110] FePt || (001) MgO for in-plane orientation. Figure III.20c presents further information regarding grown FePt film quality, which can be obtained from the rocking curves recorded through the (001) reflection of FePt film. The *FWHM* gives the mosaicity of the film, which is about 0.73°. The epitaxial

relationships between FePt film and MgO substrate obtained in this work is different with epitaxial cube-on-cube growth for a granular film suggested from other authors for films developed by PLD and magnetron sputtering [123,124,134,221], for which the FePt grown cube-on-cube fashion but not rotated $\sim 45^\circ$, or [001] FePt || (001) MgO for in-plane orientation.

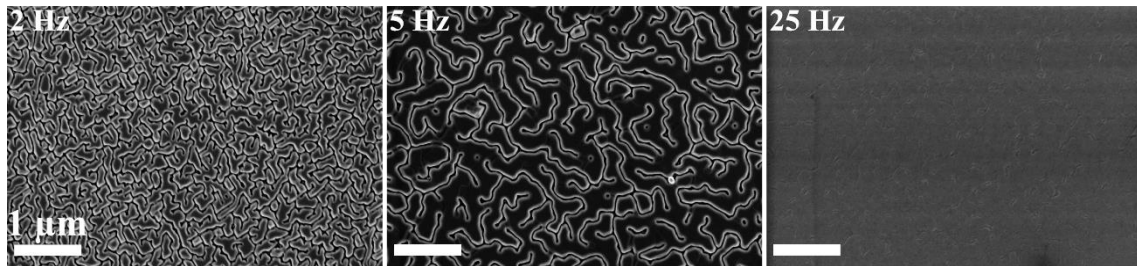


Figure III.21: The evolution in microstructure observed by SEM as a function of KrF laser deposition repetition rates, of the MgO/FePt (50 nm) thin films deposited from Fe₅₀Pt₅₀ target, at 750°C.

Figure III.21 presents a remarkable change in surface morphologies of the FePt deposited at various repetition rates, obtained by SEM (plane-view images). While film deposited at 2 Hz presents a smaller interconnected island microstructure, film deposited at 5 Hz displays relatively bigger interconnected islands spreading throughout the film surface. These microstructural features are highly distinctive in comparison with film deposited at 25 Hz, which exhibits a densely continuous microstructure. The surface morphologies are coherent with the rms roughness performed on the film surface by AFM. Figure III.19d reveals that the rms roughness is very low for all the thin films. The coalescence or continuous morphology can be assigned to the film thickness, which already surpasses the critical film thickness for granular FePt films obtained by depositing film using magnetron sputtering [221]. The microstructural differences between these films could be further attributed to the characteristic of Volmer-Weber island growth mode, which is considerably affected by the mutual relation between the lifetime of adatoms (τ), the laser pulse duration ($\tau_p = 25$ ns, in this KrF laser), and the PLD period ($1/f$), and is driven by balancing between the re-evaporation effect and diffusion process. The study for dependence of deposited film's microstructure on PLD repetition rates was discussed in details by other authors [136], at which they showed that the island density being proportional dependence on the PLD frequency with the $\tau_p f$ is supposed to be a constant. Additionally, the droplet formation was not observed by both AFM and SEM for FePt film.

VSM-SQUID magnetometry measurements performed at RT, on oop directions or magnetic easy axis revealing the dependence of hysteresis loops on deposition repetition rates are shown in Figure III.22a. The sharpness of the hysteresis loop as it approaches coercivity becomes lower when the deposition frequency increases. At low deposition frequency ($f \leq 5$ Hz), films show two magnetic phases behavior of poor overall loop shape, while at higher deposition frequency ($f \geq 10$ Hz), films show quasi-single magnetic phase property. The magnetic phase properties of the deposited film can be evidently observed from normalized dM/dH plots, depicted in Figure III.22a. In all cases, there are always peaks close to the coercivity, and they might have additional peaks such as for films deposited at 2 Hz and 5 Hz, which have one peak approaching to coercivity and the other at higher applied field of around 2 T. Thus the multiple-magnetic phase behavior of the films relates to the number of peaks in the dM/dH plots. With increasing the deposition repetition rate, (i) the coercivity decreases slowly and exhibits a value around ~ 1 T and 0.75 T at 2 Hz and 5 Hz respectively; (ii) the remanence ratio M_{0T}/M_{6T} is mostly unchanged of about 0.85; and (iii) the magnetization becomes easier to be saturated for the magnetic easy axis. However, a drastic change of the $M(H)$ curves is observed between films deposited at 5 Hz and 10 Hz. Namely, the coercivity reduces from 0.75 T at 5 Hz to about 0.2 T at 10 Hz. Further changing up the deposition

frequency no longer affects the coercivity, it however forces the remanence ratio M_{0T}/M_{6T} to jump down from ~ 0.86 at 10 Hz to ~ 0.4 at 25 Hz. Due to the maximum applied field of 6 T in the VSM-SQUID, which may not be sufficient to saturate the magnetization of the granular FePt film, the actual coercivity, and saturation magnetization can be higher. The reduction in coercivity of the deposited film can be accounted for both structure (shown by XRD, Figure III.19a), in which the films are of increasing disordered A1 phase, and microstructure, which become continuous fashion as increasing deposition frequency. As indicated in previous section III.1.2, the coarsening and further continuous microstructure may facilitate magnetization reversal through the domain wall and thus coercivity reduces as a must.

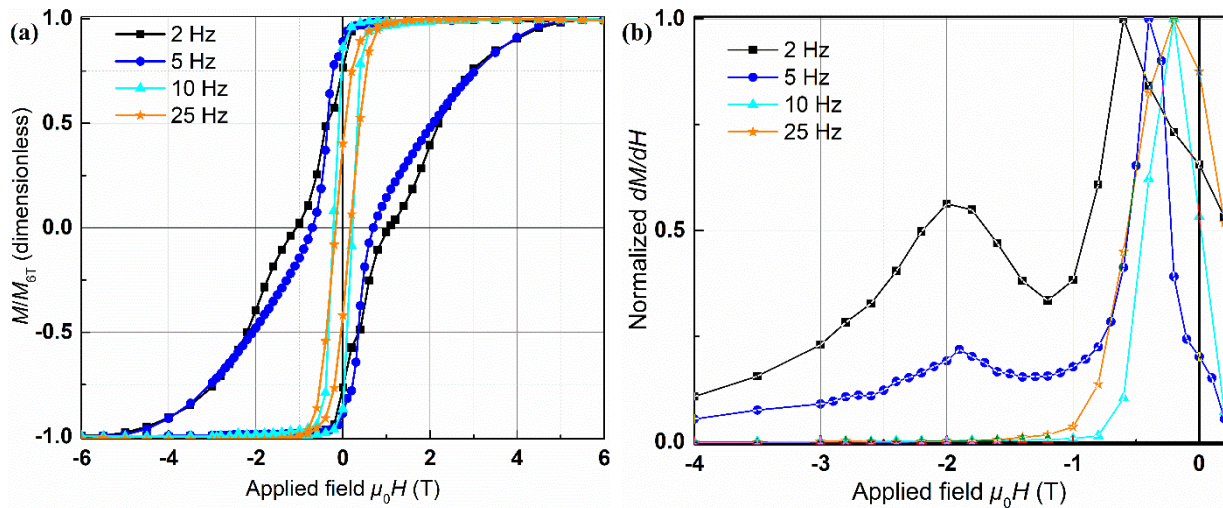


Figure III.22: (a) The normalized and uncorrected with demagnetizing field oop hysteresis loops of the MgO/FePt (50 nm) thin films deposited from Fe₅₀Pt₅₀ target, at 750°C, at laser fluence 5 J.cm⁻², with respect to the KrF laser deposition frequencies; and (b) The normalized dM/dH plots of such oop hysteresis loops.

This work has demonstrated the effect of deposition frequency on structural, microstructural, and magnetic properties of the films. In terms of coercivity and remanence ratio M_{0T}/M_{6T} , film deposited at the lowest possible repetition rate exhibits the best magnetic properties. Thus hereafter additional investigation will be performed at this deposition frequency of 2 Hz.

III.3.2. Deposition temperatures (T_d)

One of the first notice relating to the FePt by PLD, the 50 nm-thin films in previous investigation in section III.3.1 are mostly interconnected/continuous films, which dramatically reduce the magnetic properties of the film, i. e., the coercivity, the remanence ratio M_{0T}/M_{6T} . The deposition temperature – T_d dependence of lower thickness of nominal 35 nm FePt films is therefore investigated. Figure III.23a shows the XRD diffraction patterns for films deposited at various deposition temperatures – T_d ranging from RT ($\sim 25^\circ\text{C}$) to 750°C. Raising up to a T_d of 500°C, the (200) reflection of the disordered phase A1-FePt and (200) orientation of the ordered phase L1₀-FePt (overlapping one each other) are visible besides the single crystal substrate MgO (200) or (002) peak, demonstrating a phase mixture of the A1 and L1₀ phases. Owing to the simultaneous appearance of the both phases, it is believed that the A1 phase is transformed to L1₀ phase by means of first order phase transition, which is presented by nucleating and growing of ordered domains [123]. A slight shift of the A1-FePt peak toward the reflection of (200) of L1₀ phase has

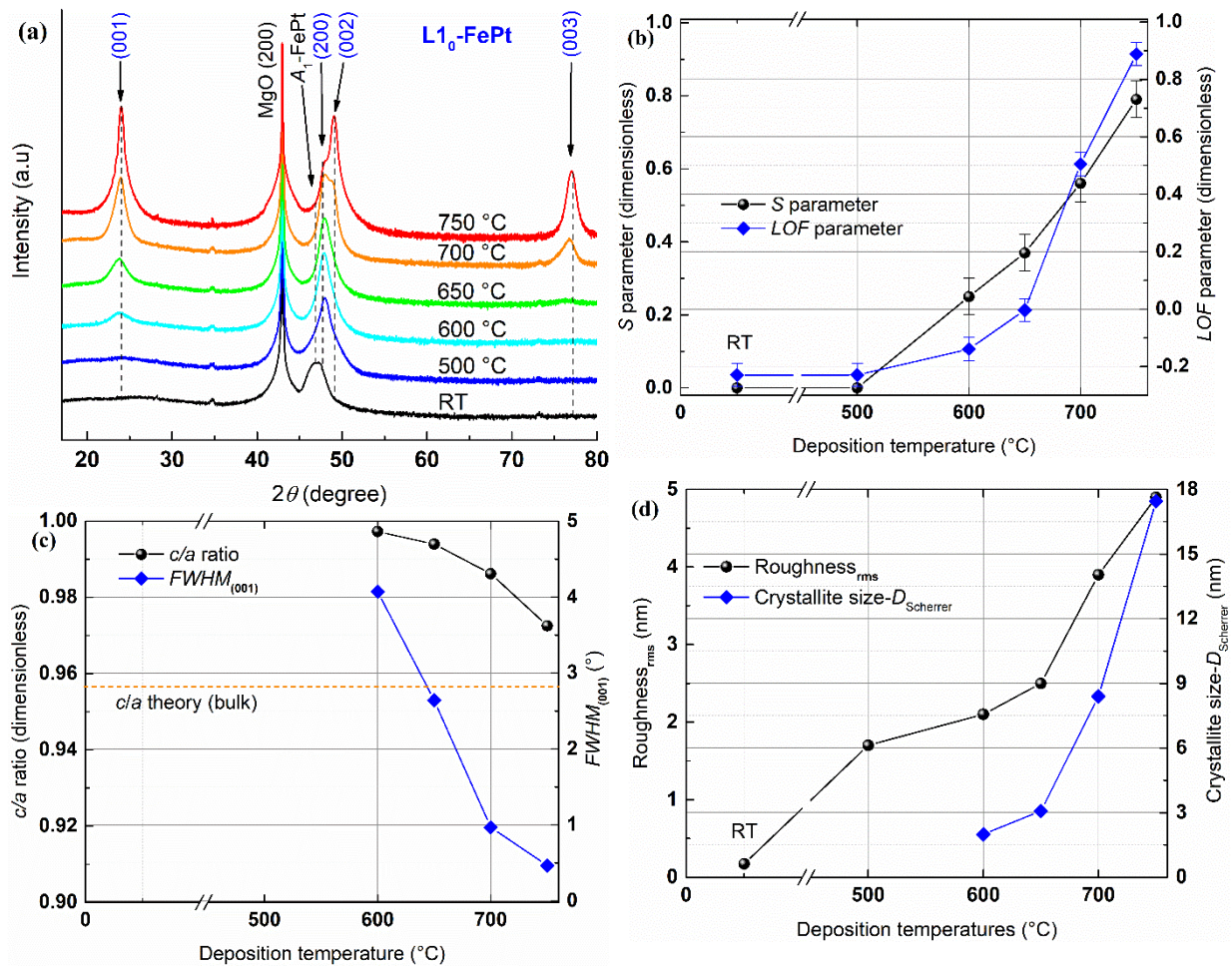


Figure III.23: The evolution in (a) structure (XRD patterns); (b) the S parameter and the LOF parameter; (c) the c/a ratio and $FWHM$; and (d) Crystallite sizes obtained from Scherrer equation followed by XRD and AFM rms surface roughness as a function of deposition temperatures – T_d ranging from RT to 750 °C, of the MgO/FePt (35 nm) thin films deposited from Fe₅₀Pt₅₀ target, at 2 Hz, at laser fluence 5 J.cm⁻².

been found when increasing T_d from 600 °C to under 700 °C, at which the shape of the L₁₀ (200) orientation at 47.38° is mostly gaussian distribution revealing the purity of L₁₀ (200). As the T_d goes beyond above 700 °C, a significantly augmented intensity is observed at the positions of orientations corresponding to L₁₀ (001) at 24.02° and L₁₀ (003) at 77.15°. Moreover, at the peak position of L₁₀ (002) at 49.28°, a shoulder on the peak (not fully gaussian) indicates that there is coexistence of the two reflections of L₁₀ (002) and L₁₀ (200) (or maybe minor phase of A1-FePt) demonstrating not a fully ordered single phase but a signature of perpendicular alignments of c axis of L₁₀-FePt film. The formation of A1 phase low T_d and even at RT, could be attributed to the sufficiently high energy FePt particles of about 100 eV [192] deposited during the PLD process. Such energetic FePt particles can implant through the MgO substrate surface a few monolayer in the so-called process of subplantation [191,222]. Thus, the FePt can be grown in a disordered state to form A1-FePt phase. High T_d above 700 °C helps transformation from disordered state of A1-FePt phase to ordered state of L₁₀-FePt more efficiently. The maximum T_d of 750 °C in this work may not be sufficiently high enough to promote a fully ordered single phase of L₁₀-FePt.

Figure III.23b shows the S and LOF parameters as a function of deposition temperatures – T_d , from XRD patterns. At low $T_d \leq 500$ °C, because of the major disordered phase of A1-FePt, the samples have not revealed any signature of fundamental L₁₀ (002) orientation or the L₁₀ (001) superlattice peak, which leads the deducted S parameter is about zero. Ordered state starts at around 600 °C with S value of ~0.25. A nonlinear development in S parameter is observed above 600 °C. This S value achieves a

Tuan NGUYEN VAN | Thèse de doctorat | Université de Limoges | 7 Mai 2021 64
Licence CC BY-NC-ND 3.0

maximum value of about ~ 0.79 at 750°C due to the rapid increase of diffusion length leading to strong signature of $\text{L1}_0\text{-FePt}$ ordered phase. This maximum value is under the value of 0.95 at $\sim 780^\circ\text{C}$ in island-like microstructure FePt films reported by others [123,130]. This observation indicates that the deposition temperature of 750°C falls under the optimum T_d to achieve fully ordered FePt granular films. In a similar way, the LOF parameter at low $T_d \leq 500^\circ\text{C}$, is of negative value suggest that the deposited films form other preferential orientations (in this case, it is A1-FePt or $\text{L1}_0(200)$) rather than $(00l)$ orientations of $\text{L1}_0\text{-FePt}$ phase, which is in good agreement with direct analysis of XRD patterns shown in Figure III.23a. The samples start to achieve preferentially $(00l)$ reflections of $\text{L1}_0\text{-FePt}$ phase, reflected by positive values of LOF parameter, from 600°C . Almost the same tendency of increase in LOF parameter as S value has been seen for sample deposited at higher $T_d \geq 600^\circ\text{C}$. The quantification of LOF provide a useful parameter in showing the ordered state of FePt film become better and better as a function of deposition temperatures in the investigated range from RT to 750°C .

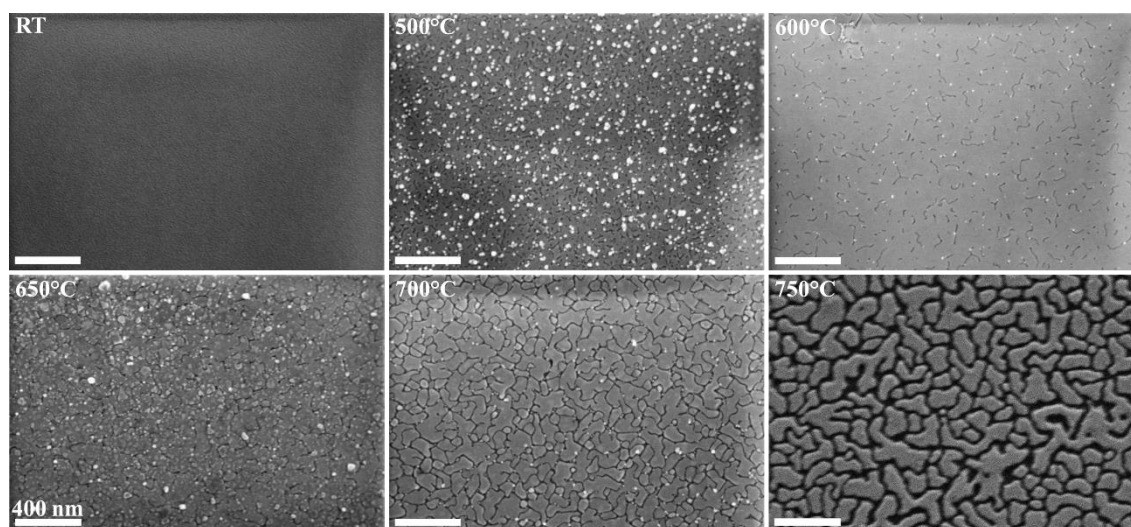


Figure III.24: The evolution in microstructure observed from SEM plan-view as a function of deposition temperatures ranging from RT to 750°C , of the MgO/FePt (35 nm) thin films deposited from $\text{Fe}_{50}\text{Pt}_{50}$ target, at 2 Hz, at laser fluence 5 J.cm^{-2} .

Further details in structural properties of deposited films are presented in Figure III.23c, at which the c/a ratio and $FWHM_{(001)}$ of the $\text{L1}_0\text{-FePt}$ phase are given. At 600°C and above, the c/a ratio and $FWHM_{001}$ decrease with increasing deposition temperatures – T_d . The c/a ratio approaches the theoretical c/a value of fully ordered $\text{L1}_0\text{-FePt}$ phase, reflecting a significant transformation of A1 phase to L1_0 phase when T_d increases. The c/a ratio is about ~ 1.0 at 600°C showing the dominant of A1 phase, and falls to ~ 0.97 at 750°C showing the majorly transformed A1 phase to L1_0 phase. Meanwhile, the $FWHM_{(001)}$ reduces about $\sim 88\%$ globally from $\sim 4^\circ$ at 600°C to $\sim 0.5^\circ$ at 700°C . These observed results are in good agreement with increasing proportion of major $\text{L1}_0\text{-FePt}$ phase at higher T_d shown above (as evidenced from XRD patterns in Figure III.23a, S and LOF parameters in Figure III.23b). The additional crystallite size – D_{Scherrer} , in the out-of-plane direction, as a function deposition temperature was estimated from XRD patterns presented in Figure III.23a. When T_d rises up, the calculated D_{Scherrer} increases nearly eight folds globally from $\sim 1.9 \text{ nm}$ to $\sim 17.5 \text{ nm}$ at 600°C and 700°C respectively.

The granular FePt films are observed on heated MgO substrates at elevated temperatures while continuous fashion is promoted through low deposition temperature, or films with high thickness [131,132,134]. In this work, films developed at deposition temperatures lower than 600°C have microstructures governed by densely filled and continuous patterns with some rack of spaces inside the patterns as depicted in Figure III.24. As the T_d increased to 650°C such continuous one started breaking

into connected platelet-like grains. The procedure of separated films become evident for films deposited at 700°C and above. Finally, the granular-like microstructure of multiple islands is formed. The rms roughness increases with temperatures, but it is lower than 5 nm.

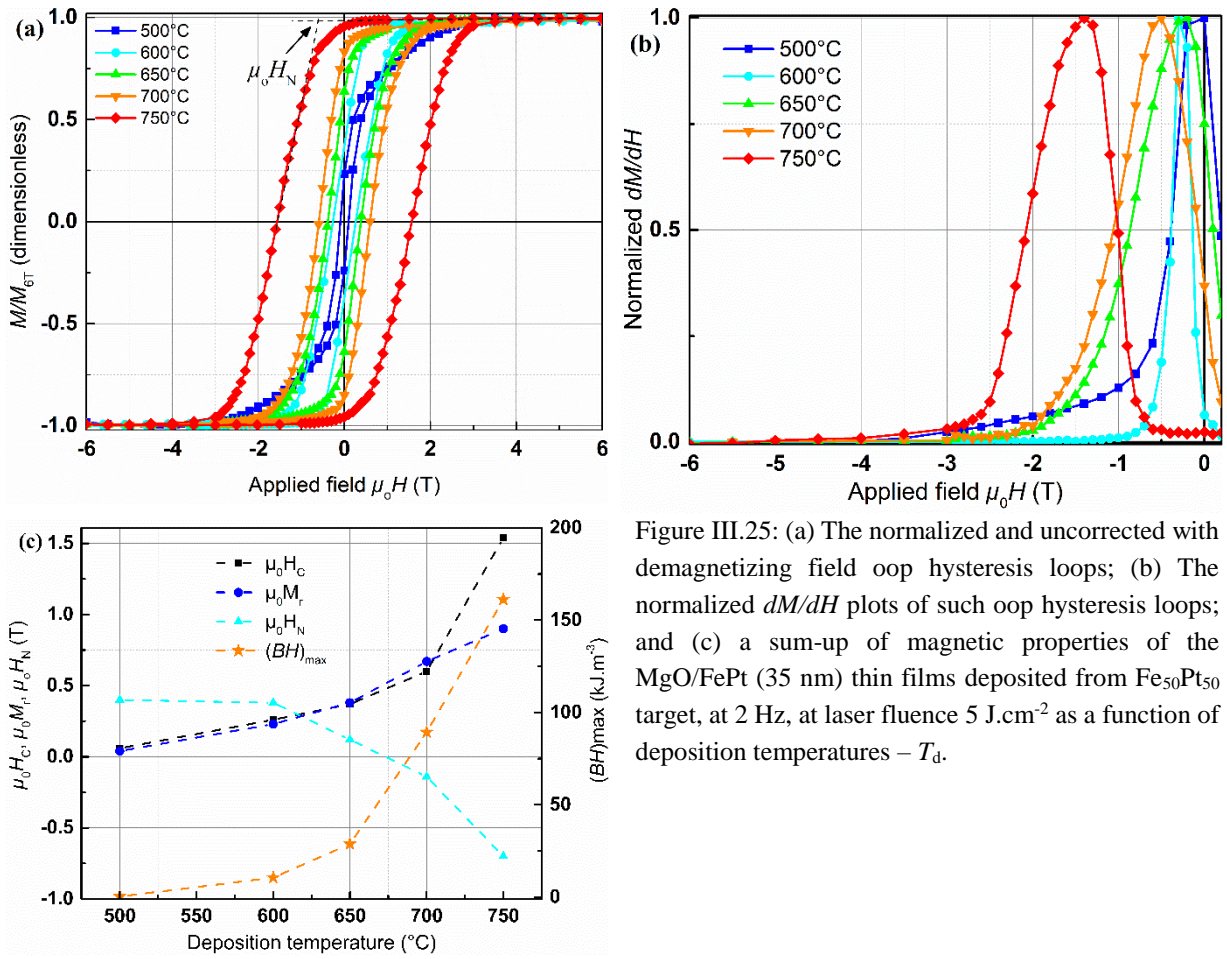


Figure III.25: (a) The normalized and uncorrected with demagnetizing field oop hysteresis loops; (b) The normalized dM/dH plots of such oop hysteresis loops; and (c) a sum-up of magnetic properties of the MgO/FePt (35 nm) thin films deposited from Fe₅₀Pt₅₀ target, at 2 Hz, at laser fluence 5 J.cm⁻² as a function of deposition temperatures – T_d .

Figure III.25a presents oop hysteresis loops of the 35 nm FePt films deposited on MgO 001) substrate at various deposition temperatures – T_d . The overall sharpness of the $M(H)$ hysteresis curves as it reaches coercivity becomes when T_d decreases from 750°C to 500°C. All films exhibit one single-magnetic phase behavior, which is certainly demonstrated by single peaks at close to coercive field, as indicated in normalized dM/dH plots in Figure III.25b. Film fabricated at low $T_d = 500^\circ\text{C}$ (or RT, do not show here) is magnetically soft due to relatively low magnetocrystalline anisotropy of the disordered A1-FePt phase (discussed in Figure III.23). Higher $T_d \geq 650^\circ\text{C}$ significantly enhances magnetic properties of the films due to major L1₀ hard magnetic phase, as illustrated in Figure III.23. Increase in T_d induces improvement in all coercivity - $\mu_0 H_c$, remanence - $\mu_0 M_r$, magnetic energy product – $(BH)_{max}$ (after being corrected with demagnetizing field of demagnetizing factor $N = 0.73$), as shown in Figure III.25c. Not only the $\mu_0 H_c$ steadily develops, but also the $\mu_0 M_r$ constantly grows when T_d increases. The $(BH)_{max}$ depicts a robust increase due to the nonlinear dependence on $\mu_0 M_r$ for hard, and on both $\mu_0 M_r$ and $\mu_0 H_c$ for soft magnetic thin films. In order to comprehend better magnetization process of the deposited films, a new parameter has been introduced, which is often called the nucleation field – $\mu_0 H_N$, at which the magnetization starts to fall with decreasing magnetic field after being saturated or technically is defined at the cross point by extrapolating the values of saturation magnetization and the tangent of the coercivity (presented in Figure III.25a). Dependence of the nucleation field on deposition temperatures is interpreted in Figure III.25c. The tendency of $\mu_0 H_N$ is logical with the variation in the degree of order. Positive values

of $\mu_0 H_N$ present poor magnetic properties of the films. While the continuous films allow the switching throughout the film by nucleation of one reversed domain (and inducing the left domains) at low applied field, the multiple interconnected islands films inhibit such switching of magnetization reversal through domain wall motion and thus magnetic properties (i. e., coercivity) are augmented. This microstructural effect will be more visible in section III.4 describing the behavior of FePt processed by RTP.

III.3.3. MgO versus Si/SiO₂ substrates (towards to silicon compatibility)

In this section, the effect of used substrates on structural, microstructural and magnetic properties of the FePt films will be revealed and compared. 35 nm FePt film was deposited from the Fe₅₀Pt₅₀ target, on Si/SiO₂ (100nm), at 750°C, at 2 Hz, at laser fluence 5 J.cm⁻². These parameters are chosen as optimal parameters obtained from films on MgO substrate.

Figure III.26a compares the XRD patterns of a couple of films fabricated on both substrates. The peaks from L1₀ – FePt together with peaks from substrates are both indexed. While film deposited on MgO substrate depicts strong intensity of (00*l*) reflections of L1₀ – FePt with a minor signature of L1₀ (200) and/or maybe be A1 – FePt phase (as discussed in section III.3.2), film deposited on Si substrate exhibits weaker intensity of (00*l*) reflections of L1₀ – FePt and an additional (111) orientation. In terms of *S* and *LOF* parameters, the values for film on MgO are both slightly higher compared to the ones deducted from film on Si. The *c/a* ratio and *FWHM*₍₀₀₁₎ for film on Si are both higher compared to values from MgO. Note that the {111} close-packed planes have the lowest surface free energy among the other planes. These differences can be attributed to the variation in substrate nature, e. g., while the lattice mismatch between MgO and L1₀ – FePt is about 10 %, Si substrate is of 100 nm amorphous SiO₂, which can act as a free buffer layer and give rise for L1₀ – FePt growing freely. Additionally, the variation in substrate nature in MgO induces huge difference of four folds higher in coefficient thermal expansion compared the value in Si [223], which further preserve the tensile stress of FePt film during the growth and favor the *c*-textured (on MgO) as a result. This effect will be discussed in details in section III.4.

Figure III.26b presents the plane-view microstructure of film deposited on Si substrate showing compact isolated island patterns. These isolated islands are well defined with arbitrary shape throughout the film surface, with an average size below 100 nm, while microstructural patterns on MgO disclosed a multiple-isolated island microstructure with size of such islands rising up to nearly ~1 μm (as illustrated in Figure III.24). An estimate for FePt grain density (the number of FePt grains/area) for film on Si ~722 grains/μm² is considerably higher than that of ~31 grains/μm² on MgO.

The magnetic properties of oop *M(H)* curves of the two films on MgO and Si substrate are compared in Figure III.26c. Though the couple of films display single magnetic phase behaviors, the overall loop shape for film on Si is a little poorer than that of film on MgO. While coercivity of the both films are comparable of around ~1.5 T, the remanence ratio *M*_{OT}/*M*_{6T} for film on Si (~0.85) is relatively lower than value of ~0.95 for film on MgO. And again, the nucleation field of film on MgO (~ -0.7 T) is about two folds better than ~ -0.3 T obtained from film on Si, which suggests that the magnetization reversal in film on Si occurs sooner than that of film on MgO. The slight lowness in magnetic properties of film on Si may be ascribed to the fact that the film was not well crystallized and did not have a fully *c*-textured, as indicated in Figure III.26a. Owing to the comparable magnetic properties for FePt films on MgO and Si/SiO₂, experiments conducted hereafter concerning films, stacks of NPs, nanocomposites will be on Si/SiO₂ (100 nm).

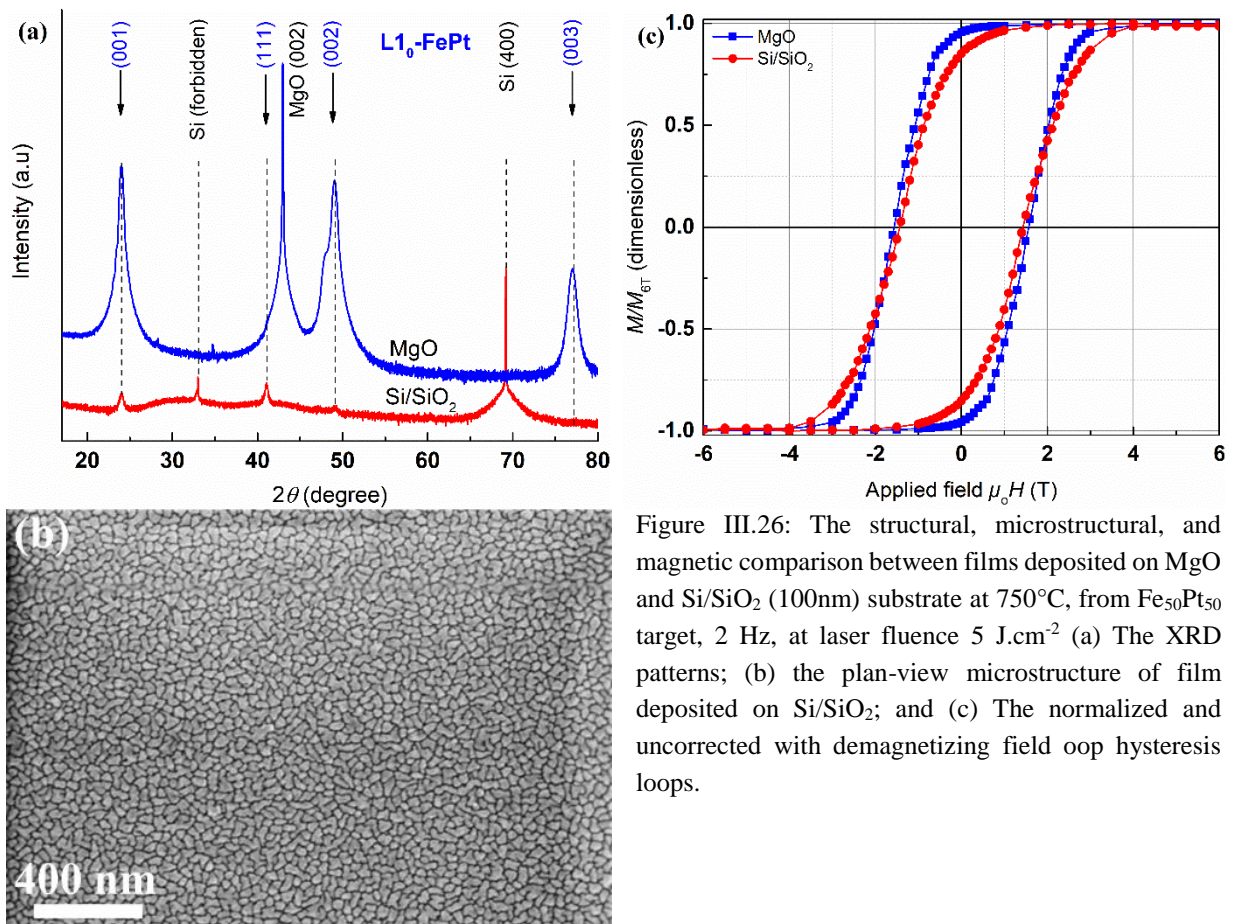


Figure III.26: The structural, microstructural, and magnetic comparison between films deposited on MgO and Si/SiO₂ (100nm) substrate at 750°C, from Fe₅₀Pt₅₀ target, 2 Hz, at laser fluence 5 J.cm⁻² (a) The XRD patterns; (b) the plan-view microstructure of film deposited on Si/SiO₂; and (c) The normalized and uncorrected with demagnetizing field oop hysteresis loops.

III.4. As-deposited FePt matrix with RTP

To provide additional degrees of freedom in fabricating good hard magnetic FePt films and further embedding NPs in the matrices to create nanocomposites with limited diffusion, a series of nominal 15 nm single layer FePt thin films will be deposited on silicon substrate at RT (nominal configuration of Si (100)/SiO₂ (100 nm)/FePt (15 nm), base pressure of 1×10^{-6} mbar, laser fluence of 5 J.cm⁻², laser repetition rate of 2 Hz, from an equiatomic alloy FePt target). The nominal thickness of 15 nm FePt is to avoid the continuous thin films (induced during RTP), which will be shown in section V.2. The Fe/Pt atomic ratio of the deposited film is around ~ 0.87 (approved by multiple iterations from EDS). The use of a single alloy target is supposed to reduce the effective annealing time, which might be a good option as anneal the nanocomposite. In this part, various RTP conditions are applied. The RTP procedure was schematically shown in previous section III.2, in Figure III.12, at a constant ambient pressure of 1×10^{-1} mbar of Argon flow, and various annealing conditions by changing the annealing temperatures – T_a (°C), heating rates (°C/s), and annealing time (s).

III.4.1. Annealing temperatures

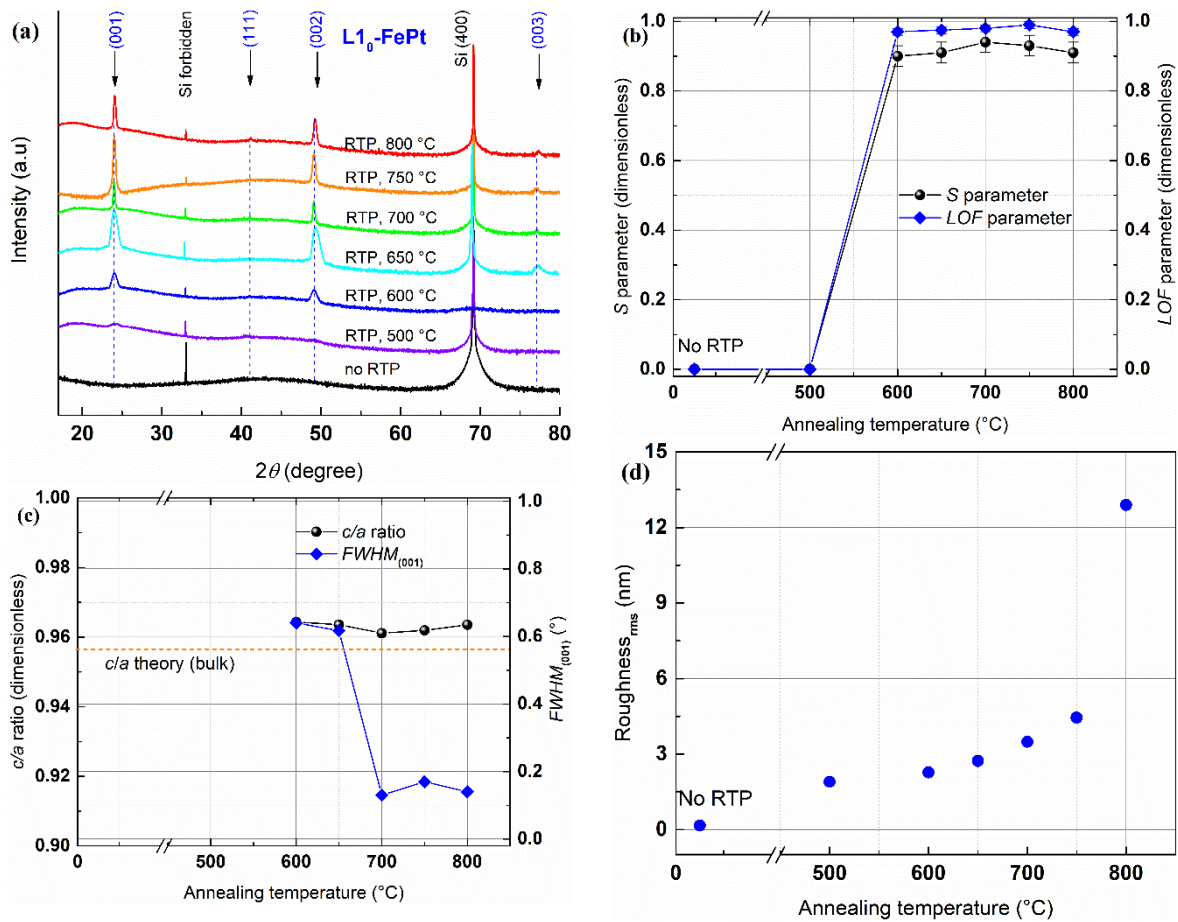


Figure III.27: The evolution in (a) structure (XRD patterns); (b) the S parameter and the LOF parameter; (c) the c/a ratio and $FWHM$; and (d) AFM rms surface roughness of the as-deposited sample and annealed samples at 50 °C/s, in 60 s, and in 1×10^{-1} mbar of Ar flow as a function of annealing temperatures – T_a .

A set of 15 nm FePt thin film was firstly subjected inside the RTP system at various annealing temperature – T_a from 500 °C to 800 °C, in a fixed annealing time of 60 s, and with a constant heating rate of 50 °C/s, which is above the reported heating rate (30 °C/s) for well crystallization of long range order FePt [224]. Figure III.27a compares the XRD patterns of as-deposited and annealed samples at various temperatures. In all presented patterns, the Si (400) along with its forbidden orientation from the substrate is indexed. The as-deposited sample does not show any peaks of signature of FePt crystallization, which is different with film deposited at the same condition on MgO substrate showing (200) reflection from disordered A1-*fcc* phase [123]. Up to an annealed temperature of 500 °C, only peaks from substrate are shown. Perhaps due to the crystallization occurring in a very short range, reflections of either A1 or $L1_0$ -FePt-*fcc* phase do not appear. Increasing T_a to 650 °C leads to pronounced *c*-textured (00 l) reflections from $L1_0$ -FePt with broaden orientations of (001) and (002). This broaden reflection could be attributed to the mixture A1 and $L1_0$ -FePt phases. The simultaneous appearance of the both phases illustrate the transformation from disordered A1 to ordered $L1_0$ phases concerning first order phase transition while inducing the tensile stress [225]. A surged intensity and sharper peaks (the degree of oop orientation) are observed at the position of the superlattice- $L1_0$ (001) and fundamental- $L1_0$ (002) peaks for all samples annealed at above 650 °C, indicating that a majority/superiority in fraction of ordered $L1_0$ phase exists in the films. This confirms that the highly ordered or even single phase $L1_0$ -FePt phase is strongly induced by the current annealing conditions from 700 °C. The annealed films here do not possess very flat surfaces characterized by satellite peaks around either fundamental and superlattice reflections [225].

The *LOF* and *S* parameters for the annealed samples calculated from XRD diffractograms are graphed as a function of T_a in Figure III.27b, in which they are of the same tendency. The *LOF* and *S* at low $T_a \leq 500$ °C reveals a random oriented corresponding to 0 value. The ordering starts right after above T_a of 500 °C, and a rise in both *LOF* and *S* is observed clearly, i. e., the *LOF* is about 0.97 at 600 °C, while *S* is around 0.90. These parameters remain high at a constant in the range $T_a \sim 600^\circ\text{C} - 750^\circ\text{C}$. These values are comparable with what obtained from other works in either a granular FePt thin films directly crystallized on MgO substrate at ~ 780 °C [123,130], or in a post annealing approach at 800 °C on glass substrate [225], and at 700 °C on Si substrate [224]. Figure III.27c depicts the axial *c/a* ratio extracted from *S* parameter depending on the T_a . A tetragonal distortion slightly shifted towards that of the fully ordered L1₀-FePt bulk material (orange dotted line) has been seen, which is well agreed with high *S* value of long range order in the nearly equiatomic compositional film [226]. It suggests that tensile ip stress favors the *c*-textured grains [143,225] with *c* longer axis being out-of strain direction or preferentially perpendicular to the film plane [223]. Taking into account the difference in thermal expansion coefficient between the Si/SiO₂ substrate ($2.5 \times 10^{-6} \text{ K}^{-1}$) and the FePt thin film ($10.5 \times 10^{-6} \text{ K}^{-1}$), the stress appeared in the system is given by [223] $\sigma = E\Delta\alpha\Delta T / (1 - \mu)$, where *E*, $\Delta\alpha$, ΔT and μ represent the elastic modulus of the film ~ 180 GPa, the change in thermal expansion factor of thin film and substrate, the variation between RT and annealing temperature, and the Poisson's ratio ~ 0.33 . It can be seen that the stress is of a positive value under the annealing conditions and linearly proportional to T_a , which means that the FePt film is in traction to withstand the thermal stress in the system and leads to the strongly *c*-textured orientation (as indicated in Figure III.27a) [223]. Note that the tensile stress strongly depends on which kind of substrate and how much the thickness of the under/buffer layer in use due to the thermal expansion coefficient related via the light absorption during the annealing process. The Full Width at Half Maximum (*FWHM*) of the (001) peaks fitted by Woldemar Voigt profile (Voigt function) as a function of T_a is given in Figure III.27c. At low T_a (< 650 °C), the *FWHM* is of comparable value of ~ 0.6 °, while this value plunges quickly to about ~ 0.2 ° at higher T_a (≥ 700 °C) and further increasing T_a no longer affects the *FWHM*. These values are equivalent to the *FWHM* values obtained from epitaxial FePt film grown onto expensive single crystal substrates [224,227]. The variation in *FWHM* demonstrates sensible change in both stress-strain and microstructure (will be indicated more details in Figure III.28) accumulated in the film, and convinces that the transformation from A1 phase to L1₀ phase is not completed at $T_a < 700$ °C until higher T_a is reached.

Figure III.28 presents a very distinctive evolution in surface morphologies of the as-deposited and annealed samples, probed by AFM and SEM, with respect to the T_a . Plane-view AFM image of film in an as-deposited state shows a very flat continuous surface with very low rms roughness. By applying heat treatment to the samples, the surface morphologies start changing significantly depending on T_a . At $T_a = 500$ °C, annealed sample forms small grains on the surface, while higher T_a leads to a drastic variation in microstructure from connected platelet-like grains spreading over the film surface ($T_a = 600$ °C and 650 °C) to granular fashion with completely separated islands ($T_a = 700$ °C – 800 °C), as shown in by AFM and SEM images. At $T_a = 600$ °C, some small holes appear and break the continuous film surface. These holes start expanding and increasing in density, making the continuous remaining films divided into smaller islands ($T_a = 650$ °C) but still connected one to each other. Though the distinct like-island microstructure, at higher T_a (700 °C – 800 °C), are co-observed, they have some distinct features.

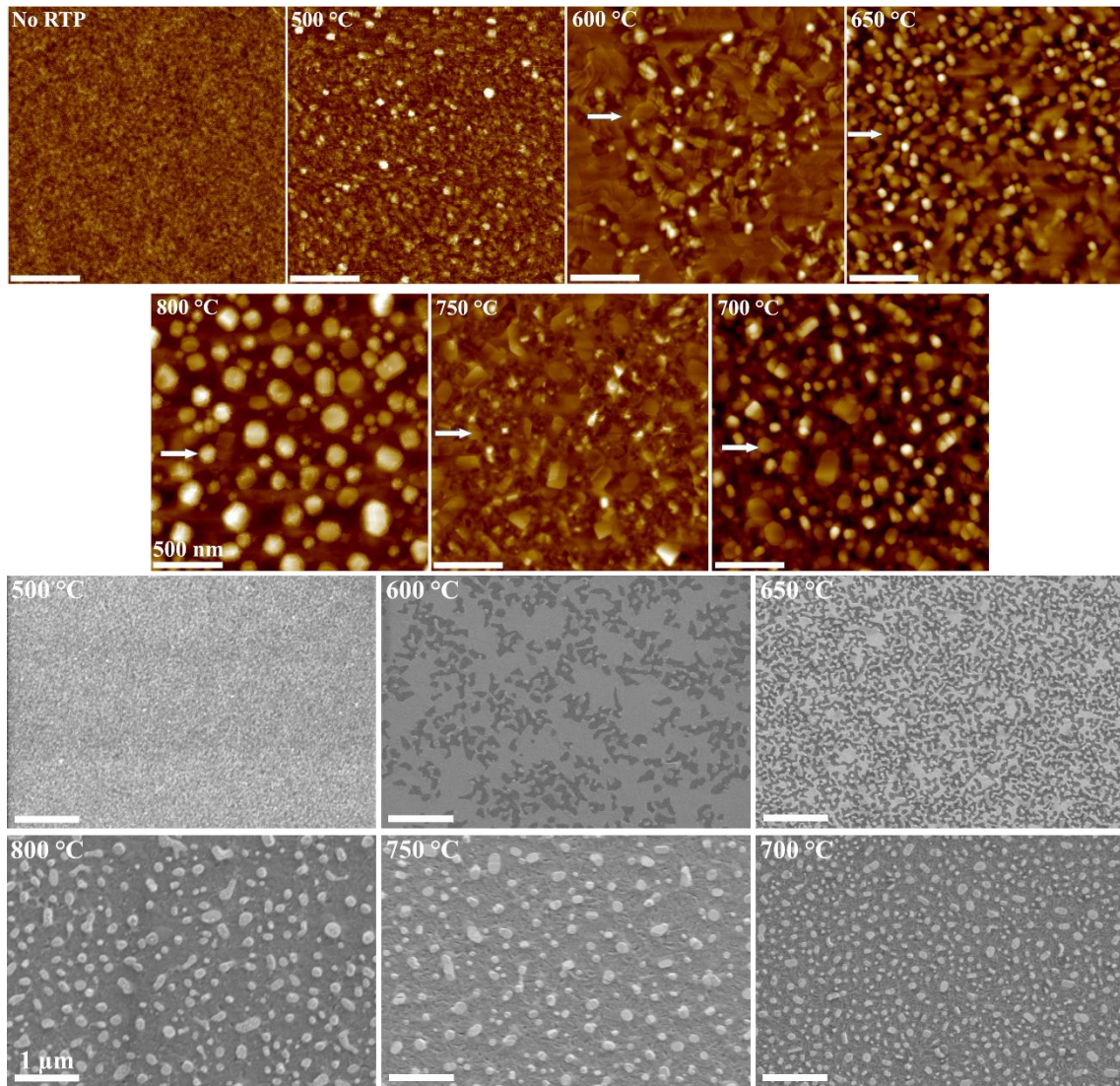


Figure III.28: The evolution in microstructures of annealed samples (at 50 °C/s, in 60 s) as a function of T_a for two kinds of equivalent characterizations AFM and SEM.

The AFM confirms that at either $T_a = 700$ °C or 750 °C, single grain has a flatter surface compared to those of rougher grains at higher T_a of 800 °C (Figure III.28, AFM). The rms surface roughness is approximately linear increase with T_a (500 °C – 750 °C from 1.9 nm – 4.5 nm) and jumps to 13 nm at $T_a = 800$ °C (as evidenced in Figure III.27d), which is coherent with the evolution in surface microstructures of continuous to granular films. A SEM estimation for this series of annealed films indicated a significant reduction in grain density when increasing T_a . At $T_a = 700$ °C the grain density is about 33.6 grains/ μm^2 , this value reduces to 15.6 grains/ μm^2 and 11.3 grains/ μm^2 at $T_a = 750$ °C and 800 °C respectively. Moreover, the coverage ratio (area covered percentage) plummets from 100% ($T_a = 500$ °C) to $\sim 40\%$ ($T_a = 650$ °C) and latter decreases to $\sim 17\%$ ($T_a = 700$ °C) and $\sim 15\%$ ($T_a = 800$ °C). The rms surface roughness, grain density, and coverage ratio of such films is in agreement with observation in AFM and SEM for all continuous, interconnected island, and granular microstructures. The variation in microstructure with respect to T_a can be understood through the solid-state dewetting of (FePt) alloy like-metal films at which the melting point (1500 °C) occurs at well far exceed $T_C \sim 477$ °C [7]. The driving physical mechanism for this dewetting lies in the minimization of the total energy between the substrate, thin film and their interface. Other approaches have been made to prevent the dewetting during the RTP process by introducing a buffer layer of Ag, which allows to keep the coercivity of the FePt thin film while the

continuous film is preserved without forming the granular structure [228]. With a remarkable variation in granular microstructure of films annealed at 700 °C, 750 °C, and 800 °C, all films exhibit random shape and various broad grain size distribution as depicted in the histogram in Figure III.29a. At $T_a = 700$ °C film produces single modal grain size distribution ($73 \text{ nm} \pm 10 \text{ nm}$), while at higher T_a of 750 °C and 800 °C films reveal tri-modal ($27 \text{ nm} \pm 2 \text{ nm}$; $83 \text{ nm} \pm 9 \text{ nm}$; $210 \text{ nm} \pm 60 \text{ nm}$) and bi-modal ($21 \text{ nm} \pm 2 \text{ nm}$ and $84 \text{ nm} \pm 10 \text{ nm}$) grain size distribution respectively. This multiple-modal grain size distribution at $T_a \geq 750$ °C could be attributed to the rougher surface of the underlying layer of SiO_2 induced by RTP procedure as happened on MgO [229].

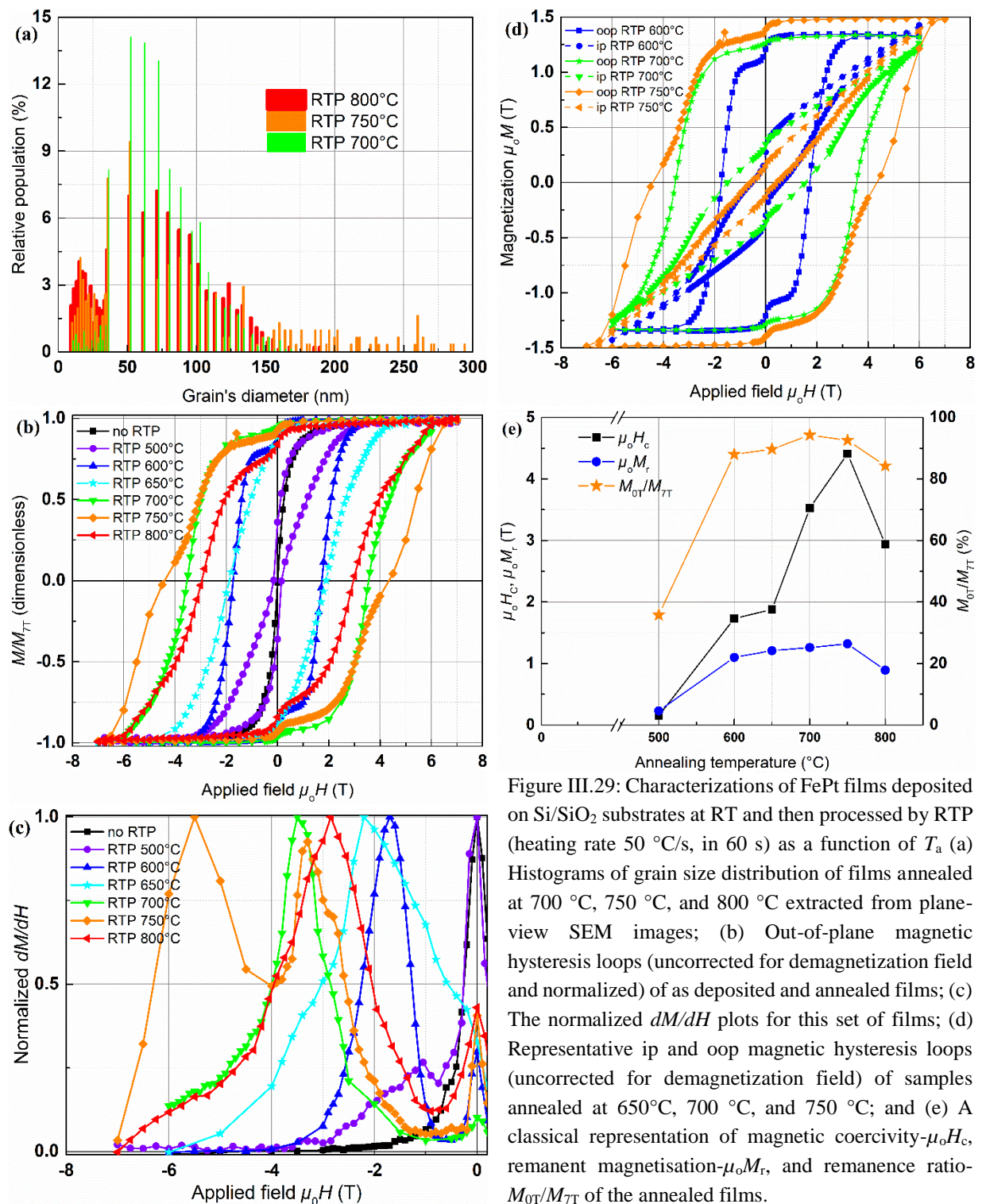


Figure III.29: Characterizations of FePt films deposited on Si/SiO₂ substrates at RT and then processed by RTP (heating rate 50 °C/s, in 60 s) as a function of T_a (a) Histograms of grain size distribution of films annealed at 700 °C, 750 °C, and 800 °C extracted from plane-view SEM images; (b) Out-of-plane magnetic hysteresis loops (uncorrected for demagnetization field and normalized) of as deposited and annealed films; (c) The normalized dM/dH plots for this set of films; (d) Representative ip and oop magnetic hysteresis loops (uncorrected for demagnetization field) of samples annealed at 650°C, 700 °C, and 750 °C; and (e) A classical representation of magnetic coercivity- $\mu_0 H_c$, remanent magnetisation- $\mu_0 M_r$, and remanence ratio- M_{0T}/M_{TT} of the annealed films.

Uncorrected for demagnetizing field and normalized oop magnetic hysteresis curves of a set of films annealed at various T_a are compared in Figure III.29b and the evolutions in μ_0H_c , μ_0M_r , and M_r/M_{7T} ratio with T_a are plotted in Figure III.29e. It is not surprising that as-deposited and annealed films at 500 °C have the poorest magnetic properties due to lack of hard magnetic L1₀ phase as indicated in XRD (Figure III.27a). Further going up T_a drives effectively the augmentation in magnetic properties, and the optimal properties of $\mu_0H_c \sim 4.4$ T, $\mu_0M_r \sim 1.3$ T, and $M_{0T}/M_{7T} \sim 0.93$ are obtained at $T_a = 750$ °C. Exceeding this T_a leads to poorer magnetic properties of all coercivity, remanent magnetisation, remanence ratio M_{0T}/M_{7T} . All films in this set, however, show at least two-phase magnetic behavior. In addition, a growth in μ_0H_c , μ_0M_r is clearly seen in Figure III.29c, at which the ip and oop magnetic hysteresis loops (absolute scale) are drawn. The easy axes of magnetization for the annealed films are perpendicular to the film planes corresponding to preferential *c*-texture films, which are coherent with XRD patterns. Increasing T_a not only induces the strong *c*-textured magnetic properties but also enhances the magnetic anisotropy constant- K_U and magnetocrystalline anisotropy- μ_0H_A (linearly extrapolated from ip and oop $M(H)$ loops, where $H_A = 2K_U / \mu_0M_S$). In this study, M_S is considered as M_{7T} from ($K_U = 2.9$ MJ.m⁻³, $\mu_0H_A = 5.4$ T) at 650°C, ($K_U = 3.4$ MJ.m⁻³, $\mu_0H_A = 6.3$) at 750 °C to ($K_U = 4.0$ MJ.m⁻³, $\mu_0H_A = 6.8$ T) at 750 °C. These values slightly fell short of theoretical values of the L1₀-FePt phase [7,18] indicating that good properties of the films are obtained in the optimal annealed RTP conditions. The lower magnetic properties (i. e., coercivity) for films annealed at $T_a < 700$ °C are attributed to both lack of fully ordered L1₀ phase and observed coarsening microstructure giving rise to reversed domains to freely move throughout the whole films. The better magnetic properties achieved for annealed films at 800 °C $\geq T_a \geq 700$ °C are referred to completely ordered L1₀ phase and granular microstructure possibly confining domain wall motion within a grain caused the grain to switch independently from others, prohibiting the switching of the entire films [230]. Further drop corresponding to higher $T_a \geq 800$ °C might originate from either formation of oxidation or FePt₃, which is not visible owing to existing at very short-range order of such phases [123].

III.4.2. Heating rate influence

A series of films was applied by other heat treatment recipe, for which the T_a was remained at 750 °C, in 60 s, at various heating rates (as the optimal parameter to obtain good magnetic properties indicated in section III.4.1). The XRD patterns of these annealed films are shown in Figure III.30a. In the invested heating rate range from 10 °C/s to 100 °C/s, all films show preferential out-of-plane crystallographic *c*-axis texture of (00 l) orientations, in which both (001) and (002) peaks are visible. Concerning peaks from (003) reflections, the relatively highest intensity is for film annealed at 10 °C/s, while others are gradually decreased as increasing heating rates and disappeared in film annealed at 100 °C/s. The S , LOF parameters, c/a ratio, and $FWHM$ estimated from XRD patterns are all compared in Figure III.30b and Figure III.30c. The S , LOF parameters and c/a ratio are constant, however the $FWHM$ is higher for the sample annealed at 10°C/s ($FWHM \sim 0.25^\circ$), compared with others at 100°C/s ($FWHM \sim 0.13^\circ$). In all cases, the c/a ratios are all larger than the bulk one. It is suggested that these parameters are independent of the heating rates owing to no major variation in the XRD patterns. These parameters strongly depend on the oop *c*-texture of the L1₀ phase, which is substantially replied upon by the tensile stress induced by RTP as shown above. Based on the same assumption as others, it is noteworthy that the residual stress under annealing conditions with heating rates 20 °C/s – 100 °C/s is about 2.5 °C/s – 3.5 GPa [225].

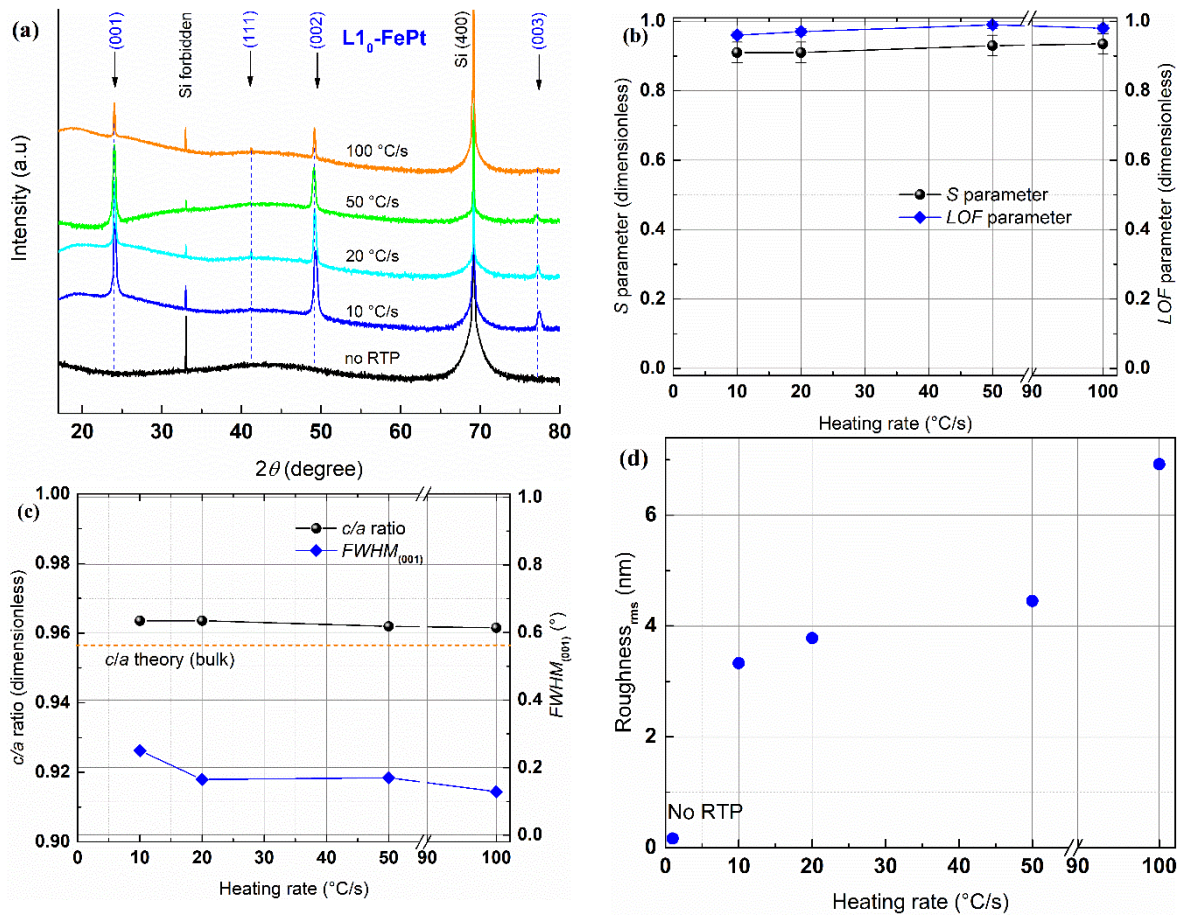


Figure III.30: The evolution of (a) structure (XRD patterns); (b) the S parameter and the LOF parameter; (c) the c/a ratio and $FWHM$; and (d) rms roughness of the as-deposited sample and annealed samples at $750\text{ }^{\circ}\text{C}$, in 60 s, and in 1×10^{-1} mbar of Ar flow as a function of heating rates.

Though the influence of changing heating rate has not been seen clearly from structural examination, it unquestionably imitates the surface morphologies of the samples. Figure III.31 exhibits a microstructural analysis for annealed FePt films, for which the AFM shows a structural analysis for FePt films accomplished at the film surfaces by and later approved microstructural transformation in grain size. The microstructure is transformed from interconnected island to entirely isolated islands with respect to heating rates from $10\text{ }^{\circ}\text{C/s}$ to $100\text{ }^{\circ}\text{C/s}$ respectively. The rms surface roughness of films increases by two folds of magnitude from 3.3 nm when flowing the heating rate from $10\text{ }^{\circ}\text{C/s}$ to $100\text{ }^{\circ}\text{C/s}$, which is consistent with the AFM and SEM data for variation of grain size. The SEM- Inlen mode image (Figure III.31, at $100\text{ }^{\circ}\text{C/s}$) offers some normal (gray) together with some irregular (white) FePt grains, at which gray FePt grains are typically lower height in the z direction, while white FePt grains are higher for film annealed at $100\text{ }^{\circ}\text{C/s}$. A gradual tumble in intensity has been observed for well-defined granular island samples (at higher heating rates). A profound estimation from SEM images exhibits that films annealed at $50\text{ }^{\circ}\text{C/s}$ displays tri-modal grain size distribution as discussed above, and others at $20\text{ }^{\circ}\text{C/s}$ and $100\text{ }^{\circ}\text{C/s}$ show $\sim 100\text{ nm} \pm 13\text{ nm}$ and $82\text{ nm} \pm 11\text{ nm}$ respectively. The film annealed at $10\text{ }^{\circ}\text{C/s}$ has island-like morphology, hence it is not a proper route to consider the grain size distribution. Furthermore, a decline in grain size density is also coarsely evaluated, e. g., a value of $13.2\text{ grains}/\mu\text{m}^2$ is at $20\text{ }^{\circ}\text{C/s}$ and reduces to $7.6\text{ grains}/\mu\text{m}^2$ at $100\text{ }^{\circ}\text{C/s}$. To date, these microstructural investigations demonstrate the pivotal roles of the annealing temperature accompanied by heating rates that discriminates the morphology of the FePt film without virtually adjusting the S , LOF parameters, c/a ratio, and $L1_0$ phase. Moreover, these analyses partly illustrate the distribution of residual stress during RTP through surface morphology evolution.

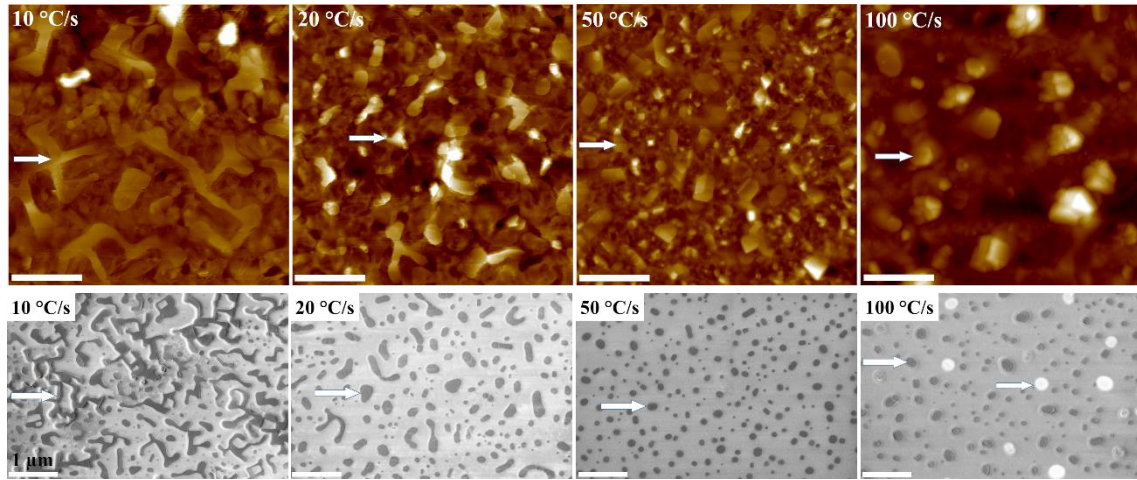
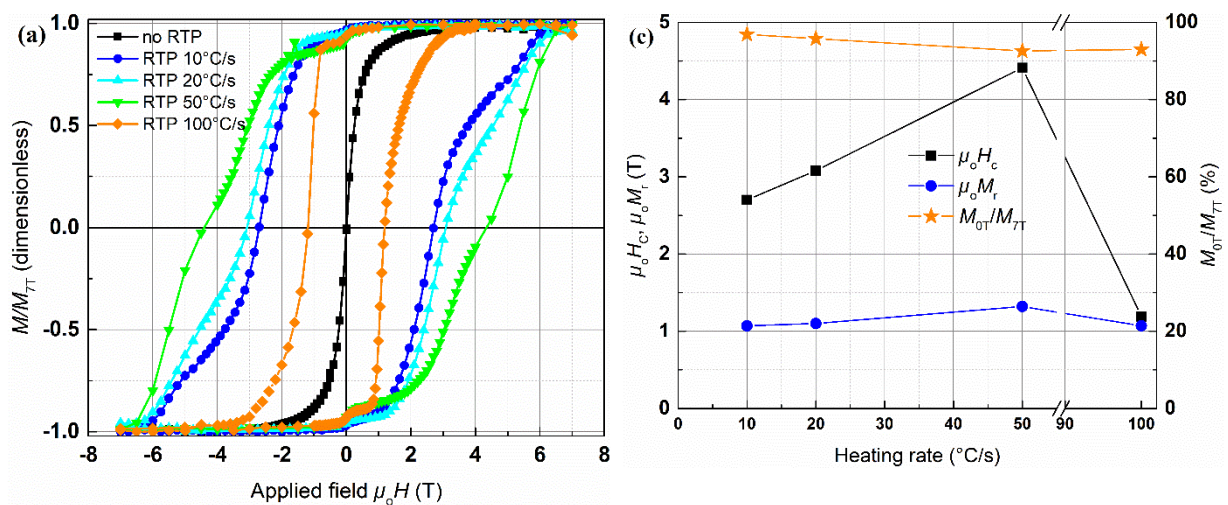


Figure III.31: The microstructures of annealed samples ($T_a = 750 \text{ }^\circ\text{C}$, in 60 s) as a function of heating rates, characterized by AFM and SEM. The scale bar in AFM images is 500 nm.

The corresponding oop magnetization curves of the films annealed at $750 \text{ }^\circ\text{C}$, 60 s, and at various RTP heating rates are presented in Figure III.32a. Note that these hysteresis loops are not corrected for demagnetization field and normalized with magnetisation at 7 T (M_{7T}). Figure III.32b is a sum-up of deduced $\mu_0 H_c$, $\mu_0 M_r$, and M_{0T}/M_{7T} of the annealed films. Coercivity is drastically augmented as increased RTP heating rates, i. e., from 2.7 T to 3.1 T at $10 \text{ }^\circ\text{C/s}$ and $20 \text{ }^\circ\text{C/s}$, respectively, and reaches a maximum of 4.4 T at $50 \text{ }^\circ\text{C/s}$. M_{0T}/M_{7T} ratio reduces from 97% at $10 \text{ }^\circ\text{C/s}$ to 93% at $50 \text{ }^\circ\text{C/s}$. The annealed films are of again multiple magnetic phase behaviors. For instance, sample annealed at $10 \text{ }^\circ\text{C/s}$ shows two-phase behavior, in which one phase with coercivity is at 2.7 T, and others is at ~ 4 T. Films annealed at $50 \text{ }^\circ\text{C/s}$ show three-phase behavior corresponding to coercivities at ~ 0 T, 3.5 T, and 5.5 T, which will lead to a broader switching field distribution followed by tri-modal grain size distribution (identified previously). These kinds of multiple phase behaviors can be definitely viewed from the first derivative of the $M(H)$ loop of dM/dH plot. The rise in $\mu_0 H_c$ and $\mu_0 M_r$ could be attributed to the fully ordered $L1_0$ phase and the change in morphology of granular films with a perfectly isolated island microstructure. A lower coercivity is obtained at lower heating rate due to the interconnected microstructure, which favors magnetization reversal through domain wall propagation [230]. Note that the drop in coercivity at $100 \text{ }^\circ\text{C/s}$ might be attributed to the irreversibly microstructural variation inducing a relaxation from elastic strain energy presented in the film [225].



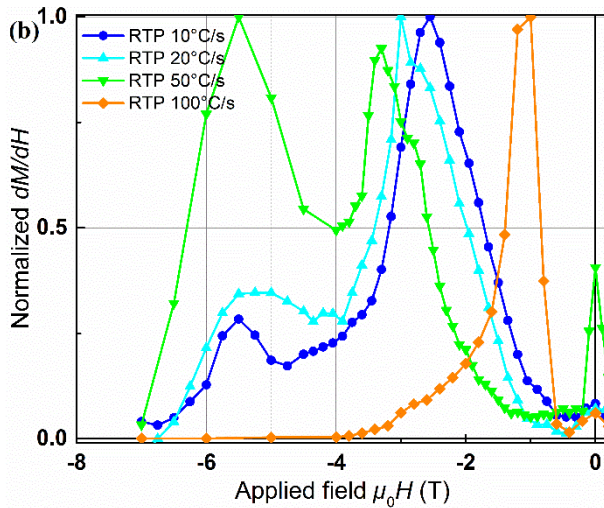


Figure III.32: Characterizations of FePt films deposited on Si/SiO₂ substrates at RT and then processed by RTP (at $T_a = 750$ °C, in 60 s) as a function of heating rates (a) Out-of-plane magnetic hysteresis loops (uncorrected for demagnetization field and normalised) of as deposited and annealed films; (b) The normalized dM/dH plots for this series of annealed films; and (c) A representation of magnetic coercivity- μ_0H_c , remanent magnetisation- μ_0M_r , and remanence ratio- M_{OT}/M_{TT} of the annealed films.

III.4.3. Effect of annealing time

In order to positively comprehend the importance of RTP conditions to the properties of annealed films, a final step of changing annealing time is considered. The other set of films was finally applied RTP heat treatment at 750°C, at 50°C/s, and in various annealing time. The annealed FePt films grown with an oop crystallographic c -textured reflections perpendicular with film planes, and diffraction reflections from other texture, i. e., (111) peaks barely observed, are compared in Figure III.33a, which is indicated by the predominance of the superstructure at 24.02° and fundamental reflections at 49.18° from

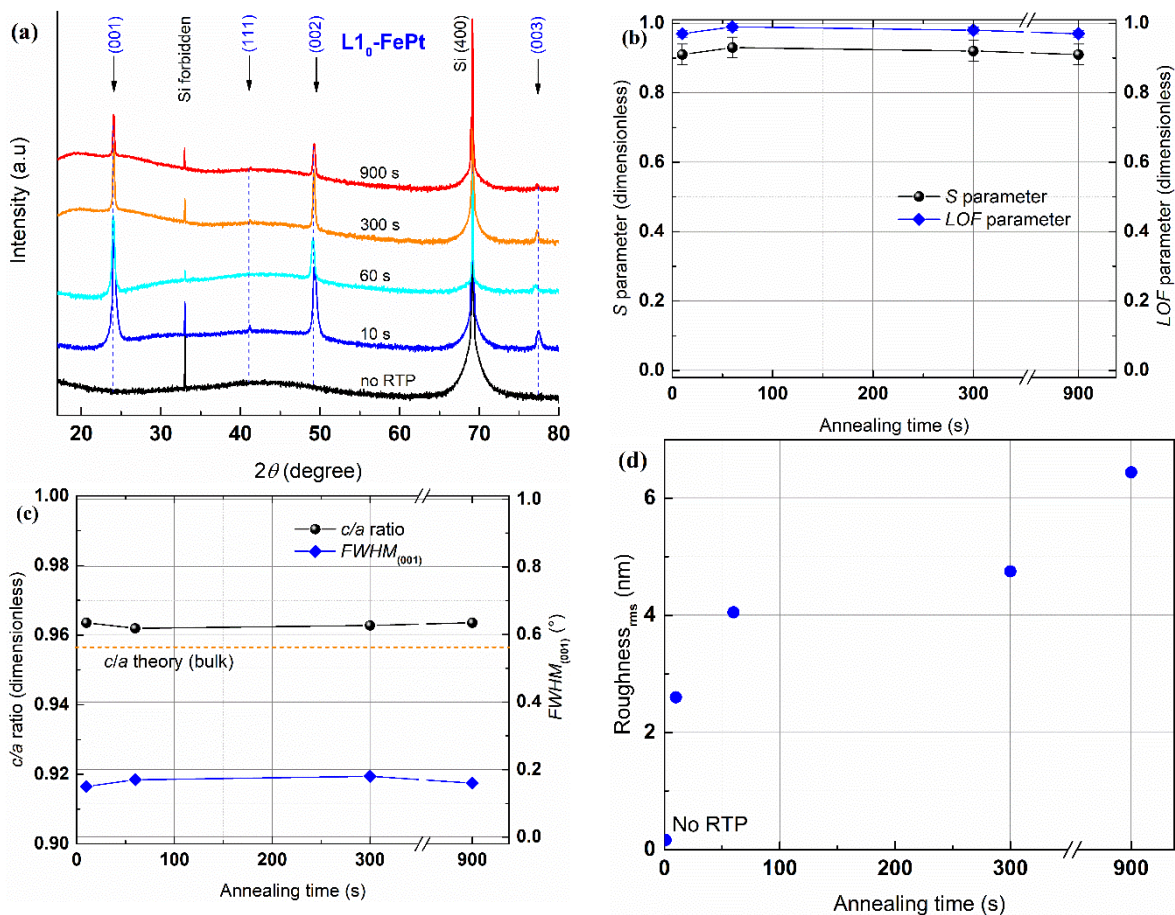


Figure III.33: The evolution of (a) structure (XRD patterns); (b) the S parameter and the LOF parameter; (c) the c/a ratio and $FWHM_{(001)}$; and (d) rms roughness of the as-deposited sample and annealed samples at 750 °C, at 50 °C/s, and in 1×10^{-1} mbar of Ar flow as a function of annealing time.

L1₀ phase. It demonstrates that 10s of annealing is sufficient enough to obtain the L1₀ phase. Further increase in annealing time do not lead to any clear improvement of the hard magnetic phase L1₀ from XRD pattern point of view. This observation is in good agreement with the calculated Time-Temperature-Transformation (TTT) diagrams from others [129,226]. They illustrate that achieving $\geq 95\%$ fraction transformed from A1 to L1₀ phase in 10 nm film, at 700°C of annealing, followed by: (i) the Pt-rich compositional film (as in this work), requires considerably longer time ($\sim 5 \times 10^0 \text{ s} - 10^3 \text{ s}$) to achieve a certain fraction transformed from A1 to L1₀ phases compared with the Fe-rich film ($\sim 10^1 \text{ s} - 10^3 \text{ s}$ depending on the model being used); (ii) the annealing in conventional furnace also requires longer time compared to laser annealing ($\sim 10^{-3} \text{ s} - 10^{-2} \text{ s}$). However, they do not indicate what the condition of ambient gas pressure is used, and the TTT diagrams are just purely theoretical calculations. The *S* and *LOF* parameters estimated from the given XRD patterns of the annealed films are shown in Figure III.33b. They have almost the same tendency of approaching a maximum value of 1. Film annealed in 10 s acquires relatively little smaller values in *S* and *LOF* of 0.91 and 0.97 respectively, while longer annealing time induces almost sluggish values of both *S* and *LOF*. The *c/a* ratio and *FWHM* also correlated in Figure III.33c. These values are comparable between films at different annealing time. From annealing time of 60s and above, the *S*, *LOF*, *c/a*, *FWHM* seem likely independent on RTP time. These experimental results are consistent with other authors, at which they performed the RTP at 800°C, 20°C/s for Fe-rich FePt films on glass substrates and showed that the *LOF* ~ 0.99 , residual stress $\geq 1.2 \text{ GPa}$ are almost constants over the range as in this study from 17 s to 900 s [231]. This tensile stress is the source inducing L1₀ phase formation in the annealed films and the A1-L1₀ phase transformation is completed with annealing time as low as 10^1 s [231].

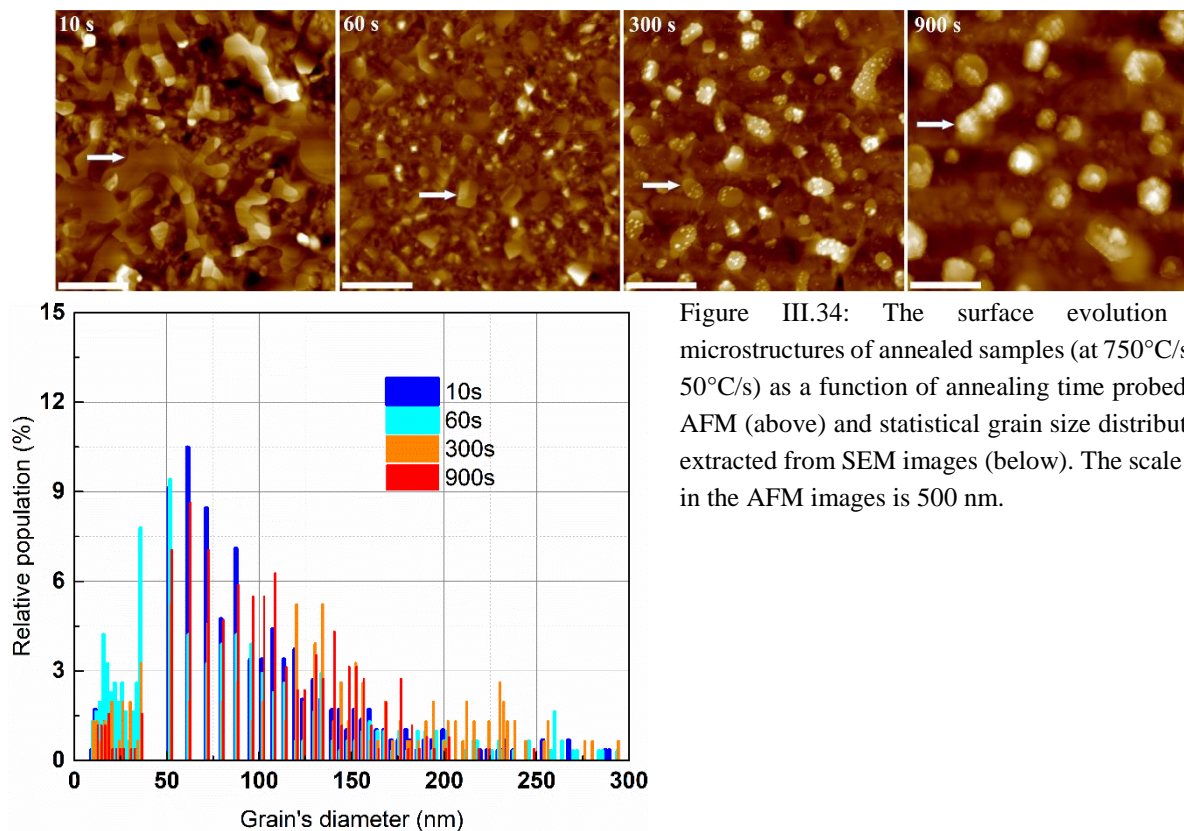


Figure III.34: The surface evolution in microstructures of annealed samples (at 750°C/s, at 50°C/s) as a function of annealing time probed by AFM (above) and statistical grain size distribution extracted from SEM images (below). The scale bar in the AFM images is 500 nm.

With pulsed laser annealing, a certain fraction transformed could be achieved in millisecond scale, the RTP might reply in the same manner but the magnetic properties of thin films are strongly dependent on both structure and microstructure (as shown in the two previous parts). The surface morphologies of annealed films (AFM images) as a function of annealing time are compared in Figure III.34-above. The Tuan NGUYEN VAN | Thèse de doctorat | Université de Limoges | 7 Mai 2021 77
Licence CC BY-NC-ND 3.0

discontinuous state of island-like microstructure transformed from continuous state in the as-deposited film is disclosed with annealing time of 10s. Increasing annealing time up to 900s promotes well-separated islands microstructure, and these islands tend to increase in height in the z direction. Longer annealing times lead to increase in rms roughness. A SEM estimation presents a slump in coverage percentage from ~19% in 10s to ~14% in 300s and to 11% in 900 s. The grain density follows the same shift from 11.5 grains/ μm^2 in 300s to 6.8 grains/ μm^2 at 900s. RTP in a short time of 10 s favors big grains but single-modal grain size distribution, any addition of longer annealing time, however, promotes multi-modal grain size distribution (Figure III.34-below). It suggests that the use of RTP process in annealing time as low as 10 s already completed the transformation from A1 to L1₀ phases, reflected by a strongly pronounced c -texture. The accumulated tensile stress induced in such annealing procedure play a crucial role in modifying the surface morphologies, in which the granular microstructure is gathered for films annealed in more than 60s.

The representative oop hysteresis curves of the films annealed at 750 °C, 50 °C/ s, and at various RTP time are compiled in Figure III.35a. These loops are not corrected for demagnetization field and normalized with magnetisation at 7 T. The dependence of μ_0H_c , μ_0M_r , and M_{OT}/M_{7T} ratio of the annealed films on annealing time is compared in Figure III.35b. Films annealed in 10 s or 900 s have a comparable coercivity of ~2.3 T, while increase annealing to 60s and 300s leads to higher coercivity films. All films show multiple magnetic phase behaviors and equivalent loop shape except single-phase behavior for film annealed in 10 s with quasi square loop shape. All of the films have a high value of remanence ratio of more than 90 %, and reach a maximum of 96.3% for film annealed in the shortest time of 10s. The multiple phase behaviors of films are attributed to the various grain size distributions in both xy direction and z direction (as evidenced from AFM in Figure III.34a), inhibiting all the FePt grains are switched simultaneously under a certain applied field. Single magnetic phase behavior film (annealed in 10s) with interconnected island microstructure assisted with the domain wall movement during the magnetization reversal process, which diminishes coercivity but allows the FePt grains being switched spontaneously. The reduction in magnetic properties for films annealed in longer time than 60 s might be ascribed to the oxidation or the formation of FePt₃ owing to a possible evaporation during RTP process [123]. It is noticeable that though the FePt grain-like island dimensions are diversified as has been reviewed so far in this study, the z -height of each single grain with flat surface at proper annealing conditions (depending on annealing temperatures, heating rates, and annealing time) has been realized.

The rigorous results presented in this section have demonstrated that it is flexible to control magnetic properties of the FePt thin films, which had been deposited on inexpensive Si/SiO₂ at room temperature. One of the main targets of the ANR SHAMAN project (ANR-16-CE09-0019) is to investigate the true potential of the soft in hard magnetic nanocomposite, for which the integrity of the soft magnetic NPs should remain unchanged (without or limited diffusion). Though NdFeB is a good hard magnetic matrix, it displays some drawbacks such as high variation in thickness, surplus of Nd content in the film, which can create unwanted phases with NPs during RTP. Such NdFeB thin films are also sensitive to oxidation, which leads to poorer magnetic matrices, in case of either RT deposition or elevated temperatures, with very thin film thickness. Hence, NdFeB based material will be eliminated as a matrix in the nanocomposites and FePt matrix will play its role acting as a skeleton for soft in hard magnetic nanocomposites.

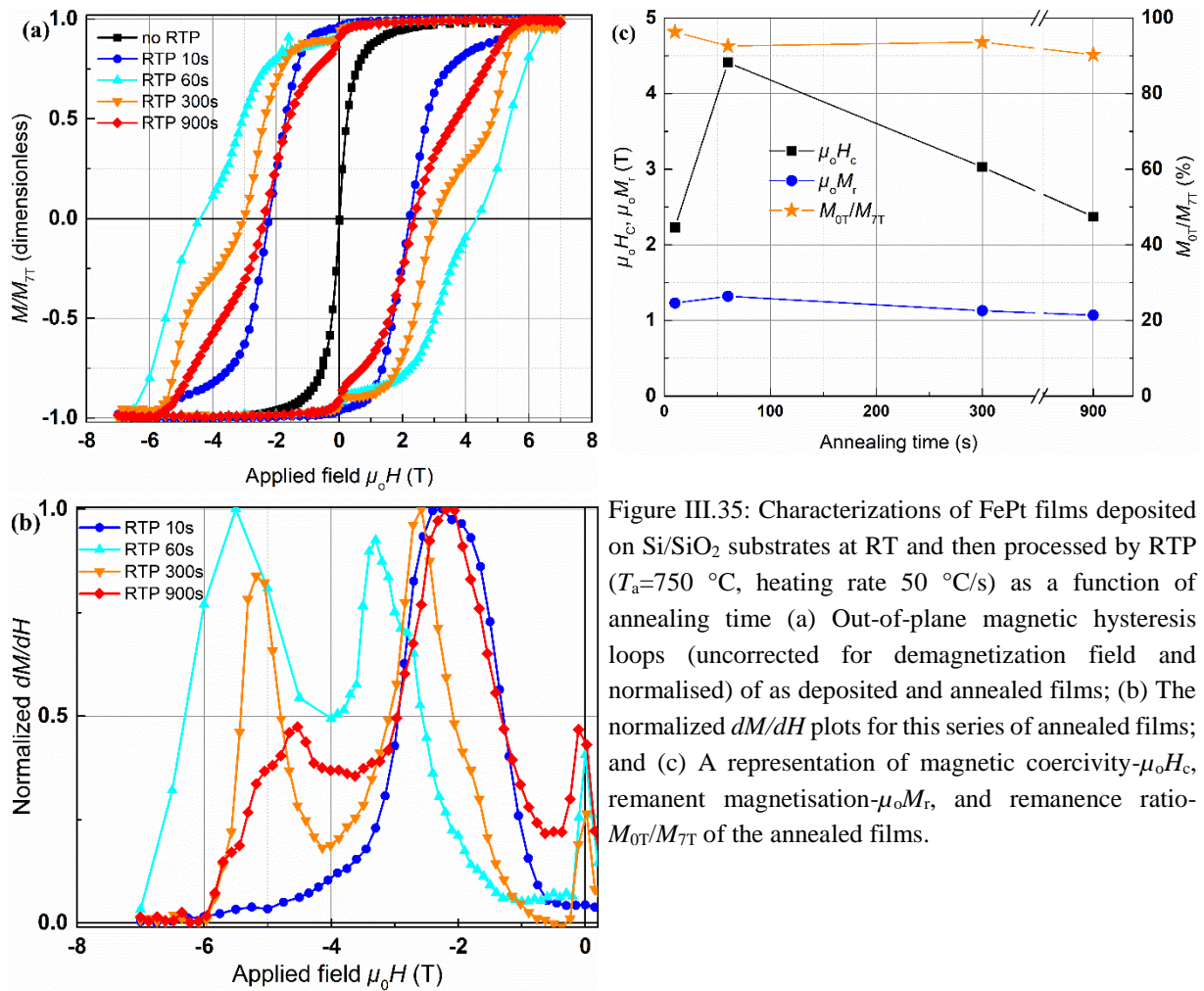


Figure III.35: Characterizations of FePt films deposited on Si/SiO₂ substrates at RT and then processed by RTP ($T_a=750$ °C, heating rate 50 °C/s) as a function of annealing time (a) Out-of-plane magnetic hysteresis loops (uncorrected for demagnetization field and normalised) of as deposited and annealed films; (b) The normalized dM/dH plots for this series of annealed films; and (c) A representation of magnetic coercivity- $\mu_0 H_c$, remanent magnetisation- $\mu_0 M_r$, and remanence ratio- M_{OT}/M_{TT} of the annealed films.

III.5. Chapter highlights

Various fabrication parameters were tested in depositing hard magnetic thin films based on NdFeB and FePt materials, from one-step to two-step annealing.

Regarding NdFeB thin films, the influence of Nd/Fe ratio (0.47-0.18) from a single ternary alloy target, deposition temperatures (T_d) and substrates (Si/SiO₂, Al₂O₃) on phase formation, microstructure and magnetic properties of trilayers Si/SiO₂ (100nm)/Ta (nominal 50nm)/NdFeB (150nm)/Ta (50nm) has been examined. Films from target with Nd/Fe = 0.45 have shown good magnetic properties with quasi-single magnetic phase and square loop shape. At low T_d (<550°C) due to lack of crystallization, it is responsible for depressed magnetic properties, meanwhile at high T_d (≥ 650 °C) it leads to strong reduction in both magnetic coercivity and remanence because of formation of oxidized phases or non-textured thin films. Films deposited at optimum T_d (550°-630°C) makes sure the growth of Nd₂Fe₁₄B phase together with Nd rich phase of partly decoupling Nd₂Fe₁₄B grains to enhance magnetic properties. The good out-of-plane textured magnetic properties have been obtained on both kinds of Si/SiO₂ and sapphire *c*-cut substrates with $\mu_0 H_c \sim 1.3$ T and $\mu_0 M_r > 1$ T. Moreover, the magnetic contrast reveals film possessing stripe domain pattern, which is a signature of good perpendicular magnetic properties (section III.1).

In the two-step annealing method, NdFeB films were first deposited at 450°C, and then applied the optimized RTP conditions, which are obtained when processed with FePt system. The Nd rich phase decoupling from Nd₂Fe₁₄B grains was observed by both XRD and FIB-EBS, with annealing temperature

of $\sim 500^\circ\text{C}$, which significantly augments the magnetic properties of the annealed films. Such films demonstrate single magnetic phase properties with both $\mu_0 H_c$ and $\mu_0 M_r$ close to 1 T (section III.2III.1).

Concerning FePt thin films, the effect of laser deposition frequencies (2 Hz-25 Hz), T_d and substrates (MgO, Si/SiO₂) has been investigated carefully. At relatively high thickness (>30 nm), while films deposited at lower deposition repetition rates (2 Hz-5 Hz) or high T_d ($>700^\circ\text{C}$) depicts isolated like-island microstructure, films fabricated at higher frequencies and low T_d ($<700^\circ\text{C}$) show continuous microstructure. All films show strong signatures of L1₀-FePt phase. At high T_d , films demonstrate the epitaxial growth on the MgO substrate with cube-on-cube relation. Comparable magnetic properties have been achieved for FePt films single crystal MgO and conventional Si/SiO₂ substrate, with $\mu_0 H_c \sim 1.5$ T and $\mu_0 M_r$ close to 1 T (section III.3).

In the indirect-crystallization approach, 15 nm FePt thin films were initially deposited at RT and latter applied RTP heat treatment at various conditions, e.g., annealing temperatures (T_a), heating rates and annealing time. Films annealed in optimal conditions ($T_a > 700^\circ\text{C}$, 50°C/s , 10s-60s) illustrate out-of-plane texture, strong perpendicular anisotropy properties, with $\mu_0 H_c$ up to 4.4 T and $\mu_0 M_r > 1$ T. Depending on the annealing recipes, processed films can show single or multiple-phase behavior, which provides additional degrees of freedom in controlling the properties of future soft-hard nanocomposites (section III.4).

Chapter IV. Soft magnetic nanoparticles

This part is mainly focused on the synthesis of soft magnetic nanoparticles, e. g., FeCo NPs. This choice is motivated by the desire to observe the influence of these NPs on magnetic properties of soft-hard nanocomposites consisting soft magnetic nano-inclusions inside a hard magnetic matrix. The NPs size is expected no larger than twice of domain wall width of the hard phases of NdFeB and FePt thin films, well-developed in Chapter III. The size, shape, crystallization of the NPs and/or stacks of NPs deposited at RT on TEM grids and Si/SiO₂ at RT and elevated temperatures or applied optimal RTP heat treatment will be studied by TEM, XPS, AFM, SEM, XRD and VSM-SQUID.

IV.1. FeCo NPs properties

Owing to Cobalt nanoparticles (NPs) containing one single element of Co, it is convenient to just pay close attention in depositing and investigating the properties of alloy compound NPs of FeCo. In this Chapter, the properties of FeCo NPs will be unearthed. The experimental device of Pulsed Laser Deposition (PLD) + Free Cluster Generator (FCG) is described in Chapter II. Here, for NPs fabrication only FCG will be used. A pulsed laser Nd: YAG laser (wavelength: 532 nm, 2ω , pulse duration: 7 ns) is employed for the generation of NPs. The ejected plasma plume is quenched in order to favor collision and also nucleation of NPs. The growth of NPs is strongly dependent on the opening t – time of the He pulsed valve. Many other parameters are involved in the nucleation process of NPs within the plasma plume, in particular the nature and pressure of the gas injected to quench/cool the plasma, and the residence time of the species in the cavity. In the case study, the selected gas is helium (purity 99.995%), in particular because of its high thermal conductivity, specific heat, and relative small Van der Waals radius (156.7 mW.m⁻¹.K⁻¹, 3160 J.kg⁻¹.K⁻¹, and 140 pm respectively at 300 K, 1 atm). It is injected under a pressure of 10 bar by the pulsed valve. The laser fluence made by Nd: YAG laser has been adjusted experimentally in order to control the deposition rates (8 J.cm⁻², at 4 Hz, which is highly dependent on the target material). Distance from nozzle outlet to substrate placed in the PLD chamber is about 30 cm. The base pressure prior to deposition is about 1×10^{-6} mbar, and the Fe₆₅Co₃₅ target will be used in this experiment.

IV.1.1. Initial parameters for NPs fabrication

The fabrication the NPs needs to define some initial parameters such as the deposition rate or the flow of the clusters/NPs in order to obtain sufficient deposition rate for synthesizing the fined magnetic nanocomposites. Thus, numerous tests were carried out with a stack of NPs on Si/SiO₂ (native oxide layer of around 5 nm) at room temperature (schematic diagram of sample presented in Figure II.8b), deposited from Fe₆₅Co₃₅ alloy target. Figure IV.1 shows the dependence of the normalized (per hour) deposition rate of the FCG system on the opening t – time of the helium pulsed valve. As the pulsed valve delivered the helium gas in a small time interval, $\leq 150 \mu\text{s}$, there is no signature of

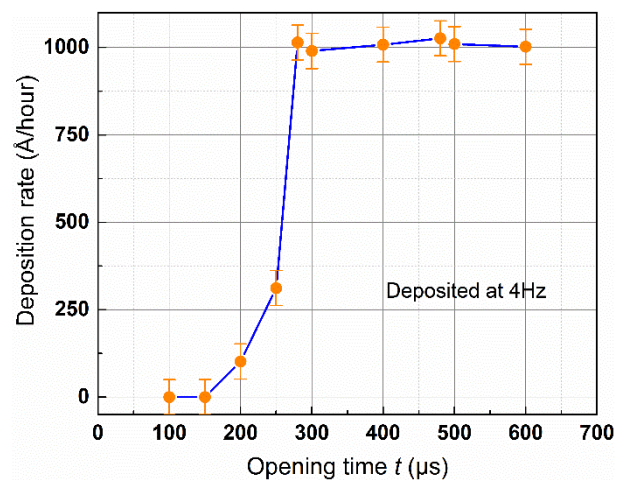


Figure IV.1: The experimentally normalized (per hour) deposition rate as a function of the opening t – time of the helium pulsed valve determined by AFM (from Fe₆₅Co₃₅ alloy target). In each single measurement, a stack of NPs

clusters/NPs flow. At a higher duration of time of around 280 μs , which is the so-called opening threshold, a sufficient deposition rate of clusters/NPs of about 100 nm/hour is observed. A

corresponding to 15 minutes of deposition, the helium pressure of 10 bar, the Nd:YAG laser fluence $\sim 8 \text{ J.cm}^{-2}$, laser repetition of 4 Hz and the delay between the laser and the helium pulsed valve of 1.650 ms, PLD chamber base pressure of 1×10^{-6} mbar are applied.

longer opening t – time duration for gas delivery above this opening threshold of 280 μs does not significantly promotes the deposition rate of the clusters/NPs. In the operating conditions, an upper limit for the pulsed valve duration of 600 μs is applied. Thus, the fabrication with opening t – time interval between 280 μs and 600 μs will be investigated.

IV.1.2. Size distribution

In order to investigate the size distribution with respect to the opening t – time of the He pulsed gas valve, a first set of low energy FeCo NPs beams deposited on commercial copper-TEM grid, 400 meshes coated by a 50 \AA thick amorphous carbon membrane (Ted Pella Inc), at various t from 300 μs to 600 μs , was characterized by TEM (schematic diagram of sample presented in Figure II.8a). The other deposition parameters were kept constants, i. e., the Nd:YAG laser fluence of $\sim 8 \text{ J.cm}^{-2}$, the gas pressure before entering the pulsed valve of around 10 bar. During the deposition, the TEM grid had been placed inside the conventional PLD with base pressure as low as 1×10^{-6} mbar and after the deposition the NPs were capped by another 30 \AA - 50 \AA amorphous carbon layer deposited by PLD to prevent oxidation. The deposition rate was identified experimentally by both QCM and AFM (stack of NPs), of about 100 nm/hour or $\sim 16.7 \text{ \AA.minute}^{-1}$. Transmission electron microscopy – TEM provides access to a great deal of information such as the shape, crystal structure, size dispersion of the nanoparticles as well as possible segregation phenomena. The analyses were carried out on a TEM-JEOL 2100F, 200 kV. In the TEM characterizing procedure, the nanocrystallized clusters/NPs diffusing the electrons (especially for atoms with high atomic number) and coated amorphous carbon layer appear as shadows and bright background on the recorded images respectively. The images were analyzed by using deep a learning algorithm, which is available in the Fiji software. The error bar in estimating the clusters/NPs' diameters by using the software is a challenge but it will not exceed 5%. The corresponding size distribution as well as size dispersions obtained for clusters/NPs with various t is compiled in the Table IV.1. Note that, the size distribution and the size dispersion are both obtained from fitted curves of the size histogram of clusters/NPs by using either lognormal function or gaussian function, which is given by:

- Lognormal function:

$$\rho(D) = \frac{1}{\sqrt{2\pi}} \frac{1}{\omega} \frac{1}{D} e^{-\left(\frac{\ln(D/D_m)}{\sqrt{2}\omega}\right)^2} \quad (\text{Equation IV.1})$$

- Gaussian function

$$\rho(D) = \frac{1}{\sqrt{\pi/2}} \frac{1}{\omega} \frac{1}{D_m} e^{-\left(\frac{(D-D_m)}{\sqrt{2}\omega D_m}\right)^2} \quad (\text{Equation IV.2})$$

where $\rho(D)$, ω , D , D_m denote the size distribution, the size dispersion (dimensionless), the diameter of a particle supposed to be spherical and the mean diameter, respectively. The product ωD_m is often called standard deviation, σ , of the distribution.

Figure IV.2 shows TEM images and clusters/NPs' diameters of all samples of FeCo binary system at various opening t – time. At the first glance to the size distribution, any addition of the opening t – time in the investigated range 300 μs to 600 μs induces the expansion in the mean diameter D_m and the

corresponding *FWHM* but the size dispersion varies little. Namely, at $t = 300 \mu\text{s}$, the size distribution is centered at $D_m = 2.69 \pm 0.26 \text{ nm}$ with *FWHM* of $\sim 1.24 \text{ nm}$, while at $t = 600 \mu\text{s}$, the size distribution is centered at $D_m = 4.73 \pm 0.42 \text{ nm}$ with *FWHM* of $\sim 1.86 \text{ nm}$ with the size dispersion keeping almost constant of $\omega = \pm 0.6$.

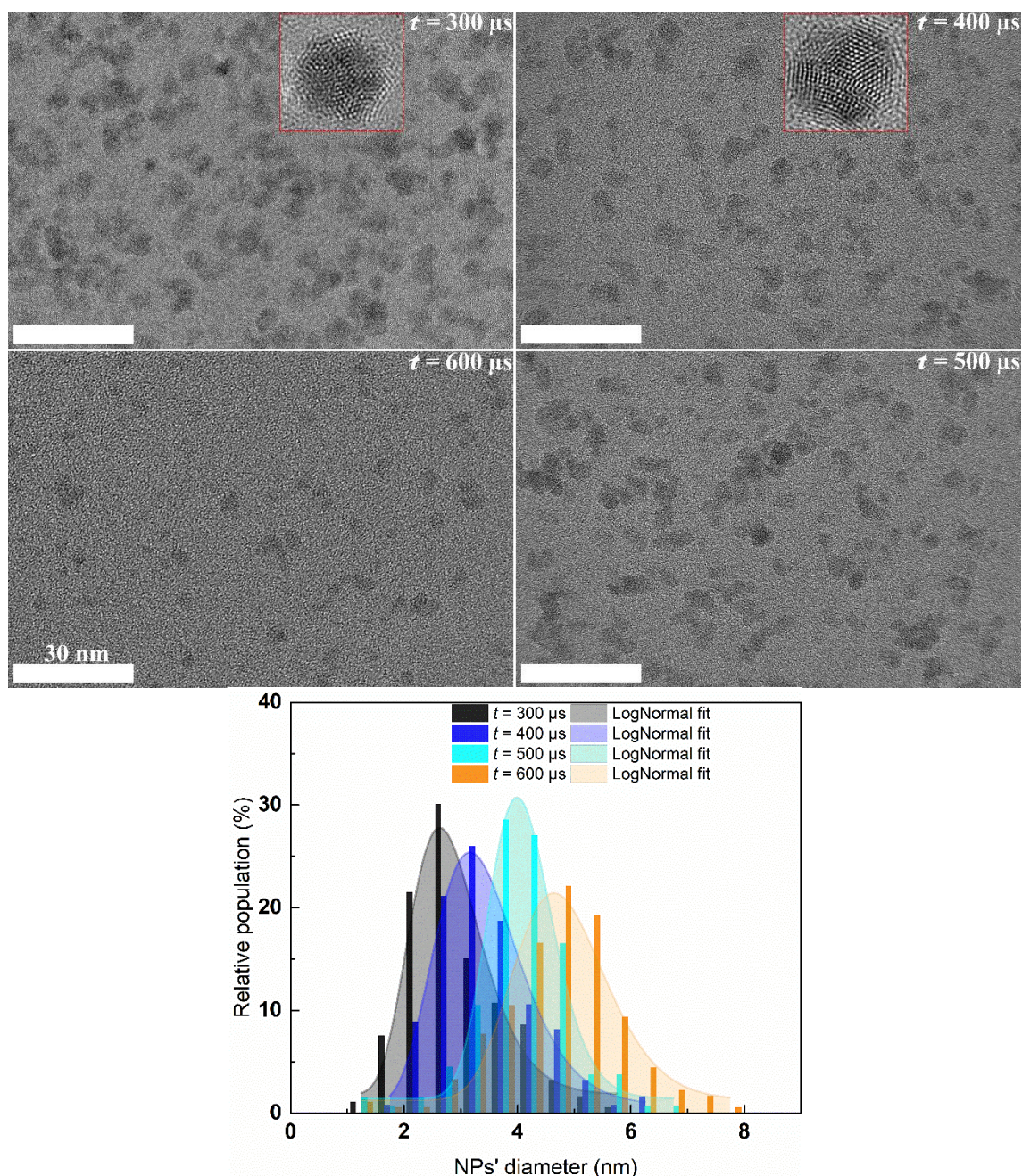


Figure IV.2: TEM images for Fe-Co clusters/NPs and their corresponding size histogram together with lognormal/gaussian fitted curves with a variety of opening t – time of (a) 300 μs ; (b) 400 μs ; (c) 500 μs and (d) 600 μs . The number of nanoparticles in the histogram is about 400 NPs.

All the derived values obtained from fitting with either lognormal function or gaussian function are compiled in Table IV.1. It is clear that the mean diameter of the NPs does not really depend on which functions are used. Note that owing to not possessing one single stack of NPs, the some plane-view TEM images composed of multiple coalesced NPs, thus procedure of analyzing NPs with Fiji software was repeated around five times.

Table IV.1: The mean diameter and size dispersion of the clusters/NPs deposited on TEM grid with various opening t – time ranging from 300 μs to 600 μs .

opening t – time (μs)	Lognormal fit		Gaussian fit	
	D_m -Diameter (nm)	Standard deviation (nm)	D_m -Diameter (nm)	Standard deviation (nm)
300	2.78	0.23	2.69	0.26
400	3.34	0.23	3.28	0.34
500	4.07	0.14	4.05	0.29
600	4.78	0.17	4.73	0.42

The modification of the mean diameter D_m of the clusters/NPs with respect to opening t – time could be comprehended by the consequential effects of regional gas pressure and resident time of the clusters/NPs accumulated in the nucleation chamber of the FCG. Based on the clusters/NPs growth model proposed for CO_2 monomer by Soler [232], the successive atom absorption is the prerequisite process, which steadily evolves to coagulation once the density of clusters/NPs is sufficiently high enough for coalescence. This exemplary model allows for fitting the clusters/NPs size distribution as a function of a single variable of τ characterizing for the degree of condensation or nucleation rate. By neglecting the evaporation effect compared to the condensation one, the kinetic equations governing clusters/NPs-

clusters/NPs reactions can be expressed as: $dn_k^* / d\tau(t) = \sum_{i+j=k, i \leq j} C_{ij}^* n_i^* n_j^* - \sum_i C_{ik}^* n_i^* n_k^*$ and

$$\tau(t) = \int_0^t 16\pi R_1^2 \left(\frac{k_B T(t')}{\pi m_1} \right)^{1/2} \frac{N}{V(t')} dt', \text{ where the first term } \sum_{i+j=k, i \leq j} C_{ij}^* n_i^* n_j^* \text{ and the second term } \sum_i C_{ik}^* n_i^* n_k^*$$

present the rate in which k -size clusters/NPs are formed by coagulation and are lost by growing to larger sizes, respectively; C_{ij}^* are the normalized coagulation rate with C_{11} depending on the mass m_i of the i^{th} cluster, cross-sectional area (σ_{ij}) of coagulation of an i with j -size clusters/NPs; $V(t')$, $n_i^* = N_i/N$ are the volume enclosing N number of molecules at t' – time and N_i presenting the number of i -size clusters/NPs in the same volume; R_1 and m_1 is the radius and mass of the initial cluster/NP. The growth of clusters/NPs by coalescing drives to gaussian distribution of the logarithm of the clusters/NPs' sizes. The observations achieved in this study are coherent with gaussian distribution and other practical observations [99,232]. To be specific, an increase τ time leads to widening the distribution shape and $FWHM$, as well as increasing the distribution center (as indicated in Figure IV.2 and will be shown below).

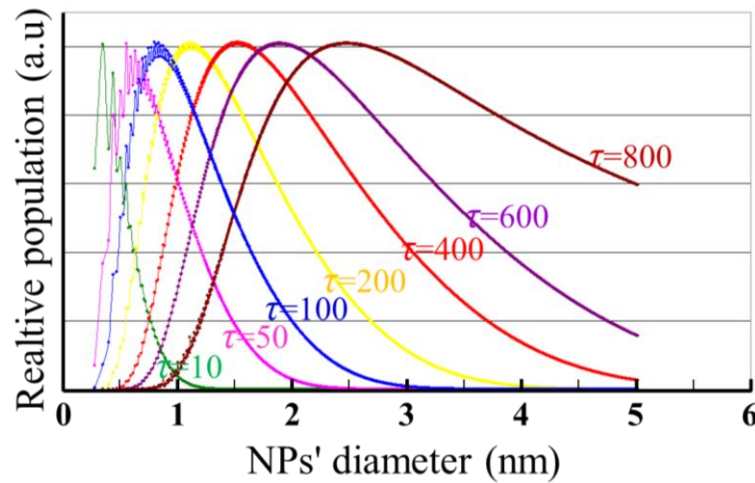


Figure IV.3: The calculated and normalized relative population of number of Ag metal NPs as a function NPs' diameter induced by changing τ – the degree of condensation. Note that τ will be again controlled by the opening t – time. The figure is partly adapted from [99,181].

Figure IV.3 presents the calculated size distribution of the NPs' diameter as a function of τ – the degree of condensation, which was induced by changing the opening t – time. In this case study, the n_i^* was 3, while the initial number of atoms in the modeled system was kept at constant of 6000. Note that the initial atoms did not significantly affect the overall shape of the size distribution. As it can be seen that increasing the τ leads to a widening of the size distribution together with the NPs' diameters. A raw estimate indicates the $\tau = 800$ corresponding to $t \sim 300 \mu\text{s}$, and increasing τ should lead to rising up of opening t – time. To date, the calculated results for size distribution of NPs' diameters suggesting the model used here is in good agreement with the experimental development of controllable NPs.

The observations clearly demonstrate that the size distribution of the clusters/NPs fabricated in this work is of narrow size distribution. This indicates that the physical/magnetic properties of the clusters linked to the size effect could be well controlled. To avoid the further coalescence effect in the magnetic nanocomposites based NdFeB and/or FePt matrices, the NPs can be capped with the thin films simultaneously and independently, that means the hard magnetic matrices/thin films will act as a skeleton to pin the clusters/NPs in the nanocomposites.

IV.1.3. Composition

Starting from the $\text{Fe}_{65}\text{Co}_{35}$ single alloy induction melted target (since this alloy has the highest saturation magnetisation, section I.4), several FeCo clusters/NPs samples on TEM grid were inspected for EDS analysis by TEM. In all the case, there is almost no signature of oxidation of the NPs. Figure IV.4 presents a representative EDS spectrum of the deposited Fe-Co alloy clusters/NPs on TEM grid. In the EDS, the predominantly strong intensities of Fe and Co are shown in comparison with Cu signature from the Cu meshes of TEM grid.

The analysis confirms average values of about 66.5 % and 33.5 % of Fe and Co in atomic percentage, respectively, in the investigated samples. This result validates the quasi – congruent process of FeCo NPs made by PLD [79]. Note that Fe and Co atoms are just one electron difference in their shells. Different deposition or annealing conditions might have influence on the compositional, structural, microstructural, and magnetic properties of the NPs/stacks of NPs. The properties of a set of $\sim 100 \text{ nm}$ stacks of Fe-Co NPs deposited at various deposition temperatures – T_d on Si/SiO_2 (100 nm) are investigated. Samples are covered with a few nm of carbon on top to prevent oxidation, and later characterized for the above properties. Note that the C protective layer was deposited at RT and the porosity of about 50 % – 62 % has not been taken into account [100,101,191].

In this section, the characterization with X-ray photoelectron spectroscopy (XPS) has been made to the

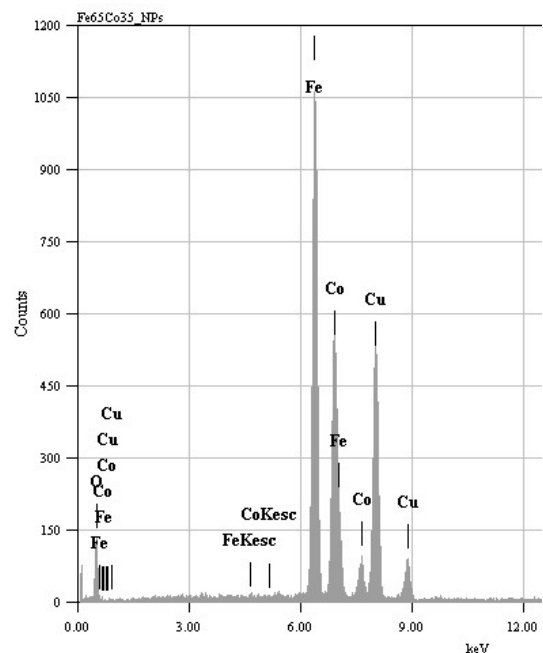


Figure IV.4: The EDS spectrum for a Fe-Co clusters/NPs on TEM grid characterized by TEM JEOL 2100F.

series of stacks of Fe-Co NPs. The stacks of Fe-Co NPs were first introduced to high vacuum chamber of the XPS system, then the samples were etched by ion to investigate the physical and chemical properties

of the Fe-Co stacks, because the XPS investigate a few nm on top of material, in depth (~5 nm). The compositional profiles of etched samples (deposited at RT, 500°C, 730°C) are depicted in Figure IV.5 a, b and c. Note that the etching process would modify the sample surface at a certain degree. It is obviously seen that on top of the samples (no etching or etching time = 0), the C is predominant. After etching deeply inside the samples as expected, the C contribution dramatically reduces, while other elements' contribution increases, especially for Si and O (Figure IV.5a and b). However, sample deposited at 730°C (Figure IV.5c) shows different behaviors, for which the C concentration monotonically decreases, meanwhile Fe and Co aggregations are of the same tendency compared to the two other samples.

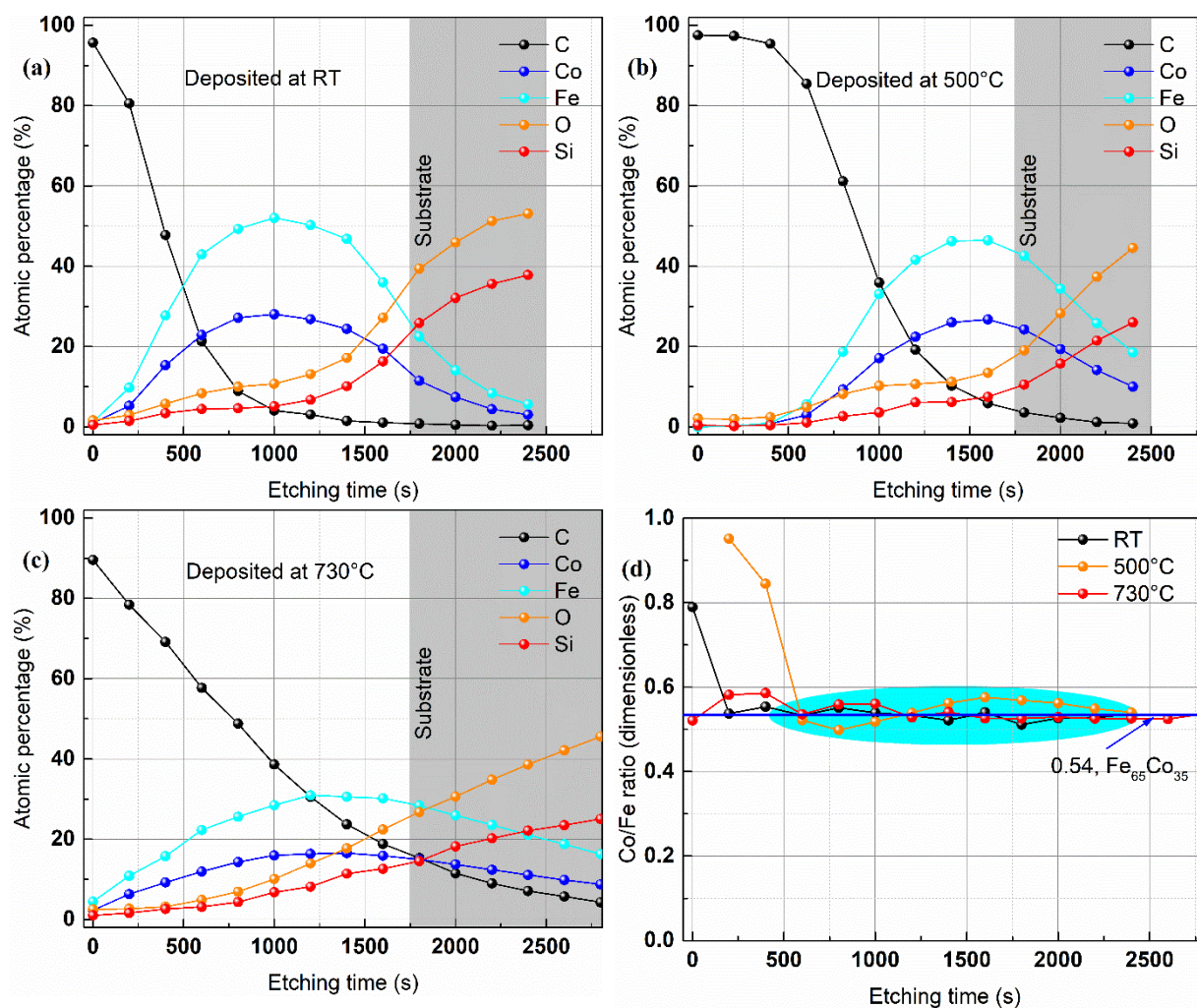


Figure IV.5: The XPS compositional analysis for stacks of FeCo NPs deposited from Fe₆₅Co₃₅ target, at various deposition temperatures – T_d of (a) RT; (b) 500°C; (c) 730°C. (d) The Co/Fe ratio from such sample is lately compiled in, the blue straight line at Co/Fe = 0.54 ~35/65 representing guide to the eye. Note that the XPS etching profile is of raster size of 16 mm², etched with 5 keV, 7 mA, and photoelectrons is at 1s, 2p, 2p, 1s, 2p level for C, Co, Fe, O, Si respectively. The gray region qualitatively presents for start of etching to the substrate.

Consider at the position (or the etching time, at which the Fe or Co concentration is highest, the Si and O contents, in the sample deposited at 730°C, are relatively higher than those of samples deposited at either RT or 500°C. These results are in agreement with the observation in microstructure (see section IV.1.4) followed by the following reasons: (i) the roughness for sample deposited at 730°C is much higher than the two others; (ii) the two microstructure populations (big grain ~200 nm (upper layer) and small grain ~50 nm (underlying layer)), which leads to strongly rough surface, therefore the C, O (from surrounding environment) are easily occupied; and (iii) At relatively high T_d of 730°C, there should exist

a certain degree of Si and O diffusion from the substrate (Si/SiO₂) to the Fe-Co layers. As results, after being etched, high contents of C and O were observed. The appearance of O inside the FeCo layer might be a signature of oxidation during the deposition process owing to poor base vacuum pressure of 1×10^{-6} mbar, or it might initiate from the etching process inside the XPS machine and it is well agreed with the TEM characterization shown previously.

Figure IV.5d is a sum-up of Co/Fe contents as a function of etching time (proportional to the thickness of the film) at various T_d . Neglecting about the first 500 s of etching time (there are high possibility of contamination from surrounding environment due to etching process, which will modify the surface of etched sample), a good approximation of Co/Fe ratio of 0.54 (~35/65) was observed. Thus, the XPS verifies the concentration of the stacks of Fe-Co system with 66 % of Fe and 34 % of Co. The both results from TEM and XPS illustrate that the atomic ratio between Fe and Co does not depend on the opening t – time of the pulsed valve or the deposition temperature – T_d . This confirmation is well agreed with the congruent process made by PLD [79] and from the fact that Fe and Co are neighbors of each other's in the chemical periodic table, which are both transition metals with only one electron difference.

As indicated above, the XPS saw clearly the oxidation inside the deposited stacks of NPs. In order to quantify the total contribution of oxidized phases (which could be contaminated during the deposition procedure and XPS etching process), a detailed analysis was made at this point for the survey spectra corresponding to the middle of the stacks of NPs. It is noteworthy that XPS is a surface-sensitive quantitative spectroscopic method that determines the both elemental and chemical compositions accompanied by electronic states. The XPS detailed analysis depicts that stacks of Fe-Co NPs deposited at 730°C have: (i) relating Co element ~84.47 % of Co metal and 15.53 % of CoO_x; (ii) relating Fe element ~63.43 % of Fe metal and ~36.57 % of iron oxide (FeO+Fe₂O₃+Fe₃O₄). The pure metal percentage (Co and Fe) is improved at lower deposition temperatures, while the oxidized phase contribution is significantly reduced, e. g., at RT, there are ~89.78 % Co metal, ~10.22 % CoO_x, and ~74.98 % Fe metal, ~25.02 % Fe_xO_y. These observed results are coherent with the effect of monolayer formation time on partial deposition pressure of O₂ at various deposition temperatures (discussed in section III.1.2). Though the formation time at lower T_d is lower compared to higher T_d , the oxidized form contribution is higher higher T_d , which may be attributed to the favourable reaction between either Co or Fe and O₂ at higher T_d compared to the lower ones. Hence, the study of XPS provides additional comprehending in explaining the properties of the deposited stacks of NPs. Details for these high resolution XPS analyses are provided in Appendix A.8.

IV.1.4. Structure and microstructure

The structural and microstructural properties of the Fe-Co NPs system will be first investigated "individually" (by TEM), and then studied with stacks of Fe-Co NPs at different deposition conditions (by XRD, AFM, SEM). Detail characterizations of FeCo cluster/NPs on TEM grid (deposited at RT) about structural properties is shown Figure IV.6. The TEM image reveals the presence of individual NPs with a mean diameter of 4.07 ± 0.14 nm (lognormal fit, Figure IV.6a). It has long been known that upon depending on deposition time, the aggregated formation of clusters of magnetic NPs can be formed owing to the RKKY interaction between NPs dispersed in the TEM grid. During the deposition, several kinds of NPs in terms of shapes can be built. Figure IV.6b displays HRTEM images of two kinds of NPs with a variety of shapes and their corresponding Fast Fourier Transforms (FFT), one of which is cuboctahedral NPs. By selecting diffraction spots on the representation of the FFTs, the direction and the spacing between the diffracting planes appear. Note that the representative (hkl) miller indices here just present for the plane families. The XRD (SAED) patterns performed for collection of clusters/NPs (inset of Figure

IV.6a) and FFTs applied on these NPs both clearly indicate the presence of mixture between the two phases of *fcc* and *bcc* structures of FeCo.

Table IV.2: The extracted structural parameters of stacks of NPs deposited on TEM grid at RT employed by the indirect approach from XRD/SAED patterns.

Circle	Reciprocal distance- $C_i/2$ (1/nm)	Inter-reticular distance (Å)	Structure (<i>hkl</i>)
C ₁	3.977	2.514 ± 0.007	{111} <i>fcc</i> -No. 04-9067
C ₂	4.842	2.065 ± 0.005	{110} <i>bcc</i> -No. 03-5298
C ₃	6.819	1.467 ± 0.006	{102} <i>bcc</i> -No. 03-5298

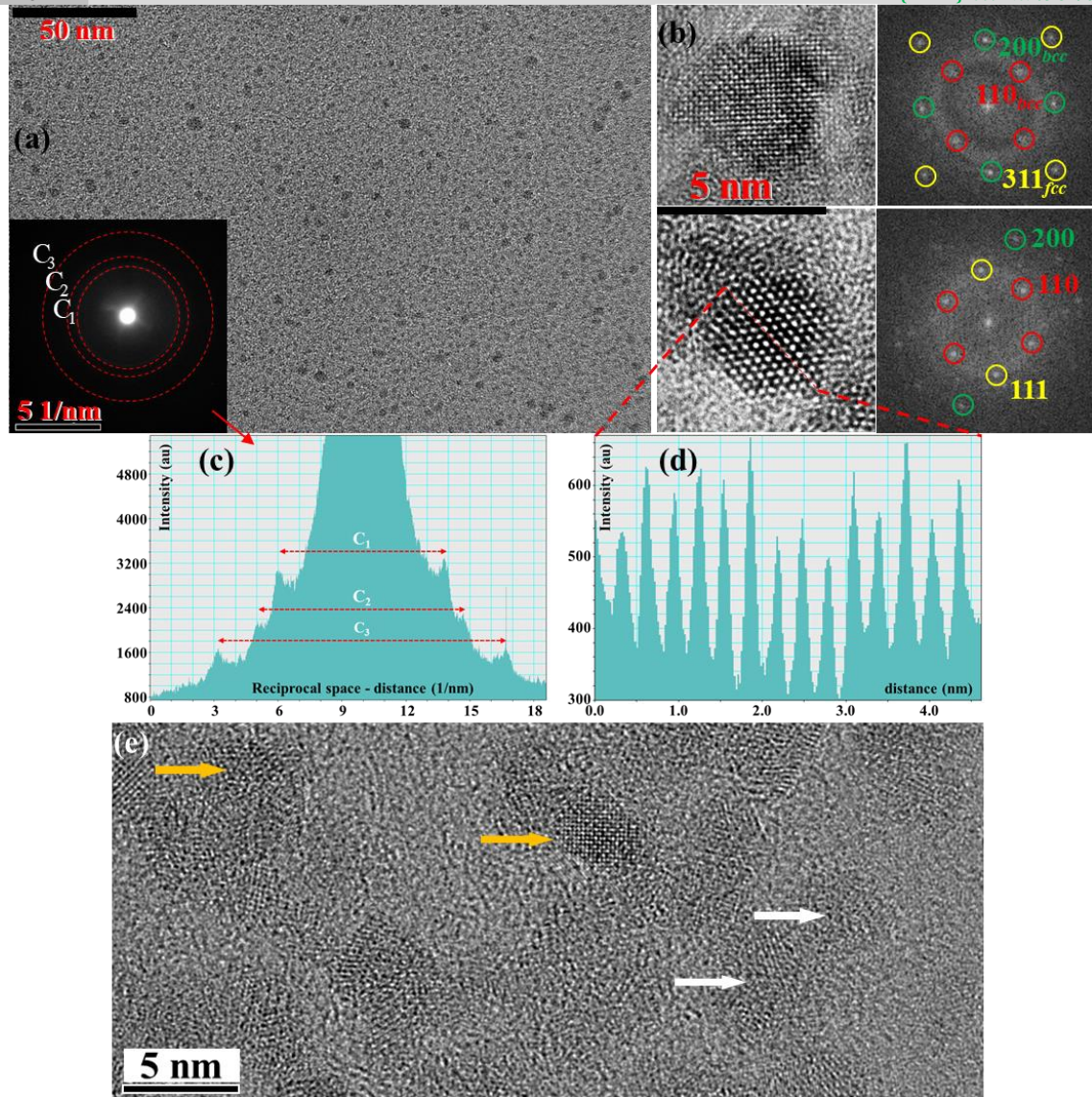


Figure IV.6: Characterizations of stacks of FeCo clusters/NPs deposited on TEM grid at RT with opening t – time, $t = 500 \mu s$ (a) TEM image with the inset of representative SAED pattern extracted from the whole TEM image; (b) Zooms (HRTEM images) of some NPs focused from TEM images and their corresponding Fast Fourier Transforms (FFTs), for which the (*hkl*) indices are indicated; (c) A precisely indirect approach to extract the inter-reticular distance from SAED patterns (averagely collected from all of the clusters/NPs in the image); (d) A precisely direct approach to obtain the inter-reticular distance from a single NPs; and (e) a HRTEM image consists of several NPs showing well crystallized NPs (orange arrows) and being crystallized in short range order (white arrows).

Figure IV.6c and d demonstrate two methods of "indirect" and "direct" identification of structural properties such as the structure type and the distance between two lattice planes of the atoms. From the

SAED patterns, the circles' diameters were extracted from a precise technique based on the intensity of the diffraction rings' intensities, at which the diameters in the reciprocal space (unit of 1/nm) were measured. Comparing the inter-reticular distances obtained from such circles' radii with the diffraction library, one could access to the crystallographic information of crystal structure type and the lattice spacing between the two planes of the atoms, etc. These parameters are compiled in Table IV.2. It is obvious that, at RT the NPs are crystallized with families of planes being in agreement with diffraction planes picked up from FFTs patterns. The NPs are crystallized, which is evidenced visibly in the Figure IV.6e exhibiting the HRTEM image for a collection of NPs. Namely, FFTs were further carried out for other NPs indicated by orange arrows, which exhibit almost clearly crystallographic structure (Figure IV.6b).

In the direct approach of acquiring more information on structural properties from individual NPs, the lattice spacing between the two planes can be derived directly as revealed in Figure IV.6b. The lattice spacing parameters obtained from this approach, in this work, are seemingly higher than those of values drawn out from the indirect approach from 3 % to 10 %. Indeed, the lattice spacing extracted directly from direct approach is accurate, however, it is not really reliable for NPs that are both not tilted properly and affected by the edge effects of NPs [233]. The error becomes considerable when the NPs become smaller [234]. In order to constantly improve the accuracy and reliability of the lattice spacing implied from this direct approach, several routes could be employed such as (i) tilt the interested NPs down to low order region but it seems to be challenging for small NPs; (ii) make a comparison between the measured NPs and either simulated NPs or tilted NPs; and (iii) take an average value of a large number of NPs, however, this could lead to time-consuming measurement which increases a prolonged exposure of NPs under the electron beam, thus the imaging surface modification could take place. Other authors show that upon annealing, the chemical transition from disordered of *fcc* A2 phase to ordered of *bcc* CsCl-B2 phase can occur [163].

In case of annealing the NPs, it is believed that the crystallographic structure of stacks of NPs could be enhanced by crystallizing all of the NPs which are not crystallized in the as-deposited state. Hence, as a result, the magnetic properties of the system could be improved through heat treatment with and without post-annealing [163].

A set of stacks of NPs with opening t – time, $t = 500 \mu\text{s}$, was deposited onto Si/SiO₂ (100 nm) at different deposition temperatures – T_d from RT up to 730°C, i. e., RT, 300°C, 500°C, and 730°C, which are below and above the Fe₆₅Co₃₅ transition temperature of 647°C from ordered CsCl-B2 (α') to disordered (A2) phases. The nominal thickness of the stacks of NPs is about 100 nm corresponding to one hour of deposition

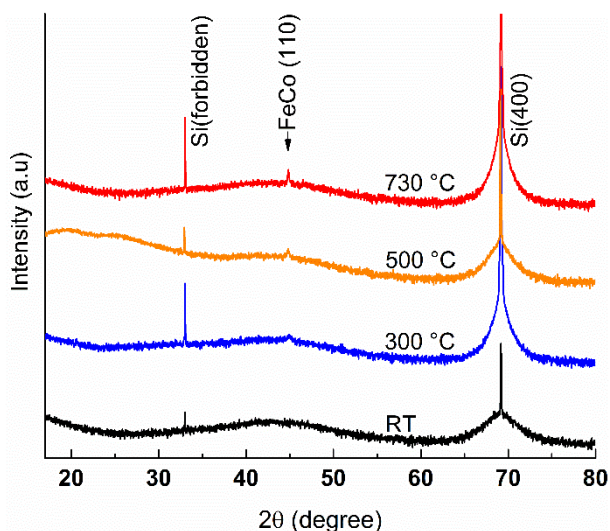


Figure IV.7: The XRD diffractograms of stacks of FeCo clusters/NPs, with opening t – time, 500 μs , as a function of deposition temperatures – T_d on Si/SiO₂ substrate.

(schematic diagram of sample presented in Figure II.8b). Figure IV.7 compares the XRD patterns of a set of stacks of NPs deposited at various temperatures from RT up to 730°C. In all presented patterns, the Si (400) and Si forbidden orientations from the substrate are identified. Besides the substrate peaks, there is

only one peak corresponding to *bcc* FeCo (110) reflection appeared in the investigated range for samples deposited at elevated temperatures (> RT). As shown in the XRD patterns of cluster/NPs on TEM grid (see above), the NPs were crystallized even at RT. No crystallization, however, was observed for stacks of NPs deposited at RT using conventional XRD of θ - 2θ measurement, which could be attributed to crystallization occurring in a very short range order. The relative intensity of this peak is somewhat increasing with T_d , while the *FWHM* of this reflection becomes sharper. Taking into account the broadening effect from the machine, the crystallite size as a function of T_d is given in Table IV.3, which is calculated from Scherrer equation $D_{Scherrer} = \frac{K\lambda}{FWHM \cos\theta}$, where K is a dimensionless shape factor (~0.9), λ is the XRD wavelength (Cu $K_{\alpha 1}$ ~0.15406 nm), *FWHM* is the full width at half maximum (radian), and θ is the Bragg angle. The corresponding values in the Table IV.3 are obtained from fitting with Voigt function. Such crystallite size is grown with T_d from 9.4 nm at 300°C to 31.8 nm at 730°C, which is consistent with the observation from AFM cross-sectional analysis in Figure IV.8.

Table IV.3: Crystallite sizes obtained from Scherrer equation based on by XRD spectrum.

Deposition temperature- T_d (°C)	2θ (°)	β - <i>FWHM</i> (°)	$D_{Scherrer}$ (nm) at (110) peak
RT	N/a	N/a	N/a
300	44.98	0.914	9.4
500	45.14	0.337	25.5
730	45.20	0.270	31.8

Figure IV.8 compares the AFM surface morphology and AFM cross-sectional analysis of stacks of Fe-Co clusters/NPs deposited at distinct temperatures. Up to a deposition temperature – T_d of RT (~25 °C), the grain size is identified small as much as 10 nm with homogeneous distribution in microstructure.

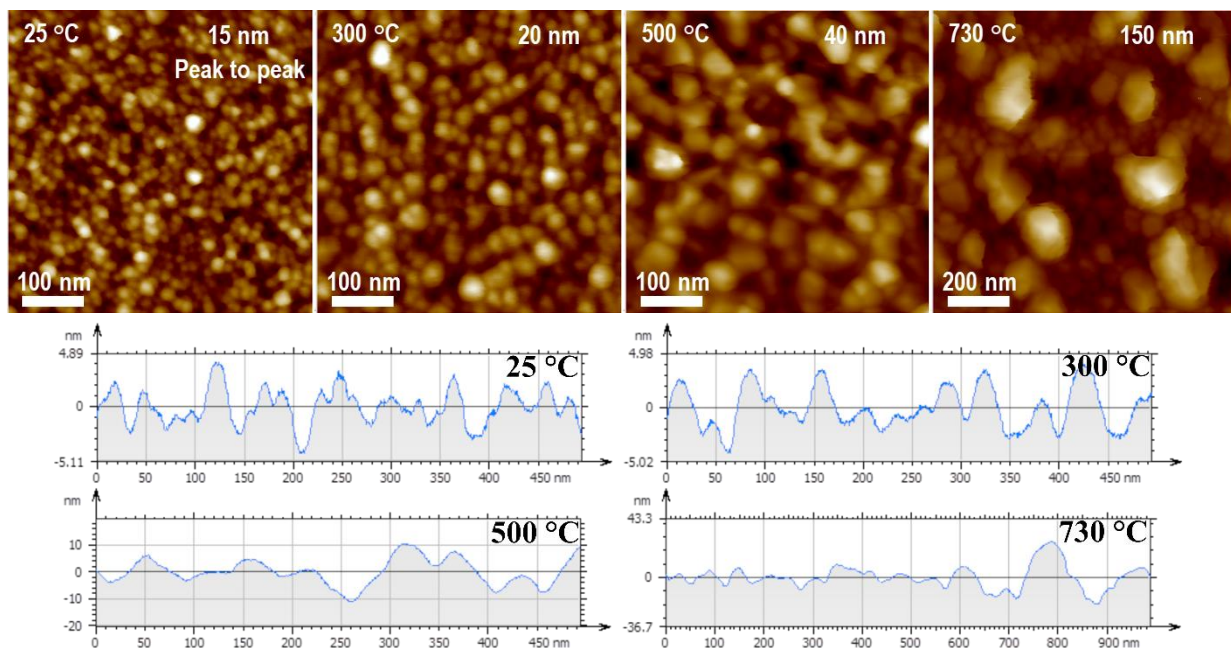


Figure IV.8: The AFM cross-sectional analysis of lines crossing the middle images and the surface morphology of stacks of Fe-Co clusters/NPs deposited onto Si/SiO₂ (100 nm) in one hours at various deposition temperatures – T_d , which are below and above the transition temperature of 647°C for Fe₆₅Co₃₅ from ordered phase (B2) to disordered phase (A2).

Note that, with AFM measurement and this scale, the actual grains size can be smaller (see the cluster/NPs on TEM grid analyzed previously) owing to the convolution of the AFM probe (reference ACT series, the nominal spring constant of $k = 34$ N/m and frequency of $f_0 = 300$ kHz, tip ROC 6 nm guaranteed <10

nm). The average grain sizes apparently increase with T_d , which is corresponding to the results deduced from XRD (shown in Table IV.3). The coalescence of the microstructure starts being observed with samples deposited at higher T_d of 300°C, 500°C and 730°C. At the T_d above and close to FeCo alloy transition temperature of 647°C, it is clear that the microstructure is of two layers (top and underlying layers). While the underlying layer has homogeneous microstructure (average grain size is relatively smaller than those deposited at 500 °C), there exists some big grains are grown on top of underlying layer, evidenced for stacks of NPs deposited at 730 °C, which leads the peak to peak value for this sample rise up to 150 nm. The observed coarsening of the microstructure with increased T_d is mostly taken place in the x and y directions (samples' planes) (as evidenced in AFM cross-sectional profiles), which is indicated by the relative height of cross-sectional analysis for the four stacks of NPs. These observations are re-confirmed in the SEM images in Figure IV.9.

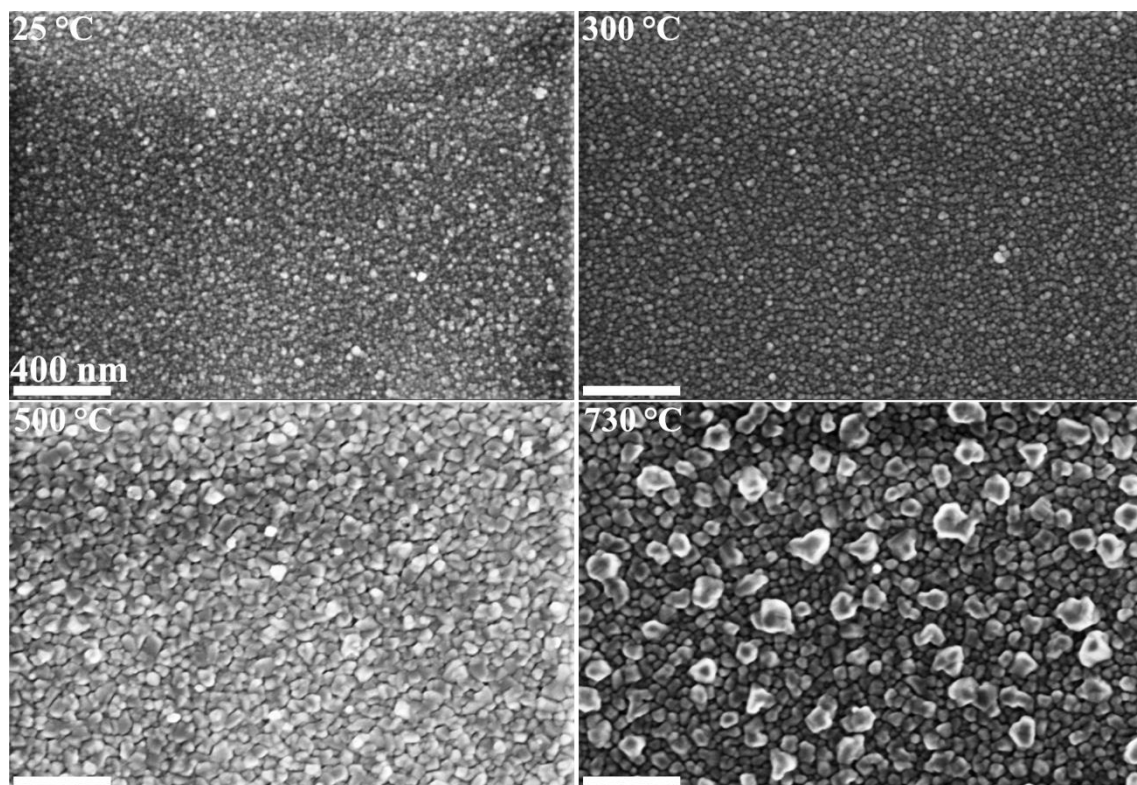


Figure IV.9: Plane-view SEM images (Inlens mode) for stacks of NPs deposited at various deposition temperatures – T_d from RT to 730°C, on Si/SiO₂ substrates.

Samples deposited at RT ~25°C, 300°C and 500°C depict a relatively low z -height, in stark contrast, 730°C deposited sample shows obvious bi-layers with the underlying has comparable z -height as the others. An estimation reveals grain size of such stacks of NPs increasing with the deposition temperatures, e. g., from ~10 nm (RT), ~40 nm (500°C) up to 200 nm (730°C). Figure IV.9 demonstrates the plan-view SEM images of those stacks of NPs. It is clearly that microstructure is distributed homogeneously through the samples' surfaces (deposited at temperatures \leq 500°C), while higher deposition leads to at least bimodal grain size distributions owing to the coarsening effect, which could enable Ostwald ripening [209]. This Ostwald ripening could be comprehended in terms of thermodynamics, for which, larger particles are more favorably energetic than the smaller ones (more stable). In other words, larger grains grow bigger at the expense of smaller ones, which are attributed to the surface area to volume ratio (S/V), the smallest particles (crystallites) are of the largest S/V ratio. These crystallites are more likely to be melted and steadily deposited on the remaining crystals, which

were previously larger to begin with once temperature rises up. This kind of growth gives chance on bigger grains becoming bigger, while smaller grains get smaller [209]. Increasing deposition temperatures – T_d simply raises the high possibility of the Ostwald ripening taking place and leading to the growth in grain size. The increase in grain sizes with respect to T_d is in good agreement with the XRD observation, at which the relative highest intensity of FeCo (110) reflection is observed compared to the same

orientation of other samples deposited at lower temperatures. This means that bigger grains give rise in a long range crystallized order.

Figure IV.10 shows the dependence of rms roughness, deduced from AFM surface morphologies displayed in Figure IV.8, on deposition temperatures – T_d . The rms roughness remains low in all the samples, it increases from ~2-4 nm at 500°C to about ~18 nm at 730°C, which coincides with the formation of bimodal grain size distribution (very separated larger grains and compact smaller ones of ~200 nm and ~40 nm respectively shown Figure IV.9).

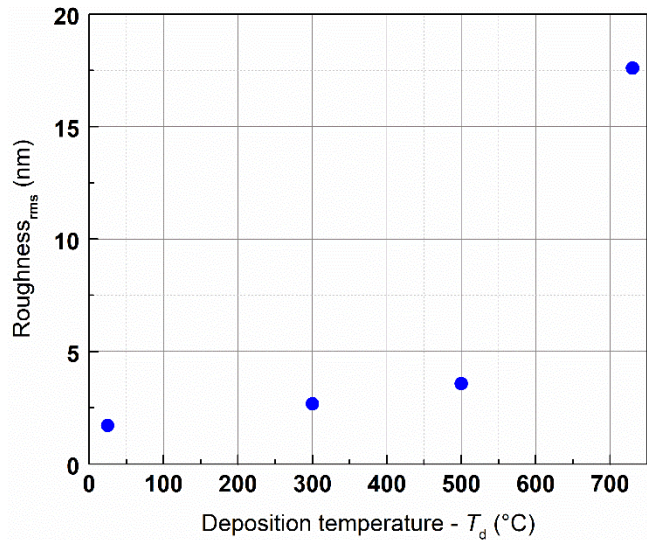


Figure IV.10: The AFM rms surface roughness of stacks of FeCo NPs as a function of deposition temperatures – T_d .

IV.1.5. Magnetic properties

The development of NPs (stacks of NPs) described in IV.1.4 including deposition at various temperatures and on sufficiently large enough surfaces that are able to be characterized with magnetic measurement. It is worth noting that the samples were covered by a few nm of C to prevent the oxidation problem. This section is about presenting the results from the characterizations of stacks of soft NPs, i. e., Fe₆₅Co₃₅ NPs.

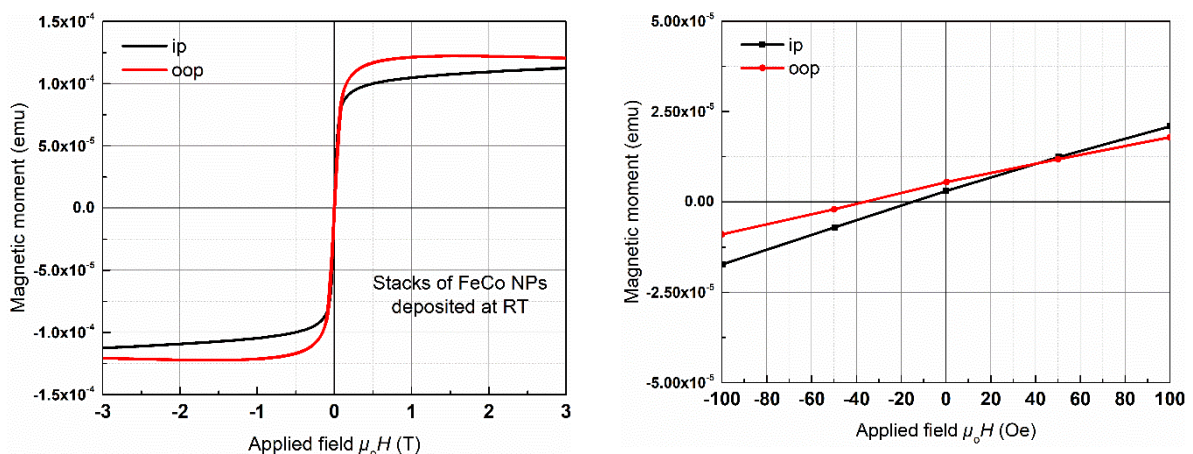


Figure IV.11: The magnetic response of 100 nm thickness of stacks of FeCo NPs (averaged diameter of around 4 nm) measured as the applied field is perpendicular (*oop*) and parallel (*ip*) with the substrate at RT in (left) large range of applied field (± 3 T) and (right) a zoom (± 10 mT).

Full magnetic hysteresis loops at RT of such stacks of NPs deposited at RT and later carried out for both *ip* and *oop* measurements are shown in Figure IV.11. In Figure IV.11-left, both *ip* and *oop* hysteresis loops are of the same shape and show single phase behavior, in which the sample is more

readily saturated in ip direction than oop one. However, the saturation magnetization at 3 T, $\mu_0 M_{s-3T}$, depicts a slight variation, i. e., ~ 2.1 T for ip and ~ 2.3 T for oop, which might be attributed to the difference in preferential crystallization direction of the NPs with respect to the substrate surfaces.

An enlarged range of half cycle of hysteresis loops is compared in Figure IV.11-right. A coercivity $-\mu_0 H_c$ of about ~ 15.6 Oe (1.56 mT) is observed for ip measurement, while a higher coercivity of ~ 35.8 Oe (3.58 mT) is obtained for oop measurement. It is also visible that the sharpness of the hysteresis loop when it approaches coercivity is higher for ip measurement than oop loop. The coercivity and saturation at high applied field suggest that the sample might have isotropic properties.

From (Equation I.7) for simplicity, the anisotropy field can be rewritten as $H_a = 2K_{\text{eff}} / \mu_0 M_s$, where K_{eff} is the effective anisotropy constant. Thus, the effective anisotropy constant for the stack of FeCo NPs, extracted from ip and oop hysteresis loops in Figure IV.11a, was estimated of about ~ 72 kJm $^{-3}$. This K_{eff} is higher than the value of ~ 42 kJm $^{-3}$ in a system of NPs with average diameter ~ 3.2 nm obtained from effective Magnetic Anisotropy Energy (MAE) approach at 2 K [163]. This variation might be attributed to both (i) the different NPs' sizes, which profoundly influence the magnetic properties of the system of NPs; and (ii) the measurement temperature is at 2 K, which practically favors the magnetic properties. Moreover, in the case of stacks of the NPs, magnetic properties of isolated NPs [163] is usually enhanced as compared with the interconnected NPs (evidenced in the TEM image in section IV.1.2).

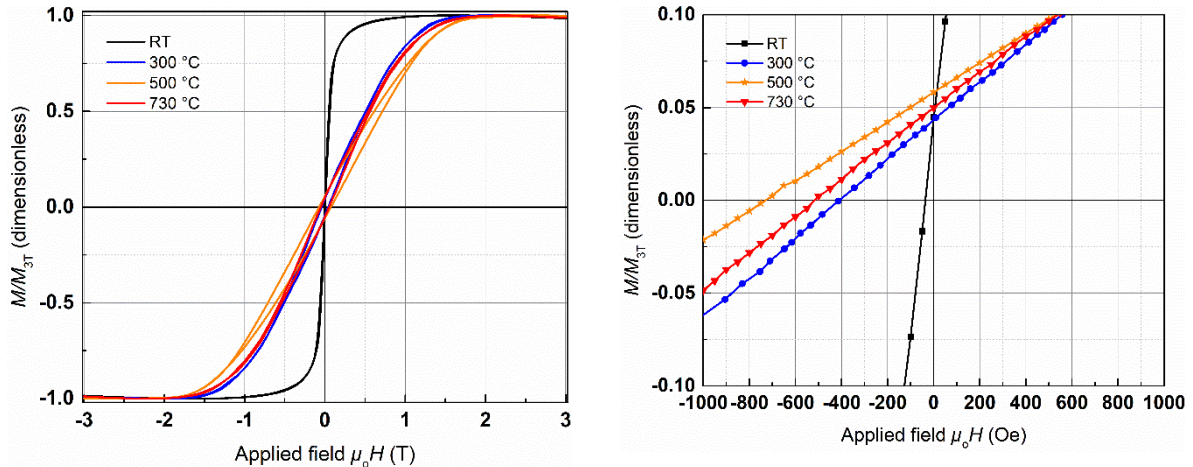


Figure IV.12: The magnetic response of 100 nm thickness of stacks of FeCo NPs at different deposition temperatures $- T_d$ (averaged diameter of around 4 nm) measured as the applied field is perpendicular (oop) with the substrate in (a) large range of applied field (± 3 T) and (b) a zoom (± 100 mT).

Hysteresis loops at RT were carried out for all four samples deposited at different T_d in a full scale (± 3 T, Figure IV.12-left) and an expanded scale (± 100 mT-Figure IV.12-right), and the experimental magnetic results for these measurements are presented in Table IV.4. Generally, while the $M(H)$ loops of samples deposited at RT behaves like NPs alone, the other samples deposited at higher T_d magnetically acts as thin films. The variation in structural and microstructural properties is discussed previously in section IV.1.4 as well as reflected by the other magnetic properties, whose values are varied with T_d . From Table IV.4, while the coercivity is jumped from ~ 3.6 mT for RT deposited sample to a maximum of ~ 70.4 mT for 500 °C deposited sample and later reduces as T_d goes beyond, the other extracted magnetic properties of saturation magnetization- $\mu_0 M_{s-3T}$, remanence ratio- M_{r-0T}/M_{s-3T} are varied very little but also reach maxima for 500 °C deposited sample. Additionally, the critical diameters of domain size, given by

$2r_c = 9\sigma_w^B / (\mu_0 M_s^2)$ (see section I.1) extracted from $M(H)$ loops, are practically stagnant and achieve a minimum for 500 °C deposited sample. It is noteworthy that the Bloch domain wall-width of Fe $_{65}$ Co $_{35}$ is

about 113 nm (given in Table I.2, section I.1). The reduction in magnetic properties may be ascribed to either the phase transformation from ordered B2 phase to disordered A2 phase when T_d exceeds more than transition temperature of 647°C, or the significant modification in microstructure with respect to critical domain size. As indicated in section IV.1.4, the grain sizes, for stacks of NPs deposited at elevated temperatures, ranging from ~40 nm ($T_d \leq 500^\circ\text{C}$) up to ~200 nm ($T_d = 730^\circ\text{C}$) will contain multiple domains. When the grain sizes become bigger ($T_d = 730^\circ\text{C}$) that will give rise to facilitate magnetization reversal through domain wall motion and cause a reduction of coercivity. Contrary to samples deposited at lower $T_d \leq 500^\circ\text{C}$, the microstructural defects being present at the interface region and/or limitation in grain sizes will act as pinning centers that hinder the magnetization reversal during domain wall motion under the external applied field and lead to enhancement of coercivity. It is obvious that applying heat treatment is required, which encourages better crystallization and variation in microstructure, and hence the magnetic properties of NPs/stacks of NPs will be accordingly controlled.

Previous discussion shows that applying heat treatment is necessary to improve the crystallization and magnetic properties. Nevertheless, conventional annealing (low heating rate and longer annealing time) will destroy the magnetic properties of soft-hard nanocomposites owing to the diffusion (details in Chapter V). In order to understand the change in properties of stacks of FeCo NPs under RTP conditions, the stacks of FeCo NPs deposited at RT was later subjected to optimized RTP conditions (obtained in section III.4), i. e., at 750°C, 50°C/s, 60 s and 1×10^{-1} mbar of Ar flow. The structural and microstructural properties (examined by $\theta - 2\theta$ XRD, AFM and SEM) of the RTP annealed sample exhibit mostly unchanged when compared with the sample in as-deposited state.

Table IV.4: The experimental magnetic properties of stacks of Fe₆₅Co₃₅ NPs deposited at various temperatures ranging from RT to 730°C.

Magnetic properties	Deposition temperatures – T_d (°C)			
	RT	300	500	730
<i>oop</i> – $\mu_0 H_c$ (mT)	3.6	40.9	70.4	51.6
<i>oop</i> – $\mu_0 M_{s-3T}$ (T)	2.3	2.37	2.4	2.39
Critical domain size – $2r_c$ (nm)	4.9	4.6	4.4	4.6
<i>oop</i> – M_{T-0T}/M_{s-3T} (%)	4.2	4.4	5.8	5.0

* Note that there might be a certain error bar of about 5 – 10 % relating to the saturation magnetization at 3 T ($\mu_0 M_{s-3T}$) owing to porosity problem. All the calculation for magnetization revealed in this work concerning either stacks of NPs or magnetic nanocomposite (NPs inside the matrices), is subjected to 50 % porosity.

Figure IV.13-left shows $M(H)$ loops, for 100 nm stacks of FeCo NPs annealed at optimum RTP conditions, in different directions of ip and oop. Though the ip and oop $M(H)$ loops have slightly different loop shapes, they both display single phase magnetic behavior and behaves as soft magnetic thin films, which attributed to the effect of annealing. Likely the stacks of NPs in as-deposited state presented above, the sharpness of the hysteresis loop when it approaches coercivity is lower for oop loop than ip one. It is evident that the sample measured in ip direction much easier approaches saturated state than oop direction, e. g., almost saturated at applied field of ~0.5 T in ip direction compared with ~1 T in oop measurement. In addition, not only the saturation magnetization at 3 T, $\mu_0 M_{s-3T}$, for both ip and oop measurement is augmented in comparison with as-deposited state sample, namely, ~2.2 T and ~2.4 T, but also the M_{T-0T}/M_{s-3T} increases from 2.8 % to 6.3 % and from 4.2% to 7.0 % for ip and oop measurements respectively. The effective anisotropy constant boosts up to $K_{\text{eff}} \sim 780 \text{ kJm}^{-3}$ from a value of 72 kJm^{-3} , which is of the same increasing tendency with the development of coercivity for the annealed stacks of NPs. An enlarged

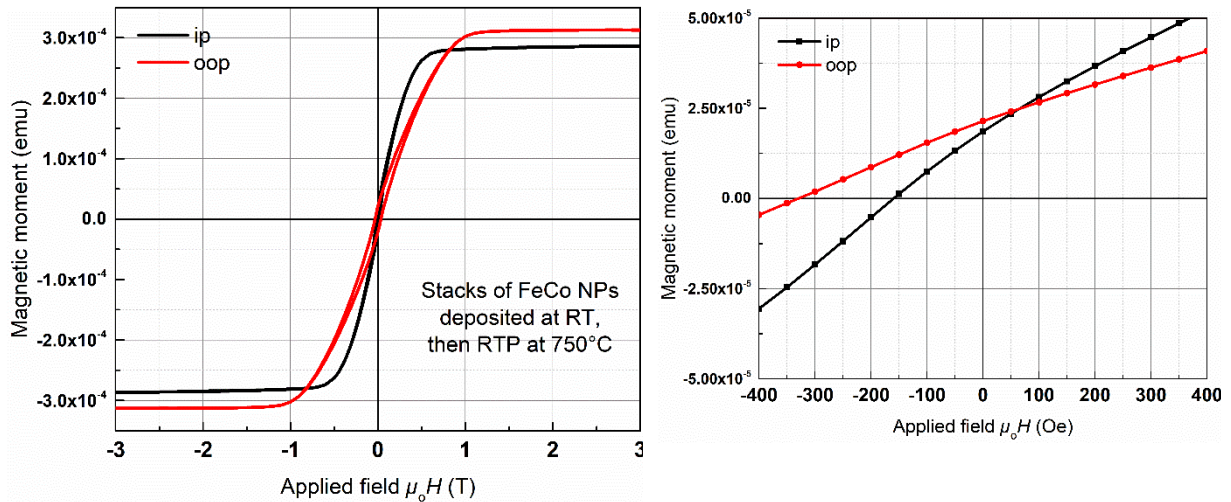


Figure IV.13: The magnetic response of 100 nm thickness of stacks of FeCo NPs (averaged diameter of around 4 nm) measured as the applied field is perpendicular (*oop*) and parallel (*ip*) with the substrate in (a) large range of applied field (± 3 T) and (b) a zoom (± 40 mT) for sample annealed at 750°C by RTP, 60s.

zoom of half cycle hysteresis loops of annealed sample is shown in Figure IV.13-right. By applying RTP the coercivity of the stacks of NPs is also enhanced, i. e., it expands nearly 10 folds in magnitude from 15.6 Oe to ~ 156.5 Oe (15.7 mT) and from 35.8 Oe to ~ 329.5 Oe (~ 33 mT) accordingly when measured in *ip* and *oop* directions (to the substrate surface). The values of saturation magnetization are just slightly under the value of 2.45 T for B2-Fe₆₅Co₃₅ phase, which might be the partially oxidized stacks of NPs as indicated previously by XPS. Additionally, the augmentation of other properties such as $\mu_0 H_c$, $M_{T=0T}/M_s$ and K_{eff} might be assigned to crystallization at long range order of most NPs with the help of RTP, even RTP process does not affect much on NPs in terms of structural and microstructural properties (based on $\theta - 2\theta$ XRD and SEM investigations). These observations are well agreement with the results obtained from others, where NPs were analyzed (by TEM) after annealing and were proved that the long range order crystallization is obviously enhanced [163].

IV.2. Chapter highlights

This chapter is concentrated on the fabrication and characterizations of FeCo NPs using a Free Cluster Generator (FCG) based on the nucleation of NPs induced by a strong gas-quenching of the plasma plume created by laser ablation into a dedicated cavity. The varying in opening t – time of the pulsed gas valve strongly involves both deposition rate and size of the NPs. Under the synthesizing condition, the diameters of the FeCo NPs are well-controlled in the range 2 nm – 5 nm, with very narrow size distribution (± 0.2 nm). The sizes of the NPs are below the twice domain wall width of the hard magnetic phases, 8.0 nm and 12.8 nm for Nd₂Fe₁₄B₁ and L1₀-FePt phases respectively. All the NPs are crystallized at RT. The composition of the NPs depends on the target. No major variation in compositional ratio has been observed in the case of Fe₆₅Co₃₅ NPs when changing the deposition temperature. The evolution in microstructure of stacks of NPs is strongly induced by Ostwald ripening with respect to deposition temperatures. High saturation magnetisation values of > 2 T are obtained for the stacks of NPs (with both one-step and two-step annealing).

Chapter V. Nanocomposites-soft magnetic NPs assemblies embedded in hard matrices

This chapter elucidates the results and discussions mostly related with Soft in **HA**rd **MA**gnetic Nanocomposites based FePt matrices. The elemental blocks of hard magnetic matrices and soft magnetic nanoparticles presented in Chapter III and Chapter IV were integrated, building FePt/FeCo, FePt/Co trilayers and FeCo and Co NPs embedded in FePt matrices (various soft volume contents, soft phase dimensions, architectures). The soft magnetic assemblies inside the FePt matrices will be investigated and discussed in more details. The nanocomposites based NdFeB material are not selected in this thesis owing to the surplus of Nd in excess, and sensitivity in oxidation, which strongly influences the overall properties of the nanocomposites and it is challenging to quantify the contribution of soft and hard phases.

As indicated in section III.4 for FePt thin films subjected to RTP, the annealed RTP sample (at 1×10^{-1} mbar of Argon flow, 750°C , 50°C/s and 60s) achieved highest coercivity of around 4.4 T with multiple-magnetic phase behavior, while other annealed RTP film (at 1×10^{-1} mbar of Argon flow, 750°C , 50°C/s and 10s) revealed single magnetic phase behavior with elevated coercivity of ~ 2.3 T. It is therefore, all the nanocomposites with fixed 15 nm FePt thin film reported hereafter will be annealed inside RTP system with the recipe of 1×10^{-1} mbar of Argon flow, 750°C , 50°C/s , 60s and/or 10s, at which the RTP schematic was presented in Figure III.12. The important role of diffusion is also investigated in theoretical and experimental approaches. For better preventing diffusion, Ta spacers are introduced between the FePt layer and NPs.

V.1. Tri-layer FePt/FeCo (or Co)/FePt systems of continuous layers

This section presents the results obtained for an FePt/FeCo (or Co)/FePt trilayer fabricated by conventional PLD at RT, and then applied optimal RTP conditions.

V.1.1. Structural and microstructural characterizations

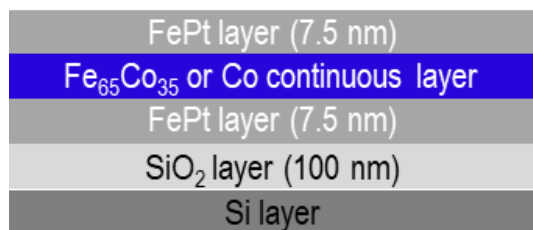


Figure V.1: The schematic diagram of FePt-FeCo/Co sandwich structured continuous film.

This section is about to reveal the results related to a sandwich structured sample of Si/SiO₂/FePt/Fe₆₅Co₃₅ (or Co)/FePt with soft magnetic continuous layers fabricated by pure conventional PLD. The trilayers were deposited at the sample conditions described in section III.4 and later subjected at the optimum RTP conditions given above in 60s.

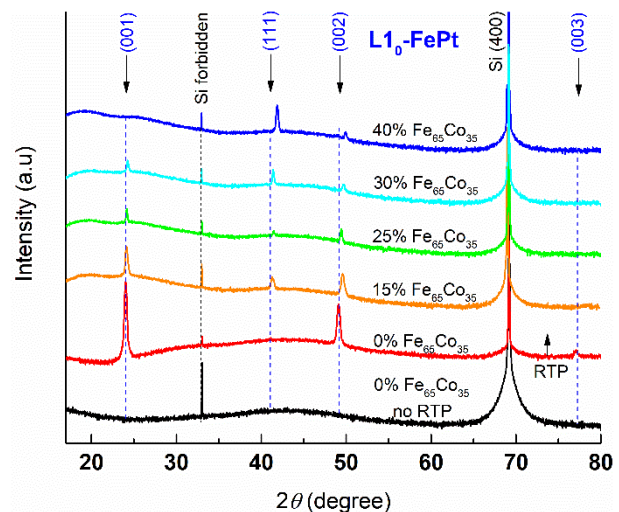


Figure V.2: The evolution in structure of the as-deposited sample and annealed samples with RTP at 750°C , 50°C/s , in 60 s, and in 1×10^{-1} mbar of Ar flow as a function of the Fe₆₅Co₃₅ volume content.

The FePt, Fe₆₅Co₃₅/Co layers were all deposited at laser fluence of $\sim 5 \text{ J.cm}^{-2}$. Figure V.1 presents the schematic diagram of such heterogeneous sandwich system, in which the total FePt thickness will be kept

at a constant of 15 nm, while the Fe₆₅Co₃₅ (or Co) continuous layer is varied corresponding to the dilution of Fe₆₅Co₃₅ (referred as soft) volume fractions. The central goal of this section is about to explain the effect of either Fe₆₅Co₃₅ (or Co) continuous layers with different volume fractions on properties of the system. Note that across through this chapter, once this study mentions to soft or hard phase/layer, which means Fe₆₅Co₃₅ (or Co) or FePt materials. Note that the FeCo is sometime written instead of Fe₆₅Co₃₅.

A set of sandwich sample with various soft content ranging from 0% (or 0 nm) to 40% (or 10 nm, 60% FePt) capped in a constant thickness of 7.5 nm of each FePt layer. Figure V.2 compares the XRD patterns of the as-deposited sample and annealed samples (RTP at 750°C, 50°C/s, 60s) as a function of the Fe₆₅Co₃₅ volume content. For sample with 0% Fe₆₅Co₃₅ content (100% FePt), after annealing, the film demonstrates significant signature of (001) L1₀-FePt. Previous discussion in section III.4.1 demonstrated this annealed sample has strong oop texture, with high values of *LOF* and *S* parameters close to the unity (details about calculation of *LOF* and *S* were given in section III.3). Any addition of Fe₆₅Co₃₅ content reduces such oop texture by introducing the (111) L1₀-FePt reflection. Additionally, the relative intensity of the (001) L1₀-FePt peak decreases gradually with increasing Fe₆₅Co₃₅ content, at which the (001) L1₀-FePt orientation disappear for sample with 40% Fe₆₅Co₃₅ content. As a result, an estimation indicates that the values of *LOF* and *S* parameters are weaken to negative and close to 0, respectively, for sample with 40% Fe₆₅Co₃₅ content. This is coherent with preferential (111) reflection rather than (001) of L1₀-FePt phase at high Fe₆₅Co₃₅ content.

Moreover, there is a shift in the peak positions of both (111) and (002) orientations. This shift becomes higher and higher when the Fe₆₅Co₃₅ content increases. The shift in peak position might be attributed to the diffusion between the tri-layers, and thus destroy the L1₀-FePt phase in sample with notably high Fe₆₅Co₃₅ content. The TEM observations (Figure V.9, section V.2.2) show that the layer deposited by PLD, at RT, has a very smooth surface. In the samples studied here, the flat Fe₆₅Co₃₅ continuous layer is capped by two smooth FePt layers, under the annealing, high possibility of diffusion will occur. The lost in L1₀-FePt in sample with 40% Fe₆₅Co₃₅ (total 70% Fe and Co in the sample) agrees well with the phase diagram given in Figure I.11a, at which the L1₀-FePt is preserved with the soft content of Fe (and/or Co) as high as 65%. In comparison between the layer-layer structured samples and NPs inside the matrix (which will be presented in section V.3), the layer-layer studied here is of higher diffusion, which is in agreement with other magnetic XMCD observation [235].

Figure V.3 presents the variation in surface topographies of the samples with different volume fraction of the hard phase FePt, inspected by SEM. In comparison between the tri-layer samples of 85 % FePt with soft magnetic layer from Co (Figure V.3a) and Fe₆₅Co₃₅ (Figure V.3b), they have similar microstructure with a mixture of isolated islands and interconnected islands. A high resolution SEM image taken with Inlens mode shown inset of Figure V.3b illustrates that besides the grains (gray color) on top, an underlying layer composed from multiple smaller grains are observed (the gray grains inside the white background). The inset of Figure V.3b might suggest that (i) These islands (composed of mixture of FePt and FeCo (or Co)) residing on the surface of SiO₂, which means the RTP the global change for the whole tri-layer samples; or (ii) These islands (composed of just FePt-top layer) residing and implanting into FeCo (or Co) layer, which means the RTP induces a local change taking place on the surface of the samples. Details on this effect will be discussed in the section V.2. Not only the density of grains but also the reduction in grain sizes increase with increasing volume fraction of soft phase (or reversely proportional to the hard phase of FePt volume fractions), which clearly demonstrated in the Figure V.3c and d. Such either increase of grain density or reduction of grain size could be ascribed to the variation in chemical composition traversing through film thickness (because of tri-layer structured with different composition), which induces the defect favoring the grain growth. Note that the grain sizes from tri-layer

structured sample are all smaller than sample with FePt on presented in Figure III.31 at the same annealing conditions. The AFM performed on these surface morphologies reconfirmed the observation from SEM results. While rms roughness for samples (with 15% of either Co or Fe₆₅Co₃₅) is equivalent to ~2.6 nm, it becomes slightly higher in sample with 30% Fe₆₅Co₃₅ and higher in sample with 40% Fe₆₅Co₃₅ (10 nm).

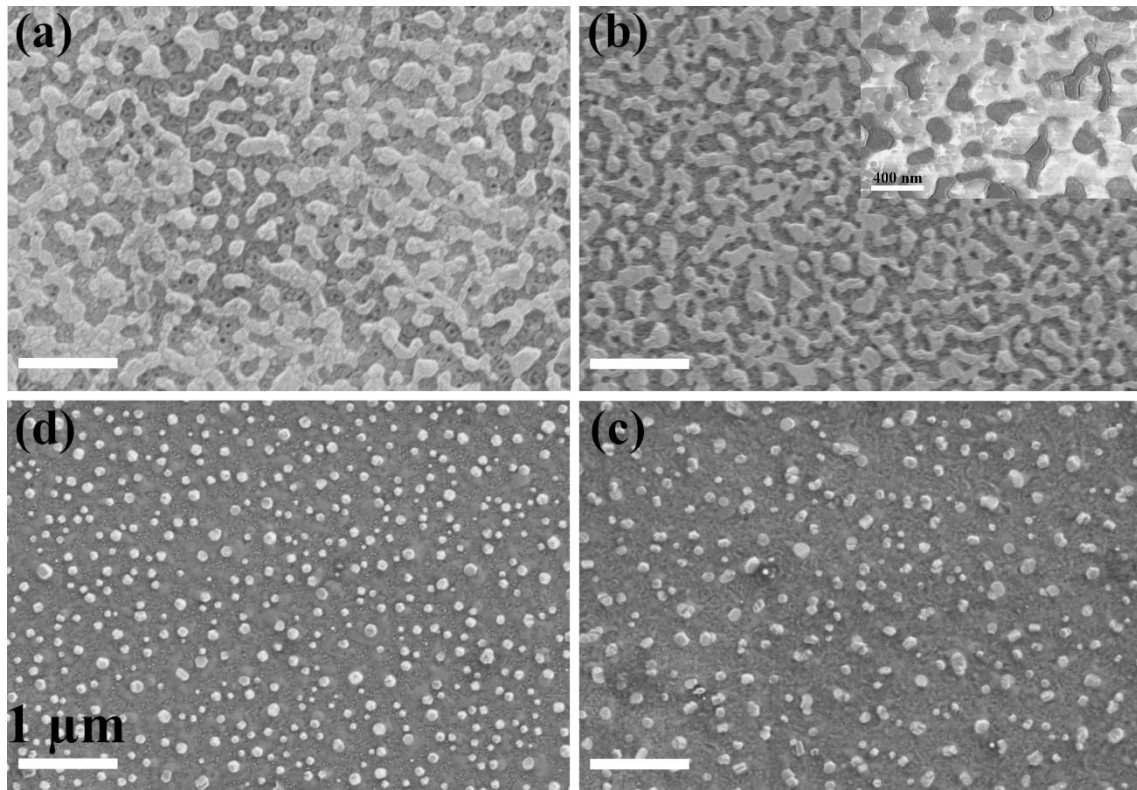


Figure V.3: Plane-view SE – SEM images of the tri-layer FePt/Fe₆₅Co₃₅ (or Co)/FePt films as a function of Fe₆₅Co₃₅ (or Co) volume content, deposited at RT on Si/SiO₂ and then applied RTP heat treatment at 750°C, 50°C/s, 60s, 1×10⁻¹ mbar of Argon flow. (a) 15% Co; (b) 15% Fe₆₅Co₃₅; (c) 30% Fe₆₅Co₃₅; and (d) 40% Fe₆₅Co₃₅. Inset of figure (b) displays a high resolution plane-view Inlens SEM image of the film. Note that the contrast (black and white parts) is reserved between the SE and Inlens images.

V.1.2. Magnetic characterizations

The dependence of magnetic hysteresis loops of tri-layer structured samples as a function of soft phase percentage is given in Figure V.4a. The overall loop shape of hysteresis curves is proportional to the soft phase percentage inside the tri-layer systems. Namely, $M(H)$ loops are almost independent to the elements inside the structures, reflected by the similar loop shapes, coercivity, remanence ratio – M_{0T}/M_{7T} for samples deposited with 15% of soft phase of either Co or Fe₆₅Co₃₅. Increasing the soft phase content induces poorer magnetic properties in terms of loop shapes, coercivity, and M_{0T}/M_{7T} . However, all of the samples demonstrate single magnetic phase behavior indicated in Figure V.4b, for which there is one single peak centered close to the coercive field. Note that 100% FePt sample possesses poorer loop shape but better coercivity of 4.4 T and M_{0T}/M_{7T} of 0.93 (presented in Figure III.29). The variation of coercivity, remanence – $\mu_0 M_r$, and M_{0T}/M_{7T} with the Fe₆₅Co₃₅ volume content, modulated by changing the thickness soft magnetic layer (Co or Fe₆₅Co₃₅), is plotted in Figure V.4c. While magnetic properties ($\mu_0 M_r$, M_{0T}/M_{7T}) vary little as long as the soft magnetic content increased to 15% of the total volume, the coercivity plummets from 4.4 T to approximately 1 T in sample with 15% soft phase content. Further increase in the soft magnetic volume leads to reduction of all investigated magnetic properties.

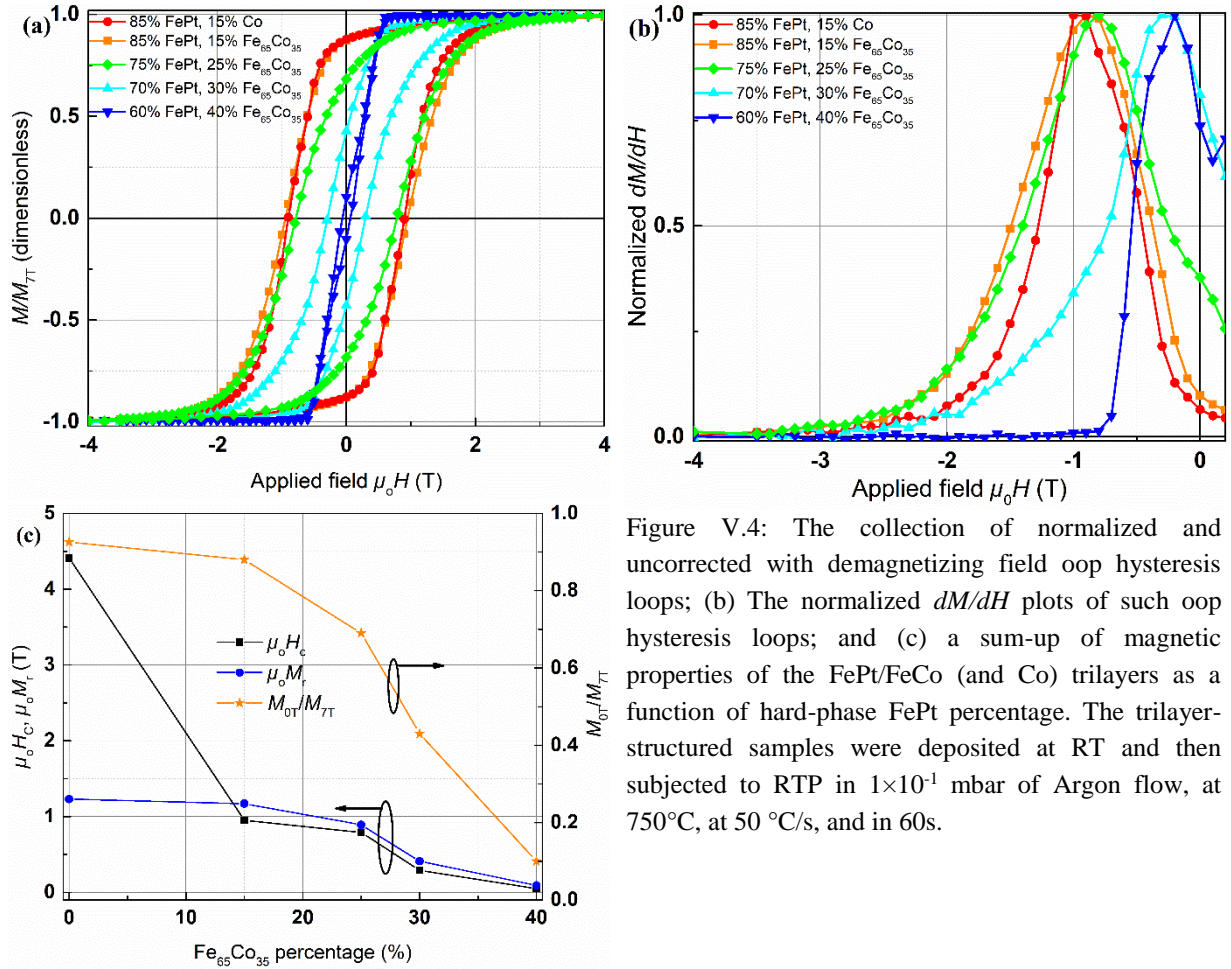


Figure V.4: The collection of normalized and uncorrected with demagnetizing field oop hysteresis loops; (b) The normalized dM/dH plots of such oop hysteresis loops; and (c) a sum-up of magnetic properties of the FePt/FeCo (and Co) trilayers as a function of hard-phase FePt percentage. The trilayer-structured samples were deposited at RT and then subjected to RTP in 1×10^{-1} mbar of Argon flow, at 750°C , at 50°C/s , and in 60s.

The single magnetic behavior observed in all tri-layer structured samples (with soft phase content) suggests that exchange coupling between the soft magnetic layer (Co or $Fe_{65}Co_{35}$) capped by the two hard magnetic layers of FePt was initiated. One possibility in explaining such properties might be attributed to the interdiffusion between the soft and hard magnetic layers, which introduces different intermixing states. The interdiffusion between the tri-layer systems could happen owing to the adjustment of the composition with an intermediate diffused layer between the soft and hard layers to form CoFePt mixing state [235]. That means the interdiffusion leads to a reduction of anisotropy of the FePt layer, and the coercivity is reduced as a result. The coercivity of up to 1 T with 15% soft phase is still achievable thanks to the phase diagram of FePt system in Figure I.11a, the content of Fe (and/or Co) in the material could be as high as 65% at, while the $L1_0$ -FePt (and/or CoPt) phase is still being kept. Other authors indicate that in layer-layer of hard-soft structured sample, the magnetization of the soft layer (in this case, it is Co and/or $Fe_{65}Co_{35}$) is pinned at the interface of the hard layer and would switch reversibly [28]. The reduction of coercivity observed in this work is in good agreement with results obtained from others [28] as the thickness of the soft layer increases. The square $M(H)$ loop for sample with 15% addition of soft phase is coherent with single magnetic phase behavior and suggests that the soft magnetic layer is strongly coupled to the hard layer. The saturation magnetization $-\mu_0 M_s$ is found to grow with increase of soft phase content.

A detailed analysis for the magnetic reversal of such soft-hard magnetic heterostructures is also revealed, which mostly deals with how the dimensions, relative volume fractions, and geometry of the soft and hard phases affect properties such as the coercivity, $(BH)_{\max}$. Thanks to the theoretical/simulation approaches, it turns out that the dimensions of the soft phase contribute the key role in controlling the switching behavior of soft-hard magnetic samples [31]. According to Table I.2, the domain wall width –

δ_w of the hard phase L1₀-FePt is about 6.4 nm, while the anisotropy constant K_1 of the soft phase (Fe₆₅Co₃₅, 20 kJm⁻³) is much smaller than that of hard phase (L1₀-FePt, 6600 kJm⁻³). In all case studies in Chapter V, the total thickness of the hard phase-FePt is kept at a constant of 15 nm, while the soft phase content (with 2.45 T = $M_{s,soft}$ of Fe₆₅Co₃₅ ~0.58 $M_{s,hard}$ of L1₀-FePt) can be modulated and expressed in percentage (%) or thickness (nm). For instance, a tri-layer sample with 25 % soft phase Fe₆₅Co₃₅ corresponds to (15 nm/75 %)×25 % = 5 nm Fe₆₅Co₃₅ layer, 30 % is equivalent to ~6.4 nm. Hence, magnetic reversal of the tri-layer structured films is given by one of the two following cases depending on the thickness of the soft phase – t_{soft} [31]:

- **Case 1:** With $t_{soft} \leq \delta_w$, the two phase are well coupled, and the average nucleation field is re-written from (Equation I.13) as follows:

$$\mu_o H_N = 2(t_{soft} K_1^{soft} + t_{hard} K_1^{hard}) / (t_{soft} M_s^{soft} + t_{hard} M_s^{hard}) \quad (\text{Equation V.1})$$

in which the two magnetic phases of the two layers (soft and hard) switch at the same H_N , inducing a rectangular hysteresis loop.

- **Case 2:** With $t_{soft} > \delta_w$, the coercivity of the soft layers reduces drastically, thus the properties of the tri-layer samples are degenerated, which could be attributed to the soft layer nucleates magnetic reversal at the applied field well below than that of the hard layer.

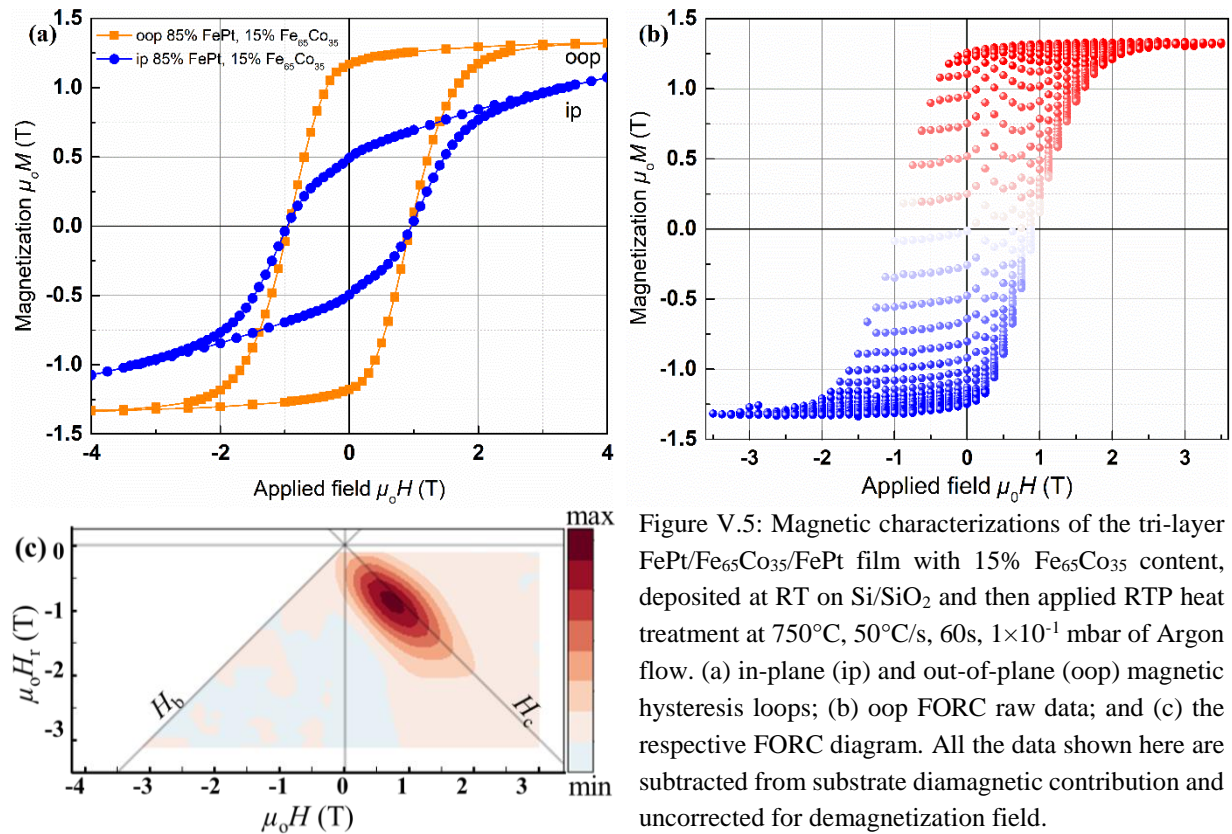


Figure V.5: Magnetic characterizations of the tri-layer FePt/Fe₆₅Co₃₅/FePt film with 15% Fe₆₅Co₃₅ content, deposited at RT on Si/SiO₂ and then applied RTP heat treatment at 750°C, 50°C/s, 60s, 1×10⁻¹ mbar of Argon flow. (a) in-plane (ip) and out-of-plane (oop) magnetic hysteresis loops; (b) oop FORC raw data; and (c) the respective FORC diagram. All the data shown here are subtracted from substrate diamagnetic contribution and uncorrected for demagnetization field.

Regarding the **case 1**, the variation in thickness of the soft layer of Fe₆₅Co₃₅ from ~2.6 nm (15 % soft) to 5 nm (25% soft), and from 5 nm to 6.4 nm (30% soft, ~ δ_w) leads to 7.5% (6.1 T to 5.6 T) and 4.5% (5.6 T to 5.4 T) reduction in nucleation field (obtained from (Equation V.1)), respectively. However, the coercivity falls far short of 22% (0.88 T to 0.69 T) and 38% (0.69 T to 0.43 T) for the same variation of thickness. While the **case 1** leads to intermediate decrease in the values of both nucleation field and coercivity, the **case 2** induces a dramatic decline of up to 10% (5.4 T to 4.9 T) and 77% (0.43 T to 0.10

T), respectively, when the Fe₆₅Co₃₅ thickness varies from 6.4 nm (30% soft, $\sim\delta_w$) to 10 nm (40% soft). The larger change in coercivity compared to nucleation field suggests that other factors involve to the reversal process, e. g., the variation of anisotropy of the hard phase (with soft layer), defects, interdiffusion between the soft and hard phase, and inhomogeneity.

More advanced and time-consuming measurement was made on tri-layer structured films containing 15% Fe₆₅Co₃₅ (or $2.6 \text{ nm} < \delta_w = 6.4 \text{ nm}$ of L1₀-FePt) to explore more details the effect of soft layer on overall magnetic properties of the tri-layer system. Figure V.5a compares the uncorrected for demagnetization field of ip and oop hysteresis loops. The comparable coercivity of $\sim 0.95 \text{ T}$ in ip and oop measurements reflects that the oop-texture property was not induced in the annealed tri-layer structured films. This observation agrees very well with the XRD patterns for this sample, at which the additional (111) reflection is indicated. Extrapolating the ip and oop $M(H)$ loops provide an intercepted value of around 7 T, which is $\sim 40 \%$ lower than the magnetocrystalline anisotropy of the L1₀-FePt phase (11.6 T). A small kink at small applied field ($\mu_0 H \sim 0 \text{ T}$) in the ip hysteresis loop suggests that the magnetic properties of the presented sample do not come up with dipolar coupling, which according to other authors' implication, any extra spacer layer (or other phases) between the soft and the hard layer could induce a shoulder (kink) in the in-plane $M(H)$ loop [32]. However, the square easy-axis oop loop indicates that the soft magnetic layer of Fe₆₅Co₃₅ is rigidly coupled to the neighboring hard layers of FePt, which induces the layers coherently switched [87]. The drop in magnetocrystalline anisotropy, coercivity of the tri-layer thin films in comparison with single FePt layer could be ascribed to the possible atomic diffusion/interdiffusion at the interfaces between these soft and hard layers [235,236], which could decrease the pinning field up to 50% [237].

Figure V.5b illustrates the First Order Reversal Curves (FORC) raw data plot with a thousand data points, in which the absolute magnetisation is plotted as a function of applied field and the dotted paths present reversal curves. Note that the outline of the FORC contour represented in Figure V.5b is the oop major hysteresis loop as in Figure V.5a. From such FORC data associated with (Equation II.3), the 2D – FORC diagram as a contour plot is obtained and presented in Figure V.5c, for which the irreversible process is highlighted. From the FORC diagram, the switching field distribution of the tri-layer films can be recognized. The presence of only one somewhat broader peak with a center at reversal field of $\sim 0.84 \text{ T}$, which is around the respective coercivity of $\sim 0.95 \text{ T}$, indicates that the single magnetic phase behavior is accompanied by the exchange coupling between the hard-soft layers. This means that the magnetization switching took place at the same applied field though the sample contains both soft and hard layers. This is in agreement with the case study of **case 1** presented above, for which the thickness of the soft phase is less than the domain wall width of the hard phase. In addition, the FORC diagram demonstrates a symmetrical reversible ridge distributed little out of the four-quadrant diagonal axis (H_c) and there is no negative region (for negative applied field) coming along with this ridge. Because this ridge is the presence of reversible magnetization process [238], hence, all magnetic phases are magnetically switched simultaneously at the same applied field, as observed in non-interacting single domain particles coherent rotation of the magnetic moment in uniformly magnetized particles. Note that the completely enclosed contours are one of the main characteristics of a fingerprint of single-domain particles [239].

Regarding other studies [203,240], in the non-interacting single domain particles, the introduction of interacting field induces a shift of the peak of the FORC distribution out of the four-quadrant diagonal axis (H_c). While the FORC distribution shifting upward off the H_c axis (corresponding to positive value of the third-quadrant diagonal axis $-H_b$) is attributed to dipolar interaction or magnetostatic interaction, the shifting downward off (negative value of the H_b axis) the axis is attributed to exchange interaction. Here, in the case study, the single FORC peak shifted downward off the H_c axis (ridge center at $H_b < 0$),

the mean interacting field occurring between the particles (in the tri-layer film) is exchange interaction. This conclusion is partly agreed with the ip hysteresis loop measurement indicated above, by which the dipolar coupling was eliminated.

V.2. Does diffusion exist?

Keeping the integrity of the soft magnetic phase inside the hard magnetic phase is one of the fundamental premises in this work. And as a result, the study of diffusion/interdiffusion become considerably meaningful but it seems challenging to observe experimentally. In order to achieve this goal, in this work, the diffusion of the soft-hard nanocomposite before/after annealing will be discussed theoretically and will be revealed experimentally in terms of TEM observation.

V.2.1. Theoretical estimation

In the theoretical approach, consider the following case study of the classical Fick's second law of diffusion. Two pieces of materials with different homogenous concentration C with $C_o > C_1$ are in contact across a plane interface as demonstrated in Figure V.6-left. The diffusion is occurred by annealing at a constant temperature T during an annealing time t . The distribution of concentration in the system is determined by the general partial form from of Fick's second law, which are written in terms of both position and time, for unidirectional flow under non-steady state conditions as follows [241]:

$$\frac{\partial C(x,t)}{\partial t} = -\frac{\partial}{\partial x} \left[-D \frac{\partial C(x,t)}{\partial x} \right].$$
 D generally varies with concentration, and if D varies little in the

investigated concentration range from C_1 to C_o , a simple form can be deduced from partial one, which can be expressed as:
$$\frac{\partial C(x,t)}{\partial t} = D \frac{\partial^2 C(x,t)}{\partial x^2}.$$
 Take into account the following boundary conditions:

For $t = 0$, $C(x, 0) = C_1$ at $0 \leq x \leq \infty$

For $t > 0$, $C(0, t) = C_o$ (constant surface concentration) at $x = 0$.

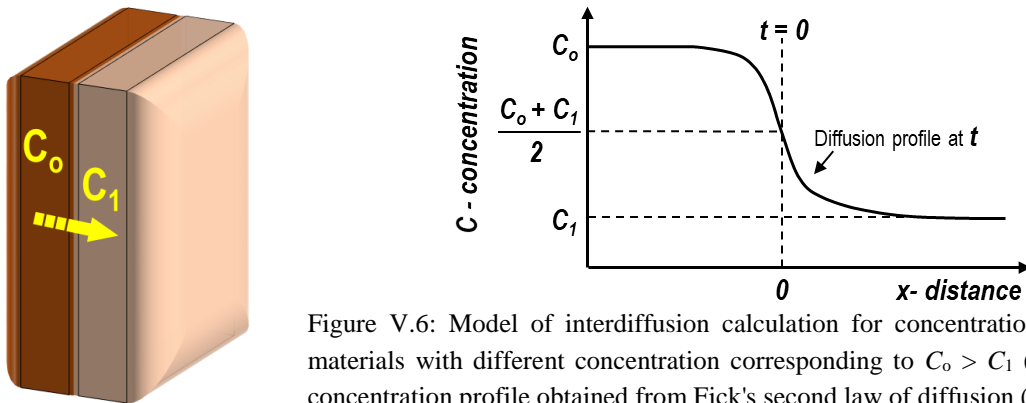


Figure V.6: Model of interdiffusion calculation for concentration – C of the materials with different concentration corresponding to $C_o > C_1$ (left), and the concentration profile obtained from Fick's second law of diffusion (right).

Hence, the solution of the Fick's second law of diffusion demonstrating the relationship between concentration, position, and time is given as follows [241]:

$$C(x,t) = \left(\frac{C_o + C_1}{2} \right) - \left(\frac{C_o - C_1}{2} \right) \operatorname{erf} \left(\frac{x}{2\sqrt{Dt}} \right) \quad (\text{Equation V.2})$$

where $C(x, t)$, erf, and D are the concentration at depth x (m) after annealing time t (s), the Gauss error

function – erf followed by $\text{erf}(x) = \frac{2}{\sqrt{\pi}} \int_0^x e^{-u^2} du$, and the diffusivity ($\text{m}^2.\text{s}^{-1}$), respectively. Note that the integral of erf function can be only solved computationally, the term \sqrt{Dt} is so-called the diffusion length – L_d (m), and the concentration $C(x, t)$ will be calculated as long as all the unknowns are known. The concentration profile for the above equation at time t and position x is shown in Figure V.6-right.

Most theoretical calculations for diffusion are often expressed in terms of both frequency factor – D_0 and activation – Q in lieu of D itself. These two both parameters allow to explain more clearly the diffusion/self-diffusion mechanism in metals such as atoms diffusion by means of thermal jumps. Thanks to the solution of the Fick's second law of diffusion (Equation V.2), the diffusion profiles are computed to observe the potential diffusion occurring with the nanocomposites. To our best knowledge, it has been not accessible to obtain the values of D_0 and Q for either the soft-hard magnetic nanocomposites (NPs inside a matrix) or the Co soft phase inside FePt hard phase. Therefore, the assumption of soft-hard nanocomposite composing of Fe (thin film) and FePt matrix (thin film) is applied. Note that the D_0 and Q are both nonlinearly increasing temperature-dependent parameters, and they also varied with different directions corresponding to the unit cell orientation. Because the FePt matrix was already crystallized (at RT with A1 phase, or L10 phase after annealing), the diffusion behavior occurs as interdiffusion, which normally happens at the length scale much smaller compared to the one induced by free pure metals [241].

Table V.1: The diffusing activation parameters for the diffusion in the Fe/FePt system [241–243].

Diffusion species	Activation energy – Q (eV)	Frequency factor – D_0 ($\text{m}^2.\text{s}^{-1}$)
Fe to L1 ₀ -FePt (ordered)	1.65	3.45×10^{-13}
Pt (in L1 ₀ -FePt) to Fe *	2.97	2.7×10^{-4}

* The values obtained for Pt in FePt system at **1100°C**, it is believed that the value of D_0 will be drastically reduced in the order of $10^{-12} \text{ m}^2.\text{s}^{-1}$ at 750°C [241].

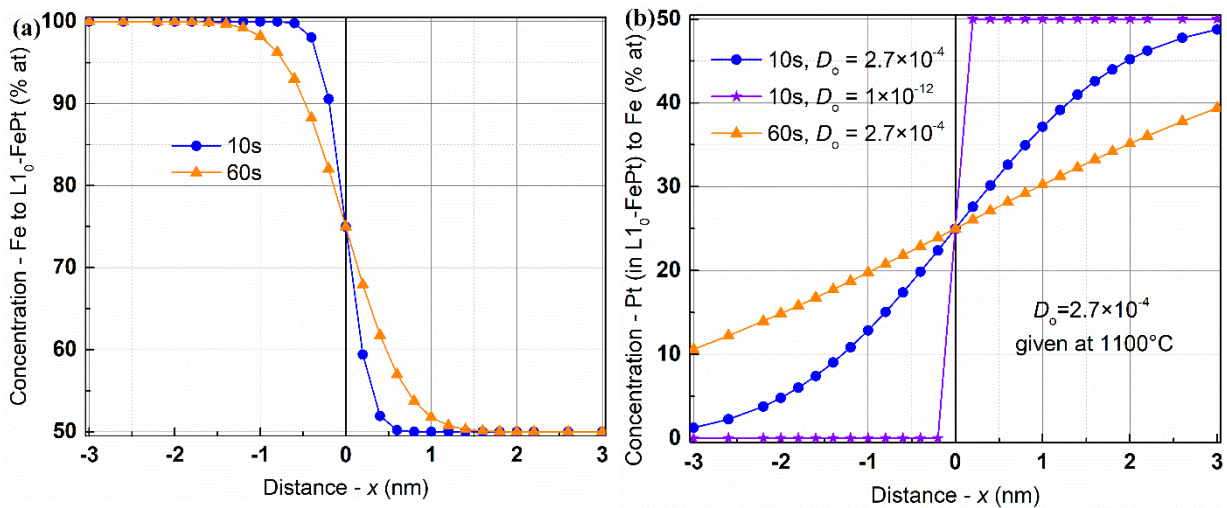


Figure V.7: The calculated diffusion profiles for Fe diffusion to L1₀-FePt (a) and Pt (in L1₀-FePt) diffusion to Fe (b) during the annealing 10s and 60s at 750°C. The position distance $x = 0$ is originated the side edges between Fe layer (left side of graph/Figure V.6-left) and FePt layer (right side of graph/Figure V.6-left).

The origin of the distance coordinate x is chosen at the bonding interface (the side edges) between the two materials, as demonstrated in Figure V.6-left. Note that the frequency factor D_0 obtained for Pt (in L1₀-FePt) is given at 1100°C, which would be much smaller at lower temperatures because in crystallized compounds or intermetallic alloys, the D (and D_0) is sensitive with composition, temperature through the correlation effects in the tracer diffusion and the thermodynamic driving force [241–243]. Following the data compiled in Table V.1, the diffusion concentration profile of Fe/FePt systems is

calculated and shown in Figure V.7. Figure V.7a illustrates the two distinct diffusion profiles of Fe (from continuous soft magnetic Fe layer, left side) into the hard matrix (FePt, right side) corresponding with the two different annealing time, which are going to be presented in this study. Obviously, the Fe continuous layer is not diffused much into the FePt structure because the diffusion exists at very short range order, i. e., no more 0.5 nm in 10s, and 1 nm in 60s of annealing. Figure V.7b demonstrates the three different diffusion profiles of Pt into the soft magnetic layer of Fe. The Pt diffusion seems to occur stronger compared to Fe diffusion (Figure V.7a), which might be attributed to the relatively high value $D_0 \sim 2.7 \times 10^{-4} \text{ m}^2 \cdot \text{s}^{-1}$ (obtained at 1100°C). Such high value D_0 could result in an overestimation of diffusion of Pt into the soft layer of Fe. A reasonable value $D_0 \sim 10^{-12} \text{ m}^2 \cdot \text{s}^{-1}$ can be concluded at proper temperature much closer with the temperature used in this study (750°C). Thus, the Pt diffusion profile corresponding to this value of $\sim 10^{-12} \text{ m}^2 \cdot \text{s}^{-1}$ is presented in Figure V.7b (denoted as 10s, $D_0 = 1 \times 10^{-12} \text{ m}^2 \cdot \text{s}^{-1}$). Clearly, the Pt diffusion decreases largely of no more than 0.25 nm. In general speaking, the diffusion process is not a simple one, which strongly relies upon a variety of parameters such as the crystallographic structures, the diffusion direction with respect to the orientations of crystal structures, the interface between the materials, etc. Interestingly, other authors [235] experimentally indicate that the diffusion process should be less in case of stacks of NPs compared to the thin layer used in the theoretical calculation.

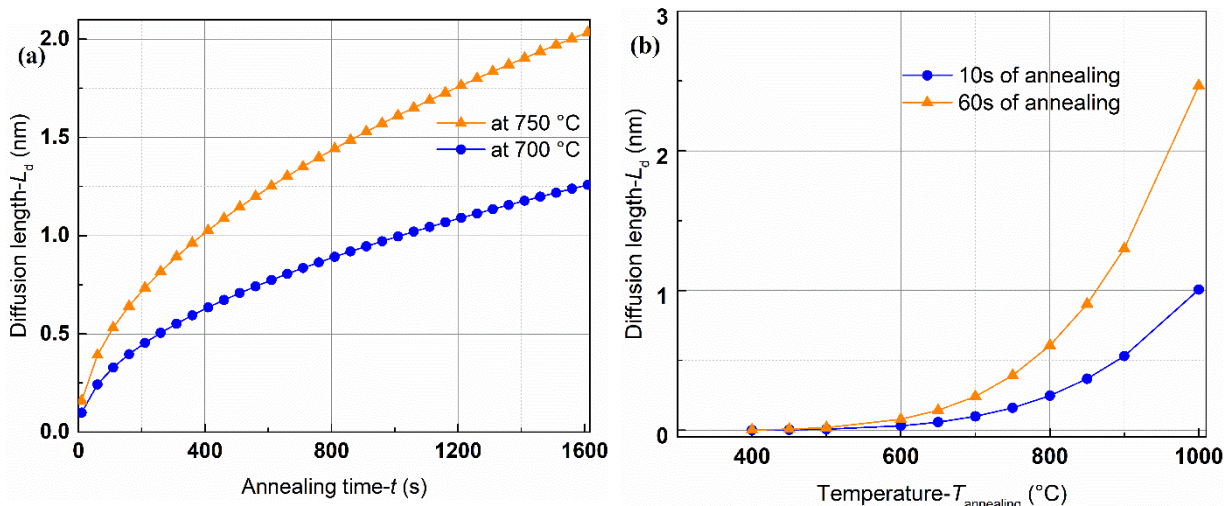


Figure V.8: The calculated diffusion length followed by the Arrhenius equation at various annealing conditions as a function of (a) annealing time; and (b) annealing temperatures.

Another theoretical attempt to complete the understanding the diffusion process exploited in this study, which is not based on Fick's second law of diffusion, often called indirect method. In solids, taking into account other phenomena, i. e., the thermally activated motion of atoms (Snoek effect), internal friction owing to stress-induced reorientation from redistribution of atoms (Zener relaxation)... [241], the diffusivity D is usually determined with respect to temperatures. Thus, the D_0 and Q are extrapolated from

the experimental curves expressed as the Arrhenius equation: $D = D_0 e^{-\frac{Q}{k_B T}}$ where k_B is Boltzmann constant ($\text{J} \cdot \text{K}^{-1}$) and T is the annealing temperature (K). The diffusion length also given in the form of $L_d = \sqrt{Dt}$ where t is the annealing time (s). In polycrystals, there exists an additional diffusion through the grain boundaries. This grain boundary diffusion speed could be more rapid locally through the disordered zones of the grain boundaries. If the grain become sufficiently larger enough, such grain boundary can be negligible [241]. Here in this study, the sample FePt is crystallized with A1 phase at RT, the total diffusion rate reflected by D_0 could be again reduced compared to literature. It is therefore the calculated results can be overestimation. The calculated diffusion lengths at various annealing conditions is shown in Figure

V.8. Figure V.8a compares the calculated diffusion lengths as a function of annealing time, at constant temperatures of 700°C and 750°C. At a certain annealing temperature, the longer annealing time is the more diffusion length reaches. Figure V.8b illustrates the nonlinear dependence of diffusion length on annealing temperatures. Similarly, the higher annealing temperature is the more diffusion length obtains. With the annealing parameters used in this study, the maximum diffusion length is about 0.4 nm at 750°C and 60s. Lower annealing temperature and shorter annealing time induce a smaller diffusion effect reflected by diffusion length.

The two above indicators of theoretical calculation both suggest that the diffusion process occurs during the annealing process. However, thanks to rapid annealing in RTP (annealed in 10s and 60s), the diffusion length exists in a short range order of 1 nm, especially the diffusion process in NPs or stacks of NPs will be less compared to continuous layer [235]. This means that the soft magnetic phase is not dissolved into the hard magnetic FePt structure and vice versa under heat treatment used in this work. Hence, the integrity of the NPs is expected to be preserved as results. Following discussion is experimentally examined the diffusion in the soft in hard magnetic nanocomposites.

V.2.2. Experimental confirmation

In this work, a direct approach in observing the diffusion will be made by TEM. The TEM characterization will be made on a tri-layer heterogeneous structured sample of FePt/Co (stacks of NPs)/FePt onto Si/SiO₂ substrate ((schematic diagram of sample presented in Figure II.8d). Note that the stack of Co NPs was deposited by Free Cluster Generator (FCG), the FePt continuous layer made by conventional PLD as in section V.1 and the nanocomposite was deposited at RT. Because Co is really close to Fe in physical behavior, the use of Co in this investigation will allow to distinguish easily the elemental materials induced by diffusion process occurring inside the nanocomposite. The nominal thickness of each layer is about 40 nm, with the porosity of stacks of Co NPs being about 50%, which means the equivalent thickness of the densified Co layer is ~20 nm without any porosity. The purpose of relatively high thickness of each single layer aims to statistically increase the probability to observe the NPs inside FePt matrix of the nanocomposites owing to relative small grain after annealing (will be discussed in details in section V.3).

Figure V.9 presents a TEM cross-sectional image prepared by FIB of the tri-layer heterogeneous structured sample of Si/SiO₂/FePt/Co (stacks of NPs)/FePt, before annealing. Figure V.9a clearly distinguishes each single layer of the heterogeneous composite. The first deposited FePt layer follows the topography imposed by the very fine underlying layer of thermally oxidized SiO₂ (~100 nm), which is in good agreement with the flat surface of FePt deposited at RT (evidenced in Figure III.27 and Figure III.28). The second deposited stacks Co NPs was deposited with the smooth interface between these two layers. Interestingly, depositing stacks of NPs induces a certain degree of roughness, which is obviously visible at the interface between the stacks of Co NPs layer and the last FePt layer (partly discussed in section IV.1.4). A varied thickness layer on top of the last FePt layer is ascribed to the Pt deposited during the FIB-TEM preparation. The inset of Figure V.9a displays an HRTEM image of an intermixing region between the first FePt layer and SiO₂. Such typical interface is indicated by the capped intermixing layer from the two red dashed lines, with the thickness of about ~2nm. The intermixing layer was induced by the process of subplantation [191,222], which was followed by the high energetic species 100 eV [192] deposited during the PLD process (discussed in section III.3.2). Figure V.9b is an HRTEM image of the three layers, which shows apparently the long range crystallization of some Co NPs (white arrow). Such crystallization of the NPs was discussed in section IV.1.4. Furthermore, the last FePt layer is entered slightly into the stacks of NPs layer due to the increasing roughness at the interface.

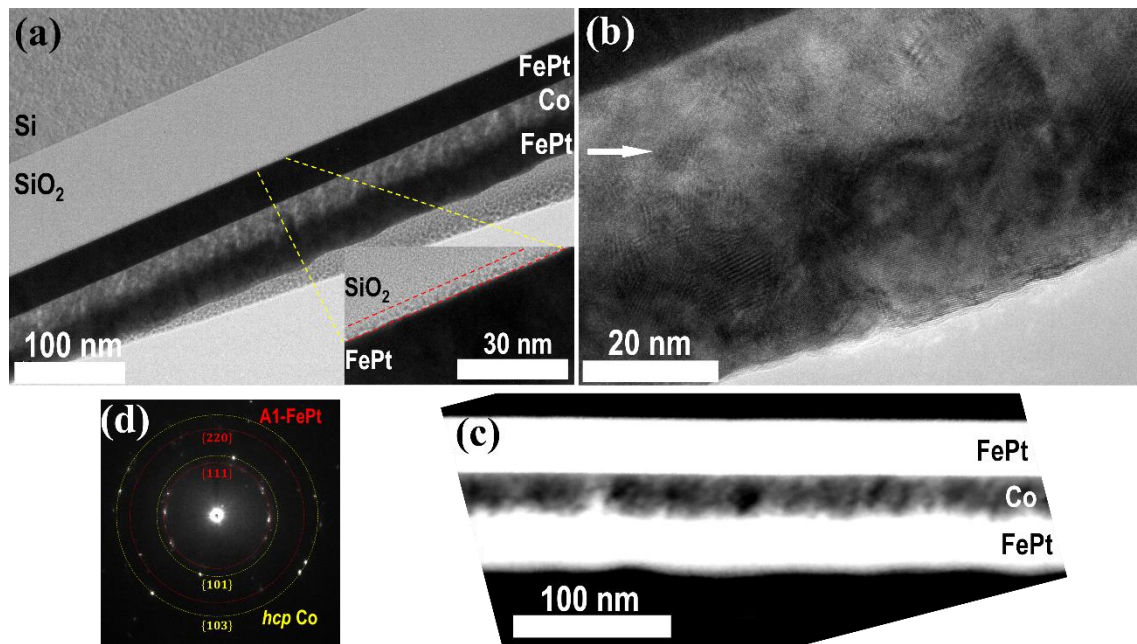


Figure V.9: TEM cross-sectional images of the tri-layer heterogeneous structured sample of FePt/Co (stacks of NPs)/FePt before annealing. (a) the TEM overview image with the inset of HRTEM images for the interface between the SiO₂ and FePt layers; (b) The HRTEM image for the three layers; (c) The dark field (HAADF) STEM image of the tri-layer system; and (d) The SAED pattern of a region crossing through the three layers with the indicated (*hkl*) indices.

Figure V.9c emphasizes a typical dark field STEM image, for which the three deposited layers are absolutely distinguishable. While the white regions are assigned to FePt presenting high average atomic Z number, the capped black/grays region is assigned to stacks of Co NPs presenting lower atomic Z number. The STEM image reaffirms either very flat or rough interface between the tri-layers. Figure V.9d interprets the SAED pattern obtained from the area of the three layers of FePt/Co/FePt. The procedure in indexing the $\{hkl\}$ miller indices was given in section IV.1.4. At RT, the FePt is crystallized under the disordered phase of A1-FePt, which follows the intermixing layer and induces such disordered phase (detailed is provided in section III.3.2). It is not surprising that the stacks of NPs is crystallized with hexagonal closed packed structure, which is typically stable structure of Co NPs at low temperature, i. e., under 450°C (723 K) [7]. Note that the SAED ring pattern is characterized for crystallized grains but these grains crystallized with various orientations.

A TEM cross-sectional image of FIB-cut of the sample with the same configuration as in Figure V.9a, taken after annealing with RTP at 750°C, 50°C/s, 30s, is visualized in Figure V.10. Just sample annealed in 30s was characterized with TEM. The goal of using 30s annealing aims to demonstrate the possible diffusion process for both 10s and 60s employed in this work, using just one TEM observation. It is still possible to see the tri-layers of the annealed nanocomposites in Figure V.10a. The average thickness is about 99 nm (Figure V.10a) compared to 115 nm in as-deposited state (Figure V.9a). It turns out that the thickness decreases 14% in total, which is attributed to the porosity problem of stacks of NPs. This 14% decrease is obtained by supposed that after annealing, the stacks of NPs become denser. Of course, the evaporation during annealing would have possibly occurred [123], but here, the study in this work neglected this effect. Thus, the experimentally re-estimated porosity of stacks of NPs is about ~57%. Figure V.10b and c compare the high and low magnification dark field STEM – HAADF images, respectively. The low magnification HAADF image discriminates fairly the sandwich structure of the sample, at which the FePt is characterized by brighter color and the NPs come up with gray color indicated

by the arrows (because HAADF is sensitive to the change in atomic Z number, which permits to distinguish the NPs and matrix). Obviously, various sizes of NPs (Figure V.10b, larger than nominal diameter of ~4 nm obtained by depositing on TEM grid as using the same parameters as here) are formed during the annealing process, which is mainly attributed to the relative high thickness of stacks of NPs induced by Ostwald Ripening mechanism [209] (discussed in section IV.1.4) and the dewetting process as observed the formation of Ge nanocrystals inside amorphous matrix [244].

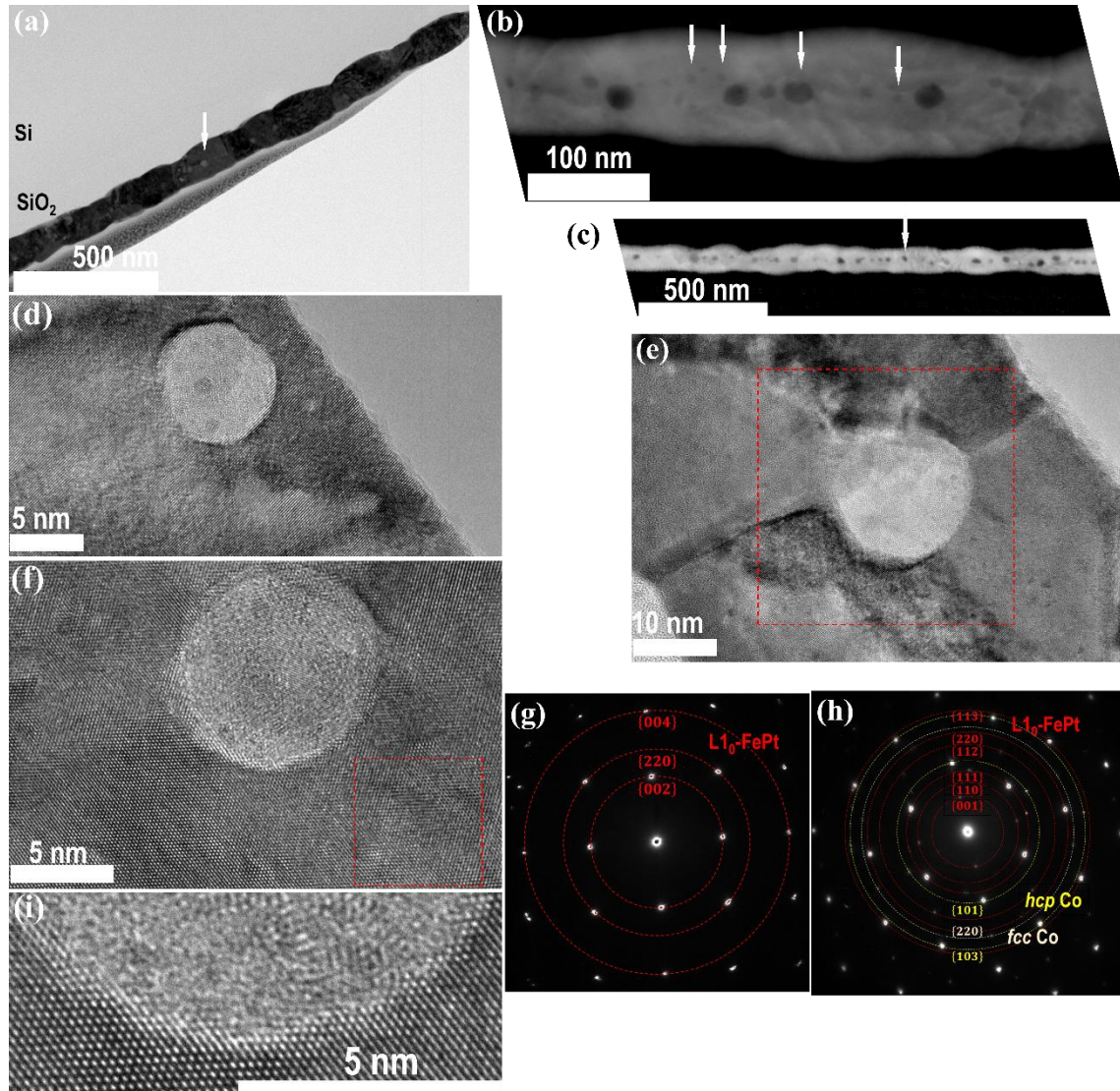


Figure V.10: TEM cross-sectional images of the tri-layer heterogeneous structured sample of FePt/Co (stacks of NPs)/FePt after annealing by RTP at 750°C, 50°C/s, 30s. (a) The TEM overview image; (b) The HAADF image with high magnification; (c) The HAADF image with low magnification for the three layers; (d), (e), (f) A collection of soft magnetic Co-NPs inside the hard magnetic FePt matrix – HRTEM images; (g) The SAED pattern of the area without NPs in (f) image – red dashed square; (h) The SAED pattern of the area with both NPs and several hard magnetic FePt grains in the (h) image – red dashed square; and (i) the HRTEM image focusing on the intermixing region between the NPs and the matrix of image (f). Note that the white arrows in (a), (b) and (c) indicate the NPs; and the (hkl) indices are indicated in (g) and (h).

Figure V.10d, e and f illustrate a variety of sizes of NPs. Such HRTEM images indicate that the crystallized NPs appearing quite neat and distinctive contrast are well embedded in the crystallized surrounding media of the FePt matrix. However, owing to the effect of annealing process, the locations of the NPs could be anywhere inside the matrix. Note that, for high thickness of FePt layers, after

annealing, the FePt still remains continuously, which are striking different in comparison with very thin thickness, i. e., 15 nm inducing granular structure (discussed in section III.4 or the nanocomposites which will be mentioned below). Figure V.10e exhibits a HRTEM image of a NPs in the middle of a cross junction made from four distinct hard FePt grains. The SAED pattern of this region is presented in Figure V.10h. The many crystallized FePt grains and NPs reflected by the high intensity of distinctive diffraction spots in the SAED pattern. While various "red" orientations are attributed to the $L1_0$ -FePt phase (PDF No. 65-1051), the preferential crystallization for yellow color – *hcp* Co (PDF No. 05-0727) at low temperature and ivory color – *fcc* Co (PDF No. 15-0806) at high temperature (above 723 K) [7], are both co-existed. The other SAED pattern of a region free NPs (from Figure V.10f) is presented in Figure V.10g. The hard FePt matrix is successfully transformed from disordered A1 phase (Figure V.9d) into ordered $L1_0$ -FePt phase, reflected by clearly high intensity of diffraction spots. The HRTEM image displayed in Figure V.10f allows to see clearly the crystallized NPs inside the crystallized hard FePt matrix. Additionally, more information about diffusion could be extracted directly, e. g., there exists a specific region limited between the outer surface of the NPs and the matrix – an intermixing area dedicated in Figure V.10i. Such regions are not actually voids but can be referred to as the Kirkendall marker region/plane or Kirkendall void-like layer [245–247], which is not necessary to be empty [247] and spreading over the interdiffusion zone. From the HRTEM images (as in Figure V.10i), this intermixing region has a width of ~ 0.7 nm and it is ascribed to the region for diffusion occurring [248]. This intermixing is expected to have enrich of Fe (plus Co) to form Fe_3Pt owing to higher content of Fe (or Co) in NPs diffused. While the Ostwald ripening mechanism [209] and dewetting process [244] are responsible for formation of various sizes of NPs, the formation of the Kirkendall marker region during the annealing is attributed to the Kirkendall effect owing to the difference in diffusion rates between two distinct materials of Co and FePt, which promotes the intermixing region. Such Kirkendall marker region acts as a defect, debris at nano material configurations, and thus could stop or weaken the further diffusion because the diffusivity will become much smaller in the debris or disordered region [241]. The intermixing region has approximate order of diffusion length obtained in the theoretical calculations shown previously (section V.2). For experimental annealing conditions of the nanocomposites, which will be presented in below (section V.3), the use of annealing in 10s is expected a shorter length scale of diffusion, in contrast, the 60s annealing is expected stronger diffusion compared to 30s annealing. All of the TEM preparation, measurement and analysis presented in this work were made by me with valuable help from specialist – Pierre CARLES at IRCER.

Though the use of annealing is necessary to favor the crystallization for both soft and hard magnetic materials, annealing also brings some consequences related to diffusion, which can degenerate the quality of the sample by introducing the intermixing region, dissolving part of NPs, etc. This part has demonstrated that different driving forces of Ostwald ripening mechanism, dewetting process and Kirkendall effect are explored in nanotechnology of fabricating soft in hard magnetic nanocomposites, thanks to that the soft crystallized magnetic NPs are mostly preserved in hard crystallized magnetic matrix. The theoretical calculations and TEM observations validate the results of samples before and after annealing. Hence, the results presented here is a blueprint to understand in details the atomic structural, microstructural properties of annealed nanocomposites, which would be a benefit in comprehending the properties of the following presented nanocomposites (in section V.3).

V.3. Nanocomposites based FePt matrix

Previous section V.2 has indicated that deposition at RT for FePt layer is very smooth, in contrast, deposition for stacks of NPs creates a rough surface. Thanks to such rough surface, depositing layer (FePt)/(stacks of NPs), with sufficient enough number of layers, helps to embed NPs inside the FePt matrix homogeneously. Here, starting with 4 layers of FePt and 3 layers of stacks of NPs ($\text{Fe}_{65}\text{Co}_{35}$ or Co NPs, deposited by FCG), the influence of the NPs volume content, NPs materials, nanocomposites' architectures (NPs' diameter of ~ 4.0 nm and ~ 2.7 nm deposited from FCG, the continuous $\text{Fe}_{65}\text{Co}_{35}$ layer deposited by PLD), and the Ta spacer, on overall structure, microstructure and magnetic properties of the fabricated nanocomposites will be discussed. Note that the total thickness of FePt remains constant of 15 nm and the nanocomposites will be annealed with RTP during 60s or 10s at 750°C , 50°C/s , 1×10^{-1} mbar of Argon flow.

V.3.1. Nanocomposites with various FeCo diluted percentage (NPs vol content)

Three equivalent thickness of stacks of 4 nm- $\text{Fe}_{65}\text{Co}_{35}$ NPs (abbreviated as soft) are well mixed in four equivalent 3.75 nm FePt layers (abbreviated as hard) to produce a nanocomposites. The thickness of stacks of NPs is controllable followed by the expected volume percentage of NPs. The 50% porosity of stacks of NPs is taken into consideration. The schematic presentation of such nanocomposites is shown in Figure V.11, for which FePt continuous layers and stacks of NPs are both deposited at RT by conventional PLD and FCG, as illustrated in section II.1, Figure II.8d.

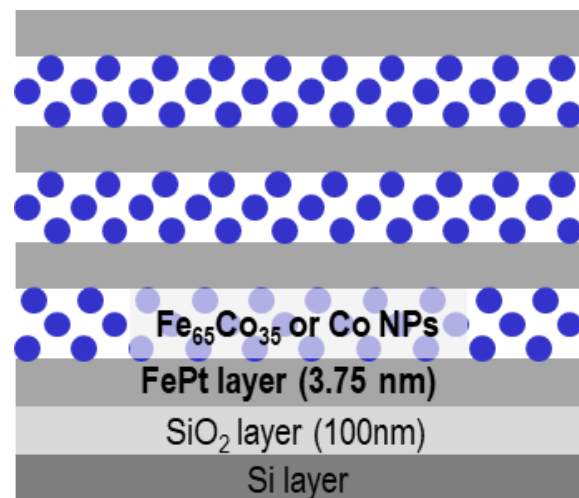


Figure V.11: The schematic diagram of FePt-FeCo/Co nanocomposite structure.

A set of nanocomposites with various volume contents of stacks of 4 nm $\text{Fe}_{65}\text{Co}_{35}$ NPs (soft) ranging from 0% up to 25%, and configurations, are all deposited at RT and later RTP annealed at 750°C , 50°C/s , 60s. Figure V.12 compares the XRD patterns of such composites at different annealed, configuration conditions. The sample with 100% of FePt deposited at RT shows no long range order of crystallization. After annealing, all of the annealed samples depict crystallization with $L1_0$ -FePt phase, which is attributed to the FePt matrix in the nanocomposites. There is no visible diffraction peaks ascribed to the $\text{Fe}_{65}\text{Co}_{35}$ stacks of NPs, which can be due to the crystallization occurred in a very short range order corresponding to the length scale of the NPs (indicated in section IV.1.4 and V.2.2). Increasing the soft magnetic volume $\text{Fe}_{65}\text{Co}_{35}$ content gradually reduces the

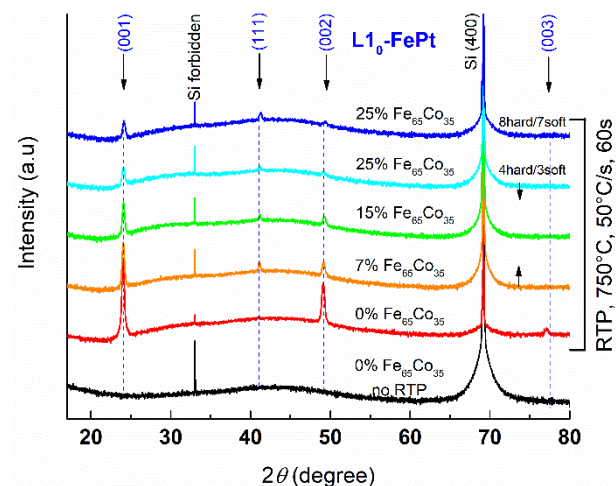


Figure V.12: The XRD diffraction patterns as a function of 4 nm – $\text{Fe}_{65}\text{Co}_{35}$ ($t = 480 \mu\text{s}$) soft magnetic NPs' percentage, embedded in 15 nm FePt matrix, at RT on Si/SiO₂ and then processed by RTP, at annealing temperature of 750°C , heating rate of 50°C/s , annealing time of 60s, and in 1×10^{-1} mbar of Ar flow.

relative intensities of (00l) reflections of L1₀-FePt phase compared to the sample with 0% Fe₆₅Co₃₅. Moreover, the (111) reflection of L1₀-FePt phase is promoted by diluting the FePt matrix with the Fe₆₅Co₃₅ NPs. Doubling the number of layers for both FePt and Fe₆₅Co₃₅ does not contribute any major difference in XRD patterns (seen with cyan and blue XRD patterns). Almost no variation when doubling the number of layers (but the total thickness of FePt is fixed at 15 nm) shows that the significant roughness when depositing stacks of NPs does help embedding the NPs inside the matrix homogeneously.

The peak positions of L1₀-FePt phase (i. e., (111)) remains fixed in the nanocomposites contained NPs, while there are shifts in peak positions in the continuous layer structured nanocomposites (section V.1). This variation related to the shift of diffraction peaks is attributed to the difference in degree of diffusion taking place between the two kinds of nanocomposites. By XMCD, other authors magnetically confirms that the diffusion occurs stronger in continuous composites than that of stacks of NPs nanocomposites [235].

Table V.2: Nanocomposites crystallite sizes obtained from Scherrer equation based on XRD patterns.

NPs volume content (%)	0	7	15	25
<i>FWHM</i> (°)	0.174	0.257	0.281	0.338
<i>D</i> _{Scherrer} (nm) at (001) peak	47	32	29	24

A profound estimation for Lotgering orientation factor – *LOF* and the long range chemical ordering – *S* parameters based on XRD patterns (details given in section III.3), demonstrates that the *S* shows little variation fluctuated around 0.94 to 0.92, the *LOF* steadily decreases from 0.99 to 0.75 in nanocomposites with 0% and 25% Fe₆₅Co₃₅, respectively. The decline of *LOF* with increasing soft Fe₆₅Co₃₅ volume content is coherent with the introduction of (111) orientation and reductions in L1₀-FePt signature. Additionally, regarding L1₀-FePt (001) reflection, the fitted *FWHM* gradually deteriorates with the increasing the Fe₆₅Co₃₅ content, and thus the Scherrer crystallite size does (details are given in Table V.2). It is also worth noting that the crystallite size is calculated with respect to the out-of-plane direction of the substrate (sample thickness). In case studies, the crystallite sizes are all greater than those of nominal nanocomposites thickness, which is attributed to the fact that the RTP modifies the morphology of samples and promotes the growth in the oop direction (which will be discuss below).

The evolution in microstructure of the as-deposited and annealed nanocomposites as a function of Fe₆₅Co₃₅ content is depicted in Figure V.13. AFM measurement performed on nanocomposite surface indicates very low surface roughness with flat morphology in as-deposited state, while annealed nanocomposites illustrate rougher surfaces with granular microstructures. The measured rms roughness increases from 1.9 nm (as-deposited state) to 4.5 nm (annealed state, 0% Fe₆₅Co₃₅). Increasing the Fe₆₅Co₃₅ content induces finer grain microstructures represented by lower rms roughness and peak-to-peak values. In other words, the refinement of microstructure is improved with increasing Fe₆₅Co₃₅ content. Rms roughness declines ~20% from 4.5 nm to 3.5 nm in nanocomposites with 0% and 25% Fe₆₅Co₃₅ volume content, respectively. It is also visible to see that grains in annealed sample with 0% Fe₆₅Co₃₅ is of shaper edges compared to samples with additional Fe₆₅Co₃₅ content. A thorough estimation with high resolution SEM microstructure suggests that annealed sample with 0% Fe₆₅Co₃₅ has tri-modal grain size distribution (presented in section III.4.1, Figure III.29a). Such multi-modal distribution reduces to bi-modal (in nanocomposites with 7% and 15% Fe₆₅Co₃₅) and reach to unique single modal in 25% Fe₆₅Co₃₅ nanocomposite. Namely, while the nanocomposites with 7% and 15% Fe₆₅Co₃₅ have size distribution of (33 nm ± 4 nm and 77 nm ± 6 nm) and (30 nm ± 4 nm; 56 nm ± 5 nm), the 25% Fe₆₅Co₃₅ nanocomposite has distribution of 45 nm ± 4 nm. Obviously, the average sizes of the nanocomposites reduce with respect to the soft phase dilution, and the homogeneity in grain size distribution becomes more uniformly when the content of Fe₆₅Co₃₅ increases (SEM Figure V.13). The last but not least, not

only the coverage percentage (area of nanocomposites covers the substrate) see a steady increase from 16% to 27%, the number of grains per unit area supports a rapid development from 15.6 grains/ μm^2 to 95.5 grains/ μm^2 , for nanocomposites from 0% to 25% $\text{Fe}_{65}\text{Co}_{35}$ content, respectively. In comparison between the two kinds of nanocomposites with different number of layers (e. g., 8/7 layers and 4/3 layers), there is no major variation has been observed, which is assigned to the significant homogeneity already obtained during the as-deposited state, at RT.

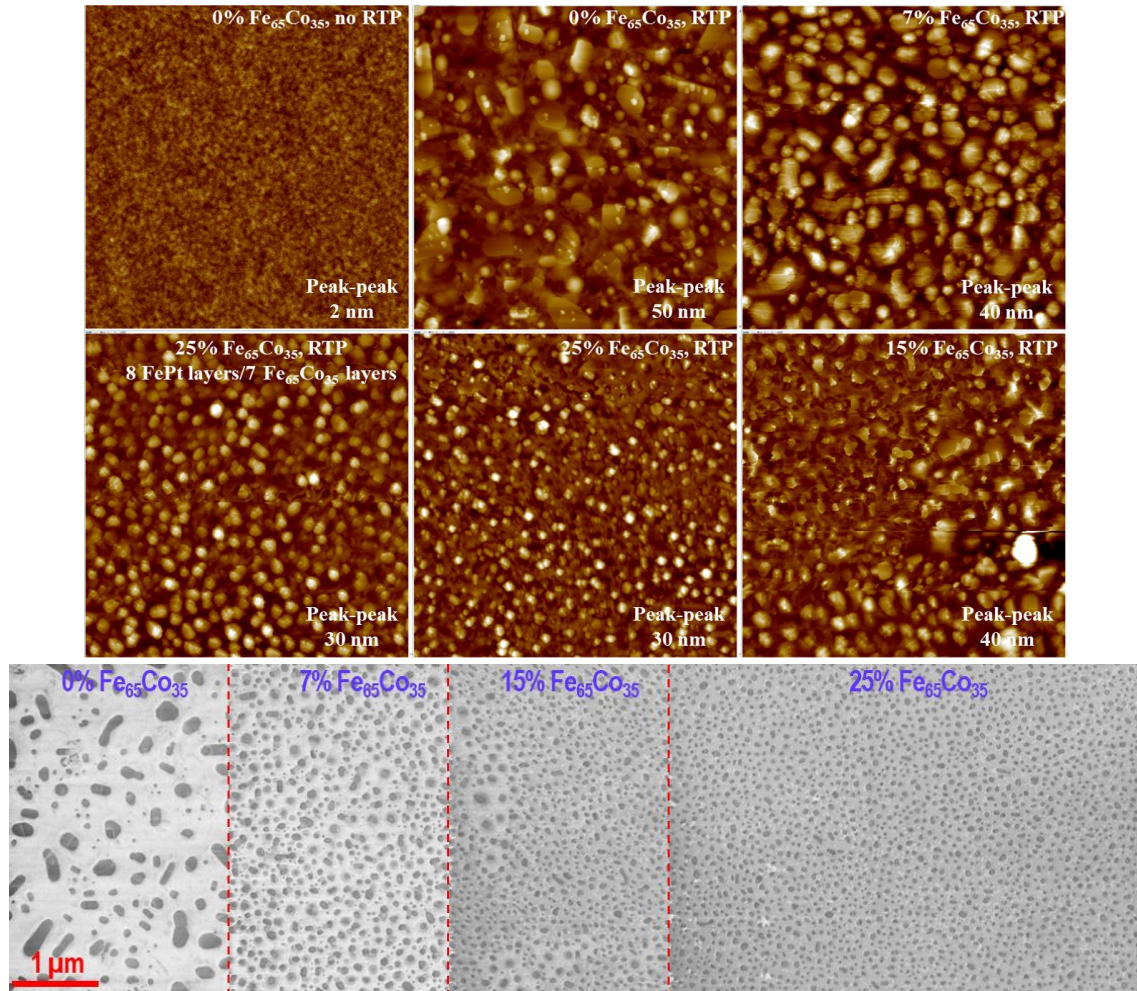


Figure V.13: The AFM morphological and SEM (SE mode) microstructural evolution of as-deposited and annealed nanocomposites as a function of 4 nm – $\text{Fe}_{65}\text{Co}_{35}$ NPs volume content, embedded in 15 nm FePt matrix, at RT on Si/SiO₂ and then processed by RTP, at annealing temperature of 750°C, heating rate of 50°C/s, annealing time of 60s, and in 1×10^{-1} mbar of Ar flow. Size of each AFM image is $2 \times 2 \mu\text{m}^2$.

The notable modification in microstructure due to the introduction of $\text{Fe}_{65}\text{Co}_{35}$ content could be explained by: (i) the $\text{Fe}_{65}\text{Co}_{35}$ generates a discontinuity in chemical content inside the FePt matrix, which induces grains division during the RTP and modifies the dewetting effect; (ii) The $\text{Fe}_{65}\text{Co}_{35}$ NPs are sufficiently small and rough enough at nanometric scale to create defects/dislocations inside the FePt matrix, which benefits the grain development. Furthermore, as discussed previously, in the highest $\text{Fe}_{65}\text{Co}_{35}$ content nanocomposites, the grain sizes become much smaller with diameter of $45 \text{ nm} \pm 4 \text{ nm}$ and they are quite separated. Thus, the successful possibility to discover the NPs inside the FePt matrix is really low and relatively high thickness nanocomposites (shown in section V.2) are necessary to examine the diffusion and NPs inside the matrix.

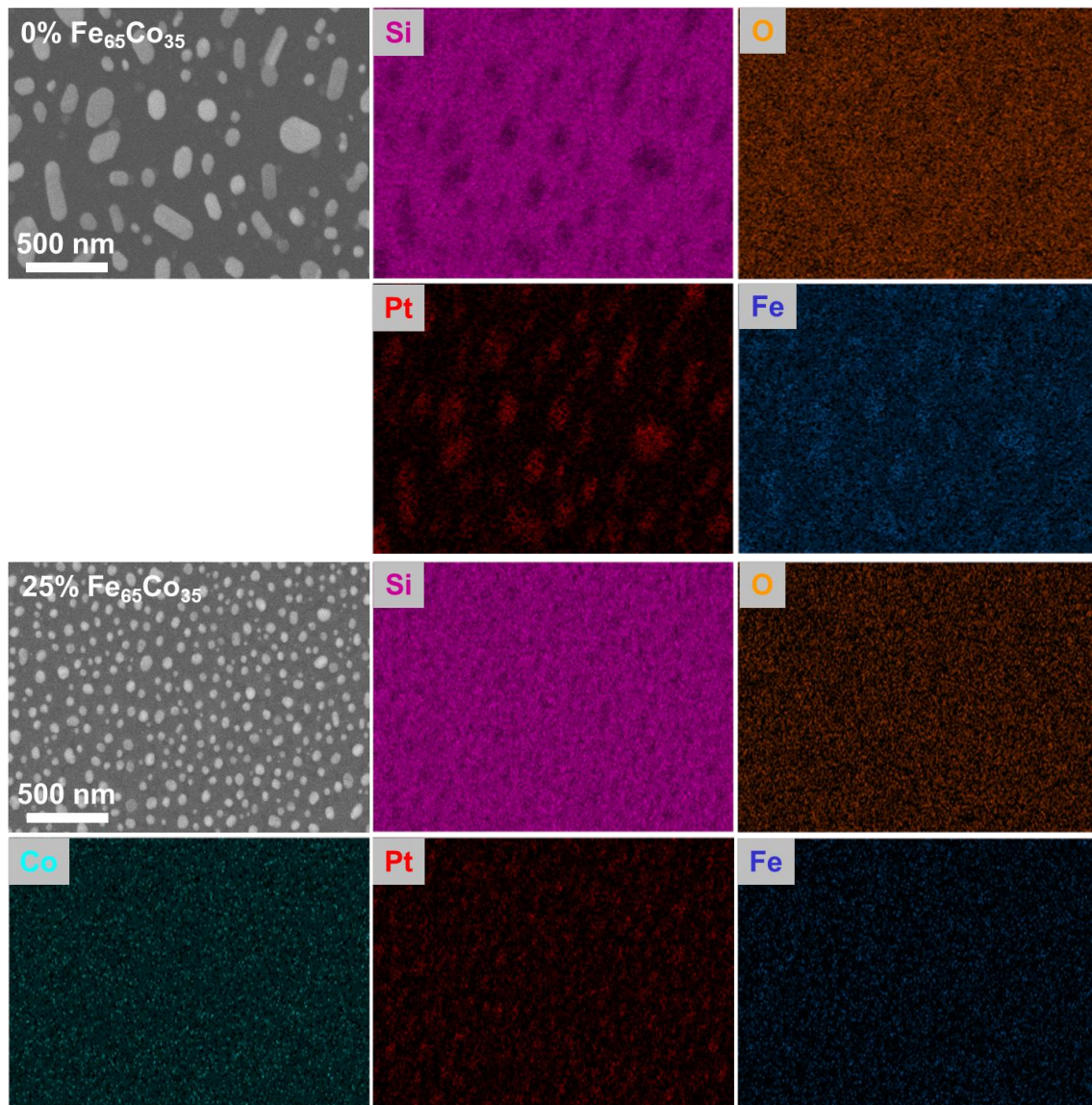


Figure V.14: The plane-view SEM (Inlens mode) and EDS maps observed with (FIB-SEM) for the two annealed samples of only FePt matrix (upper) and nanocomposites with 25% volume content of 4 nm – $\text{Fe}_{65}\text{Co}_{35}$ NPs, embedded in 15 nm FePt matrix (under). All were deposited at RT on Si/SiO₂ and then processed by RTP (750°C, 50°C/s, 60s, and in 1×10^{-1} mbar of Ar flow).

Figure V.14 illustrates the plane-view SEM and chemical element maps for the two annealed samples with only FePt matrix and nanocomposites with 25% of $\text{Fe}_{65}\text{Co}_{35}$ volume content. The brighter grains are attributed to either FePt or FePt+FeCo. Note that the difference in brightness of the grains is due to different heights of the grains (as an advantage when observed in Inlens mode). While the Si and O (attributed to contamination during sample preparation) present almost everywhere as expected, the Fe and Pt highly concentrate within the grains. Additionally, the Co seems to present inside the grains but owing to the poor resolution in FIB (due to charging effect), it is somewhat arguable. The relative bigger grains in the FePt matrix sample allow to observe the elemental mapping easily, which runs quite contrary to the case of nanocomposites with more homogeneous smaller grain sizes. However, it is still possible to recognize the grains by the eyes by focusing on either Si or Pt maps.

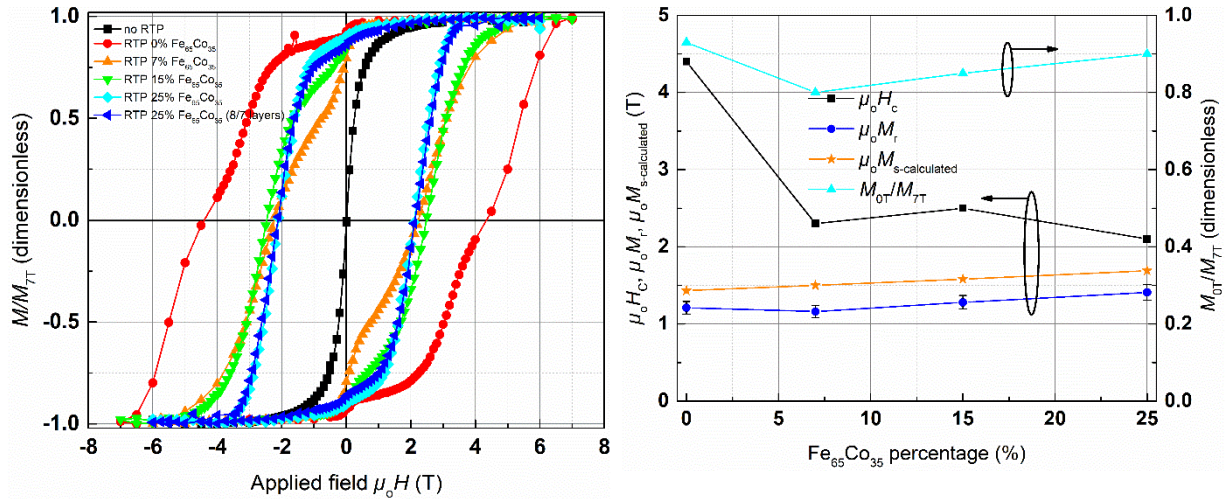


Figure V.15: The magnetic characterizations of nanocomposites based FePt deposited on Si/SiO₂ substrates at RT and then processed by RTP (750°C, 50 °C/s, 60 s) as a function of 4 nm – Fe₆₅Co₃₅ NPs volume content (left) Out-of-plane magnetic hysteresis loops (uncorrected for demagnetization field and normalized) of as deposited and annealed films; (right) A classical representation of magnetic coercivity- μ_0H_c , remanent magnetisation- μ_0M_r , remanence ratio- M_{0T}/M_{7T} , and calculated saturation magnetisation- μ_0M_s corresponding to the Fe₆₅Co₃₅ volume content of the annealed films. Note that the μ_0M_s of L1₀-FePt and Fe₆₅Co₃₅ are 1.43 T and 2.45 T are applied to the calculated estimation.

Figure V.15 – left compares the uncorrected for demagnetizing field and normalized oop $M(H)$ loops for a set of nanocomposites with different Fe₆₅Co₃₅ volume contents. The two samples in as-deposited state and annealed one with 0% Fe₆₅Co₃₅ were discussed previously in section III.4. Magnetic coercivity – μ_0H_c of nanocomposites, with any additional content of Fe₆₅Co₃₅ in the investigated range from 7% to 25%, varies little and fluctuates ~2.2 T. Higher Fe₆₅Co₃₅ volume content in nanocomposite induces better overall loop shape, i. e., more rectangular. The slope of the oop $M(H)$ loops, as it approaches to coercivity, become higher with increasing Fe₆₅Co₃₅ volume content, while doubling number of FePt and Fe₆₅Co₃₅ layers does not make any wide difference. The first derivatives of such $M(H)$ loops reveal that the number of magnetic phases reduces in higher Fe₆₅Co₃₅ content nanocomposites, e. g., three to two and to single magnetic phase behavior in 0% to 15% and to 25% Fe₆₅Co₃₅ nanocomposites. Figure V.15 – right presents the evolution in magnetic properties of this set of samples. At the first glance, the measured remanent magnetisation – μ_0M_r follows the tendency of the calculated saturation magnetisation – $\mu_0M_{s\text{-calculated}}$ but μ_0M_r it always falls under the $\mu_0M_{s\text{-calculated}}$ values, which could attributed to the fact that (i) the remanence ratio – M_{0T}/M_{7T} is always less than the unity; (i) probably there is a partly diffusion between the NPs and matrix existed at short range order of length scale, which would reduce the anisotropy, and remanent of the nanocomposites (as indicated previously, in section V.2). The largely initial decrease (in 0% Fe₆₅Co₃₅ to 7% Fe₆₅Co₃₅ nanocomposites) in μ_0H_c and M_{0T}/M_{7T} are assigned to the extensive modification in microstructure of the nanocomposites associated with the partly diffusion between the NPs and matrix. While the μ_0H_c is sluggish, the M_{0T}/M_{7T} and μ_0M_r are augmented with further increasing Fe₆₅Co₃₅ volume content in the nanocomposites. These augmentations are ascribed to the great refinement in microstructure (from tri-modal grain size distribution in 0% Fe₆₅Co₃₅ nanocomposite to homogeneous single modal distribution in 25% Fe₆₅Co₃₅ nanocomposite) and significant high Fe₆₅Co₃₅ content. Note that there are variety of different driving forces affecting the magnetic properties of the magnetic materials such as structure (phase), microstructure, grain boundaries-intergranular structure/microstructure between the grains, grain size distribution, shape of grain, etc. In terms of μ_0M_r , the value has grown by nearly 18% in the 25% Fe₆₅Co₃₅ nanocomposite compared to 0% Fe₆₅Co₃₅ nanocomposite (or FePt matrix). This significant improvement in μ_0M_r is due to the sufficient high content

of soft magnetic materials of 4 nm – Fe₆₅Co₃₅. Note that the measured $\mu_0 M_r$ presented for nanocomposites hereafter could have additional error bar related to the exact value of porosity problem and homogeneity in sample thickness. Owing to the variation in shapes and edges of grains (as visible in the AFM and SEM images), the demagnetizing factors for those grains are also varied, which strongly influences the correction procedure in estimate the $(BH)_{\max}$. Thus, the estimated $(BH)_{\max}$ is not included in the nanocomposites based on FePt materials.

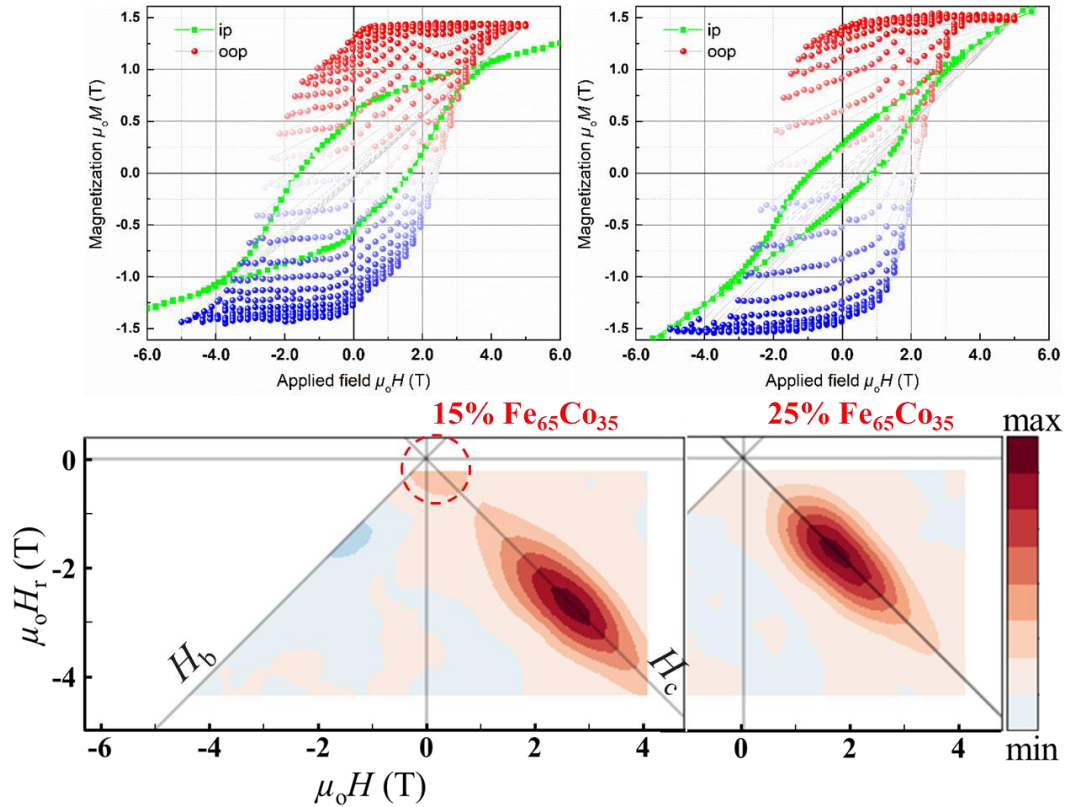


Figure V.16: Advanced magnetic characterizations (oop FORC raw data, ip $M(H)$ loops, and the respective oop FORC diagrams) of the nanocomposites with different volume content of 4 nm – Fe₆₅Co₃₅ NPs, after annealing at 750°C, 50°C/s, 60s. All the data has been subtracted from substrate diamagnetic contribution and uncorrected for demagnetization field.

In order to comprehend deeper the reversal process in nanocomposites, First Order Reversal (FORC) characterizations were made and FORC diagram distribution were plotted to investigate the coupling between the two magnetic phases of soft and hard. As discussed earlier, FORC is a useful approach to characterize magnetic composites. In this section, FORC measurements were performed on two nanocomposites with 15% and 25% Fe₆₅Co₃₅ volume content. First, the raw FORC data measured in out-of-plane (oop) direction accompanied by the in-plane $M(H)$ loops are compiled in the first row in Figure V.16. The ip and oop measurements indicate that the nanocomposites have oop textured. While the anisotropy field is almost constant at sufficiently low content of Fe₆₅Co₃₅ ($\mu_0 H_A \sim 7$ T, for 0 – 15% Fe₆₅Co₃₅ nanocomposites presented in this section and section III.4.1), increasing Fe₆₅Co₃₅ content leads to reduction in anisotropy field ($\mu_0 H_A \sim 5$ T in 25% Fe₆₅Co₃₅ nanocomposite). Secondly, the small shoulders at $\mu_0 H \sim 0$ T (in 15% Fe₆₅Co₃₅ nanocomposite in both ip and oop $M(H)$ loops) suggests that the grain size of nanocomposite does not come up with single distribution, which is agreed well with the microstructural analysis above. Finally, the square easy-axis oop loop in 25% Fe₆₅Co₃₅ nanocomposite indicated that the NPs inside the matrix are well coupled, which would lead to coherent switch under a certain applied field [87].

The FORC diagram distributions allow to directly observe the coercivity $-H_c$ (in H_c axis) and interaction field distribution $-H_b$ (in H_b axis), which appears in the four-quadrant (H_c) and third-quadrant (H_b) diagonal axes, respectively. Both FORC diagrams demonstrate the entirely enclosed contours showing the non-interacting single-domain particles in the nanocomposites [239]. While the first FORC diagram (in the second row in Figure V.16 – left) displays two peaks in the H_c axis, one at ~ 2.6 T and a pronounced soft signature at 0 T (denoted in a red dashed circle) demonstrating a partially coupled or decoupled exchange-spring magnet of the nanocomposite, the second FORC diagram (in the second row in Figure V.16 – right) presents a single peak at reversal events at ~ 1.8 T illustrating a well exchange coupled nanocomposite. The main reversal events occur at field higher than the coercivity of ~ 2.3 T in 15% Fe₆₅Co₃₅ nanocomposite, and in contrast, at lower field compared to the coercivity of ~ 2.1 T obtained from the major hysteresis loop in 25% Fe₆₅Co₃₅ nanocomposite. These distinct magnetic reversal behaviors might be related to the homogeneity in grain size distribution in the nanocomposites as discussed above. Moreover, in both cases, the high field tail in the reversal field stretches almost greater than the coercivity values. The roughly enclosed symmetric contours and central ridges located exactly on the H_c diagonal axis suggest that [203,239,249,250] (i) the nanocomposites contain non-interacting single domain particles; (ii) the residual exchange coupling interaction exist between such single domain particles; and (iii) such single magnetic domain particles have uniaxial anisotropy allowing the particles switched in unison under the same applied magnetic field event.

While the partially coupled exchange nanocomposite in 15% Fe₆₅Co₃₅ sample leads to the magnetization switching occurred at two distinct magnetic fields (one at low and other at relatively high coercivity regions), the well exchange coupled nanocomposite in 25% Fe₆₅Co₃₅ sample induces the magnetization reversal taken place at the same magnetic field although the soft and hard phases coexist in this sample. Regarding hard magnetic materials (indicated in section III.1.2), bigger grains come up with low coercivity, and vice versa for smaller grains. Since the size of soft magnetic NPs developed here is about 4 nm, which is smaller than the domain wall width $-\delta_w = 6.4$ nm of L1₀-FePt matrix, thus the effect of soft signature at reversal event closed to 0 T might originate from the sharp, big grains of nanocomposites, which are considerably induced by the high content of FePt matrix at this annealing condition rather than the soft fingerprint from the NPs. In addition, owing to the diffusion during annealing, the size of the soft phase Fe₆₅Co₃₅ NPs has been modified. Indeed, it is quite possible that the diffusion might lead to formation of different soft phases (rather than only Fe₆₅Co₃₅ NPs), a graded soft phase and/or an intermixing graded interface between the soft and hard materials, all of these phases could regulate the FORC distribution variously. However, such different soft phases could not be ruled out because of limited acquisitions in this work.

V.3.2. FeCo nanocomposites architecture (NPs size, layer-layer)

In this section, the influence of the size of soft magnetic Fe₆₅Co₃₅ NPs (2.7 nm and 4 nm) on overall properties (structure, microstructure, and magnetic properties) in 15% vol Fe₆₅Co₃₅ nanocomposites will be compared to those of layer-layer one. While the size of the NPs was tuned by changing the opening t – time of the He pulsed valve and deposited by the FCG (section V.3.1 deals with composites with 4 nm NPs), the deposition of layer-layer (tri-layer) sample was simpler by using only conventional PLD (see section V.1 for more details).

The evolution of structure of nanostructured composites is compared in Figure V.17. After RTP, the L1₀-FePt phase is promoted with strong signature of $(00l)$ reflections. Introducing 15% vol Fe₆₅Co₃₅ content in the nanocomposites leads to reduction in the LOF and S parameters (as discussed in section V.1 and section V.3.1) by having a rapid growth of (111) reflection. It is noteworthy that there is a slight

shift in $L1_0$ -FePt peak positions in the layer-layer sample compared to those of FePt matrix and nanocomposites with NPs inside. Such variations in peak positions might be assigned to the stronger diffusion occurring after annealing (section V.1). This observation is in good agreement with the other authors [235] when they studied the composites annealed with a conventional furnace. In fact, it is challenging to draw a solid conclusion for the overall properties of the nanocomposites by only discussing the XRD diffraction. Therefore, the next step is about to examine the microstructures of the fabricated nanocomposites.

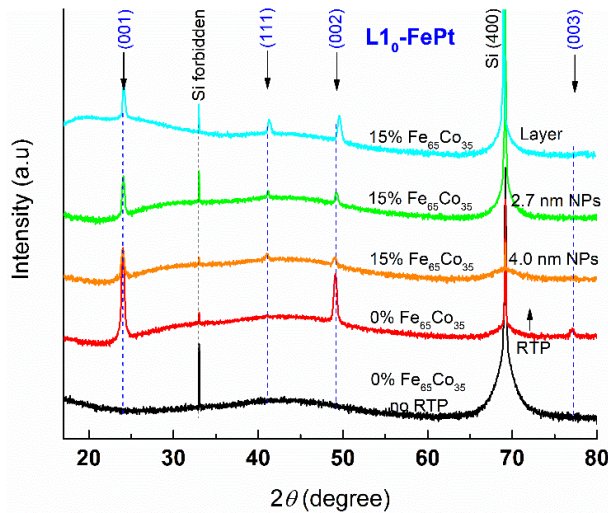


Figure V.17: The dependence of XRD diffraction patterns on the structured nanocomposites with different configurations in terms of NPs sizes (2.7 nm and 4 nm) deposited by FCG and layer deposited from PLD. Note that the case study is dedicated to 15% of $Fe_{65}Co_{35}$, in 15 nm FePt matrices. Samples were deposited at RT on Si/SiO₂ and then processed by RTP, at annealing temperature of 750°C, heating rate of 50°C/s, annealing time of 60s, and in 1×10^{-1} mbar of Ar flow.

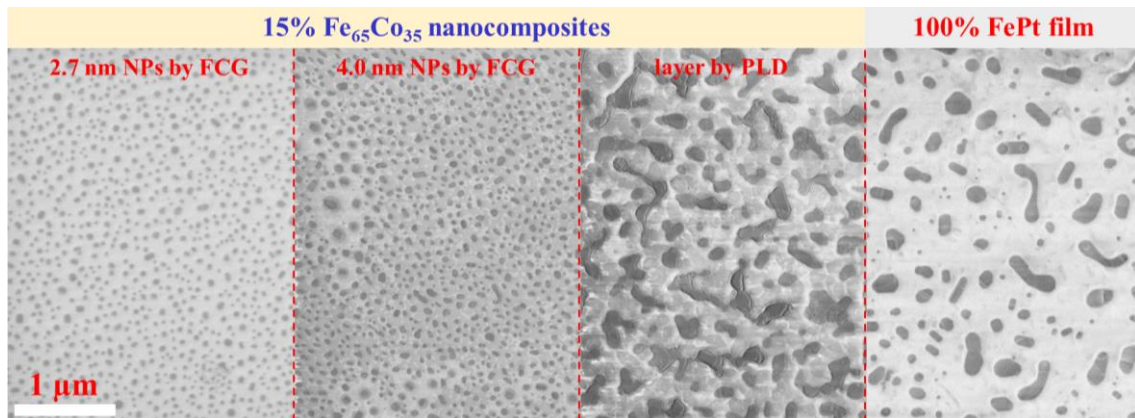


Figure V.18: The dependence of microstructure (SEM images, Inlens mode) on the structured nanocomposites with different configurations in terms of NPs sizes (2.7 nm and 4 nm) deposited by FCG, layer deposited from PLD, and 100% FePt film. Note that the case study is dedicated to 15% of $Fe_{65}Co_{35}$ with fixed 15 nm FePt matrices, all compared to the 100% FePt film. Samples were deposited at RT on Si/SiO₂ and then processed by RTP, at annealing temperature of 750°C, heating rate of 50°C/s, annealing time of 60s, and in 1×10^{-1} mbar of Ar flow.

Figure V.18 compares the microstructural properties as a function of structured nanocomposites (different sizes of NPs embedded in the matrix, the continuous soft layer deposited by PLD and 100% FePt film). The 100% FePt film (the matrix) shows prominently isolated like-island microstructure with various sizes, shapes and shape edges. Diluting the matrix with soft phase of 15% vol $Fe_{65}Co_{35}$ content induces a significant modification in microstructural properties. While continuous layer sample (with soft continuous layer $Fe_{65}Co_{35}$) have comparable grain size compared to that of 100% FePt film, the nanocomposites embedded with NPs have completely distinctive morphologies with relatively smaller grain size. Since the Inlens mode in SEM imaging also provides qualitative information about the height

of the grains, the brighter background regions are dominated predominantly by the Si/SiO₂, and darker grains (nanocomposite grains) are the mixture of FePt and FeCo.

Regarding the grain sizes, an estimate shows that the continuous soft layer (15% vol) composites is of interconnected islands, while 100% FePt has tri-modal size distribution (section III.4.1), and reduces to bi-modal and later single modal grain size distribution in 4 nm and 2.7 nm NPs nanocomposites (15% vol in soft phase), respectively. Namely, grain size distribution of (30 nm ± 3 nm; 56 nm ± 5 nm) the in 4 nm NPs nanocomposites compared to distribution of (39 nm ± 4 nm) in 2.7 nm NPs nanocomposites. Moreover, the number of grains per unit area also increases from right to left samples presented in Figure V.18. These microstructural properties suggest that soft content in the matrix promotes the discontinuity inside the matrix. After annealing, such discontinuity promotes island formation. AFM analysis performed on the sample surfaces indicates that the rms roughness reduces from 4.5 nm for 100% FePt films to about ~2.6 nm in composites with soft continuous layer. The rms roughness in 15% vol Fe₆₅Co₃₅ composites with NPs sizes of 2.7 nm and 4 nm is equivalent ~3.8 nm.

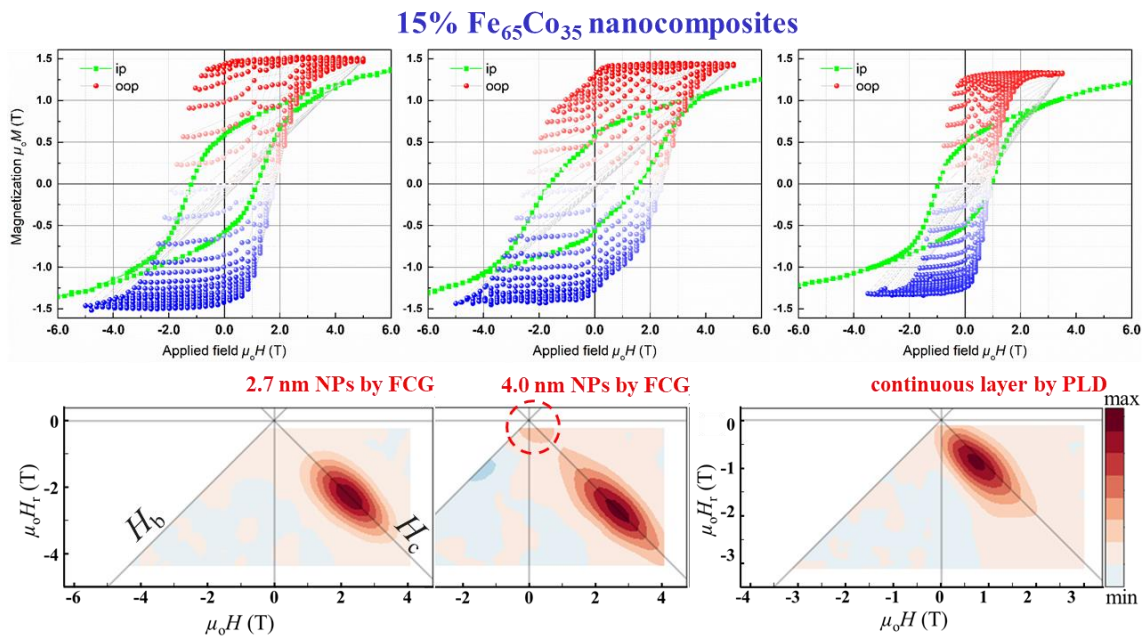


Figure V.19: Magnetic characterizations (oop FORC raw data, ip $M(H)$ loops, and the respective oop FORC diagrams) of the nanocomposites with different configurations (size of NPs embedded and continuous soft layer), after annealing at 750°C, 50°C/s, 60s. All the data has been subtracted from substrate diamagnetic contribution and uncorrected for demagnetization field.

The magnetic measurements for this series of samples are presented in Figure V.19, at which the first row compares the ip and oop $M(H)$ loops, and the second row demonstrates the oop FORC diagram distributions of the oop $M(H)$ loops. The slope as it approaches the coercive field and the anisotropy field extracted from oop and ip loops are equivalent in all the samples ($\mu_0 H_a \sim 7$ T, compared to the magnetocrystalline anisotropy of 11.6 T of the L10-FePt phase). While the oop coercivity values in nanocomposites embedded with NPs (2.7 nm and 4 nm) are comparable ~2 T, the oop coercivity for sample with soft continuous layer presents a lower value of around 1 T. Moreover, the lowerness in ip coercivities compared to oop ones, and high magnetization at high applied field suggest that the nanocomposites embedded with NPs come up with oop texture, which is in contrast to the case of sample with soft continuous layer (discussed in details in section V.1). It is also worth to note that just one nanocomposite with 4 nm NPs embedded has a small shoulder at applied field ~0 T, out of three studied samples.

Concerning the remanence value $-\mu_0 M_r$, 100% FePt thin film (section III.4.1) has oop $\mu_0 M_r$ of about 1.2 T. Introducing the soft content (Fe₆₅Co₃₅) induces better magnetic remanence, e. g., in the 15% Fe₆₅Co₃₅ nanocomposites, while soft continuous layer and 4 nm NPs samples are increased an amount of 3% and 7% respectively, the 2.7 nm NPs nanocomposite displays an outstanding increase of up to ~20 %. Note that the saturation magnetisation of the both nanocomposites embedded with NPs is comparable to around 1.5 T.

Oop nucleation field $-\mu_0 H_N$ (the procedure in extracting $\mu_0 H_N$ was presented in Figure III.25a, section III.3.2) of 2.7 nm and 4 nm NPs nanocomposites have values of -0.96 T and -0.92 T that are nearly three folds higher than that of soft continuous layer sample. The reduction in oop nucleation field (for three nanocomposites) is in good agreement with simulated tendency from other authors [10]. Though the sizes of NPs or the soft continuous thickness used here are smaller than domain wall width of the hard phase L1₀-FePt, the nucleation field still fall far short (~50% lower) of $\mu_0 H_N \sim -1.95$ T obtained in 100% FePt thin film). This reduction in nucleation field compared to the 100% matrix thin film might be explained by the diffusion occurred during the RTP. Moreover, the augmentation in values of remanence, nucleation field and coercivity of nanocomposites with NPs embedded as compared to the one from soft continuous layer sample is attributed to (i) difference in degree of diffusion taken place during the annealing process, for which the diffusion in soft continuous layer sample is stronger than that of nanocomposites embedded with NPs [235]; (ii) the soft continuous layer sample has 2D soft content larger than domain wall width of the hard phase (6.4 nm); and (iii) microstructure of isolated islands which could inhibit the magnetic switching during magnetization reversal process, while the interconnected island facilitate such process (as discussed in sections III.1.2, III.3, III.4.1, and III.4.3).

Other authors [10] suggests that if the distance between the neighboring soft magnetic NPs is significantly small, (i) these soft regions interact and thus coercivity will be destroyed (as the case of soft continuous layer sample); (ii) the magnetization modes can tunnel through the hard region, for which the hard region no longer acts as an effective potential barrier, thus the magnetic properties of the nanocomposites will reduce. Nominal 2.7 nm soft NPs is very small compared to the domain wall width of the hard phase L1₀ – FePt (6.4 nm), the micromagnetic exchange interaction and effective anisotropy constant could be treated in perturbation theory [10]. Neglecting further pinning of the nucleus, a rectangular hysteresis loop is obtained [10] (see the outline of oop FORC raw data, Figure V.19) for 2.7 nm NPs nanocomposites in lieu of 4 nm NPs one.

The oop FORC diagrams of these samples are also discussed. The main switching field distribution in three samples happens at high field. All the FORC diagrams have enclosed contour which is the signature of non-interacting single magnetic domain particles [203,239,249,250]. While the central ridge of the soft continuous layer sample is downward with respect to the four-quadrant (H_c) diagonal axis, the ridge centers of the nanocomposites embedded with NPs are exactly on the H_c axis. The nanocomposite FORC diagrams reflect reversal of exchange coupling of (i) a well exchange coupled between soft-hard phases in the nanocomposite embedded with 2.7 nm NPs; (ii) an uncoupled soft magnetic phase component in the nanocomposite embedded with 4 nm NPs (discussed in section V.3.1); and (iii) the mean field interaction in nature dominated by exchange interaction between particles in the sample with soft continuous layer (discussed in section V.1). In addition, the large vertical spread (H_b axis) with respect to horizontal spread (H_c axis) in 2.7 nm NPs and soft continuous layer nanocomposites as compared to the 4 nm NPs nanocomposite might be due to the existence of a randomly changing local interaction field [203]. The 2D FORC diagrams obviously allow to observe the exchange interaction, in the soft continuous layer sample, which is the major reason to destroy the coercivity [10]. Indeed, one could extract more detailed information about the magnetic properties of the investigated sample from

Tuan NGUYEN VAN | Thèse de doctorat | Université de Limoges | 7 Mai 2021 119
Licence CC BY-NC-ND 3.0

FORC measurement, such as from the slope of the contours, inner contours and outer contours [203,239,249,250], but in the context of this thesis, the investigation to find out the coupled exchange nanocomposites is sufficient.

V.3.3. Effect of annealing time (FeCo NPs nanocomposites, 10s)

As discussed in section III.4.3, among the annealing conditions with varying annealing time, the annealing recipe of 750°C, 50 °C/s and 10s induces a single magnetic phase behavior in the FePt matrix. Thus in this part, the effect of annealing time (10s) on properties of the nanocomposites will be investigated and compared to those of the 60s-annealed nanocomposites (shown previously).

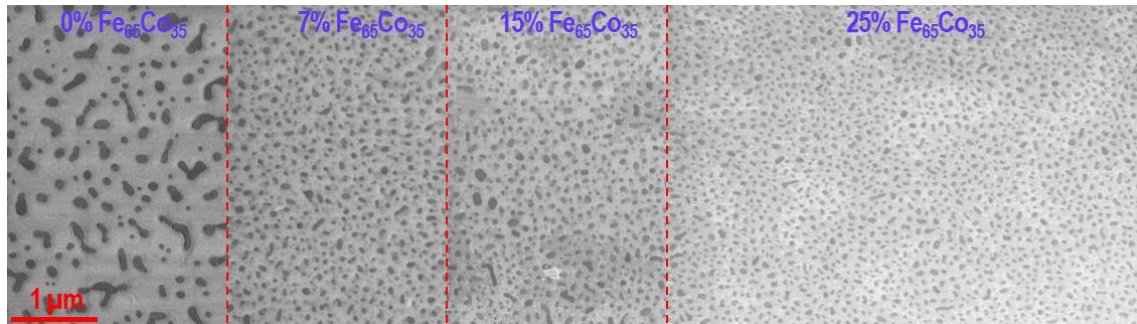


Figure V.20: The microstructural evolution SEM (Inlens mode) of annealed nanocomposites as a function of 4 nm – Fe₆₅Co₃₅ NPs volume content embedded in 15 nm FePt matrix. Nanocomposites was initially deposited at RT on Si/SiO₂ and then processed by RTP, at annealing temperature of 750°C, heating rate of 50°C/s, annealing time of 10s, and in 1 × 10⁻¹ mbar of Ar flow.

The XRD diffraction patterns for this series of nanocomposites annealed during 10s do not show distinctive differences compared to samples annealed during 60s (section V.3.1). It is therefore not necessary to re-discuss here. Figure V.20 compares the evolution in microstructure of the nanocomposites as a function of 4 nm NPs of Fe₆₅Co₃₅ vol content. Once again, the microstructure is strongly influenced by the soft Fe₆₅Co₃₅ vol content available in the nanocomposites. With 0% Fe₆₅Co₃₅ volume content, the microstructure is mostly dominated by the random shape and size of isolated islands. Increasing the Fe₆₅Co₃₅ content leads to constantly refine the microstructure, e. g., the average diameter of the grains as follows: 94 nm ± 7 nm, (37 nm ± 3 nm and 62 nm ± 5 nm), (32 nm ± 4 nm and 58 nm ± 4 nm), and (28 nm ± 3 nm and 56 nm ± 4 nm) in the 0%, 7%, 15%, and 25% Fe₆₅Co₃₅ nanocomposites, respectively (details for modals of grain size distribution are given in section III.4.1, Figure III.29a) . It is clearly seen that the nanocomposites with different Fe₆₅Co₃₅ contents (with 10s annealing) illustrate a constant of bi-modal grain size distribution, which is slightly different compared to the reduction in the number of modals of grain size distribution observed with 60s annealing. Generally, the grain sizes of the nanocomposites with 10s annealing are relatively smaller than those of nanocomposites with 60s annealing. The behavior in grain size with different annealing time could be comprehended by considering the Ostwald Ripening effect [209] and dewetting process [244]. After suddenly being annealing with a high heating rate of 50°C/s, the nanocomposites start dividing into smaller grains from the continuous form in the as-deposited state. 10s annealing allows to form such smaller grains, however, increasing the annealing time to 60s gives rise to collect the smaller grains to generate bigger ones followed by the Ostwald Ripening mechanism and dewetting process [244].

The AFM measurement performed on the surfaces of the nanocomposites with various Fe₆₅Co₃₅ contents indicates that the rms roughness reduces to lower values from 2.6 nm (0% Fe₆₅Co₃₅ sample) to 2.3 nm (7% Fe₆₅Co₃₅ sample) and become gradually lower again to 2.1 nm in 25% Fe₆₅Co₃₅

nanocomposites. A good agreement between the SEM microstructural observation and AFM analysis suggest that the granular nanocomposites was formed after being annealed even with high Fe₆₅Co₃₅ content. Note that like the FePt thin film, the nanocomposites deposited at RT and latter applied heat treatment do not show droplet formation as in the case of NdFeB thin films.

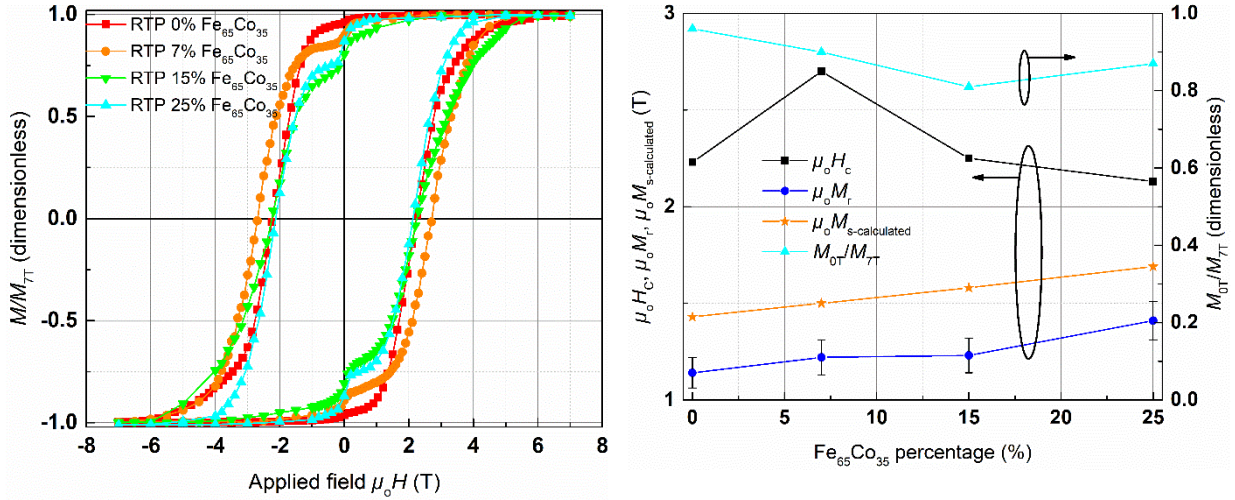


Figure V.21: The magnetic characterizations of nanocomposites based FePt deposited on Si/SiO₂ substrates at RT and then processed by RTP (750°C, 50 °C/s, 10 s) as a function of 4 nm – Fe₆₅Co₃₅ volume content (left) Out-of-plane magnetic hysteresis loops (uncorrected for demagnetization field and normalized) of annealed films; (right) A classical representation of magnetic coercivity- $\mu_0 H_c$, remanent magnetisation- $\mu_0 M_r$, remanence ratio- M_{0T}/M_{7T} , and calculated saturation magnetisation- $\mu_0 M_s$ corresponding to the Fe₆₅Co₃₅ volume content of the annealed films. The $\mu_0 M_s$ of L1₀-FePt and Fe₆₅Co₃₅ are 1.43 T and 2.45 T are applied to the calculated estimation, respectively.

Oop $M(H)$ loops of the representative nanocomposites with various Fe₆₅Co₃₅ contents ranging from 0% to 25% are compared in Figure V.21-left. While sample with 0% Fe₆₅Co₃₅ content depicts single magnetic-phase behavior (as discussed in section III.4.3), the other nanocomposites with higher Fe₆₅Co₃₅ contents, all show obvious two-magnetic-phase behavior. All samples show comparable coercivity value – $\mu_0 H_c$ of around 2 T and the sharpness of $M(H)$ loop as it reaches to the coercivity. The magnetic properties of this annealed series of samples are compiled and presented in Figure V.21-right. Although the coercivity for all the samples is stagnant, the remanence ratio – M_{0T}/M_{7T} slightly decreases with increasing the Fe₆₅Co₃₅ content from 0.96 (0% Fe₆₅Co₃₅) to 0.87 (25% Fe₆₅Co₃₅). The remanence – $\mu_0 M_r$ of the nanocomposites follows the trend of the calculated saturation magnetisation – $\mu_0 M_s$ -calculated, which means that increasing the Fe₆₅Co₃₅ content induces the $\mu_0 M_r$ value. The $\mu_0 M_r$ is augmented by 24% in the 25% Fe₆₅Co₃₅ nanocomposite compared to $\mu_0 M_r$ value of 1.15 T in the FePt thin film only (0% Fe₆₅Co₃₅). It is noteworthy that the $\mu_0 M_s$ of L1₀-FePt and Fe₆₅Co₃₅ are 1.43 T and 2.45 T, respectively. Clearly, in the case of 10s annealing, the coercivity is kept at a constant meanwhile the remanence of the nanocomposites is improved with increasing the soft Fe₆₅Co₃₅ content. This is a strong point for one of the objectives of the thesis.

The nominal 4 nm NPs size is smaller than domain wall width of the L1₀-FePt hard phase, however, the $M(H)$ loops display two phase behaviors, at which the presence of the uncoupled phase at low applied field of ~0 T might be attributed to the variation in grain size distributions rather than the size of the NPs. The similarity in overall loop shape, coercivity in the nanocomposite systems could be assigned to the equivalent in structure and microstructure of the samples. The improvement in remanence $\mu_0 M_r$ in 25% Fe₆₅Co₃₅ content nanocomposites compared to 100% FePt thin film annealed at the sample conditions, e.g., increase 24% (10s annealing) compared to increase 18% (60s annealing). This means that 10s annealing induces weaker diffusion than samples annealed with 60s (section V.2), thus the

remaining NPs inside the nanocomposites with 10s annealing is larger than that of 60s. Such higher remaining NPs will be (partly) exchanged couple with the hard FePt matrix to increase the remanence of the nanocomposite [10]. To distinguish the contribution of each phase or the origin of magnetic properties of the nanocomposite, more advanced measurements based on synchrotron radiation X-ray Magnetic Circular Dichroism (XMCD) should be employed.

V.3.4. Difference between Co and FeCo NPs embedded NPs (10s)

To follow better the diffusion and understand deeper the properties of the soft in hard magnetic nanocomposite, another series of nanocomposite were prepared by replacing 4 nm Fe₆₅Co₃₅ NPs by 4 nm Co NPs, which is composed of a single element and has lower value of saturation magnetisation ($\mu_0 M_s \sim 1.7$ T) compared to Fe₆₅Co₃₅ material. The main aim was to observe the differences in using NPs' materials on properties of the nanocomposites because Co is pure metal (not an alloy as FePt or FeCo).

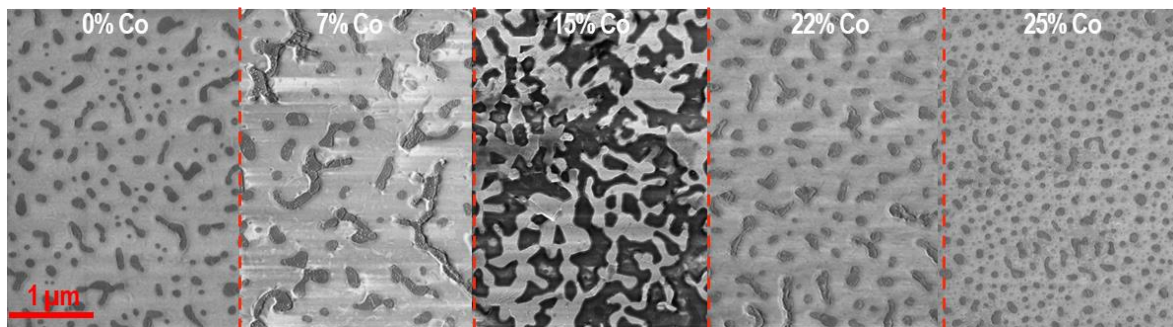


Figure V.22: The microstructural evolution SEM (Inlens mode) of annealed nanocomposites as a function of 4 nm – Co NPs volume content embedded in 15 nm FePt matrix. Nanocomposites was initially deposited at RT on Si/SiO₂ and then processed by RTP, at annealing temperature of 750°C, heating rate of 50°C/s, annealing time of 10s, and in 1×10^{-1} mbar of Ar flow.

A set of nanocomposites with different (nominal) 4 nm Co NPs volume content was first deposited at RT on Si/SiO₂ (100 nm) substrate and later applied by RTP at 750°C, 50°C/s, 10s. While the XRD diffraction patterns of this series look similar to those of nanocomposites with Fe₆₅Co₃₅ NPs (section V.3.1 and V.3.3), the microstructure behaves differently. Figure V.22 presents the evolution of microstructure of nanocomposites with various 4 nm Co NPs contents ranging from 0% to 25%. Up to 15% Co NPs content, the microstructure is largely dominated by the interconnected islands. Higher soft Co NPs content of more than 15% leads to the separation of the isolated grains. The average grain size increases with Co NPs content in the nanocomposites from 0% to 15%. Further increasing Co NPs content causes the reduction in grain sizes.

While the microstructural evolution in Fe₆₅Co₃₅ NPs nanocomposites follows the same tendency of decreasing grain sizes with increasing the Fe₆₅Co₃₅ content, the Co NPs nanocomposites vary wildly awkward kind of complex microstructure as indicated previously. These variations might be related to the difference in nature of the NPs, which are pure metal for Co and alloy for Fe₆₅Co₃₅. Such pure metal and alloy materials might induce different behaviors during the RTP process, i. e., the dewetting process. Other studies on dewetting of metal and alloy [248,251] reveal that the morphology can fall into three regions of (i) remaining continuous as in as-deposited state; (ii) Partly dewetting phenomenon; and (iii) completely dewetting phenomenon and the alloy has greater influence than the thickness and/or pure metal. Furthermore, the difference in wettability between the pure metal and alloy is also pointed out [74,252], for which the pure metal surface induces low wettability. In a nutshell, though the embedding of different NPs (Co and Fe₆₅Co₃₅) materials does not show any striking variation in the structure of the nanocomposites (by XRD patterns), changing the NPs' materials modifies the microstructure heavily.

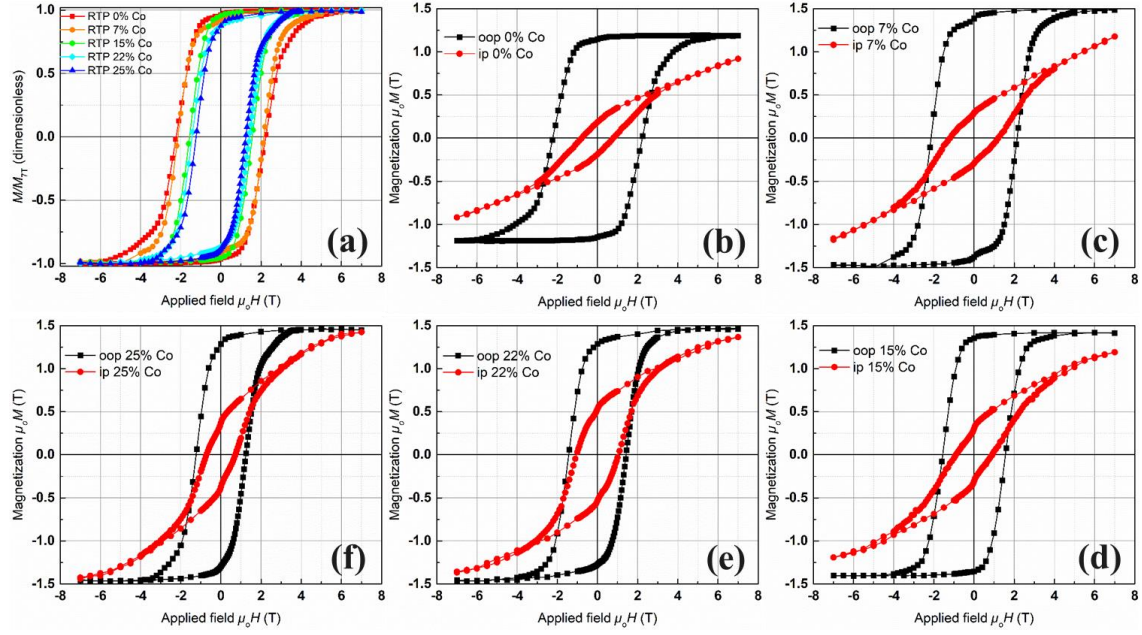


Figure V.23: (a) The Out-of-plane magnetic hysteresis loops (uncorrected for demagnetization field and normalized) of annealed nanocomposites based FePt deposited on Si/SiO₂ substrates at RT and then processed by RTP (750°C, 50 °C/s, 10 s) as a function of of 4 nm – Co NPs vol content. The ip and oop $M(H)$ loops of the annealed nanocomposites with different soft Co NPs concentrations (b) 0%; (c) 7%; (d) 15%; (e) 22%; and (f) 25 %.

Figure V.23a compares the oop, normalized and uncorrected for demagnetizing field hysteresis loops of this set of nanocomposites as a function of 4 nm Co NPs contents. The oop $M(H)$ loops demonstrate that most of the nanocomposites are of single magnetic phase behavior and they have comparable overall loop shapes. The slopes of the $M(H)$ loops are equivalent, nonetheless the sharpness of the $M(H)$ loops become narrower with increasing the Co NPs content, as it approaches to the coercive field. Figure V.23 from (b) to (f) present the dependence of the ip and oop $M(H)$ loops on the Co NPs volume content with the absolute scale of magnetization. In the 0% Co film (Figure V.23b), along the oop direction, a well-behaved rectangular loop shape and high remanence ratio- M_{OT}/M_{7T} have been reached. Relating to the ip measurement, the relative lower in coercivity- $\mu_o H_c$, remanence- $\mu_o M_r$ compared to the oop one, and high magnetization at high applied indicate that the films have oop texture and strong perpendicular anisotropy, which is agreed well with the XRD analysis (section III.4.3). Increasing the Co NPs content in the nanocomposites leads to increasing in saturation magnetisation – $\mu_o M_s$ but the nanocomposites still keep the oop texture and high value of M_{OT}/M_{7T} ratio (Figure V.23 from (c) to (f), and Figure V.24). It is also noteworthy that the oop $\mu_o H_c$ is decreasing with higher content of Co NPs, nevertheless, the ip $\mu_o H_c$ remains at a constant of about ~1 T. Though the signature of two-magnetic-phase behavior in the nanocomposites with Co NPs content (> 0%) is hidden in the oop measurement, it is displayed through small shoulders at small applied field of ~0 T in the ip $M(H)$ loops. Extracting the oop and ip loops provides the anisotropy field- $\mu_o H_a$ of the nanocomposites, and thus the effective anisotropy constant, $K_{eff} = \mu_o M_s H_a / 2$, can be also estimated. Details about the $\mu_o H_a$ and K_{eff} are compiled in Table V.3. Other general magnetic properties of the investigated nanocomposites are provided in Figure V.24. The $\mu_o M_r$ follows the same trend of increasing Co NPs content in the nanocomposites. An increase of about 16% in $\mu_o M_r$ was observed in the 25% Co NPs content nanocomposites compared to that of pure FePt thin film (0% Co). Note that the $\mu_o M_r$, M_{OT}/M_{7T} , $\mu_o H_a$ and K_{eff} values are estimated from $M(H)$ loops without being corrected with demagnetizing factor.

Table V.3: The effective anisotropy constant and anisotropy field of the nanocomposites based FePt as a function of 4 nm NPs Co volume content.

Co NPs vol content (%)	0	7	15	22	25
K_{eff} (MJ.m ⁻³)	4.59	5.91	5.02	4.44	4.1
$\mu_0 H_a$ (T)	9.7	10.1	8.9	7.7	7.1

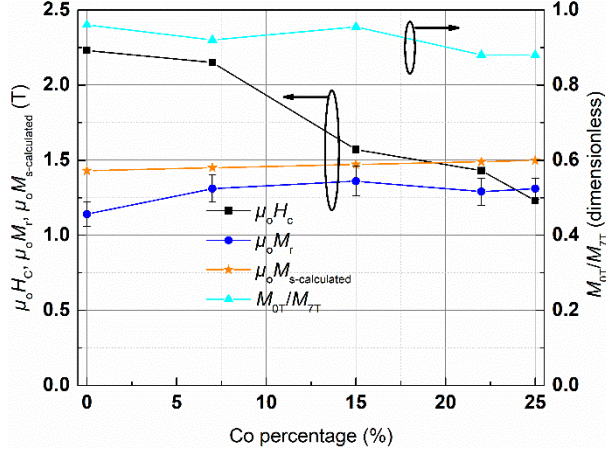


Figure V.24: A summary of magnetic coercivity- $\mu_0 H_c$, remanent magnetisation- $\mu_0 M_r$, remanence ratio- M_{0T}/M_{7T} , and calculated saturation magnetisation- $\mu_0 M_s$ corresponding to the 4 nm Co NPs volume content of the annealed films. The $\mu_0 M_s$ of L10-FePt and Co are 1.43 T and 1.7 T are applied to the calculated estimation, respectively.

Along the oop direction, nice rectangular loop shapes with single magnetic phase behavior are obtained, which suggest a complete exchange coupling of the soft Co NPs to the neighbouring FePt hard magnetic matrix. However, relatively weak shoulder is observed in all nanocomposites in the ip $M(H)$ loops indicating the partial coupling between the soft and hard phases in the nanocomposites [32], for which it might be due to (i) another phase inducing by the intermixing regions (indicated in section V.2.2) being inserted besides the soft and hard phases; and/or (ii) not all the Co magnetic moments being pinned by the FePt (or some other free moments existed) and having separated magnetization reversal along ip direction. Such partial decoupling between the two phases in the ip direction also suggests that the diffusion took place at the same length scale, which is coherent with the same annealing time for all nanocomposites. The partial decoupling originating from the size of NPs is eliminated because the nominal 4 nm NPs is smaller than the domain wall width – 6.4 nm of the L1₀-FePt. Moreover, it can be concluded that the unique phase behavior in the oop $M(H)$ loops and small kink in the ip $M(H)$ loops could also be associated with dipolar coupling as suggested by other authors [32]. While the coercivity for nanocomposites with soft Fe₆₅Co₃₅ NPs (section V.3.3) has little variation, the nanocomposites with soft Co NPs produces a slight reduction, which might be mainly attributed to the differences in microstructures between the two systems. Note that the great unaware modification in microstructure may be due to the difference in Co pure metal compared to that of Fe₆₅Co₃₅ alloy as discussed previously and in references [74,248,251,252]. Hence, doping different soft magnetic NPs materials offers another degree of freedom to control both the intrinsic magnetic properties and the extrinsic property of microstructure.

V.3.5. Effect of Ta spacer

The theoretical calculation and experiment have indicated (section V.2) the diffusion occurring at short length scale with RTP. In order to better prevent the diffusion during annealing process, in this part, a Ta layer will be introduced between the Co NPs and FePt layers. The main idea was inspired from other authors [32], for which the work deals with the nanocomposites based NdFeB material with annealing at high temperature during the deposition of NdFeB layers, to keep the coercivity while enhancing the remanence.

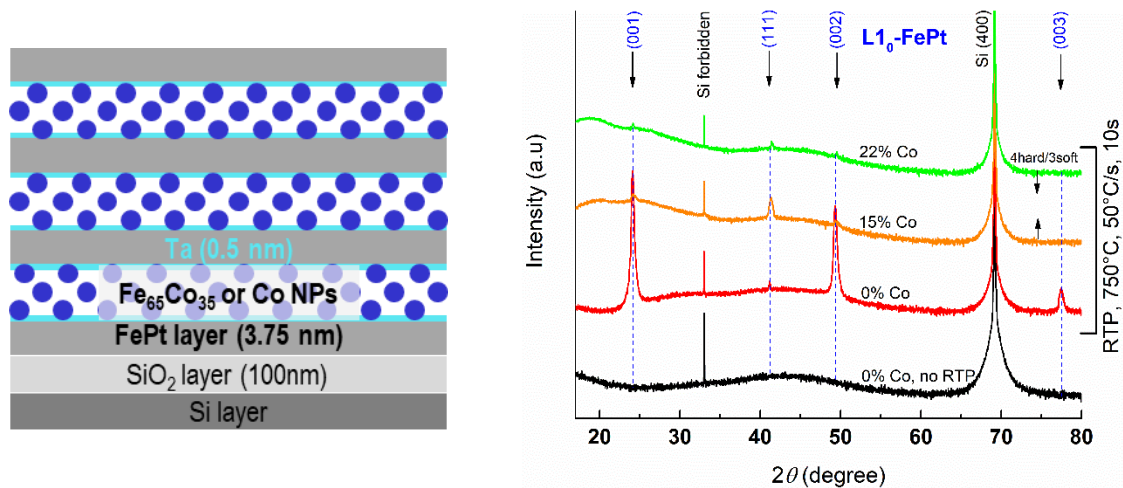


Figure V.25: (left) The schematic diagram of FePt (3.75nm)/Ta (0.5 nm)/Co nanocomposite with multi-layer system. The thickness of stack of 4 nm Co NPs depends on how much dilution of the nanocomposite is. (right) The XRD diffraction patterns as a function of 4 nm – Co ($t = 480 \mu\text{s}$) soft magnetic NPs' percentage, embedded in 15 nm FePt matrix, at RT on Si/SiO₂ and then processed by RTP, at annealing temperature of 750°C, heating rate of 50°C/s, annealing time of 10s, and in 1×10^{-1} mbar of Ar flow.

In this case study, the nanocomposites were deposited with 15 nm of FePt dividing into four layers of 3.75 nm each, 3 nm of Ta spacer dividing into six layers of 0.5 nm each, and three stacks of 4 nm Co NPs capped by the two neighboring Ta layers, as shown in the schematic diagram in Figure V.25-left. First, a set of three nanocomposites with various volume contents of stacks of 4 nm Co NPs (soft) ranging from 0% up to 22%, was all deposited at RT and then annealed at 750°C, 50°C/s, 10s. Figure V.25-right compares the representative XRD patterns of such annealed samples. In all annealed samples, the signature of the hard magnetic phase of L1₀-FePt is still visible. Increasing the Co volume content leads to reduction in pronounced *c*-texture of L1₀-FePt phase through presence of (111) reflections. Hence, the *LOF* and *S* parameters (defined in section III.3) are reduced as results.

Figure V.26-1st row presents the variation in microstructural properties of the annealed nanocomposites. The microstructure of 100% FePt thin film (0% Co) is governed by separately arbitrary grains with various shapes and sizes of up to 500 nm. Increasing Co content leads to interconnected island-like feature in 15% Co nanocomposite, higher Co content (22%) induces various smaller grain configurations. The grain formation of nanocomposites (15% Co) seems to take place for the top FePt layer because of low contrast in the *z* direction, which might be ascribed to the low wettability of the alloys on pure Ta surface [74,248,251,252].

Figure V.26-2nd to 5th rows, display the plane-view FIB-SE images associated with corresponding EDS elemental maps of the two annealed nanocomposites (15% and 22% Co volume content). Thanks to the EDS maps, it can be concluded that the brighter contrast regions (high *z* direction) are the nanocomposites composed of FePt+Co and the darker contrast regions (low *z* direction) are the substrate (and sometimes Ta element). In 15% Co sample, there is no doubt that Si and Ta present everywhere. The Fe, Pt, and Co are basically inhibited within the interconnected grains. These EDS maps might also approve that the microstructural modification occurs just on the top layer of the 15% Co nanocomposite, which is in agreement with the above discussion of low wettability of alloys on Ta pure metal. In contrast for 22% Co samples, while Si presents in the areas without brighter grains, the Fe, Pt, Co, and Ta is seen to appear within the isolated brighter grains. Hence, the microstructural modification seems to happen homogeneously throughout the nanocomposite thickness, which is fairly different with microstructure in

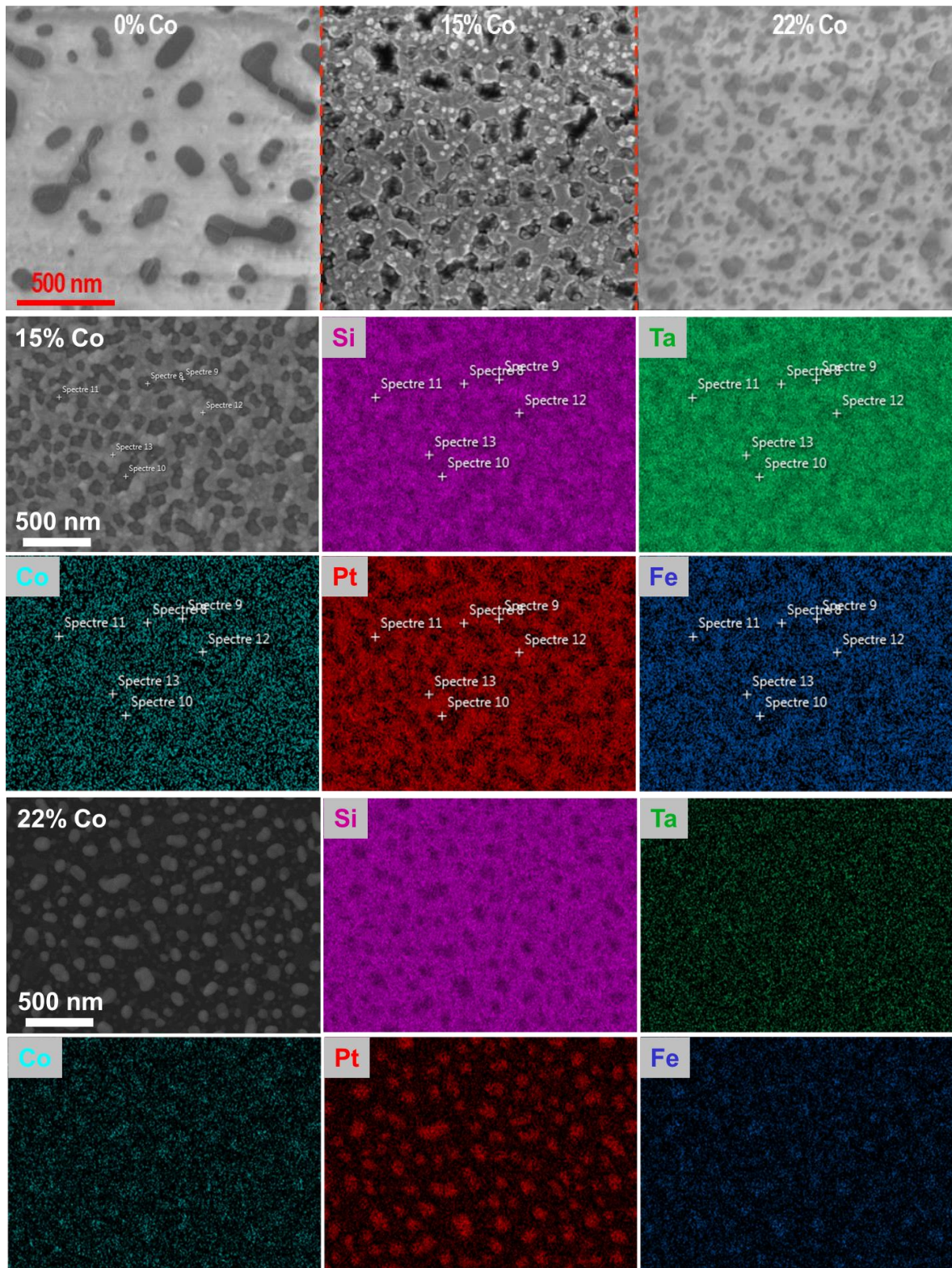


Figure V.26: The evolution of microstructure as a function of 4 nm Co NPs vol content in nanocomposites performed by plane-view SEM (Inlens mode), 1st row. The microstructures and EDS maps observed with FIB-SE mode for the two annealed nanocomposites with 15% (2nd and 3rd rows) and 22% (4th and 5th rows) volume content of 4 nm – Co NPs, embedded in 15 nm FePt matrices, respectively. All were deposited at RT on Si/SiO₂ and then processed by RTP (750°C, 50°C/s, 10s, and in 1×10^{-1} mbar of Ar flow).

15% Co nanocomposite. The different modification in 22% Co nanocomposite might be assigned to the relatively higher thickness of porous stacks of Co NPs (2.82 nm compared to 1.76 nm in 15% Co Tuan NGUYEN VAN | Thèse de doctorat | Université de Limoges | 7 Mai 2021 126 Licence CC BY-NC-ND 3.0

nanocomposite, these values are taken into account the 50% porosity). The higher thickness Co layer of 2.82 nm (22% Co sample) acts as a foamy layer which allows the dewetting process occurring easily. Differently, thinner Co layer of 1.76 nm (15% Co sample) is suppressed by the two neighboring Ta layers (partly) that inhibit the dewetting process during the annealing of 10s.

The EDS analysis in FIB performed on top-view allows to distinguish the elemental percentage of each element in the nanocomposites. While the darker regions (spectre 8-11) have majority of Ta (0.2% at-atomic percentage for each Fe&Pt, ~0.1% at Co), the brighter regions (spectre 12, 13) have significant amount of Fe, Pt and Co (1.5% at for each Fe&Pt, 0.5% at Co). In all the case studies here, the Ta content almost remains constant at ~0.7% at, and other percentage is attributed to Si and O₂. It is also worth noting that the analyzed volume in EDS mode in this case study is about 1 μm³, which will cause a certain error bar in the above atomic percentage estimation. These microstructural analyses suggest that the Ta spacer has certain contributions in preventing diffusion between the soft and hard phases.

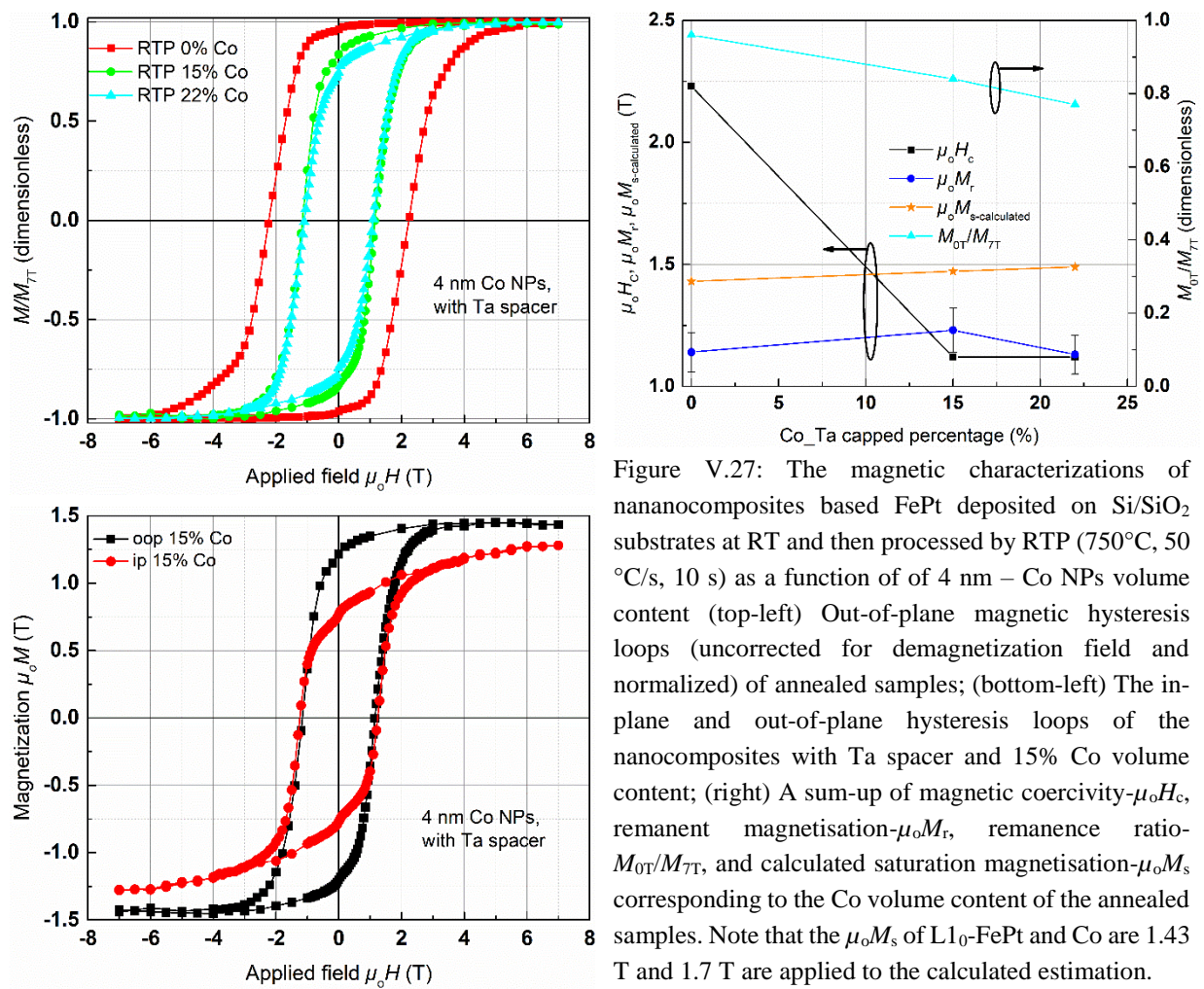


Figure V.27-top-left compares the oop $M(H)$ loops of the nanocomposites with various Co volume content. All the samples show obvious single magnetic phase behavior. The nanocomposites (15% and 22% Co) have comparable overall loop shape, at which the coercivity and sharpness as it approaches the coercive field are quite similar. It is noted that the coercivity of nanocomposites with Ta spacer is not varied with increasing the soft content, which is markedly different with that of nanocomposites without Ta spacer (as discussed in previous sections of V.3.1, V.3.2, V.3.3, and V.3.4). The coercivity – μ_0H_c and remanence ratio – M_{0T}/M_{7T} of these nanocomposites is relatively lower of about 50% and 9% from values

of 2.2 T and 0.96 of FePt thin film (0% Co). The poor magnetic properties in terms of $\mu_0 H_c$ and M_{0T}/M_{7T} ratio could be attributed to both reduction in quality structure (XRD, expressed by LOF and S parameters).

Owing to poor M_{0T}/M_{7T} ratio (0.8), the maximum enhancement in remanence $-\mu_0 M_r$ is increased about 8% compared to 100% FePt thin film (0% Co). This enhancement is much lower than the value of 16% and 24% obtained in the nanocomposites with Co and Fe₆₅Co₃₅ NPs without Ta spacer, respectively. A sum-up for the magnetic properties of the investigated sample is compiled in Figure V.27-top-right. Figure V.27-bottom-left demonstrates the ip and oop $M(H)$ loops of a nanocomposites with 15% Co NPs capped by Ta spacer. The comparable coercivity for ip, oop loops and low magnetization at high applied field for ip loop suggest that this nanocomposites is of isotropic properties, which is contrast to perpendicular anisotropy (oop texture) observed in the nanocomposites without Ta spacer (sections V.3.1, V.3.3, and V.3.4). Moreover, the small shoulder at ~ 0 T in ip loop suggest that partial coupling exists in the in the nanocomposites [32], which might be attributed to the Ta spacer rather than intermixing layer of soft-hard phases due to diffusion as observed in nanocomposites without Ta spacer. Note that partial coupling effect could be hidden in the oop direction but it could be evident in ip direction as in this case study. Hence, the introduction Ta spacer could be a solution to prevent diffusion and maintain high coercivity ($> 1T$).

V.4. Chapter highlights

A variety of soft-hard nanocomposite configurations based on 15 nm FePt matrix has been successfully developed (using two-step annealing), characterized and later compared.

The continuous tri-layer system of FePt/FeCo (or Co)/FePt with various soft material proportions (0% - 40%) was deposited by using conventional PLD. The annealed samples show great diffusion process took place during the 60s annealing, which induces poorer magnetic properties ($\mu_0 H_c$ and $\mu_0 M_r$ close to 1 T) compared to 100% FePt film ($\mu_0 H_c \sim 4.4$ T and $\mu_0 M_r > 1$ T) (section V.1).

The theoretical estimations of diffusion based on classical Fick's second law and Arrhenius equation both agree that the diffusion exists during the annealing process, e.g., higher annealing time or temperatures leads to stronger diffusion effect. The TEM experimental confirmations illustrate that the two well-crystallized phases are co-existed in soft-hard nanocomposites (with L1₀-FePt phase for the matrix). The driving forces involved in formation of the crystallized soft-hard nanocomposites are the combination of Ostwald ripening mechanism, dewetting process, and Kirkendall effect (section V.2V.3).

Nanocomposites with embedded NPs insides were deposited, by PLD+FCG, with various soft NPs volume content (section V.3.1, V.3.3, V.3.4, and V.3.5), architectures (NPs sizes versus continuous layer, section V.3.2), annealing time (section V.3.1, and V.3.3), NPs materials (section V.3.3, and V.3.4), and with introduction of Ta spacer for better preventing diffusion (section V.3.5). While increasing the soft NPs content (0% - 25%) leads to a great refinement in microstructure with average grain size becoming smaller, the signature of the L1₀-FePt hard phase is still obvious. The coercivity of the soft-hard nanocomposites remains at high value of around 2 T, and the remanence varies depending on the nanocomposite configurations. In terms of $\mu_0 M_r$, (i) with 60s annealing, an increase of +18% in 25% 4 nm-Fe₆₅Co₃₅ NPs sample, and +20% in 15% 2.7 nm-Fe₆₅Co₃₅ NPs sample compared to 100% FePt sample ($\mu_0 H_c \sim 4.4$ T and $\mu_0 M_r \sim 1.3$ T); and (ii) with 10s annealing, an increase of +24% in 25% 4 nm-Fe₆₅Co₃₅ NPs sample, and +16% in 25% 4 nm-Co NPs sample compared to 100% FePt sample ($\mu_0 H_c \sim 2.3$ T and $\mu_0 M_r \sim 1.1$ T). All the results show that the soft-hard nanocomposites are successfully achieved, which will serve as model material for understanding solid states physics.

Conclusions and Prospects

The goal of this thesis was to address two biggest challenges facing the investigation of soft inclusion inside hard magnetic matrices: fabrication and characterization to examine their performances expecting achieving new magnetic materials with higher performances than those of the market. The extended magnetic system of soft-hard nanocomposites contains both matrix and soft inclusions with the soft dimensions being restricted by twice the domain wall width of the hard phase. Such patterned nanocomposites can exhibit exceptional magnetic properties when the coercivity is maintained at a constant and the remanence is enhanced. So each single stage of optimizing the matrices and nanoparticles is necessary to give rise in understanding the magnetic properties through the correlated structure and microstructure. Indeed, in order to exploit the advantages of the magnetic properties of the soft in hard nanocomposites, one needs a rigorous attention on the influence of intrinsic and extrinsic properties on the magnetic properties. The XRD, AFM, SEM, TEM, conventional hysteresis loop and First Order Reversal Curves allow to correlate such influence and partly distinguish the origin of magnetic improvement in the nanocomposites compared to the matrix itself.

1. General conclusions

Though the fabrication of pure thin film and nanoparticles (NPs) is well established, it has been in only recent years with the advances in using the modern nanoscience tools that the production of soft NPs in hard magnetic nanocomposites has become possible. The nanocomposites have been recently achieved by chemical techniques with soft NPs [33,34,238,253], by physical deposition with soft magnetic layers [32,50,51]. However, the magnetic remanence is still limited and falls far short from the predicted values for a good nanocomposite [10] owing to the insufficient control of dimensions of the soft phases of being less than twice the domain wall width of the hard phase and also of definition and control of an adequate architecture. Thanks to a dual pulsed laser ablation system developed at IRCER and consisting of a conventional Pulsed Laser Deposition (PLD) coupled with a homemade Free Cluster Generator (FCG), various soft in hard nanocomposite configurations with the sizable soft NPs may be now reachable.

Various challenging tasks have been executed during this thesis such as fabrication and characterization of nanocomposites. Along the way towards the aim of the thesis, (i) two kinds of matrices based on NdFeB and FePt materials, (ii) two systems of FeCo and Co NPs; and (iii) the combination of soft NPs embedded inside FePt matrices were developed and investigated carefully. Each material needs optimizing with overcoming some important steps.

Preventing the oxidation during the film growth and optimizing its composition were the biggest threat to obtain good hard magnetic NdFeB thin films. Thus, a new homemade double target holder (Ta, and NdFeB or FePt targets) was designed. An investigation of NdFeB target compositions, provided by Néel Institute, and the choice of a relatively high laser fluence (5 J.cm^{-2}) combining with the exploration of the deposition temperature and of the Rapid Thermal Processing (RTP) annealing recipes allow to obtain good hard magnetic properties.

In the optimized deposition conditions (target Nd/Fe ratio = 0.45, T_d : 550°C-630°C, on Si/SiO₂ or Al₂O₃ substrates), out-of-plane textured NdFeB films supported by a Nd rich phase decoupling from Nd₂Fe₁₄B grains lead to a coercivity $\mu_0 H_c \sim 1.3 \text{ T}$ and a remanence $\mu_0 M_r > 1 \text{ T}$. With a two-step elaboration process (deposition following by RTP post-annealing), both $\mu_0 H_c$ and $\mu_0 M_r$ close to 1 T are achieved in NdFeB thin films. Despite these interesting results, NdFeB material was not selected as hard phase for

nanocomposites owing to its strong ability to oxidize, the relatively high content of Nd inducing some unexpected phase formations as embedding soft inclusions, and the droplet formation (sections III.1 and III.2).

FePt is also an interesting hard magnetic material with high resistance to corrosion and oxidation. Its fabrication by PLD induces no droplet formation, reproducibility and stability even with very thin film (sections III.3, III.4, V.1, V.2.2, and V.3), which is benefited when diluted with soft magnetic NPs. Additionally, the influence of deposition repetition rate, deposition temperature T_d , two-step procedure at various RTP conditions was studied in terms of structure, microstructure and magnetic properties. Good out-of-plane textured FePt films are successfully developed. At optimized deposition conditions (2 Hz, $T_d > 700^\circ\text{C}$, Si/SiO₂ or MgO substrate, 35 nm-film thickness), $\mu_0 H_c \sim 1.5$ T and $\mu_0 M_r$ close to 1 T are achieved for as-deposited thin films. And the best results concern 15 nm granular films obtained in a two-step process with RTP showing single or multiple-magnetic behavior with $\mu_0 H_c \sim 4.4$ T and $\mu_0 M_r > 1$ T.

Particular attention was paid to the development of soft magnetic materials of the Fe₆₅Co₃₅ binary system. Sizable NPs ranging from 2.5 nm to 5 nm with narrow size distribution were achieved in this work. While the composition of NPs can be adjusted by changing the target, the microstructure formation in stacks of NPs is mostly governed by Ostwald ripening mechanism (section IV.1.4).

Concerning the nanocomposites, in order to prevent any unexpected diffusion, the nanocomposites were first deposited at RT and then subjected to a heat treatment. Optimal conditions by using RTP during both 60s and 10s promote the L1₀-FePt hard phase formation with oop texture, and a high coercivity property. Though the annealing time is short, the diffusion still existed. A complex combination between three phenomena were involved during the annealing for the nanocomposites system, e. g., Ostwald ripening mechanism, dewetting process, and Kirkendall effect. However, distinctively crystallized soft NPs inside crystallized hard magnetic phase L1₀-FePt were well observed with TEM imaging. The experimental observation (section V.2.2) is in good agreement with theoretical estimation (section V.2.1). This is one of the most remarkable steps towards successful fabrication of soft magnetic inclusions inside hard magnetic matrices leading to an augmentation in magnetic properties. Indeed, magnetic remanence $-\mu_0 M_r$ increased about 16% and 24% in 25% vol. soft content of Co and Fe₆₅Co₃₅ nanocomposites compared to that of FePt hard matrix, respectively, showing that one of the leading premises of the project was achieved.

A comparison of various kinds of nanocomposite configurations such NPs by FCG embedded in PLD hard matrix, hard/soft/hard multilayers by PLD, was made, showing the outperformance of soft inclusions in hard matrix (FCG+PLD) over the soft continuous layer in hard matrix (PLD only). Soft continuous layer in the matrix demonstrated stronger diffusion compared to that of soft NPs inside the matrix (sections V.2 and V.3.2). The better magnetic properties are obtained (loop shape, $\mu_0 M_r$, etc) for the nanocomposites with smaller FeCo NPs and elaborated with shorter annealing. In a specific matrix of FePt, the nature of soft inclusions also plays an important role by influencing the microstructure and thus the magnetic properties of the fabricated nanocomposites (section V.3.4).

A deeper understanding of magnetization reversal was made on soft-hard nanocomposites, for which the coupling between soft inclusions (soft content, sizes of NPs, structured nanocomposites) and hard matrix was distinguished by FORC (First Order Reversal Curves) diagram distribution (sections V.3.1 and V.3.2). While these nanocomposites showed out-of-plane uncoupled or coupled soft magnetic phases for 4 nm and 2.7 nm NPs (and/or higher soft content), respectively, the mean field interaction between particles in a soft continuous sample was dominated by exchange interaction. Moreover, the

FORC diagram revealed a very distinctive signature of nanocomposites composed of non-interacting single magnetic domain particles.

All of these investigations suggest that the fabricated nanocomposites with soft inclusions embedded in hard magnetic matrix could improve the remanence, while the coercivity is kept at relatively high value of up to ~2 T.

In terms of $\mu_0 M_r$,

- (i) with 60s annealing, an increase of +18% in 25% 4 nm-Fe₆₅Co₃₅-NPs in FePt-matrix sample, and +20% in 15% 2.7 nm-Fe₆₅Co₃₅-NPs in FePt-matrix sample is obtained compared to 100% FePt-matrix sample ($\mu_0 H_c \sim 4.4$ T and $\mu_0 M_r \sim 1.3$ T);
- (ii) with 10s annealing, an increase of +24% in 25% 4 nm-Fe₆₅Co₃₅-NPs in FePt-matrix sample, and +16% in 25% 4 nm-Co NPs in FePt-matrix sample is achieved compared to 100% FePt sample ($\mu_0 H_c \sim 2.3$ T and $\mu_0 M_r \sim 1.1$ T).

Such soft-hard nanocomposites can provide a blueprint as a model material to investigate condensed matter physics, together with significantly increasing the magnetic storage data capacity especially in the era of the Internet of Things (IoT).

2. Prospects

It is noteworthy that the soft-hard nanocomposites presented in this work are of various microstructures depending on the soft vol content in the nanocomposites. The intrinsic and extrinsic (architecture, microstructure) properties both influence the overall magnetic properties. As a model material, high demands determine the origin of the constituent magnetic contribution to the overall properties. The Magnetic Force Microscopy (MFM) allows to inspect the magnetic properties of the system at local position with a spatial resolution of tens nm and sensitivity of ~10 pN. Thus, the MFM performed on nanocomposite surfaces will reveal the localized characteristics of magnetization reversal. In addition, the MFM can be performed under virgin state and various remnant states for nanocomposites such as with and without magnetic field.

An implemented powerful approach to explore the local magnetic properties is using the X-ray magnetic circular dichroism (XMCD) based Synchrotron radiation. The high energy from the hard X-ray beams is able to investigate in detail the local environment (matrix) surrounding the NPs. Using XMCD, the individual magnetic hysteresis loop of each single element constituting the nanocomposites is obtained distinguishably and the effect of exchange coupling between the two phases of interest can be pointed out by correlating with the overall magnetic behaviors. For instance, in 15% vol content of 4 nm – Fe₆₅Co₃₅ NPs nanocomposites (section V.3.1), it is expected that two-phase magnetization reversal occurred in the sample, one switching event at low field corresponding to uncoupled soft phase, and the other switching event corresponding to coupled soft phase to the hard magnetic matrix. Additionally, 25% vol content of 4 nm – Fe₆₅Co₃₅ NPs nanocomposites (section V.3.1) is expected to show single phase magnetization reversal, which takes place at high field corresponding to soft phase in coupled to the hard matrix.

An elegant approach to observe directly the NPs inside the matrix could be using TEM-EDS mapping. Using this imaging technique, the structure, microstructure of the NPs, the matrix at nanometric scale could be explored. The additional combination characterization techniques of MFM, XMCD, and TEM-EDS mapping can significantly improve the understanding about the model nanocomposites in solid state physics.

Textured SmCo based thin films with good magnetic properties do not usually require UHV deposition chamber or high deposition/annealing temperatures to promote the crystallization [254]. Note that it was indicated in the thesis that high deposition/annealing temperatures lead to stronger diffusion. In case of using nanocomposites based SmCo, the deposition/annealing temperatures is sufficiently low, therefore the diffusion between the nano-inclusions and the matrix is expected to occur at a really short range of length scale. As a result, SmCo nanocomposite will be a promising route to achieve the high performance nanocomposites.

Greatly magnetic field gradients can be produced by magnetic microflux sources [255]. These sources at macroscale hold enormous potential interest in bit patterned media, biology applications such as trapping of particles, cell development and biological separation. In the case of soft-hard nanocomposite based FePt, well controlling the architectures of the nanocomposites could generate such magnetic sources.

In a long run of practical applications, the superior permanent magnets are in voluntary agreement with the green and clean energy plans, in particular mechanical-electrical conversion (wind turbines, hybrid electric cars, computers and space commissions) or pollution prevention (reduce the RE materials, increase device efficiency).

Appendix

A.1. The Ultra-Violet and Green lasers

LASER stands for Light Amplification by Stimulated Emission of Radiation, which has been widely employed in both research and practical applications. There currently exists several kinds of lasers with distinct properties. However, as a matter of interest, this thesis just works out the essential details of the two lasers, i. e., excimer KrF laser and solid state laser of Nd:YAG (Neodymium-doped Yttrium Aluminum Garnet).

The excimer laser requires prerequisites for lasing in an exotic way, for which the radiation emitted from a specific molecule composed of noble gas (Ar, Kr, Xe) and halogen (F, Cl, Br, I) atoms, only "lives" in a very brief time interval of less than 10 ns with high power starting at around 100 kWcm^{-3} and going up to few MWcm^{-3} . The name excimer shows a molecule existing only in an excited state with

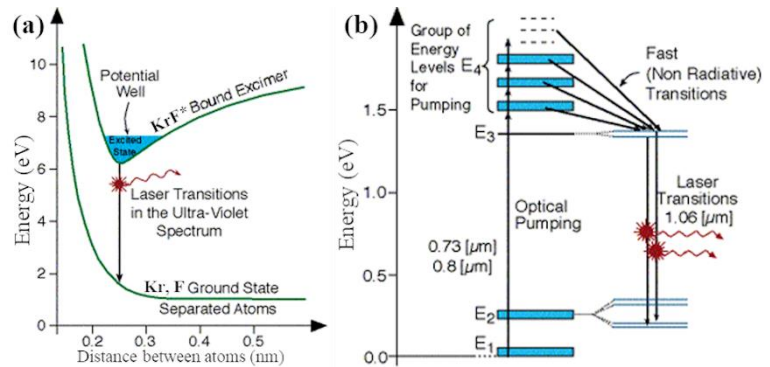


Figure A. 1: Energy levels diagram in the (a) Excimer Laser-KrF and (b) Nd-YAG Laser [256].

bound state and composed of a couple of atoms (excited dimer), while in the lowest energy level of ground state, such compositional atoms are separated completely and thus, their combination to form the molecule is not in existence. The first concept of excimer laser was proposed by a team of Soviet Union scientists of Basov, Danilychev and Popov at Lebedev Physical Institute in 1971, at which a wavelength of 172 nm was stimulated emission of lasing by pumping a beam of electrons to induce the excited state of Xenon dimer Xe_2 gas at low temperature. Two couple of years later, Searl and Hart, at Naval Research Laboratory in the US, invented and patterned the first excimer laser-XeBr of 282 nm [257]. Since then, a large number of excimer lasers has been released with wavelength ranging from 120 nm to 500 nm.

The principle working of excimer laser is that the compound atoms generate a bound state only after they are in an ionized excited state inducing by electric discharging pulses through the gas mixture, In the bound state, they obtains high energy level and the excited molecules will returns to the lower energy level of unexcited ground state. This progress of population inversion is reached at the time that there exists an excited state because the population of the lower energy level is zero as always. The energy level diagram for this excitation as a function of the atom-atom distance is presented in Figure A. 1a. The potential well in the diagram of the excited state represents the presence of momentarily stable state, in striking contrast to the ground state, at which the molecules are separated and no potential well is in existence showing no bound state. In addition, this bound state exists only in a certain distance between the atoms (e. g. 0.25 nm - 0.35 nm). With high power in a brief time, the electrons in the mixture are of high positive acceleration and thus they deliver their kinetic energy to the gas molecules by means of collision. The noble and halogen molecules are then broken to establish the excited complex of bound state. The laser pulse duration is restricted to a few tens of ns due to the fact that the lifetime of the molecules in the excited state is on the order of 10 ns. In reality, owing to the high gain of the laser medium, the rear mirror in the cavity is totally reflecting, while the front mirror is almost transparent because just a few percent of Fresnel reflection from the front window is sufficient for lasing.

A.2. Additional parameters of FCG system

Prior to depositions of thin films (with PLD) or stacks of NPs (with FCG) or magnetic nanocomposites of embedding NPs into the thin films (PLD+FCG), the targets were ablated in about 10 minutes to eliminate the oxides layer on the outer surface. Then the system will be pumped down to base pressure of high/ultrahigh vacuum of 5.0×10^{-8} mbar with the use of a vacuum pumping system including a primary pump PFEIFFER DUO 35M (flow $36 \text{ m}^3/\text{h}$) and a turbo-molecular pump OERLIKON Turbovac TMP 361 (flow $1242 \text{ m}^3/\text{h}$). In order to deposit the clusters/NPs, the pulsed valve is triggered and synchronized with the laser pulse from Nd:YAG, which makes sure a burst of inert He gas coming right after the laser plume appears in the nucleation chamber (Figure A. 2a). The pulsed valve is an electromagnetic type-PARKER Pulse Valve Series 9 with the diameter of its ejection orifice $\sim 0.5 \text{ mm}$, working with a wide range of pressure from 0 to 100 bars, and is monitored by an IOTA ONE Parker Hannifin Corporation driver permitting voltage signal transmission with a duration ranging from $5 \mu\text{s}$ to 9999 minutes (ON TIME), a period from 0.1 ms to 999.9 minutes (OFF TIME) and a frequency between 0.1 Hz to 250.0 Hz. Experimentally, taking into account the delay and closing time of the pulsed valve, the duration of gas pulse cannot be less than $160 \mu\text{s}$ and the repetition rate could not exceed 120 Hz. The definitions of the triggering delays and synchronization (from the two lasers, pulsed valve/IOTA ONE) are ensured by a four-channel STANFORD DG535 delay generator and constantly monitored by a TEKTRONIX 2440 500 MHz digital oscilloscope (Figure A. 2b).

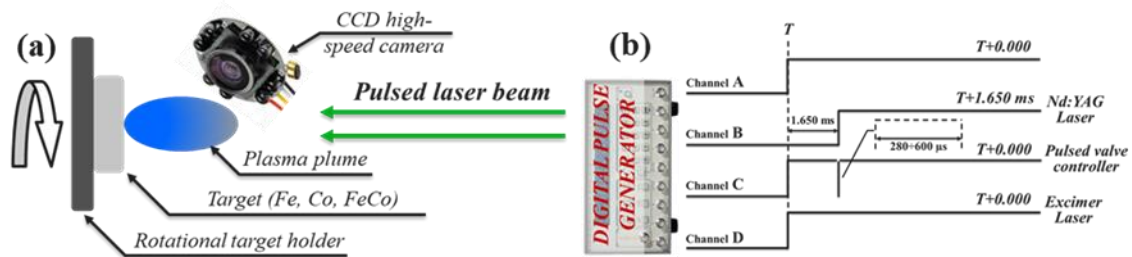


Figure A. 2: The schematic diagram of synchronizing between the two lasers and pulsed He valve/IOTA ONE to deposit nanocomposites, in which a representation (a) showing how to trigger the signal of pulsed valve (CCD high-speed camera) and Nd:YAG laser and (b) the PLD+FCG system is all triggered and synchronized by the digital pulse generator.

The interaction between the plasma plume and the pulsed helium gas to form clusters/NPs must take place at a precise moment. The following circumstances can occur: (i) If the helium is released early, the pressure in the nucleation chamber causes the limited plasma plume expansion which is totally confined; (ii) If the helium is delivered lately, it would be impossible to condense the atoms to form NPs; (iii) If there is no helium gas, of course, none NPs will be formed, the plasma plume continue expanding inside the cavity makes the quartz window dirty that absorbs the laser energy causing insufficient laser fluence, eventually even none of the plasma plume will be formed. That is why the synchronization is an essential step.

To estimate the triggering time of the pulsed valve and due to the inaccessible measurement inside the cavity, a high-speed CCD camera, whose response time is $\sim 2 \mu\text{s}$ from Fastcam 1024 PCI from Photron, is installed so that it can capture the initiation of the plasma plume (Figure A. 2a). The CCD camera is synchronized with the laser shot, it is found that the average response time of the device under the current conditions is approximately $630 \mu\text{s} \pm 50 \mu\text{s}$. Take into account the helium travelling within the valve and consider the gas speed being the same as the existed ones right before the nozzle (500 ms^{-1} [188], it took about $200 \mu\text{s}$ to travel 10 cm long of the cavity), the response time of the pulsed valve is around $430 \mu\text{s} \pm$

50 μs . Moreover, the minimum opening t -time of the pulsed valve, for which the plasma plume is interacting with the pressurized helium, has been experimentally evaluated of about 280 μs . Note that the minimum opening t -time will depend on the aging of the pulsed valve (the poppet).

Owing to being the key devices of the PLD+FCG, it is also important to synchronize them both. The response time of the excimer KrF and Nd: YAG laser are all verified using a photodiode and estimated of about 1.25 μs and 175 μs respectively. Thus, successfully estimating the response time of all the distinct devices, flight time of NPs, expansion of the plume duration, allow to operate them independently, simultaneously and sequentially, and finally develop various kinds of nanostructured films. Since there are numerous parameters involved in the synchronization procedure, obviously decisive formation of clusters/NPs ought to be handled with great care.

A.3. X-ray diffraction (XRD)

X-ray Diffractometer (XRD) is a very useful tool and has been widely used to determine the crystal structures of the investigated materials. All the XRD patterns, results, references reported in this thesis were made by θ - 2θ scan from Bruker D8 ADVANCE Eco X-ray diffraction, with the monochromatic and Ni filtered $\text{CuK}\alpha_1$ -1.54056 Å. The fundamental principle of the XRD is governed by Bragg's law [214] and given as: $2d\sin\theta = k\lambda$, where k -the integer represents for the diffraction order; λ is the incoming wavelength; d is the interplanar distance between the two adjacent diffraction planes; and θ is the glancing/Bragg angle. Note that in the normal XRD (specialized for powder, the XRD signal is collected from all the crystallite, whose orientations are parallel to the substrate, since the preparation is made with substrate alignment). In addition, a more popularly advanced formulas has been used to estimate the atomic grain size of a polycrystalline material, whose their crystalline domains are less than 100 nm in mean size, often called Scherrer equation [214] and given by: $D_{\text{Scherrer}} = K\lambda / (FWHM \cos\theta)$, where D_{Scherrer} is the mean size of the individual crystal (crystallite size), which can be smaller or equal to the grain/particle size; K is the dimensionless shape factor depending on the actual shape of the crystallite, with a typical value of ~ 0.9 ; λ is the diffraction wavelength; $FWHM$ is the line broadening at half the maximum intensity ($FWHM$, sometimes refer to as i -breath in the fitting), after subtracting the instrumental line broadening; and θ is the glancing/Bragg angle.

A more advanced technique in determining the crystalline orientation of the films is the rocking curve measurement, at which the XRD source and detector angles are well defined to each other, thus the Bragg condition is granted in any circumstances of the planes being parallel to the film's surface. When the incident beam angle is precisely adjusted, the X-ray detector receives the constructive interference from the reflected X-ray beams (after interacting with the sample), which corresponds to the angle of the crystal lattice distance of any family planes. During the satisfied Bragg condition of θ - 2θ scan, the c -axis of the oriented sample validates for out-of-plane direction of $(00l)$. In addition, the degree of this c -axis orientation can be correlated with the rocking curve measurement, while the XRD source angle is varied as much as 2° around the detector angle corresponding to the $(00l)$ plane. As a consequence, the $FWHM$ of the resultant peak indicates the degree of the c -axis sample orientation. In the epitaxial growth films, the relation between the substrate and thin film in terms of oop and ip orientation can be also revealed by θ - 2θ scan and phi (Φ) scan respectively.

A.4. Scanning electron microscopy (SEM)

The fabricated thin films (NdFeB, FePt) or nanocomposites' compositions and morphologies will be inspected by the ultra-high resolution *scanning electron microscopy* (SEM- LEO 1530VP GEMINI). A typical sketch of the SEM microscope is displayed in Figure A. 3. In the setup, the electron beam can be

accelerated from 0.5 keV to 20 keV with the help of electron cannon together with a cold cathode emitter. The beam will be then focused into a spot by a set of condenser lenses. The final objective could concentrate the beam of the specimen with spot size as small as 5 nm with a proper working parameter such as working voltage, distance, current and magnification. The output electron beam interacts with the sample placed on the stage, which create wide range kinds of signals such as *backscattered electrons (BSE)*, secondary electrons (SE), and are collected by energy dispersive X-ray spectroscopy (EDS), BSE, SE detectors. Note that the BSE signal is strongly dependent on the atomic number (Z), thus it BSE images provide chemical contrast of the sample surface, while the SE images illustrate the built-up topography. An authorized analysis system INCA (Oxford Instrumentals) is also equipped to obtain the EDS analysis which is mainly working to all elements with $Z > 5$. The analyzed volume in the EDS mode is about $1 \mu\text{m}^3$ at 15 keV.

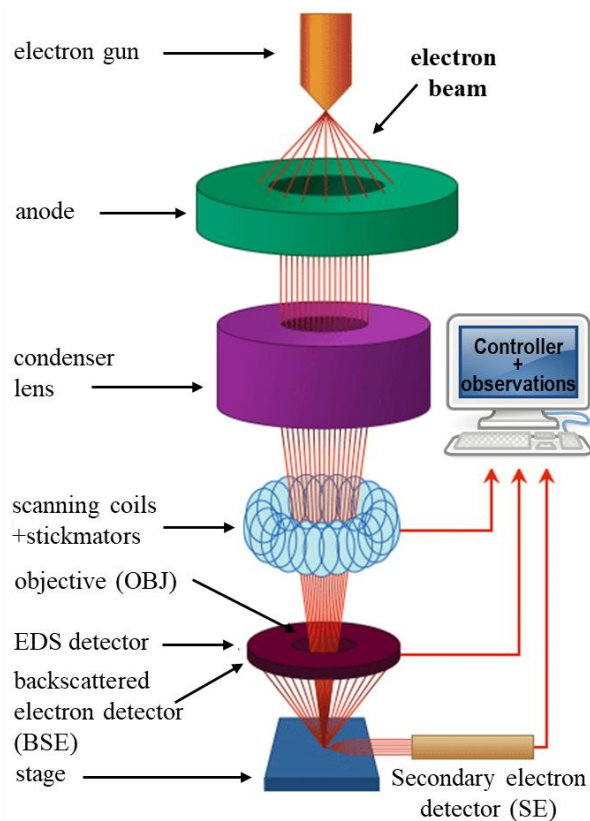


Figure A. 3: The schematic diagram of a SEM [258].

A.5. Focused ion beam (FIB)

In several circumstances such as BSE images with high resolution in which the SEM microscope does not work very well or TEM (preparation, or too big for TEM analysis), which usually requires a precisely structured specimens in order to reveal all of the original samples' properties at the small scale of nanometer, the *focused ion beam (FIB)* has been considered as the best techniques adapted well for those tasks.

The setup of the FIB is somewhat identical with SEM but it comes with an additional ion beam column (Ga^+) and a set of injector needles. Figure A. 4 describes the arrangement of the FIB chamber at

IRCER laboratory. One of the first steps to measure/prepare sample with FIB is that it will be coated with Pt in order to protect the specimen's surface during the milling process. The samples can be milled to up to 5 μm in depth using the Ga^+ focused ion beam, meanwhile the working voltage during the Ga implanted is set relatively low of 2 keV to avoid further damage to specimens. The sample will be now polished and ready for observation like in SEM, especially with BSE mode at around 100 nm scale. In case of preparation for TEM, additional steps are called such as a very precisely etched with a thickness of less than

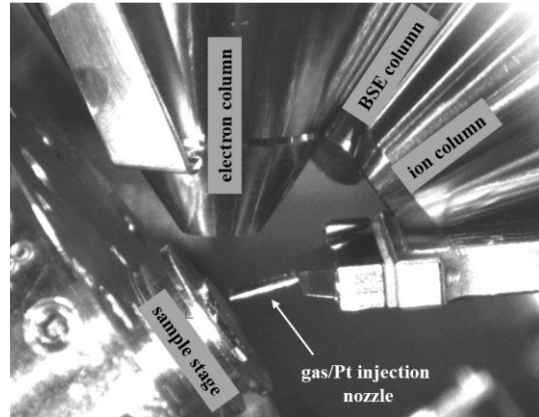


Figure A. 4: Illustration of observation chamber of the FIB-ZEISS CROSSBEAM 550 at IRCER

100 nm. The sample will be taken out and ready for TEM observation.

A.6. Atomic force microscopy (AFM)

The creation of scanning tunneling microscopy in 1982 and *atomic force microscopy (AFM)* in two couples of years later encouraged the surface science promotion. The AFM was initially introduced to measure the height steps in a sputtered patterning thin film, which allowed to estimate the thickness and roughness of the sample [259]. Currently, the AFM is of wide range of applications from observing real space of sample surface morphology to the atomic scale. The modern near-field scanning AFM includes: (i) an actuator carrying a piezoelectric tube which allows one to ten nanometer displacements; (2) a keen tip whose apex being able to approach closely to surface and interact with the samples' surfaces, and thus a distance-dependence signal is generated; (3) a closed loop feedback to adjust vertically the tip position and then set a performing point (or set point).

In the AFM and its derived method, the sensed atomic-scale force from tip-sample interaction (i. e., capillary force, electrostatic force, magnetic force, Van Der Waals force, Coulomb force) results in the deflection of a sort cantilever mounted with the probe tip while the probe is scanning over the specimens' surface at close vicinity of nanometer scale (Figure A. 5). The two types of forces, which are either repulsive forces or attractive ones acting on the cantilevers, induce the deflection of a diode laser beam and these changes will be detected by a split photodiode. The 2D graph is drawn during the low speed scanning of the tip on the sample allowing to reconstruct the topography of the sample's surface with approximately maximum scanning area of about $150 \times 150 \mu\text{m}^2$.

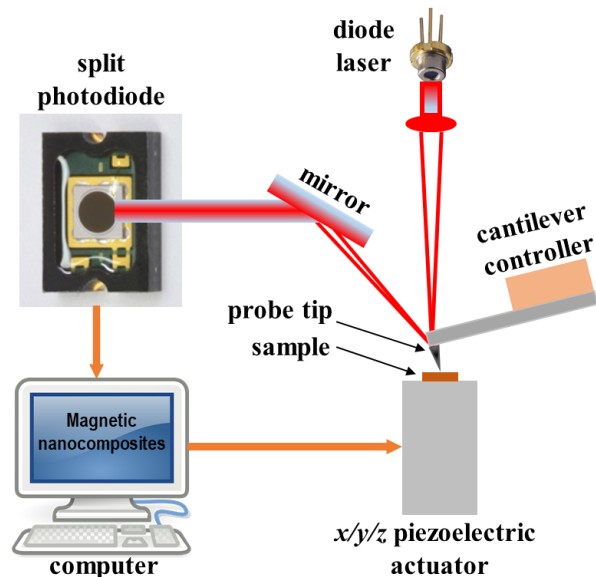


Figure A. 5: The schematic diagram of a contact AFM mode [259].

There are various approaches that AFM can work on such as tapping, non-contact and contact modes [260]. In the tapping or non-contact modes, the probe oscillates and remains at a close distance

(~nm) from the sample's surface allowing the tip to touch the surface or to prevent touching such surface respectively. The path of the tip counts on the interatomic forces presented between the tip and the sample's surface. These first two modes will bring advantages of less damage to both the tip and the sample due to lower forces, but it requires longer time scanning in comparison with the contact mode [259]. The tip, measured in the contact mode, is as its name, in contact with the sample's surface and scanned over the predefined region. Owing to the surface roughness, the cantilever carrying the probe can move up or down depending where the tip is measuring. Such movement leads to the variation in the reflected laser beam being sensed by the photodiode and associated tools to detect the topography of the surface.

In this work, a Dimension Icon AFM-BRUKER will be used to measure the patterning thin films' thickness or topography of the fabricated samples from thin films, stacks of NPs to nanocomposites. Actually, the AFM is a useful and easy technique to use because there are no prerequisite requirements for specimen preparation and the operations can be performed under an ambient condition.

A.7. Other magnetic characterization techniques of soft-hard nanocomposites

As one of the first methods, it is well known that, at low temperature, the magnetic properties should be augmented. As a consequence, the magnetic behaviors of the soft and hard magnetic components will exhibit differently. This kind of characterization is known as *low-temperature measurements*. In the nanocomposites at low temperature, due to the enhancement in magnetocrystalline anisotropy, the reduction in exchange length leads to a decoupling between the two phases [261]. Figure A. 6 reveals the magnetic behaviors measured at different temperatures of a PrCo–Co nanocomposite system. Namely, at 300 K, the magnetisation reversal loop is almost one-step mode without a shoulder at applied field of 0 T (due to exchange coupled). In stark contrast, at various lower temperatures, it is quite obvious to see two-step modes which is attributed to decoupling effect. These low-temperature measurements, however, do not induce two-step magnetisation reversal in single phase ferromagnetic magnets.

Measuring the magnetic behaviors of a ferromagnetic material by removing and reapplying a demagnetizing field, which would grow successively during a full cycling acquisition, leads to a resultant loop known as *recoil loop*. The recoil properties are responsive to the

exchange coupled interactions of investigated samples [262]. In case of the magnetizing and demagnetizing curves not overlap, this is referred to as *open recoil loops* that is a signature of breakdown in the exchange coupling and the enclosed area is responsible for the decoupled volume of the soft components in the nanocomposites. Figure A. 7 presents the two epitaxial Sm–Co/Fe bilayer magnets

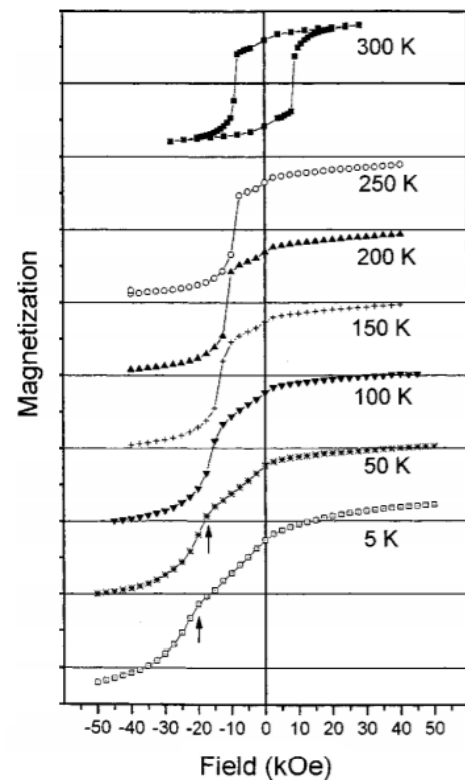
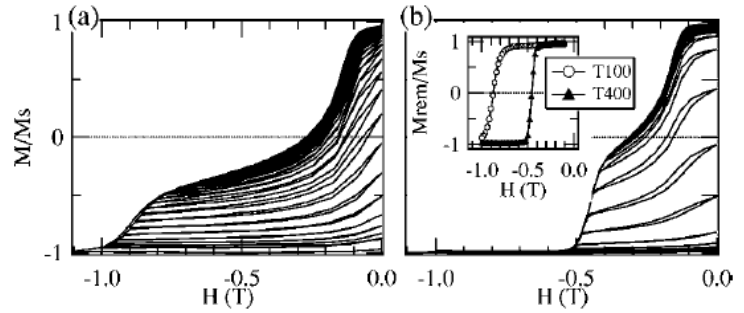


Figure A. 6: Magnetic hysteresis loops of the PrCo_x-Co nanocomposite at different temperatures. The arrows indicate the switching points [261].

with preferential ip uniaxial anisotropy. It is also interesting to note that other factors such as magnetocrystalline inhomogeneity in the hard components [263] and thermal fluctuation [264] have affected radically on the open recoil loops.



As mentioned in Chapter I, the Stoner–Wohlfarth model deals with magnetisation of single domain ferromagnets by supposing the

Figure A. 7: The easy axis demagnetizing curve and recoil loops measured at 300 K of Sm-Co/Fe nanocomposite deposited at (a) 100°C and (b) 400°C. The inset in (b) shows normalized remanence curves of sample deposited at 100°C and 400°C respectively [263].

magnetisation not varying within the ferromagnetic samples. In comparison between remanent magnetisation of the practical and Stoner–Wohlfarth particles, any magnetic interactions of such particles could be quantified. In order to do that, the two distinct remanent magnetisations have to be estimated, followed by the normalized relation $M_d(H) = 1 - 2M_r(H)$ where $M_d(H)$ and $M_r(H)$ is the *dc* demagnetization remanence and isothermal remanence respectively. The M_d is expressed as a function of a negatively applied field (applied and subsequently removed in the negative direction) and received after *dc* saturation in the positive direction, while M_r is obtained after applying and removing the applied field [265]. Experimentally, nonzero Henkel deviation of a real system with $\delta m_{\text{Henkel}}(H) = m_d(H) - (1 - 2m_r(H))$, which

is interpreted consequently of the interactions between particles. This technique is the so-called **Henkel plot** or **δM method**. In this method, positive $\delta m_{\text{Henkel}}(H)$ originates from exchange interactions favoring the magnetized state, while negative $\delta m_{\text{Henkel}}(H)$ is from the interplays assisting magnetisation reversal. For instance, in the FePt–Fe₃Pt magnetic nanocomposites with various ration of soft phase (Fe₃Pt), $\delta m_{\text{Henkel}}(H) > 0$ interprets magnetic exchange coupling and $\delta m_{\text{Henkel}}(H) < 0$ reads magnetic dipolar interaction (Figure A. 8). However, comprehending the exchanged interactions based on Henkel plot is under complex assumptions [266] of (i) all the magnetic NPs or grains switching in a coherent rotation and (ii) no domain walls exist even in the thermally demagnetized state, which requires great care in Henkel data processing.

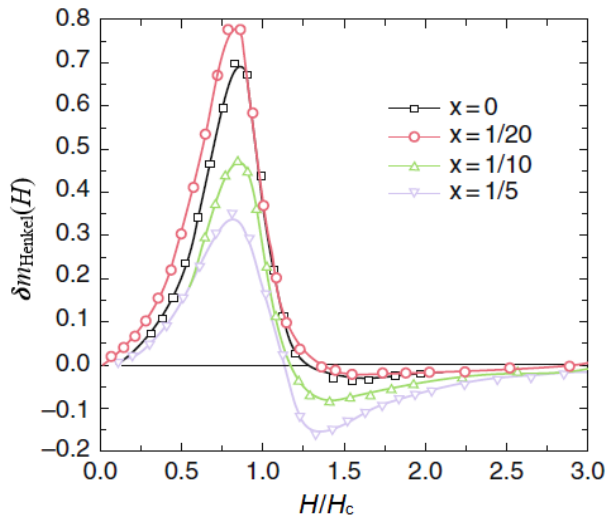


Figure A. 8: The Henkel plots of FePt–Fe₃Pt composite systems revealing the magnetic interactions between compacted nanoparticles. Here, x denotes for the weight fraction of Fe₃O₄ NPs of the precursor of the soft phase added into FePt NPs in the soft and hard magnetic phases, respectively, before a heat treatment [253].

A.8. High resolution XPS analysis for stacks of Fe-Co NPs

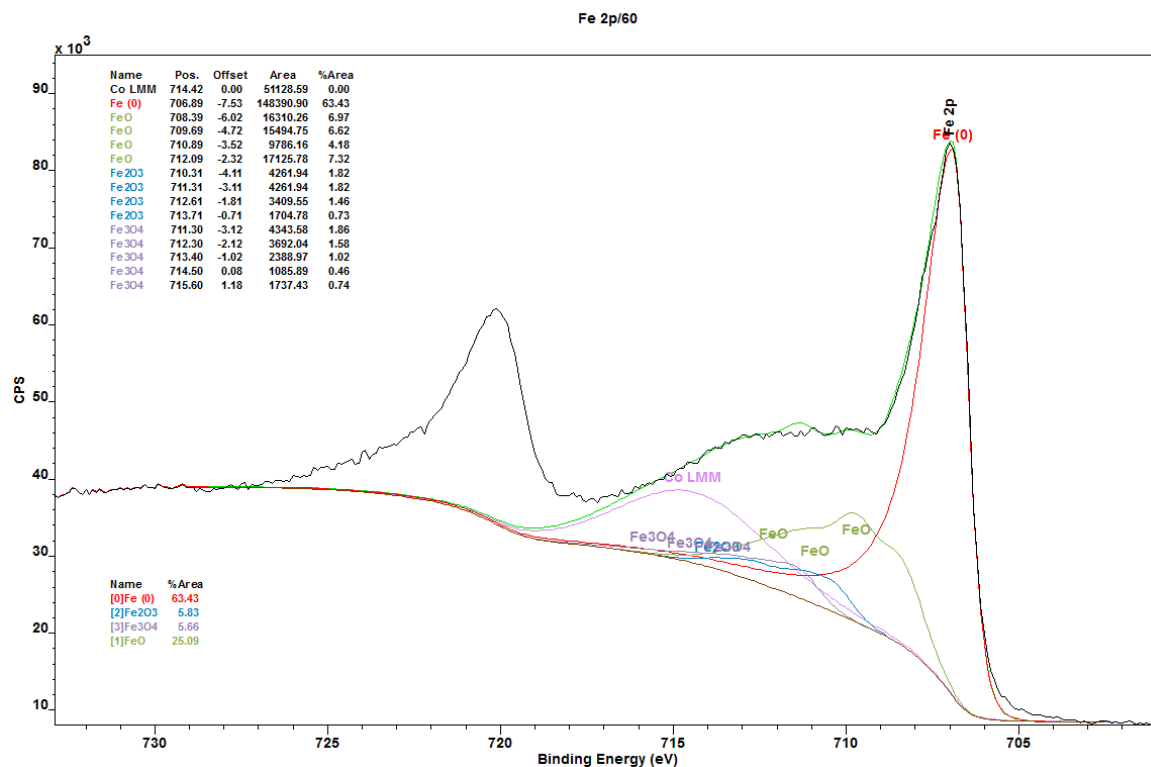
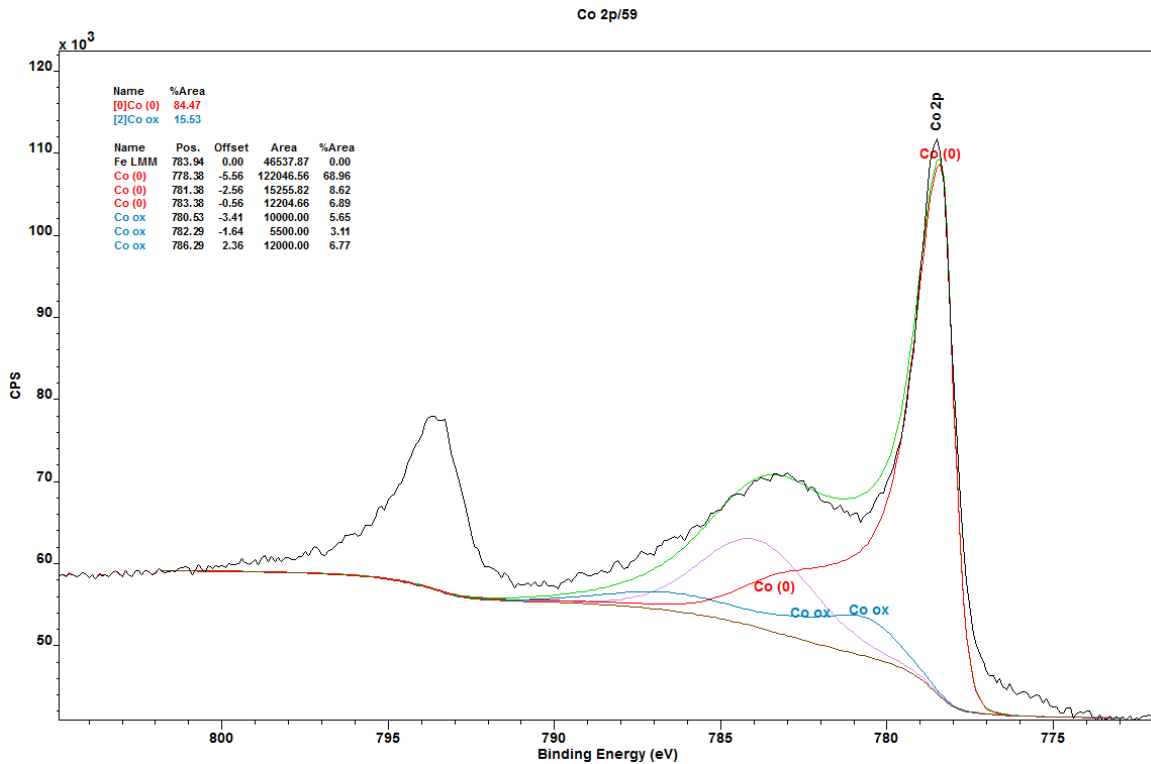


Figure A. 9: The high resolution XPS phase compositional analysis for stacks of FeCo NPs deposited from Fe₆₅Co₃₅ target, at 730°C for 2p spectra corresponding to (a) Co element core-level band; and (b) Fe element core-level band.

Figure A. 9 presents the high resolution XPS dedicated to phase quantification of the stacks of Fe-Co NPs, which was initially deposited at 730°C during the deposition. By fitting the high resolution survey curves, the percentage of each phase in the stacks of Fe-Co NPs is estimated. Note that all spectra were referenced to the C_{1s} peak of adventitious carbon at 285.0 eV, which is inexpensive and convenient

to take as a reference. The spectrum fitting procedures were decomposed by assuming that the line shapes are the sum of about 70 % Gaussian and the other of 30 % Lorentzian functions owing to the asymmetric in the survey curves. Raw areas ascertained after subtracting of a Shirley background were corrected according to several sensitivity factors. Regarding high resolution survey curves of Co element in the stacks of NPs deposited at 730°C shown in Figure A. 9a, the peak of Co corresponding to ~793.5 eV is from Co_{2p_{1/2}} of pure Co metal and it is not interested in the fitting. The most important binding energy in this high resolution survey is at lower binding energy. A rigorous fitting from ~790 eV to ~775 eV show that, in this regime, there is an existence of phases between Co pure metal and CoO_x (cobalt oxidized phase). The peak at ~783 eV is mainly attributed to Co_{2p_{3/2}} satellite peak while lower binding energy of ~778.5 eV is attributed to Co_{2p_{3/2}} main peaks. The spin – orbit splitting leads the binding energy difference between Co_{2p_{3/2}} and Co_{2p_{1/2}} to about ~15 eV. The reference peak at 778.5 eV corresponds to Co metal (Co(0)) indicating that the formation of Iron Cobalt compound, while a slightly higher reference peaks at ~781.5 eV and ~786 eV and are assigned to respective Cobalt oxidized (CoO_x) main structure and its satellite structure. And only very tiny bonding peaks for these CoO_x oxidation states was verified, which could be attributed to either CoO or Co₃O₄ groups, demonstrating that a minor contribution of oxide forms were introduced during the etching process or deposition step owing to the resident oxygen pressure being too high to grow the stacks of NPs. From such fitting curves a value of ~84.47 % of Co metal and 15.53 % of CoO_x structure have been deducted. Note that, in the estimate, the Fe LMM Auger at ~784 eV had been eliminated.

Regarding high resolution survey curves of Fe element in the sample as indicated in Figure A. 9b, the peak of Fe at ~720.5 eV is from Fe_{2p_{1/2}} of pure Fe metal and the Co LMM Auger at ~715 eV will be not considered. The Fe_{2p} region (difference in binding energy between Fe_{2p_{1/2}} and Fe_{2p_{3/2}}) has substantially split spin-orbit components of about ~13 eV. While the main contribution is ascribed to Fe metal structure (Fe(0) – Fe_{2p_{3/2}}) at ~707 eV, the directly subordinate contribution is ascribed to Fe oxidation forms of FeO (at ~710 eV), Fe₂O₃ (at ~710.5 eV), and Fe₃O₄ (at ~713.5 eV). Note that the Fe₃O₄ oxidation state could be decomposed in to the mixture of FeO and Fe₂O₃. Analysis reveals that the Fe metal structure contribute to about 63.43 %, while the other divide the left of 36.57 %, in which FeO is of up to 25.09 % and the two others shared equally of the total phases. This relative high percentage of oxidation state indicate that the oxidative valence state of Fe species in the Fe₆₅Co₃₅ bimetallic clusters, which may be note that Oxygen is more likely reactive with Iron in lieu of Co. Further analyses for other samples have been made, which show that the degree of oxidation states, in both Co and Fe high resolution core-level bands, are gradually reduced as decreasing deposition temperatures of stacks of NPs. At 500°C, there is 87.56 % Co metal, 12.44 % CoO_x, and 69.25 % Fe metal, 30.75 % Fe oxidation states. Finally, at RT there is about 89.78 % Co metal, 10.22 % CoO_x, and 74.98 % Fe metal, 25.02 % Fe oxidation states. These result is in good agreement with the dependence of monolayer formation time on partial deposition pressure of O₂ at various deposition temperatures, which was discussed in section III.1.2. Though the formation time at lower deposition temperature is lower compared to higher temperatures, the oxidation states are encouraged in this circumstance, which may be attributed to the high degree of reaction between either Co or Fe and O₂ at high deposition temperature than the lower one.

A.9. TEM sample preparation

The preparation sample procedure by FIB for TEM observation is presented in Figure A. 10. This procedure is complicated and time-consuming. Normally, ~ five hours are required to prepare for each sample, which will be handled with great care. The tri-layer sample was stuck with Ag silver paint on the FIB sample holder to make the tri-layer sample conductive, then waited around three hours to make the

silver paint dry and readily transferred to the FIB chamber. Inside the FIB chamber, the sample was covered by a layer of Pt to prevent the surface modification from Ga ion milling/etching process to cut a slide of sample, as presented in Figure A. 10a. Secondly, the sample will be milled from both sides and transferred to TEM sample holder (pin) by means of a nano-manipulator. The TEM sample was stuck on the nano-manipulator by depositing a very thin layer of Pt from Pt nozzle. The nano-manipulator with the TEM sample on the edge moved to the TEM pin, and this TEM sample was fixed on the TEM pin by depositing another thin layer of Pt from Pt nozzle. Finally, the TEM sample was separated from the nano-manipulator by using a Ga ion beam to break the nano-manipulator. The TEM sample remained in the TEM sample holder (normally with five pins), but the thickness of the TEM sample is perhaps too thick to be observed with TEM. Thus, an additional step will be made by polishing the TEM sample to thickness of less than 20 nm with the help of milling at low power of Ga ion beam (low current ~ 30 pA and low voltage ~ 2 kV), so that TEM sample is electron transparent. Now, the TEM sample with size of $\sim 20 \mu\text{m} \times 7 \mu\text{m} \times 20 \text{nm}$ is ready to be observed with transmission electron microscope for the quantitative atomic resolution TEM study.

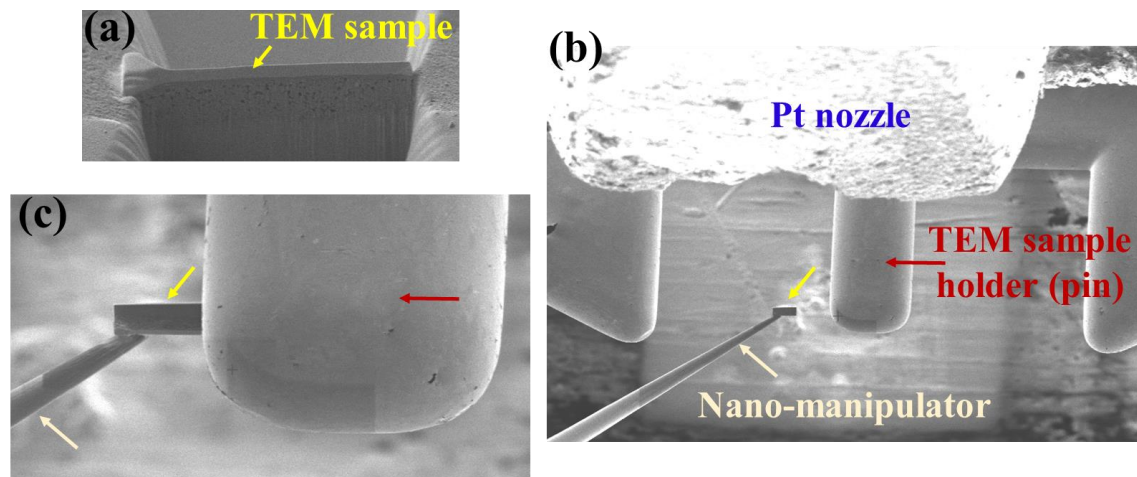


Figure A. 10: The TEM prepared sample representation soldered by FIB, in which (a) SEM images of FIB cut slide readily to be transferred to the TEM holder; (b) and (c) Procedure to place and fix the TEM sample to the pin.

List of Scientific Contribution

Publication:

1. "Textured Nd-Fe-B hard magnetic thin films prepared by pulsed laser deposition with single alloy targets"

T. NGUYEN VAN, I. de MORAES, N.M. DEMPSEY, C. CHAMPEAUX, F. DUMAS-BOUCHIAT, Journal of Magnetism and Magnetic Materials (2020), IF: 2,717

Under preparation:

2. "Textured L1₀-FePt hard magnetic thin films prepared by two-step annealing".

3. "High performance NdFeB based thin films processed by rapid thermal processing".

4. "Stacks of soft magnetic NPs towards embedding in soft-hard nanocomposites"

5. "Superior soft in hard magnetic nanocomposites".

Scientific Presentation:

6. "Dual pulsed laser deposition towards fabrication of model high performance magnets"

T. NGUYEN VAN, N.M. DEMPSEY, C. CHAMPEAUX AND F. DUMAS-BOUCHIAT, accepted, E-MRS 2021 Spring Meeting, virtual, abstract and oral presentation.

7. "Hard Magnetic Thin Films By Pulsed Laser Deposition"

T. NGUYEN VAN, I. de MORAES, N.M. DEMPSEY, C. CHAMPEAUX, F. DUMAS-BOUCHIAT, Thematic Workshop on Magnetism and Optics in Nanoalloys at Lyon, Abstract and poster, 30-31 January 2020, Lyon, France.

8. "Dual pulsed laser vaporization process dedicated to nanocomposite–Future development of soft (Fe, Co, FeCo) in hard (NdFeB) magnetic nanocomposites"

T. NGUYEN VAN, I. de MORAES, C. CHAMPEAUX, N.M. DEMPSEY, F. DUMAS-BOUCHIAT, 1-day Symposium homage to Dominique Givord, Poster, 26-27 September 2019, Grenoble, France.

9. "High performance hard magnetic Nd₂Fe₁₄B thin films by pulsed laser deposition"

T. NGUYEN VAN, N.M. DEMPSEY, C. CHAMPEAUX, F. DUMAS-BOUCHIAT, PLATHINIUM2019, Abstract and oral presentation, 23-27 September 2019, Antibes, French Riviera, France.

10. "Pulsed laser hard magnetic films for bio-microdevices"

F. DUMAS-BOUCHIAT, **T. NGUYEN VAN**, L. ZANINI, C. CHAMPEAUX, N.M. DEMPSEY, Oral Presentation, MRS - International Material Research Congress, symposium C2 Fabrication & Applications of BIO-MEMS-NEMS, 18-23 August 2019, Cancun, Mexico.

11. "Dual pulsed laser vaporization process dedicated to nanocomposite – Development of soft (Fe, Co, FeCo) in hard (NdFeB) magnetic nanocomposites"

T. NGUYEN VAN, C. CHAMPEAUX, F. DUMAS-BOUCHIAT, Poster Presentation, journée des doctorants de l'institut IRCER, 06 July 2019, Limoges, France.

12. "FePt hard magnetic thin films by pulsed laser deposition"

T. NGUYEN VAN, C. CHAMPEAUX, F. DUMAS-BOUCHIAT, Oral Presentation, MATV2L-Milieux 2D, 24-25 January 2019, Blois, France.

Other results:

The experimental results obtained during my Ph.D which have not been presented in the manuscripts (purposed to have clear manuscript):

13. NdFeB thin films on *c*-sapphire with various compositions, depositions and annealing conditions.

14. Rapid thermal annealing (RTP) for NdFeB thin films prior to depositing at RT.

15. RTP in the FePt thin films prior to depositing at 500°C.

References

- [1] J.M.D. Coey, ed., *Rare-Earth Iron Permanent Magnets*, 1 edition, Clarendon Press, Oxford : New York, 1996.
- [2] A. Goldman, *Handbook of Modern Ferromagnetic Materials*, Springer US, 1999. <https://doi.org/10.1007/978-1-4615-4917-8>.
- [3] S.C. McBain, H.H. Yiu, J. Dobson, Magnetic nanoparticles for gene and drug delivery, *Int J Nanomedicine*. 3 (2008) 169–180. <https://www.ncbi.nlm.nih.gov/pmc/articles/PMC2527670/>.
- [4] X. Zhang, T.-A. Le, A.K. Hoshidar, J. Yoon, A Soft Magnetic Core can Enhance Navigation Performance of Magnetic Nanoparticles in Targeted Drug Delivery, *IEEE/ASME Transactions on Mechatronics*. 23 (2018) 1573–1584. <https://doi.org/10.1109/TMECH.2018.2843820>.
- [5] P. Ripka, Sensors based on bulk soft magnetic materials: Advances and challenges, *Journal of Magnetism and Magnetic Materials*. 320 (2008) 2466–2473. <https://doi.org/10.1016/j.jmmm.2008.04.079>.
- [6] O. Cugat, J. Delamare, G. Reyne, Magnetic micro-actuators and systems (MAGMAS), *IEEE Transactions on Magnetics*. 39 (2003) 3607–3612. <https://doi.org/10.1109/TMAG.2003.816763>.
- [7] J.M.D. Coey, *Magnetism and magnetic materials*, Cambridge University Press, Cambridge, 2010. <https://doi.org/10.1017/CBO9780511845000>.
- [8] M. Sagawa, S. Fujimura, N. Togawa, H. Yamamoto, Y. Matsuura, New material for permanent magnets on a base of Nd and Fe (invited), *Journal of Applied Physics*. 55 (1984) 2083–2087. <https://doi.org/10.1063/1.333572>.
- [9] J.J. Croat, J.F. Herbst, R.W. Lee, F.E. Pinkerton, Pr-Fe and Nd-Fe-based materials: A new class of high-performance permanent magnets (invited), *Journal of Applied Physics*. 55 (1984) 2078–2082. <https://doi.org/10.1063/1.333571>.
- [10] R. Skomski, J.M.D. Coey, Giant energy product in nanostructured two-phase magnets, *Phys. Rev. B*. 48 (1993) 15812–15816. <https://doi.org/10.1103/PhysRevB.48.15812>.
- [11] N.M. Dempsey, A. Walther, F. May, D. Givord, K. Khlopkov, O. Gutfleisch, High performance hard magnetic NdFeB thick films for integration into micro-electro-mechanical systems, *Appl. Phys. Lett.* 90 (2007) 092509. <https://doi.org/10.1063/1.2710771>.
- [12] D. Harimoto, Y. Matsuura, Development of High Performance Nd-Fe-B Sintered Magnets, *Hitachi Metals Tech. Rev.* 23 (2007) 69–72. https://www.researchgate.net/publication/259457589_Development_of_High_Performance_Nd-Fe-B_Sintered_Magnets.
- [13] R. Coehoorn, D.B. de Mooij, C. de Waard, Meltspun permanent magnet materials containing Fe₃B as the main phase, *Journal of Magnetism and Magnetic Materials*. 80 (1989) 101–104. [https://doi.org/10.1016/0304-8853\(89\)90333-8](https://doi.org/10.1016/0304-8853(89)90333-8).
- [14] E.F. Kneller, R. Hawig, The exchange-spring magnet: a new material principle for permanent magnets, *IEEE Transactions on Magnetics*. 27 (1991) 3588–3560. <https://doi.org/10.1109/20.102931>.
- [15] R. Skomski, *Simple Models of Magnetism*, Oxford University Press, 2008. <https://doi.org/10.1093/acprof:oso/9780198570752.001.0001>.
- [16] J.A. Osborn, Demagnetizing Factors of the General Ellipsoid, *Phys. Rev.* 67 (1945) 351–357. <https://doi.org/10.1103/PhysRev.67.351>.

- [17]F. Bloch, G. Gentile, Zur Anisotropie der Magnetisierung ferromagnetischer Einkristalle, *Z. Physik.* 70 (1931) 395–408. <https://doi.org/10.1007/BF01339586>.
- [18]D. Weller, A. Moser, Thermal effect limits in ultrahigh-density magnetic recording, *IEEE Transactions on Magnetics.* 35 (1999) 4423–4439. <https://doi.org/10.1109/20.809134>.
- [19]T. Klemmer, D. Hoydick, H. Okumura, B. Zhang, W.A. Soffa, Magnetic hardening and coercivity mechanisms in L10 ordered FePd ferromagnets, *Scripta Metallurgica et Materialia.* 33 (1995) 1793–1805. [https://doi.org/10.1016/0956-716X\(95\)00413-P](https://doi.org/10.1016/0956-716X(95)00413-P).
- [20]R.C. O’Handley, *Modern magnetic materials : principles and applications*, New York, NY : Wiley, 2000. <https://cds.cern.ch/record/2131967>.
- [21]F. Bloch, Zur Theorie des Austauschproblems und der Remanenzerscheinung der Ferromagnetika, *Z. Physik.* 74 (1932) 295–335. <https://doi.org/10.1007/BF01337791>.
- [22]A. Hubert, R. Schäfer, *Magnetic Domains: The Analysis of Magnetic Microstructures*, Springer-Verlag, Berlin Heidelberg, 1998. <https://doi.org/10.1007/978-3-540-85054-0>.
- [23]S. Blundell, *Magnetism in Condensed Matter*, Oxford University Press, 2001. <http://www.physics.fudan.edu.cn/tps/people/jzhao/Book&Paper/Magnetism%20in%20Condensed%20Matter.pdf>.
- [24]S.W. Yuan, H.N. Bertram, J.F. Smyth, S. Schultz, Size effects of switching fields of thin permalloy particles, in: 1992 IEEE International Magnetics Conference (INTERMAG), 1992: pp. 432–432. <https://doi.org/10.1109/INTMAG.1992.696615>.
- [25]D. Raasch, J. Reck, C. Mathieu, B. Hillebrands, Exchange stiffness constant and wall energy density of amorphous GdTb-FeCo thin films, *Journal of Applied Physics.* 76 (1994) 1145–1149. <https://doi.org/10.1063/1.357837>.
- [26]N.I. Vlasova, G.S. Kandaurova, N.N. Shchegoleva, Effect of the polytwinned microstructure parameters on magnetic domain structure and hysteresis properties of the CoPt-type alloys, *Journal of Magnetism and Magnetic Materials.* 222 (2000) 138–158. [https://doi.org/10.1016/S0304-8853\(00\)00506-0](https://doi.org/10.1016/S0304-8853(00)00506-0).
- [27]R. Skomski, Aligned two-phase magnets: Permanent magnetism of the future? (invited), *Journal of Applied Physics.* 76 (1994) 7059–7064. <https://doi.org/10.1063/1.358027>.
- [28]J.S. Jiang, E.E. Fullerton, M. Grimsditch, C.H. Sowers, S.D. Bader, Exchange-spring behavior in epitaxial hard/soft magnetic bilayer films, *Journal of Applied Physics.* 83 (1998) 6238–6240. <https://doi.org/10.1063/1.367769>.
- [29]I.A. Al-Omari, D.J. Sellmyer, Magnetic properties of nanostructured CoSm/FeCo films, *Phys. Rev. B.* 52 (1995) 3441–3447. <https://doi.org/10.1103/PhysRevB.52.3441>.
- [30]R.J. Astalos, R.E. Camley, Magnetic permeability for exchange-spring magnets: Application to Fe/Sm-Co, *Phys. Rev. B.* 58 (1998) 8646–8653. <https://doi.org/10.1103/PhysRevB.58.8646>.
- [31]E.E. Fullerton, J.S. Jiang, S.D. Bader, Hard/soft magnetic heterostructures: model exchange-spring magnets, *Journal of Magnetism and Magnetic Materials.* 200 (1999) 392–404. [https://doi.org/10.1016/S0304-8853\(99\)00376-5](https://doi.org/10.1016/S0304-8853(99)00376-5).
- [32]W.B. Cui, H. Sepehri-Amin, Y.K. Takahashi, K. Hono, Hard magnetic properties of spacer-layer-tuned NdFeB/Ta/Fe nanocomposite films, *Acta Materialia.* 84 (2015) 405–412. <https://doi.org/10.1016/j.actamat.2014.10.008>.
- [33]J. Li, Z.L. Wang, H. Zeng, S. Sun, J. Ping Liu, Interface structures in FePt/Fe₃Pt hard-soft exchange-coupled magnetic nanocomposites, *Appl. Phys. Lett.* 82 (2003) 3743–3745. <https://doi.org/10.1063/1.1578515>.

- [34] H. Zeng, J. Li, J.P. Liu, Z.L. Wang, S. Sun, Exchange-coupled nanocomposite magnets by nanoparticle self-assembly, *Nature*. 420 (2002) 395–398. <https://doi.org/10.1038/nature01208>.
- [35] C.-M. Kuo, P.C. Kuo, Magnetic properties and microstructure of FePt–Si₃N₄ nanocomposite thin films, *Journal of Applied Physics*. 87 (1999) 419–426. <https://doi.org/10.1063/1.371878>.
- [36] J.S. Jiang, S.D. Bader, Rational design of the exchange-spring permanent magnet, *J. Phys.: Condens. Matter*. 26 (2014) 064214. <https://doi.org/10.1088/0953-8984/26/6/064214>.
- [37] G. Herzer, Grain structure and magnetism of nanocrystalline ferromagnets, *IEEE Transactions on Magnetics*. 25 (1989) 3327–3329. <https://doi.org/10.1109/20.42292>.
- [38] G. Herzer, The Random Anisotropy Model, in: B. Idzikowski, P. Švec, M. Miglierini (Eds.), *Properties and Applications of Nanocrystalline Alloys from Amorphous Precursors*, Springer Netherlands, Dordrecht, 2005: pp. 15–34. https://doi.org/10.1007/1-4020-2965-9_2.
- [39] R. Coehoorn, D.B. de Mooij, J.P.W.B. Duchateau, K.H.J. Buschow, NOVEL PERMANENT MAGNETIC MATERIALS MADE BY RAPID QUENCHING, *J. Phys. Colloques*. 49 (1988) C8-669-C8-670. <https://doi.org/10.1051/jphyscol:19888304>.
- [40] R. Hirian, O. Isnard, V. Pop, Structural and magnetic properties of SmCo₅+30% α -Fe exchange coupled nanocomposites obtained by mechanical milling, *Journal of Optoelectronics and Advanced Materials*. 21 (2019) 618–622. <https://joam.inoe.ro/articles/structural-and-magnetic-properties-of-smco530-fe-exchange-coupled-nanocomposites-obtained-by-mechanical-milling/> (accessed April 10, 2021).
- [41] R. Hirian, S. Mican, O. Isnard, L. Barbu-Tudoran, V. Pop, Influence of microstructure on the interphase exchange coupling of Nd₂Fe₁₄B + 10 wt% α -Fe nanocomposites obtained at different milling energies, *Journal of Alloys and Compounds*. 697 (2017) 19–24. <https://doi.org/10.1016/j.jallcom.2016.12.123>.
- [42] J.Y. Gu, J. Kusnadi, C.-Y. You, Proximity effect in a superconductor/exchange-spring-magnet hybrid system, *Phys. Rev. B*. 81 (2010) 214435. <https://doi.org/10.1103/PhysRevB.81.214435>.
- [43] S. Yan, W.J. Liu, J.L. Weston, G. Zangari, J.A. Barnard, Magnetization-reversal mechanism of hard/soft exchange-coupled trilayers, *Phys. Rev. B*. 63 (2001) 174415. <https://doi.org/10.1103/PhysRevB.63.174415>.
- [44] S. Yan, J.A. Barnard, F. Xu, J.L. Weston, G. Zangari, Critical dimension of the transition from single switching to an exchange spring process in hard/soft exchange-coupled bilayers, *Phys. Rev. B*. 64 (2001) 184403. <https://doi.org/10.1103/PhysRevB.64.184403>.
- [45] Z.J. Guo, J.S. Jiang, C.Y. You, V.K. Vlasko-Vlasov, U. Welp, J.P. Liu, S.D. Bader, Exchange coupling in epitaxial Sm–Co(1100)/Nd–Co exchange-spring bilayers, *Journal of Applied Physics*. 93 (2003) 8122–8124. <https://doi.org/10.1063/1.1538180>.
- [46] Z.J. Guo, J.S. Jiang, J.E. Pearson, S.D. Bader, J.P. Liu, Exchange-coupled Sm–Co/Nd–Co nanomagnets: correlation between soft phase anisotropy and exchange field, *Appl. Phys. Lett.* 81 (2002) 2029–2031. <https://doi.org/10.1063/1.1504869>.
- [47] A.J. Zambano, H. Oguchi, I. Takeuchi, Y. Choi, J.S. Jiang, J.P. Liu, S.E. Lofland, D. Josell, L.A. Bendersky, Dependence of exchange coupling interaction on micromagnetic constants in hard/soft magnetic bilayer systems, *Phys. Rev. B*. 75 (2007) 144429. <https://doi.org/10.1103/PhysRevB.75.144429>.
- [48] S.M. Parhofer, J. Wecker, C. Kuhrt, G. Gieres, L. Schultz, Remanence enhancement due to exchange coupling in multilayers of hard- and softmagnetic phases, *IEEE Transactions on Magnetics*. 32 (1996) 4437–4439. <https://doi.org/10.1109/20.538893>.

- [49] M. Shindo, M. Ishizone, A. Sakuma, H. Kato, T. Miyazaki, Magnetic properties of exchange-coupled α -Fe/Nd-Fe-B multilayer thin-film magnets, *Journal of Applied Physics*. 81 (1997) 4444–4446. <https://doi.org/10.1063/1.364970>.
- [50] W. Liu, Z.-d Zhang, J.-p Liu, L.-j Chen, L.-l He, Y. Liu, X.-k Sun, D.J. Sellmyer, Exchange Coupling and Remanence Enhancement in Nanocomposite Multilayer Magnets, *Advanced Materials*. 14 (2002) 1832–1834. <https://doi.org/10.1002/adma.200290012>.
- [51] J.P. Liu, Y. Liu, R. Skomski, D.J. Sellmyer, High energy products in exchange-coupled nanocomposite films, *IEEE Transactions on Magnetics*. 35 (1999) 3241–3246. <https://doi.org/10.1109/20.800486>.
- [52] T. Leineweber, H. Kronmüller, Micromagnetic examination of exchange coupled ferromagnetic nanolayers, *Journal of Magnetism and Magnetic Materials*. 176 (1997) 145–154. [https://doi.org/10.1016/S0304-8853\(97\)00601-X](https://doi.org/10.1016/S0304-8853(97)00601-X).
- [53] Y. Li, M. Yue, G. Zhao, H. Zhang, Effect of magnetic soft phase on the magnetic properties of bulk anisotropic Nd₂Fe₁₄B/ α -Fe nanocomposite permanent magnets, *Mater. Res. Express*. 5 (2018) 016108. <https://doi.org/10.1088/2053-1591/aaa865>.
- [54] R.F. Sabiryanov, S.S. Jaswal, Electronic structure and magnetic properties of hard/soft multilayers, *Journal of Magnetism and Magnetic Materials*. 177–181 (1998) 989–990. [https://doi.org/10.1016/S0304-8853\(97\)00364-8](https://doi.org/10.1016/S0304-8853(97)00364-8).
- [55] R.F. Sabiryanov, S.S. Jaswal, Magnetic properties of hard/soft composites: SmCo₅/Co_{1-x}Fe_x, *Phys. Rev. B*. 58 (1998) 12071–12074. <https://doi.org/10.1103/PhysRevB.58.12071>.
- [56] Y.Q. Li, M. Yue, T. Wang, Q. Wu, D.T. Zhang, Y. Gao, Investigation of magnetic properties of MnBi/Co and MnBi/Fe₆₅Co₃₅ nanocomposite permanent magnets by micro-magnetic simulation, *Journal of Magnetism and Magnetic Materials*. 393 (2015) 484–489. <https://doi.org/10.1016/j.jmmm.2015.06.023>.
- [57] J.F. Herbst, J.J. Croat, F.E. Pinkerton, W.B. Yelon, Relationships between crystal structure and magnetic properties in Nd₂Fe₁₄B, *Phys. Rev. B*. 29 (1984) 4176–4178. <https://doi.org/10.1103/PhysRevB.29.4176>.
- [58] D. Givord, H.S. Li, J.M. Moreau, Magnetic properties and crystal structure of Nd₂Fe₁₄B, *Solid State Communications*. 50 (1984) 497–499. [https://doi.org/10.1016/0038-1098\(84\)90315-6](https://doi.org/10.1016/0038-1098(84)90315-6).
- [59] S. Chikazumi, *Physics of Ferromagnetism*, Edition: 2, Oxford University Press, USA, Oxford ; New York, 2009.
- [60] W.M. Haynes, *CRC Handbook of Chemistry and Physics*, 97th ed., CRC Press, 2016.
- [61] J. Lucas, P. Lucas, T.L. Mercier, A. Rollat, W. Davenport, *Rare Earths: Science, Technology, Production and Use*, Elsevier Inc., 2014. <https://doi.org/10.1016/C2012-0-02577-X>.
- [62] D. Givord, H.S. Li, F. Tasset, Polarized neutron study of the compounds Y₂Fe₁₄B and Nd₂Fe₁₄B, *Journal of Applied Physics*. 57 (1985) 4100–4102. <https://doi.org/10.1063/1.334631>.
- [63] C. Lin, C.-X. Liu, Y.-X. Sun, Z.-X. Liu, D.-F. Chen, C. Gou, K. Sun, J.-L. Yang, Neutron diffraction study of Nd₅Fe₁₇, *Journal of Magnetism and Magnetic Materials*. 186 (1998) 129–134. [https://doi.org/10.1016/S0304-8853\(98\)00052-3](https://doi.org/10.1016/S0304-8853(98)00052-3).
- [64] R. Fruchart, P. L'heritier, P.D. de Reotier, D. Fruchart, P. Wolfers, J.M.D. Coey, L.P. Ferreira, R. Guillen, P. Vulliet, A. Yaouanc, Mossbauer spectroscopy of R₂Fe₁₄B, *J. Phys. F: Met. Phys.* 17 (1987) 483–501. <https://doi.org/10.1088/0305-4608/17/2/017>.

- [65] B.I. Min, J.-S. Kang, J.H. Hong, J.I. Jeong, Y.P. Lee, S.D. Choi, W.Y. Lee, C.J. Yang, C.G. Olson, Electronic and magnetic structures of the rare-earth permanent magnet Nd₂Fe₁₄B, *Phys. Rev. B.* 48 (1993) 6217–6224. <https://doi.org/10.1103/PhysRevB.48.6217>.
- [66] L. Nordström, B. Johansson, M.S.S. Brooks, Calculated magnetic moments of Nd₂Fe₁₄B, *Journal of Applied Physics.* 69 (1991) 5708–5710. <https://doi.org/10.1063/1.347895>.
- [67] F. Bolzoni, J.P. Gavigan, D. Givord, H.S. Li, O. Moze, L. Pareti, 3d magnetism in R₂Fe₁₄B compounds, *Journal of Magnetism and Magnetic Materials.* 66 (1987) 158–162. [https://doi.org/10.1016/0304-8853\(87\)90139-9](https://doi.org/10.1016/0304-8853(87)90139-9).
- [68] D.J. Sellmyer, M.A. Engelhardt, S.S. Jaswal, A.J. Arko, Electronic Structure and Magnetism of Nd₂Fe₁₄B and Related Compounds, *Phys. Rev. Lett.* 60 (1988) 2077–2080. <https://doi.org/10.1103/PhysRevLett.60.2077>.
- [69] A.S. Lileev, A.A. Parilov, M. Reissner, W. Steiner, Influence of the spin reorientation transition on the hysteresis characteristics of Nd–Fe–B film and bulk magnets, *Journal of Magnetism and Magnetic Materials.* 270 (2004) 152–156. <https://doi.org/10.1016/j.jmmm.2003.08.012>.
- [70] S.L. Chen, W. Liu, C.L. Chen, Z.D. Zhang, Effects of buffer layer and substrate temperature on the surface morphology, the domain structure and magnetic properties of c-axis-oriented Nd₂Fe₁₄B films, *Journal of Applied Physics.* 98 (2005) 033907. <https://doi.org/10.1063/1.1997295>.
- [71] T. Shima, A. Kamegawa, H. Fujimori, Enhanced coercive force of Nd–Fe–B thin films by the introduction of a Cr underlayer, *Journal of Alloys and Compounds.* 281 (1998) 46–49. [https://doi.org/10.1016/S0925-8388\(98\)00769-5](https://doi.org/10.1016/S0925-8388(98)00769-5).
- [72] A.R. Kwon, S. Fähler, V. Neu, L. Schultz, Effect of composition on phase formation, microstructure and magnetic properties of Nd–Fe–B thin films, *Journal of Magnetism and Magnetic Materials.* 302 (2006) 252–258. <https://doi.org/10.1016/j.jmmm.2005.09.014>.
- [73] U. Hannemann, S. Fähler, S. Oswald, B. Holzapfel, L. Schultz, Effect of Cr and Ta buffers on hard magnetic Nd₂Fe₁₄B films, *Journal of Magnetism and Magnetic Materials.* 242–245 (2002) 1294–1296. [https://doi.org/10.1016/S0304-8853\(01\)01266-5](https://doi.org/10.1016/S0304-8853(01)01266-5).
- [74] V. Neu, S. Melcher, U. Hannemann, S. Fähler, L. Schultz, Growth, microstructure, and magnetic properties of highly textured and highly coercive Nd-Fe-B films, *Phys. Rev. B.* 70 (2004) 144418. <https://doi.org/10.1103/PhysRevB.70.144418>.
- [75] D.J. Keavney, E.E. Fullerton, J.E. Pearson, S.D. Bader, High-coercivity, c-axis oriented Nd₂Fe₁₄B films grown by molecular beam epitaxy, *Journal of Applied Physics.* 81 (1997) 4441–4443. <https://doi.org/10.1063/1.364969>.
- [76] N. Tian, Y. Li, F. Hong, C. You, Fabrication of perpendicular magnetic anisotropic Nd-Fe-B based thin films through annealing Nd-Fe-B/Nd-Fe multilayer, in: 2015 IEEE International Magnetism Conference (INTERMAG), 2015: pp. 1–1. <https://doi.org/10.1109/INTMAG.2015.7157451>.
- [77] D.M. Mattox, Chapter 10 - Atomistic Film Growth and Some Growth-Related Film Properties, in: D.M. Mattox (Ed.), *Handbook of Physical Vapor Deposition (PVD) Processing (Second Edition)*, William Andrew Publishing, Boston, 2010: pp. 333–398. <https://doi.org/10.1016/B978-0-8155-2037-5.00010-1>.
- [78] I. Petrov, P.B. Barna, L. Hultman, J.E. Greene, Microstructural evolution during film growth, *Journal of Vacuum Science & Technology A.* 21 (2003) S117–S128. <https://doi.org/10.1116/1.1601610>.
- [79] E. Robert, *Pulsed Laser Deposition of Thin Films: Applications-Led Growth of Functional Materials*, John Wiley & Sons, Hoboken, New Jersey, 2006. <https://onlinelibrary.wiley.com/doi/book/10.1002/0470052120>.

- [80] D.A. King, D.P. Woodruff, *Growth and Properties of Ultrathin Epitaxial Layers*, Elsevier, 1997.
- [81] M. Nakano, S. Sato, H. Fukunaga, F. Yamashita, A method of preparing anisotropic Nd–Fe–B film magnets by pulsed laser deposition, *Journal of Applied Physics*. 99 (2006) 08N301. <https://doi.org/10.1063/1.2159411>.
- [82] M. Nakano, K. Takashima, A. Yamashita, T. Yanai, H. Fukunaga, Relationship between target materials and various properties of PLD-made isotropic Nd-Fe-B films, *Journal of Magnetism and Magnetic Materials*. 502 (2020) 166557. <https://doi.org/10.1016/j.jmmm.2020.166557>.
- [83] M. Nakano, H. Takeda, S. Sato, T. Yanai, F. Yamashita, H. Fukunaga, Enhancement in coercivity of pulse-laser-deposition-made Nd–Fe–B thick film magnets by high-speed crystallization, *Journal of Applied Physics*. 101 (2007) 09K525. <https://doi.org/10.1063/1.2712818>.
- [84] P. Zheng, Y. Haik, C.-J. Chen, Z. Jiang, J.P. Zheng, Properties of NdFeB film grown on silicon substrate by PLD under external magnetic field, *Surface and Coatings Technology*. 194 (2005) 372–377. <https://doi.org/10.1016/j.surfcoat.2004.11.033>.
- [85] S.Y. Xu, X.J. Huang, C.K. Ong, S.L. Lim, Y.L. Chang, Z. Yang, Z.W. Li, H.B. Nie, Yttria-stabilized zirconia: a suitable substrate for c-axis preferred Nd–Fe–B thin films fabricated by pulsed-laser deposition, *Journal of Magnetism and Magnetic Materials*. 222 (2000) 182–188. [https://doi.org/10.1016/S0304-8853\(00\)00530-8](https://doi.org/10.1016/S0304-8853(00)00530-8).
- [86] H. Fukunaga, T. Kamikawatoko, M. Nakano, T. Yanai, F. Yamashita, Effect of laser beam parameters on magnetic properties of Nd–Fe–B thick-film magnets fabricated by pulsed laser deposition, *Journal of Applied Physics*. 109 (2011) 07A758. <https://doi.org/10.1063/1.3566080>.
- [87] M. Venkatesan, J. Buschbeck, F.M.F. Rhen, J.M.D. Coey, Effect of annealing on magnetic properties of Nd–Fe–B films, *Journal of Magnetism and Magnetic Materials*. 272–276 (2004) E881–E882. <https://doi.org/10.1016/j.jmmm.2003.12.204>.
- [88] S.L. Chen, W. Liu, C.L. Chen, Z.D. Zhang, Effect of heat treatment on microstructure and magnetic properties of anisotropic Nd–Fe–B films with Mo or Ti buffer layer, *Journal of Applied Physics*. 98 (2005) 113905. <https://doi.org/10.1063/1.2136208>.
- [89] J. Pivetal, D. Royet, G. Ciuta, M. Frenea-Robin, N. Haddour, N.M. Dempsey, F. Dumas-Bouchiat, P. Simonet, Micro-magnet arrays for specific single bacterial cell positioning, *Journal of Magnetism and Magnetic Materials*. 380 (2015) 72–77. <https://doi.org/10.1016/j.jmmm.2014.09.068>.
- [90] U. Hannemann, S. Fähler, V. Neu, B. Holzapfel, L. Schultz, Intrinsic and extrinsic properties of epitaxial Nd₂Fe₁₄B films, *Appl. Phys. Lett.* 82 (2003) 3710–3712. <https://doi.org/10.1063/1.1576913>.
- [91] U. Hannemann, S. Fähler, V. Neu, B. Holzapfel, L. Schultz, Magnetic and microstructural properties of hard magnetic NdFeB films prepared on a Ta buffer by pulsed laser deposition, *IEEE Transactions on Magnetics*. 38 (2002) 2805–2807. <https://doi.org/10.1109/TMAG.2002.803110>.
- [92] M. Nakano, Y. Chikuba, D. Shimizu, A. Yamashita, T. Yanai, H. Fukunaga, Enhancement in (BH)_{max} of PLD-made isotropic Nd-Fe-B thick film magnets deposited on Si substrates, *AIP Advances*. 7 (2017) 056239. <https://doi.org/10.1063/1.4979688>.
- [93] L.K.E.B. Serrona, R. Fujisaki, A. Sugimura, T. Okuda, N. Adachi, H. Ohsato, I. Sakamoto, A. Nakanishi, M. Motokawa, D.H. Ping, K. Hono, Enhanced magnetic properties of Nd–Fe–B thin films crystallized by heat treatment, *Journal of Magnetism and Magnetic Materials*. 260 (2003) 406–414. [https://doi.org/10.1016/S0304-8853\(02\)01380-X](https://doi.org/10.1016/S0304-8853(02)01380-X).

- [94] B.A. Kapitanov, N.V. Kornilov, Ya.L. Linetsky, V.Yu. Tsvetkov, Sputtered permanent Nd-Fe-B magnets, *Journal of Magnetism and Magnetic Materials*. 127 (1993) 289–297. [https://doi.org/10.1016/0304-8853\(93\)90045-4](https://doi.org/10.1016/0304-8853(93)90045-4).
- [95] M. Yu, Y. Liu, S.H. Liou, D.J. Sellmyer, Nanostructured NdFeB films processed by rapid thermal annealing, *Journal of Applied Physics*. 83 (1998) 6611–6613. <https://doi.org/10.1063/1.367782>.
- [96] H. Jiang, M.J. O’Shea, Structure and magnetic properties of NdFeB thin films with Cr, Mo, Nb, Ta, Ti, and V buffer layers, *Journal of Magnetism and Magnetic Materials*. 212 (2000) 59–68. [https://doi.org/10.1016/S0304-8853\(99\)00789-1](https://doi.org/10.1016/S0304-8853(99)00789-1).
- [97] H. Jiang, J. Evans, M.J. O’Shea, J. Du, Hard magnetic properties of rapidly annealed NdFeB thin films on Nb and V buffer layers, *Journal of Magnetism and Magnetic Materials*. 224 (2001) 233–240. [https://doi.org/10.1016/S0304-8853\(01\)00017-8](https://doi.org/10.1016/S0304-8853(01)00017-8).
- [98] M. Valetas, M. V \acute{e} rit \acute{e} , A. Bessaudou, F. Cosset, J.C. Vareille, Rf-sputtering deposition and magnetic characterisation of Nd–Fe–B thin films for microwave applications, *Computational Materials Science*. 33 (2005) 163–167. <https://doi.org/10.1016/j.commatsci.2004.12.057>.
- [99] M. Gaudin, P. Carles, E. Laborde, C. Champeaux, F. Dumas-Bouchiat, A dual nanosecond-pulsed laser setup for nanocomposite synthesis—Ag nanoparticles in Al₂O₃/VO₂ matrix, *J. Appl. Phys.* 125 (2019) 054301. <https://doi.org/10.1063/1.5058107>.
- [100] F. Dumas-Bouchiat, H.S. Nagaraja, F. Rossignol, C. Champeaux, A. Catherinot, Magnetic domains in Co-cluster assembled films deposited by LECBD, *Applied Surface Science*. 247 (2005) 76–82. <https://doi.org/10.1016/j.apsusc.2005.01.036>.
- [101] F. Dumas-Bouchiat, H.S. Nagaraja, F. Rossignol, C. Champeaux, G. Trolliard, A. Catherinot, D. Givord, Cobalt cluster-assembled thin films deposited by low energy cluster beam deposition: Structural and magnetic investigations of deposited layers, *Journal of Applied Physics*. 100 (2006) 064304. <https://doi.org/10.1063/1.2335670>.
- [102] O.A. Ivanov, L.V. Solina, V.A. Demshina, L.M. Magat, Determination of the Anisotropy Constant and Saturation Magnetization and the Magnetic Properties of Powders of an Iron–Platinum Alloy, *Fizika Metallov i Metallovedenie*. (1973) 92–97.
- [103] E. J \ddot{a} necke, Bin \ddot{a} re Legierungen, in: E. J \ddot{a} necke (Ed.), *Kurzgefasstes Handbuch aller Legierungen*, Springer, Berlin, Heidelberg, 1937: pp. 18–226. https://doi.org/10.1007/978-3-662-35181-9_3.
- [104] K. Watanabe, H. Masumoto, On the High-Energy Product Fe–Pt Permanent Magnet Alloys, *Transactions of the Japan Institute of Metals*. 24 (1983) 627–632. <https://doi.org/10.2320/matertrans1960.24.627>.
- [105] T.B. Massalski, H. Okamoto, P.R. Subramanian, L. Kacprzak, *Binary alloy phase diagrams*, 2nd ed., ASM International, Materials Park, Ohio, 1990.
- [106] T. Goto, H. Utsugi, K. Watanabe, Effect of atomic order-disorder on ⁵⁷Fe hyperfine structure in Fe₆₄Pt₃₆ alloy, *Journal of Alloys and Compounds*. 204 (1994) 173–178. [https://doi.org/10.1016/0925-8388\(94\)90087-6](https://doi.org/10.1016/0925-8388(94)90087-6).
- [107] T. Goto, H. Utsugi, A. Kashiwakura, Effect of atomic environment on ⁵⁷Fe hyperfine structure in Fe–Pt alloys, *Journal of Magnetism and Magnetic Materials*. 104–107 (1992) 2051–2052. [https://doi.org/10.1016/0304-8853\(92\)91664-F](https://doi.org/10.1016/0304-8853(92)91664-F).
- [108] H. Lipson, D. Schoenberg, G.V. Stupart, The relation between atomic arrangement and coercivity in an alloy of iron and platinum, *J. Inst. Metals*. 67 (1941) 333–340.
- [109] H.P.J. Wijn, ed., *Magnetic Properties of Metals: d-Elements, Alloys and Compounds*, Springer-Verlag, Berlin Heidelberg, 1991. <https://doi.org/10.1007/978-3-642-58218-9>.

- [110] M. Sternik, S. Couet, J. Łażewski, P.T. Jochym, K. Parlinski, A. Vantomme, K. Temst, P. Piekarczyk, Dynamical properties of ordered Fe–Pt alloys, *Journal of Alloys and Compounds*. 651 (2015) 528–536. <https://doi.org/10.1016/j.jallcom.2015.08.097>.
- [111] C. Antoniak, J. Lindner, M. Spasova, D. Sudfeld, M. Acet, M. Farle, K. Fauth, U. Wiedwald, H.-G. Boyen, P. Ziemann, F. Wilhelm, A. Rogalev, S. Sun, Enhanced Orbital Magnetism in Fe₅₀Pt₅₀ Nanoparticles, *Phys. Rev. Lett.* 97 (2006) 117201. <https://doi.org/10.1103/PhysRevLett.97.117201>.
- [112] C.J. Sun, G.M. Chow, G.H. Fecher, J.S. Chen, H.-J. Lin, Y. Hwu, Spin and Orbital Magnetic Moments of FePt Thin Films, *Jpn. J. Appl. Phys.* 45 (2006) 2539. <https://doi.org/10.1143/JJAP.45.2539>.
- [113] O. Dmitrieva, M. Spasova, C. Antoniak, M. Acet, G. Dumpich, J. Kästner, M. Farle, K. Fauth, U. Wiedwald, H.-G. Boyen, P. Ziemann, Magnetic moment of Fe in oxide-free FePt nanoparticles, *Phys. Rev. B.* 76 (2007) 064414. <https://doi.org/10.1103/PhysRevB.76.064414>.
- [114] S. Imada, A. Yamasaki, S. Suga, T. Shima, K. Takanashi, Perpendicular magnetization of L10-ordered FePt films in the thinnest limit, *Appl. Phys. Lett.* 90 (2007) 132507. <https://doi.org/10.1063/1.2717516>.
- [115] G.E. Bacon, J. Crangle, W. Sucksmith, Chemical and magnetic order in platinum-rich Pt + Fe alloys, *Proceedings of the Royal Society of London. Series A. Mathematical and Physical Sciences*. 272 (1963) 387–405. <https://doi.org/10.1098/rspa.1963.0060>.
- [116] M. Fallot, Les alliages du fer avec les métaux de la famille du platine, *Ann. Phys.* 11 (1938) 291–332. <https://doi.org/10.1051/anphys/193811100291>.
- [117] Z. Lu, R.V. Chepulkii, W.H. Butler, First-principles study of magnetic properties of L10-ordered MnPt and FePt alloys, *Phys. Rev. B.* 81 (2010) 094437. <https://doi.org/10.1103/PhysRevB.81.094437>.
- [118] J. Lyubina, I. Opahle, M. Richter, O. Gutfleisch, K.-H. Müller, L. Schultz, O. Isnard, Influence of composition and order on the magnetism of Fe–Pt alloys: Neutron powder diffraction and theory, *Appl. Phys. Lett.* 89 (2006) 032506. <https://doi.org/10.1063/1.2222244>.
- [119] S.N. Piramanayagam, T.C. Chong, *Developments in Data Storage: Materials Perspective*, 1 edition, Wiley-IEEE Press, Hoboken, NJ, 2011.
- [120] W. Grange, I. Galanakis, M. Alouani, M. Maret, J.-P. Kappler, A. Rogalev, Experimental and theoretical x-ray magnetic-circular-dichroism study of the magnetic properties of $\text{Co}_{50}\text{Pt}_{50}$ thin films, *Phys. Rev. B.* 62 (2000) 1157–1166. <https://doi.org/10.1103/PhysRevB.62.1157>.
- [121] I. Galanakis, M. Alouani, H. Dreyssé, Spin-axis-dependent magnetic properties of FePt and CoPt, *Physica B: Condensed Matter*. 320 (2002) 221–225. [https://doi.org/10.1016/S0921-4526\(02\)00687-7](https://doi.org/10.1016/S0921-4526(02)00687-7).
- [122] B.E. Warren, *X-Ray Diffraction*, Reprint edition, Dover Publications, New York, 1990.
- [123] F. Kurth, M. Weisheit, K. Leistner, T. Gemming, B. Holzapfel, L. Schultz, S. Fähler, Finite-size effects in highly ordered ultrathin FePt films, *Phys. Rev. B.* 82 (2010) 184404. <https://doi.org/10.1103/PhysRevB.82.184404>.
- [124] M. Futamoto, T. Shimizu, M. Nakamura, M. Ohtake, Growth of L10 ordered crystal in FePt epitaxial magnetic thin films on (001) Oriented Substrates, *Journal of the Magnetism Society of Japan*. 42 (2018) 102–109. <https://doi.org/10.3379/msjmag.1809R001>.
- [125] Y.K. Takahashi, K. Hono, T. Shima, K. Takanashi, Microstructure and magnetic properties of FePt thin films epitaxially grown on MgO (001) substrates, *Journal of*

Magnetism and Magnetic Materials. 267 (2003) 248–255. [https://doi.org/10.1016/S0304-8853\(03\)00377-9](https://doi.org/10.1016/S0304-8853(03)00377-9).

- [126] W. Li, L. Chen, The mechanism of texture evolution in annealed L10–FePt thin films, *Appl. Phys. A*. 124 (2018) 100. <https://doi.org/10.1007/s00339-017-1523-z>.
- [127] M. Weisheit, L. Schultz, S. Fähler, Temperature dependence of FePt thin film growth on MgO(100), *Thin Solid Films*. 515 (2007) 3952–3955. <https://doi.org/10.1016/j.tsf.2006.10.116>.
- [128] M. Fanfoni, M. Tomellini, The Johnson-Mehl- Avrami-Kohnogorov model: A brief review, *Nouv Cim D*. 20 (1998) 1171–1182. <https://doi.org/10.1007/BF03185527>.
- [129] D.C. Berry, K. Barmak, Time-temperature-transformation diagrams for the A1 to L10 phase transformation in FePt and FeCuPt thin films, *Journal of Applied Physics*. 101 (2007) 014905. <https://doi.org/10.1063/1.2403835>.
- [130] T. Shima, K. Takanashi, Y.K. Takahashi, K. Hono, Coercivity exceeding 100kOe in epitaxially grown FePt sputtered films, *Appl. Phys. Lett.* 85 (2004) 2571–2573. <https://doi.org/10.1063/1.1794863>.
- [131] T. Shima, K. Takanashi, Y.K. Takahashi, K. Hono, G.Q. Li, S. Ishio, High coercivity and magnetic domain observation in epitaxially grown particulate FePt thin films, *Journal of Magnetism and Magnetic Materials*. 266 (2003) 171–177. [https://doi.org/10.1016/S0304-8853\(03\)00468-2](https://doi.org/10.1016/S0304-8853(03)00468-2).
- [132] T. Shima, K. Takanashi, G.Q. Li, S. Ishio, Microstructure and Magnetic Properties for Highly Coercive FePt Sputtered Films, *Materials Transactions*. 44 (2003) 1508–1513. <https://doi.org/10.2320/matertrans.44.1508>.
- [133] M. Nakano, W. Oniki, T. Yanai, H. Fukunaga, Magnetic properties of pulsed laser deposition-fabricated isotropic Fe–Pt film magnets, *Journal of Applied Physics*. 109 (2011) 07A723. <https://doi.org/10.1063/1.3561785>.
- [134] M. Weisheit, L. Schultz, S. Fähler, Textured growth of highly coercive L10 ordered FePt thin films on single crystalline and amorphous substrates, *Journal of Applied Physics*. 95 (2004) 7489–7491. <https://doi.org/10.1063/1.1667456>.
- [135] R. Maaß, M. Weisheit, S. Fähler, L. Schultz, Influence of hydrogen on the growth of FePt thin films, *Journal of Applied Physics*. 100 (2006) 073910. <https://doi.org/10.1063/1.2357643>.
- [136] I.A. Golovchanskiy, S.A. Fedoseev, A.V. Pan, Quantitative model for tunable microstructure in magnetic FePt thin films by pulsed laser deposition, *J. Phys. D: Appl. Phys.* 46 (2013) 215502. <https://doi.org/10.1088/0022-3727/46/21/215502>.
- [137] R.F.C. Farrow, D. Weller, R.F. Marks, M.F. Toney, S. Hom, G.R. Harp, A. Cebollada, Growth temperature dependence of long-range alloy order and magnetic properties of epitaxial $\text{Fe}_x\text{Pt}_{1-x}$ ($x \approx 0.5$) films, *Appl. Phys. Lett.* 69 (1996) 1166–1168. <https://doi.org/10.1063/1.117383>.
- [138] F.M.F. Rhen, J.M.D. Coey, Electrodeposition of coercive L10 FePt magnets, *Journal of Magnetism and Magnetic Materials*. 322 (2010) 1572–1575. <https://doi.org/10.1016/j.jmmm.2009.09.027>.
- [139] K. Leistner, J. Thomas, H. Schlörb, M. Weisheit, L. Schultz, S. Fähler, Highly coercive electrodeposited FePt films by postannealing in hydrogen, *Appl. Phys. Lett.* 85 (2004) 3498–3500. <https://doi.org/10.1063/1.1807958>.
- [140] K. Leistner, S. Fähler, H. Schlörb, L. Schultz, Preparation and characterization of electrodeposited Fe/Pt multilayers, *Electrochemistry Communications*. 8 (2006) 916–920. <https://doi.org/10.1016/j.elecom.2006.03.032>.

- [141] M.M. Schwickert, K.A. Hannibal, M.F. Toney, M. Best, L. Folks, J.-U. Thiele, A.J. Kellock, D. Weller, Temperature dependent chemical ordering in FePt(001) and FePt(110) films, *Journal of Applied Physics*. 87 (2000) 6956–6958. <https://doi.org/10.1063/1.372898>.
- [142] M.L. Yan, N. Powers, D.J. Sellmyer, Highly oriented nonepitaxially grown L10 FePt films, *Journal of Applied Physics*. 93 (2003) 8292–8294. <https://doi.org/10.1063/1.1556257>.
- [143] C. Brombacher, C. Schubert, K. Neupert, M. Kehr, J. Donges, M. Albrecht, Influence of annealing time on structural and magnetic properties of rapid thermally annealed FePt films, *J. Phys. D: Appl. Phys.* 44 (2011) 355001. <https://doi.org/10.1088/0022-3727/44/35/355001>.
- [144] S.N. Hsiao, L.H. Chen, S.H. Liu, J.L. Tsai, H.Y. Lee, Evolution of microstructure, residual stress, and texture in FePt films during rapid thermal annealing, *Journal of Alloys and Compounds*. 656 (2016) 876–880. <https://doi.org/10.1016/j.jallcom.2015.10.033>.
- [145] M. Weisheit, L. Schultz, S. Fähler, On the influence of composition on laser-deposited Fe–Pt films, *Journal of Magnetism and Magnetic Materials*. 290–291 (2005) 570–572. <https://doi.org/10.1016/j.jmmm.2004.11.537>.
- [146] C.-M. Kuo, P.C. Kuo, H.-C. Wu, Microstructure and magnetic properties of Fe₁₀₀–xPt_x alloy films, *Journal of Applied Physics*. 85 (1999) 2264–2269. <https://doi.org/10.1063/1.369536>.
- [147] T. Seki, T. Shima, K. Takanashi, Y. Takahashi, E. Matsubara, K. Hono, L10 ordering of off-stoichiometric FePt (001) thin films at reduced temperature, *Appl. Phys. Lett.* 82 (2003) 2461–2463. <https://doi.org/10.1063/1.1567053>.
- [148] B. Wang, K. Barmak, The impact of deposition temperature on L10 formation in FePt films, *Journal of Applied Physics*. 111 (2012) 07B718. <https://doi.org/10.1063/1.3679388>.
- [149] M.F. Toney, W.-Y. Lee, J.A. Hedstrom, A. Kellock, Thickness and growth temperature dependence of structure and magnetism in FePt thin films, *Journal of Applied Physics*. 93 (2003) 9902–9907. <https://doi.org/10.1063/1.1577226>.
- [150] Y.K. Takahashi, T. Ohkubo, M. Ohnuma, K. Hono, Size effect on the ordering of FePt granular films, *Journal of Applied Physics*. 93 (2003) 7166–7168. <https://doi.org/10.1063/1.1555895>.
- [151] T. Miyazaki, O. Kitakami, S. Okamoto, Y. Shimada, Z. Akase, Y. Murakami, D. Shindo, Y.K. Takahashi, K. Hono, Size effect on the ordering of L10-FePt nanoparticles, *Phys. Rev. B*. 72 (2005) 144419. <https://doi.org/10.1103/PhysRevB.72.144419>.
- [152] G.R. Trichy, J. Narayan, H. Zhou, L10 ordered epitaxial FePt (001) thin films on TiN/Si (100) by pulsed laser deposition, *Appl. Phys. Lett.* 89 (2006) 132502. <https://doi.org/10.1063/1.2357848>.
- [153] M. Nakano, S. Shibata, T. Yanai, H. Fukunaga, Anisotropic properties in Fe–Pt thick film magnets, *Journal of Applied Physics*. 105 (2009) 07A732. <https://doi.org/10.1063/1.3073928>.
- [154] C. Kittel, *Introduction to Solid State Physics*, 8th ed., John Wiley and Sons, 2004. <https://www.wiley.com/en-us/Introduction+to+Solid+State+Physics%2C+8th+Edition-p-9780471415268>.
- [155] R.M. Bozorth, *Ferromagnetism*, Van Nostrand Co., Princeton, N.J., 1951.
- [156] H. Zeng, J. Li, Z.L. Wang, J.P. Liu, S. Sun, Bimagnetic Core/Shell FePt/Fe₃O₄ Nanoparticles, *Nano Lett.* 4 (2004) 187–190. <https://doi.org/10.1021/nl035004r>.
- [157] G.V. Raynor, V.G. Rivlin, 10: Critical evaluation of constitution of cobalt-iron-vanadium system, *International Metals Reviews*. 28 (1983) 211–227. <https://doi.org/10.1179/imtr.1983.28.1.211>.

- [158] M. Cuong Nguyen, X. Zhao, M. Ji, C.-Z. Wang, B. Harmon, K.-M. Ho, Atomic structure and magnetic properties of Fe_{1-x}Co_x alloys, *Journal of Applied Physics*. 111 (2012) 07E338. <https://doi.org/10.1063/1.3677929>.
- [159] D.I. Bardos, Mean Magnetic Moments in bcc Fe–Co Alloys, *Journal of Applied Physics*. 40 (1969) 1371–1372. <https://doi.org/10.1063/1.1657673>.
- [160] M.F. Collins, J.B. Forsyth, The magnetic moment distribution in some transition metal alloys, *The Philosophical Magazine: A Journal of Theoretical Experimental and Applied Physics*. 8 (1963) 401–410. <https://doi.org/10.1080/14786436308211141>.
- [161] A. Díaz-Ortiz, R. Drautz, M. Fähnle, H. Dosch, J.M. Sanchez, Structure and magnetism in bcc-based iron-cobalt alloys, *Phys. Rev. B*. 73 (2006) 224208. <https://doi.org/10.1103/PhysRevB.73.224208>.
- [162] Y. Wang, Y. Xia, Bottom-Up and Top-Down Approaches to the Synthesis of Monodispersed Spherical Colloids of Low Melting-Point Metals, *Nano Lett.* 4 (2004) 2047–2050. <https://doi.org/10.1021/nl048689j>.
- [163] V. Dupuis, G. Khadra, A. Hillion, A. Tamion, J. Tuaille-Combes, L. Bardotti, F. Tournus, Intrinsic magnetic properties of bimetallic nanoparticles elaborated by cluster beam deposition, *Phys. Chem. Chem. Phys.* 17 (2015) 27996–28004. <https://doi.org/10.1039/C5CP00943J>.
- [164] O. Tosun, F.M. Abel, B. Balasubramanian, R. Skomski, D.J. Sellmyer, G.C. Hadjipanayis, Structure and Magnetism of Co₂Ge Nanoparticles, *Nanomaterials*. 9 (2019) 1371. <https://doi.org/10.3390/nano9101371>.
- [165] A. Kleibert, F. Bulut, R.K. Gebhardt, W. Rosellen, D. Sudfeld, J. Passig, J. Bansmann, K.H. Meiwes-Broer, M. Getzlaff, Correlation of shape and magnetic anisotropy of supported mass-filtered Fe and FeCo alloy nanoparticles on W(110), *J. Phys.: Condens. Matter*. 20 (2008) 445005. <https://doi.org/10.1088/0953-8984/20/44/445005>.
- [166] P.L. Ong, S. Mahmood, T. Zhang, J.J. Lin, R.V. Ramanujan, P. Lee, R.S. Rawat, Synthesis of FeCo nanoparticles by pulsed laser deposition in a diffusion cloud chamber, *Applied Surface Science*. 254 (2008) 1909–1914. <https://doi.org/10.1016/j.apsusc.2007.07.186>.
- [167] Happy, S.R. Mohanty, P. Lee, T.L. Tan, S.V. Springham, A. Patran, R.V. Ramanujan, R.S. Rawat, Effect of deposition parameters on morphology and size of FeCo nanoparticles synthesized by pulsed laser ablation deposition, *Applied Surface Science*. 252 (2006) 2806–2816. <https://doi.org/10.1016/j.apsusc.2005.04.026>.
- [168] X.L. Dong, Z.D. Zhang, Y.C. Chuang, S.R. Jin, Characterization of ultrafine Fe-Co particles and Fe-Co(C) nanocapsules, *Phys. Rev. B*. 60 (1999) 3017–3020. <https://doi.org/10.1103/PhysRevB.60.3017>.
- [169] S. Irvani, Green synthesis of metal nanoparticles using plants, *Green Chem.* 13 (2011) 2638–2650. <https://doi.org/10.1039/C1GC15386B>.
- [170] C. Desvaux, F. Dumestre, C. Amiens, M. Respaud, P. Lecante, E. Snoeck, P. Fejes, P. Renaud, B. Chaudret, FeCo nanoparticles from an organometallic approach: synthesis, organisation and physical properties, *Journal of Materials Chemistry*. 19 (2009) 3268–3275. <https://doi.org/10.1039/B816509B>.
- [171] S.J. Shin, Y.H. Kim, C.W. Kim, H.G. Cha, Y.J. Kim, Y.S. Kang, Preparation of magnetic FeCo nanoparticles by coprecipitation route, *Current Applied Physics*. 7 (2007) 404–408. <https://doi.org/10.1016/j.cap.2006.09.012>.
- [172] G.S. Chaubey, C. Barcena, N. Poudyal, C. Rong, J. Gao, S. Sun, J.Ping. Liu, Synthesis and Stabilization of FeCo Nanoparticles, *J. Am. Chem. Soc.* 129 (2007) 7214–7215. <https://doi.org/10.1021/ja0708969>.

- [173] C.W. Kim, Y.H. Kim, H.G. Cha, D.K. Lee, Y.S. Kang, Synthesis and Characterization of Crystalline FeCo Nanoparticles, *Journal of Nanoscience and Nanotechnology*. 6 (2006) 3417–3421. <https://doi.org/10.1166/jnn.2006.17952>.
- [174] L.-M. Lacroix, R.B. Malaki, J. Carrey, S. Lachaize, M. Respaud, G.F. Goya, B. Chaudret, Magnetic hyperthermia in single-domain monodisperse FeCo nanoparticles: Evidences for Stoner–Wohlfarth behavior and large losses, *Journal of Applied Physics*. 105 (2009) 023911. <https://doi.org/10.1063/1.3068195>.
- [175] S.J. Lee, J.-H. Cho, C. Lee, J. Cho, Y.-R. Kim, J.K. Park, Synthesis of highly magnetic graphite-encapsulated FeCo nanoparticles using a hydrothermal process, *Nanotechnology*. 22 (2011) 375603. <https://doi.org/10.1088/0957-4484/22/37/375603>.
- [176] A. Ojeda-G-P, C.W. Schneider, M. Döbeli, T. Lippert, A. Wokaun, Plasma plume dynamics, rebound, and recoating of the ablation target in pulsed laser deposition, *Journal of Applied Physics*. 121 (2017) 135306. <https://doi.org/10.1063/1.4979780>.
- [177] O. Albert, S. Roger, Y. Glinec, J.C. Loulergue, J. Etchepare, C. Boulmer-Leborgne, J. Perrière, E. Millon, Time-resolved spectroscopy measurements of a titanium plasma induced by nanosecond and femtosecond lasers, *Appl Phys A*. 76 (2003) 319–323. <https://doi.org/10.1007/s00339-002-1815-8>.
- [178] J. Perrière, E. Millon, W. Seiler, C. Boulmer-Leborgne, V. Craciun, O. Albert, J.C. Loulergue, J. Etchepare, Comparison between ZnO films grown by femtosecond and nanosecond laser ablation, *Journal of Applied Physics*. 91 (2001) 690–696. <https://doi.org/10.1063/1.1426250>.
- [179] T. Itina, *Laser Ablation - From Fundamentals to Applications*, IntechOpen, 2017. <https://www.intechopen.com/books/laser-ablation-from-fundamentals-to-applications/experimental-and-theoretical-studies-on-the-dynamics-of-transient-plasmas-generated-by-laser-ablatio>.
- [180] ILC · LASERS IN LABORATORY OF LASER MICROT TECHNOLOGY, (n.d.). <http://www.ilc.sk/en/vyskum/laboratoria/laboratorium-laserovych-mikrotechnologii/lasers-in-laboratory-of-laser-microtechnology/>.
- [181] F. Dumas-Bouchiat, Agrégats nanométriques métalliques : mise au point et optimisation d'un générateur par ablation laser : élaboration et caractérisation d'empilements d'agrégats et de composites nanostructurés, Thèse de doctorat, Université de Limoges, 2005. <http://aurore.unilim.fr/theses/nxfile/default/43482ef3-8e5d-434c-b59a-6996adfc2c2f/blobholder:0/2005LIMO0036.pdf>.
- [182] T.G. Dietz, M.A. Duncan, D.E. Powers, R.E. Smalley, Laser production of supersonic metal cluster beams, *J. Chem. Phys.* 74 (1981) 6511–6512. <https://doi.org/10.1063/1.440991>.
- [183] H.W. Kroto, The Spectra of Interstellar Molecules, *International Reviews in Physical Chemistry*. 1 (1981) 309–376. <https://doi.org/10.1080/01442358109353324>.
- [184] H.W. Kroto, J.R. Heath, S.C. O'Brien, R.F. Curl, R.E. Smalley, C60: Buckminsterfullerene, *Nature*. 318 (1985) 162–163. <https://doi.org/10.1038/318162a0>.
- [185] P. Milani, W.A. deHeer, Improved pulsed laser vaporization source for production of intense beams of neutral and ionized clusters, *Review of Scientific Instruments*. 61 (1990) 1835–1838. <https://doi.org/10.1063/1.1141103>.
- [186] O.F. Hagena, Pulsed valve for supersonic nozzle experiments at cryogenic temperatures, *Review of Scientific Instruments*. 62 (1991) 2038–2039. <https://doi.org/10.1063/1.1142362>.
- [187] O.F. Hagena, Nucleation and growth of clusters in expanding nozzle flows, *Surface Science*. 106 (1981) 101–116. [https://doi.org/10.1016/0039-6028\(81\)90187-4](https://doi.org/10.1016/0039-6028(81)90187-4).

- [188] P. Keghelian, Couches minces nanostructurées de silicium et de carbure de silicium préparées par dépôts de petits agrégats : structures et propriétés électroniques, Lyon 1, 1998. <http://www.theses.fr/1998LYO10304>.
- [189] Q. Jiang, J.C. Li, B.Q. Chi, Size-dependent cohesive energy of nanocrystals, *Chemical Physics Letters*. 366 (2002) 551–554. [https://doi.org/10.1016/S0009-2614\(02\)01641-X](https://doi.org/10.1016/S0009-2614(02)01641-X).
- [190] S.C. Vanithakumari, K.K. Nanda, A universal relation for the cohesive energy of nanoparticles, *Physics Letters A*. 372 (2008) 6930–6934. <https://doi.org/10.1016/j.physleta.2008.09.050>.
- [191] H. Haberland, Z. Insepov, M. Moseler, Molecular-dynamics simulation of thin-film growth by energetic cluster impact, *Phys. Rev. B*. 51 (1995) 11061–11067. <https://doi.org/10.1103/PhysRevB.51.11061>.
- [192] S. Fähler, M. Weisheit, S. Kahl, K. Sturm, H.U. Krebs, The interface of laser-deposited Fe/Ag multilayers: evidence for the “subsurface growth mode” during pulsed-laser deposition and examination of the bcc–fcc transformation, *Appl Phys A*. 69 (1999) S459–S462. <https://doi.org/10.1007/s003390051438>.
- [193] K. Meinander, K. Nordlund, J. Keinonen, Size dependent epitaxial cluster deposition: The effect of deposition energy, *Nuclear Instruments and Methods in Physics Research Section B: Beam Interactions with Materials and Atoms*. 242 (2006) 161–163. <https://doi.org/10.1016/j.nimb.2005.08.028>.
- [194] E. van de Riet, C.J.C.M. Nillesen, J. Dieleman, Reduction of droplet emission and target roughening in laser ablation and deposition of metals, *Journal of Applied Physics*. 74 (1993) 2008–2012. <https://doi.org/10.1063/1.354763>.
- [195] J.P. Perez, V. Dupuis, J. Tuaille, A. Perez, V. Paillard, P. Melinon, M. Treilleux, L. Thomas, B. Barbara, B. Bouchet-Fabre, Magnetic properties of nanostructured iron films obtained by low energy neutral cluster beam deposition, *Journal of Magnetism and Magnetic Materials*. 145 (1995) 74–80. [https://doi.org/10.1016/0304-8853\(94\)01615-1](https://doi.org/10.1016/0304-8853(94)01615-1).
- [196] A. Kojima, A. Makino, A. Inoue, Rapid-annealing effect on the microstructure and magnetic properties of the Fe-rich nanocomposite magnets, *Journal of Applied Physics*. 87 (2000) 6576–6578. <https://doi.org/10.1063/1.372775>.
- [197] Y. Gao, S. Zhang, B. Liu, Crystallization behavior of melt-spun Nd₇Fe₈₆Nb₁B₆ ribbons under different heating rates, *Journal of Magnetism and Magnetic Materials*. 208 (2000) 158–162. [https://doi.org/10.1016/S0304-8853\(99\)00583-1](https://doi.org/10.1016/S0304-8853(99)00583-1).
- [198] B.J. Inkson, 2 - Scanning electron microscopy (SEM) and transmission electron microscopy (TEM) for materials characterization, in: G. Hübschen, I. Altpeter, R. Tschuncky, H.-G. Herrmann (Eds.), *Materials Characterization Using Nondestructive Evaluation (NDE) Methods*, Woodhead Publishing, 2016: pp. 17–43. <https://doi.org/10.1016/B978-0-08-100040-3.00002-X>.
- [199] Y. Martin, H.K. Wickramasinghe, Magnetic imaging by “force microscopy” with 1000 Å resolution, *Appl. Phys. Lett.* 50 (1987) 1455–1457. <https://doi.org/10.1063/1.97800>.
- [200] J.J. Sáenz, N. García, P. Grütter, E. Meyer, H. Heinzelmann, R. Wiesendanger, L. Rosenthaler, H.R. Hidber, H. -J. Güntherodt, Observation of magnetic forces by the atomic force microscope, *Journal of Applied Physics*. 62 (1987) 4293–4295. <https://doi.org/10.1063/1.339105>.
- [201] Quantum Design GmbH, MPMS3 The next generation of advanced SQUID magnetometry, (n.d.). https://qd-europe.com/fileadmin/Mediapool/products/magnetometers/en/MPMS3_en.pdf.
- [202] Quantum Design, Application note 1014-824, Rev. A-0, (2003). <https://qdusa.com/siteDocs/appNotes/1014-824.pdf>.

- [203] C.R. Pike, A.P. Roberts, K.L. Verosub, Characterizing interactions in fine magnetic particle systems using first order reversal curves, *Journal of Applied Physics*. 85 (1999) 6660–6667. <https://doi.org/10.1063/1.370176>.
- [204] I. Panagiotopoulos, A simple approach to the First Order Reversal Curves (FORC) of two-phase magnetic systems, *Journal of Magnetism and Magnetic Materials*. 323 (2011) 2148–2153. <https://doi.org/10.1016/j.jmmm.2011.03.021>.
- [205] T.T. Sasaki, T. Ohkubo, Y. Takada, T. Sato, A. Kato, Y. Kaneko, K. Hono, Formation of non-ferromagnetic grain boundary phase in a Ga-doped Nd-rich Nd–Fe–B sintered magnet, *Scripta Materialia*. 113 (2016) 218–221. <https://doi.org/10.1016/j.scriptamat.2015.10.042>.
- [206] N.M. Dempsey, T.G. Woodcock, H. Sepehri-Amin, Y. Zhang, H. Kennedy, D. Givord, K. Hono, O. Gutfleisch, High-coercivity Nd–Fe–B thick films without heavy rare earth additions, *Acta Materialia*. 61 (2013) 4920–4927. <https://doi.org/10.1016/j.actamat.2013.04.055>.
- [207] E. Toyserkani, N. Rasti, Ultrashort pulsed laser surface texturing, in: J. Lawrence, D.G. Waugh (Eds.), *Laser Surface Engineering*, Woodhead Publishing, 2015: pp. 441–453. <https://doi.org/10.1016/B978-1-78242-074-3.00018-0>.
- [208] A.N. Dobrynin, T.R. Gao, N.M. Dempsey, D. Givord, Experimental determination of the magnetization dependent part of the demagnetizing field in hard magnetic materials, *Appl. Phys. Lett.* 97 (2010) 192506. <https://doi.org/10.1063/1.3514554>.
- [209] L. Ratke, P.W. Voorhees, *Growth and Coarsening: Ostwald Ripening in Material Processing*, Springer-Verlag, Berlin Heidelberg, 2002. <https://doi.org/10.1007/978-3-662-04884-9>.
- [210] M. Nakano, Y. Chikuba, M. Oryoshi, A. Yamashita, T. Yanai, R. Fujiwara, T. Shinshi, H. Fukunaga, Nd–Fe–B Film Magnets With Thickness Above 100 μm Deposited on Si Substrates, *IEEE Transactions on Magnetics*. 51 (2015) 1–4. <https://doi.org/10.1109/TMAG.2015.2438099>.
- [211] J.D. Livingston, Magnetic domains in sintered Fe-Nd-B magnets, *Journal of Applied Physics*. 57 (1985) 4137–4139. <https://doi.org/10.1063/1.334644>.
- [212] A. Mazilkin, B.B. Straumal, S.G. Protasova, S. Gorji, A.B. Straumal, M. Katter, G. Schütz, B. Barezky, Grain boundary oxide layers in NdFeB-based permanent magnets, *Materials & Design*. (2020) 109417. <https://doi.org/10.1016/j.matdes.2020.109417>.
- [213] F.K. Lotgering, Topotactical reactions with ferrimagnetic oxides having hexagonal crystal structures—I, *Journal of Inorganic and Nuclear Chemistry*. 9 (1959) 113–123. [https://doi.org/10.1016/0022-1902\(59\)80070-1](https://doi.org/10.1016/0022-1902(59)80070-1).
- [214] B.D. Cullity, *Elements of x-ray diffraction*, Addison-Wesley Publishing Company, Inc., Reading, MA, 1978.
- [215] P.J. Brown, A.G. Fox, E.N. Maslen, M.A. O’Keefe, B.T.M. Willis, Intensity of diffracted intensities, in: *International Tables for Crystallography*, International Union of Crystallography, n.d.: pp. 554–590. <http://dx.doi.org/10.1107/97809553602060000600>.
- [216] J.-S. Kim, Y.-M. Koo, Thickness dependence of (001) texture evolution in FePt thin films on an amorphous substrate, *Thin Solid Films*. 516 (2008) 1147–1154. <https://doi.org/10.1016/j.tsf.2007.06.071>.
- [217] B.W. Roberts, X-ray measurement of order in CuAu, *Acta Metallurgica*. 2 (1954) 597–603. [https://doi.org/10.1016/0001-6160\(54\)90194-7](https://doi.org/10.1016/0001-6160(54)90194-7).
- [218] P. Villars, L.D. Calvert, ASM international, *Pearson’s handbook of crystallographic data for intermetallic phases*. In3PSe3 - Zr Vol. 4 Vol. 4, ASM international, Materials Park, OH, 1991.

- [219] F. Casoli, L. Nasi, F. Albertini, S. Fabbri, C. Bocchi, F. Germini, P. Luches, A. Rota, S. Valeri, Morphology evolution and magnetic properties improvement in FePt epitaxial films by in situ annealing after growth, *Journal of Applied Physics*. 103 (2008) 043912. <https://doi.org/10.1063/1.2885339>.
- [220] J.M. Warrender, M.J. Aziz, Effect of deposition rate on morphology evolution of metal-on-insulator films grown by pulsed laser deposition, *Phys. Rev. B*. 76 (2007) 045414. <https://doi.org/10.1103/PhysRevB.76.045414>.
- [221] T. Shima, K. Takanashi, Y.K. Takahashi, K. Hono, Preparation and magnetic properties of highly coercive FePt films, *Appl. Phys. Lett.* 81 (2002) 1050–1052. <https://doi.org/10.1063/1.1498504>.
- [222] Y. Lifshitz, S.R. Kasi, J.W. Rabalais, W. Eckstein, Subplantation model for film growth from hyperthermal species, *Phys. Rev. B*. 41 (1990) 10468–10480. <https://doi.org/10.1103/PhysRevB.41.10468>.
- [223] P. Rasmussen, X. Rui, J.E. Shield, Texture formation in FePt thin films via thermal stress management, *Appl. Phys. Lett.* 86 (2005) 191915. <https://doi.org/10.1063/1.1924889>.
- [224] H. Yamane, T. Narisawa, T. Hasegawa, S. Ishio, Structural characterization for L10-ordered FePt films with (001) texture by x-ray diffraction, *Journal of Applied Physics*. 108 (2010) 113923. <https://doi.org/10.1063/1.3514081>.
- [225] S.N. Hsiao, S.H. Liu, S.K. Chen, T.S. Chin, H.Y. Lee, Direct evidence for stress-induced (001) anisotropy of rapid-annealed FePt thin films, *Appl. Phys. Lett.* 100 (2012) 261909. <https://doi.org/10.1063/1.4730963>.
- [226] K. Barmak, B. Wang, A.T. Jesanis, D.C. Berry, J.M. Rickman, L10 FePt: Ordering, Anisotropy Constant and Their Relation to Film Composition, *IEEE Transactions on Magnetics*. 49 (2013) 3284–3291. <https://doi.org/10.1109/TMAG.2013.2242445>.
- [227] K. Barmak, J. Kim, L.H. Lewis, K.R. Coffey, M.F. Toney, A.J. Kellock, J.-U. Thiele, On the relationship of magnetocrystalline anisotropy and stoichiometry in epitaxial L10 CoPt (001) and FePt (001) thin films, *Journal of Applied Physics*. 98 (2005) 033904. <https://doi.org/10.1063/1.1991968>.
- [228] S.N. Hsiao, S.C. Wu, S.H. Liu, J.L. Tsai, S.K. Chen, Y.C. Chang, H.Y. Lee, Preventing dewetting during rapid-thermal annealing of FePt films with enhanced L10 ordering by introducing Ag cap-layers, *Journal of Magnetism and Magnetic Materials*. 394 (2015) 121–125. <https://doi.org/10.1016/j.jmmm.2015.06.051>.
- [229] J. Wang, H. Sepehri-Amin, Y.K. Takahashi, T. Ohkubo, K. Hono, Magnetic in-plane components of FePt nanogranular film on polycrystalline MgO underlayer for heat-assisted magnetic recording media, *Acta Materialia*. 177 (2019) 1–8. <https://doi.org/10.1016/j.actamat.2019.07.017>.
- [230] T. Nguyen Van, I. de Moraes, N.M. Dempsey, C. Champeaux, F. Dumas-Bouchiat, Textured Nd-Fe-B hard magnetic thin films prepared by pulsed laser deposition with single alloy targets, *J. Magn. Magn. Mater.* 520 (2021) 167584. <https://doi.org/10.1016/j.jmmm.2020.167584>.
- [231] S.N. Hsiao, S.H. Liu, S.K. Chen, F.T. Yuan, H.Y. Lee, Effect of intrinsic tensile stress on (001) orientation in L10 FePt thin films on glass substrates, *Journal of Applied Physics*. 111 (2012) 07A702. <https://doi.org/10.1063/1.3670515>.
- [232] J.M. Soler, N. García, O. Echt, K. Sattler, E. Recknagel, Microcluster Growth: Transition from Successive Monomer Addition to Coagulation, *Phys. Rev. Lett.* 49 (1982) 1857–1860. <https://doi.org/10.1103/PhysRevLett.49.1857>.

- [233] S.-C.Y. Tsen, P.A. Crozier, J. Liu, Lattice measurement and alloy compositions in metal and bimetallic nanoparticles, *Ultramicroscopy*. 98 (2003) 63–72. [https://doi.org/10.1016/S0304-3991\(03\)00119-0](https://doi.org/10.1016/S0304-3991(03)00119-0).
- [234] J.-O. Malm, M.A. O’Keefe, Deceptive “lattice spacings” in high-resolution micrographs of metal nanoparticles, *Ultramicroscopy*. 68 (1997) 13–23. [https://doi.org/10.1016/S0304-3991\(97\)00005-3](https://doi.org/10.1016/S0304-3991(97)00005-3).
- [235] C. Paleo, V. Dupuis, F. Wilhelm, A. Rogalev, O. Proux, O. Boisson, I. Kieffer, T. Epicier, M. Bugnet, D. Le Roy, Interplay between local structure and magnetic properties of graded exchange-coupled Co@FePt nanocomposite films, *Phys. Rev. B*. 102 (2020) 224409. <https://doi.org/10.1103/PhysRevB.102.224409>.
- [236] G.P. Zhao, H.W. Zhang, Y.P. Feng, C. Yang, C.W. Huang, Nucleation or pinning: Dominant coercivity mechanism in exchange-coupled permanent/composite magnets, *Computational Materials Science*. 44 (2008) 122–126. <https://doi.org/10.1016/j.commatsci.2008.01.021>.
- [237] W. Si, G.P. Zhao, N. Ran, Y. Peng, F.J. Morvan, X.L. Wan, Deterioration of the coercivity due to the diffusion induced interface layer in hard/soft multilayers, *Scientific Reports*. 5 (2015) 16212. <https://doi.org/10.1038/srep16212>.
- [238] N. Sakuma, T. Ohshima, T. Shoji, Y. Suzuki, R. Sato, A. Wachi, A. Kato, Y. Kawai, A. Manabe, T. Teranishi, Exchange Coupling Interaction in L10-FePd/ α -Fe Nanocomposite Magnets with Large Maximum Energy Products, *ACS Nano*. 5 (2011) 2806–2814. <https://doi.org/10.1021/nn103286r>.
- [239] A.R. Muxworthy, A.P. Roberts, First-Order Reversal Curve (FORC) Diagrams, in: D. Gubbins, E. Herrero-Bervera (Eds.), *Encyclopedia of Geomagnetism and Paleomagnetism*, Springer Netherlands, Dordrecht, 2007: pp. 266–272. https://doi.org/10.1007/978-1-4020-4423-6_99.
- [240] D. Roy, P.S. Anil Kumar, Exchange spring behaviour in SrFe₁₂O₁₉-CoFe₂O₄ nanocomposites, *AIP Advances*. 5 (2015) 077137. <https://doi.org/10.1063/1.4927150>.
- [241] E.A. Brandes, G.B. Brook, eds., Chapter 13 - Diffusion in metals, in: *Smithells Metals Reference Book (Seventh Edition)*, Butterworth-Heinemann, Oxford, 1992: pp. 13–1. <https://doi.org/10.1016/B978-0-08-051730-8.50018-2>.
- [242] M. Rennhofer, B. Sepiol, M. Sladeczek, D. Kmiec, S. Stankov, G. Vogl, M. Kozłowski, R. Kozubski, A. Vantomme, J. Meersschaut, R. Rüffer, A. Gupta, Self-diffusion of iron in L10-ordered FePt thin films, *Phys. Rev. B*. 74 (2006) 104301. <https://doi.org/10.1103/PhysRevB.74.104301>.
- [243] J. Kučera, B. Million, Diffusion of platinum in the Fe-Pt system, *Physica Status Solidi (a)*. 31 (1975) 275–282. <https://doi.org/10.1002/pssa.2210310131>.
- [244] P.D. Szkutnik, A. Karmous, F. Bassani, A. Ronda, I. Berbezier, K. Gacem, A.E. Hdiy, M. Troyon, Ge nanocrystals formation on SiO₂ by dewetting: application to memory, *Eur. Phys. J. Appl. Phys.* 41 (2008) 103–106. <https://doi.org/10.1051/epjap:2008006>.
- [245] R. Resnick, L. Seigle, Nucleation of voids in metals during diffusion and creep, *JOM*. 9 (1957) 87–94. <https://doi.org/10.1007/BF03398461>.
- [246] J.G. Railsback, A.C. Johnston-Peck, J. Wang, J.B. Tracy, Size-Dependent Nanoscale Kirkendall Effect During the Oxidation of Nickel Nanoparticles, *ACS Nano*. 4 (2010) 1913–1920. <https://doi.org/10.1021/nn901736y>.
- [247] J. Chen, Y. Sakuraba, K. Yakushiji, Y. Kurashima, N. Watanabe, J. Liu, S. Li, A. Fukushima, H. Takagi, K. Kikuchi, S. Yuasa, K. Hono, Fully epitaxial giant magnetoresistive devices with half-metallic Heusler alloy fabricated on poly-crystalline electrode using three-

- dimensional integration technology, *Acta Materialia*. 200 (2020) 1038–1045. <https://doi.org/10.1016/j.actamat.2020.04.002>.
- [248] C. Manuela Müller, R. Spolenak, Dewetting of Au and AuPt alloy films: A dewetting zone model, *Journal of Applied Physics*. 113 (2013) 094301. <https://doi.org/10.1063/1.4794028>.
- [249] I.S. Jacobs, C.P. Bean, An Approach to Elongated Fine-Particle Magnets, *Phys. Rev.* 100 (1955) 1060–1067. <https://doi.org/10.1103/PhysRev.100.1060>.
- [250] R. Egli, A.P. Chen, M. Winklhofer, K.P. Kodama, C.-S. Horng, Detection of noninteracting single domain particles using first-order reversal curve diagrams, *Geochemistry, Geophysics, Geosystems*. 11 (2010). <https://doi.org/10.1029/2009GC002916>.
- [251] Y. Wu, J.D. Fowlkes, P.D. Rack, The optical properties of Cu-Ni nanoparticles produced via pulsed laser dewetting of ultrathin films: The effect of nanoparticle size and composition on the plasmon response, *Journal of Materials Research*. 26 (2011) 277–287. <https://doi.org/10.1557/jmr.2010.9>.
- [252] P.T. Vianco, F.M. Hosking, J.A. Rejent, Wettability of metallic glass alloys by two tin-based solders, *Welding Journal (Miami); (United States)*. 73:7 (1994). <https://www.osti.gov/biblio/7167871-wettability-metallic-glass-alloys-two-tin-based-solders>.
- [253] C. Rong, V. Nandwana, N. Poudyal, Y. Li, J.P. Liu, Y. Ding, Z.L. Wang, Formation of Fe₃Pt phase in FePt-based nanocomposite magnets, *J. Phys. D: Appl. Phys.* 40 (2007) 712–716. <https://doi.org/10.1088/0022-3727/40/3/003>.
- [254] V. Neu, J. Thomas, S. Fähler, B. Holzapfel, L. Schultz, Hard magnetic SmCo thin films prepared by pulsed laser deposition, *Journal of Magnetism and Magnetic Materials*. 242–245 (2002) 1290–1293. [https://doi.org/10.1016/S0304-8853\(01\)01264-1](https://doi.org/10.1016/S0304-8853(01)01264-1).
- [255] F. Dumas-Bouchiat, L.F. Zanini, M. Kustov, N.M. Dempsey, R. Grechishkin, K. Hasselbach, J.C. Orlianges, C. Champeaux, A. Catherinot, D. Givord, Thermomagnetically patterned micromagnets, *Appl. Phys. Lett.* 96 (2010) 102511. <https://doi.org/10.1063/1.3341190>.
- [256] Rami Arieli: “The Laser Adventure,” (n.d.). <https://web.phys.ksu.edu/vqm/laserweb/index.htm>.
- [257] S.K. Searles, G.A. Hart, Stimulated emission at 281.8 nm from XeBr, *Appl. Phys. Lett.* 27 (1975) 243–245. <https://doi.org/10.1063/1.88409>.
- [258] Jon, Scanning Electron Microscopy (SEM) Technology Overview, *NanoImages*. (n.d.). <https://www.nanoimages.com/sem-technology-overview/>.
- [259] G. Kaupp, *Atomic Force Microscopy, Scanning Nearfield Optical Microscopy and Nanoscratching: Application to Rough and Natural Surfaces*, Springer-Verlag, Berlin Heidelberg, 2006. <https://doi.org/10.1007/978-3-540-28472-7>.
- [260] F.J. Giessibl, Advances in atomic force microscopy, *Rev. Mod. Phys.* 75 (2003) 949–983. <https://doi.org/10.1103/RevModPhys.75.949>.
- [261] J.P. Liu, R. Skomski, Y. Liu, D.J. Sellmyer, Temperature dependence of magnetic hysteresis of RCox:Co nanocomposites (R=Pr and Sm), *Journal of Applied Physics*. 87 (2000) 6740–6742. <https://doi.org/10.1063/1.372826>.
- [262] D. Goll, M. Seeger, H. Kronmüller, Magnetic and microstructural properties of nanocrystalline exchange coupled PrFeB permanent magnets, *Journal of Magnetism and Magnetic Materials*. 185 (1998) 49–60. [https://doi.org/10.1016/S0304-8853\(98\)00030-4](https://doi.org/10.1016/S0304-8853(98)00030-4).
- [263] Y. Choi, J.S. Jiang, J.E. Pearson, S.D. Bader, J.P. Liu, Origin of recoil hysteresis loops in Sm–Co/Fe exchange-spring magnets, *Appl. Phys. Lett.* 91 (2007) 022502. <https://doi.org/10.1063/1.2752534>.

- [264] C. Rong, Y. Liu, J.P. Liu, Do thermal fluctuations influence the recoil loops of nanocomposite magnets?, *Appl. Phys. Lett.* 93 (2008) 042508. <https://doi.org/10.1063/1.2956392>.
- [265] S. Thamm, J. Hesse, A simple plot indicating interactions between single-domain particles, *Journal of Magnetism and Magnetic Materials.* 154 (1996) 254–262. [https://doi.org/10.1016/0304-8853\(95\)00585-4](https://doi.org/10.1016/0304-8853(95)00585-4).
- [266] B.Z. Cui, M.J. O’Shea, Hard magnetic properties of rapidly annealed NdFeB/Co films and intergrain interactions, *Journal of Magnetism and Magnetic Materials.* 279 (2004) 27–35. <https://doi.org/10.1016/j.jmmm.2004.01.041>.

Développement de matériaux nanocomposites ferro-magnétiques par ablation laser. Application à la synthèse de nanoparticules de Co et FeCo magnétiques douces noyées dans des matrices magnétiques dures de NdFeB et FePt.

Ce document est le fruit d'un travail de thèse réalisé au sein de l'institut IRCER à Limoges au cours des trois dernières années. Il présente toutes les étapes qui ont conduit à la synthèse de nanocomposites ferromagnétiques composé d'une matrice ferromagnétique dure et de nanoparticules magnétiques douces. Plus généralement, ce travail de thèse s'insère dans un projet collaboratif ANR-SHAMAN sur les composites magnétiques réunissant trois laboratoires (l'Institut Néel de Grenoble, l'Institut Lumière Matière de Lyon et l'Institut de Recherche sur les Céramiques de Limoges) et une société civile (l'European Synchrotron Radiation Facility de Grenoble). Aussi, la plupart des caractérisations magnétiques présentés dans ce document ont été réalisées à/et en collaboration avec l'Institut Néel de Grenoble.

Des films minces de NdFeB et de FePt ont été développés par dépôt par ablation laser (PLD) sur différents substrats (Si/SiO₂, Al₂O₃, MgO). Le contrôle du procédé à partir d'une cible unique ainsi que la maîtrise de la structure et de la microstructure des matériaux ont conduit à l'obtention de propriétés magnétiques tout à fait remarquables. Des films (150 nm) composés de grains de Nd₂Fe₁₄B₁ découplés grâce à une phase riche en Néodyme présentent un couple, rémanence/coercivité, de valeurs proches des meilleurs aimants macroscopiques du marché $\mu_0 H_c \sim 1.3$ T, $\mu_0 M_r \sim 1.1$ T et une courbe typique d'aimantation carré sans phase secondaire. Profitant d'un processus de démouillage induit par recuit rapide, une collection de grains isolés de FePt (15 nm) réalisés par PLD présente aussi de très bonnes caractéristiques magnétiques, $\mu_0 H_c \sim 4.4$ T, $\mu_0 M_r \sim 1.3$ T, des phases secondaires persistantes sont toutefois à déplorer.

Parallèlement à ces développements, un générateur de nanoparticules entièrement réalisé à l'institut IRCER et associé à l'enceinte principale permet la synthèse de nanoparticules ferromagnétique de Co et Fe₆₅Co₃₅. Les particules métalliques dont la taille varie de 2 à 5 nm de diamètres, en fonction des paramètres appliqués au générateur, sont cristallisées et magnétiquement douces.

Des nano-composites, d'architectures définies, composés de grains de FePt et de nanoparticules de Fe₆₅Co₃₅, à 25% volumique en proportion, ont montrées une augmentation importante (+24%) de la rémanence par rapport à un film mince de FePt conventionnel, tout en préservant intact les propriétés de coercivité. La difficulté réside dans la préservation des propriétés des composés magnétiques durs et doux malgré l'application de températures élevées $\sim 750^\circ\text{C}$ et des phénomènes de diffusion associés. Ces améliorations constituent une preuve expérimentale validant la théorie sur l'augmentation des propriétés magnétiques des composites basés sur une interaction de matériaux magnétiquement durs et doux. Ces travaux de thèse se situent dans la perspective d'une maîtrise des architectures à l'échelle micro/nanométrique de matériaux modèles afin d'en améliorer les propriétés magnétiques.

Mots-clés : Ablation laser impulsionnelle, Nano-composites magnétiques, Films minces ferromagnétiques, Nanoparticules



Dual pulsed laser vaporization process dedicated to nanocomposite -Development of soft (Co, FeCo) in hard (NdFeB, FePt) magnetic nanocomposites

The results of the thesis were carried out at the IRCER institute in Limoges, France over the past three years. It presents all the steps to synthesize ferromagnetic nanocomposites composed of hard magnetic matrix and soft magnetic nanoparticles (NPs). This work is a part of a joint project SHAMAN ANR-16-CE09-0019 on magnetic nanocomposites bringing collaboration between three laboratories Néel Institute in Grenoble, Lumière Matière Institute in Lyon and Institute of Research for Ceramics in Limoges, and the European Synchrotron Radiation Facility in Grenoble. All of the magnetic characterizations presented in this work were conducted at Néel Institute.

Thin films of NdFeB and FePt have been successfully developed by Pulsed Laser Deposition (PLD) on various substrates (Si/SiO₂, Al₂O₃, MgO) using single alloy targets. The control of the structure and microstructure of materials have led to achieve quite remarkable magnetic properties. 150 nm-thin films composed of Nd₂Fe₁₄B₁ grains decoupled by a secondary Nd-rich paramagnetic phase present values of magnetic coercivity and remanence close to the best macroscopic magnets on the market, e. g., $\mu_0 H_c \sim 1.3$ T, $\mu_0 M_r \sim 1.1$ T and a square loop shape with single magnetic phase behavior. Taking advantage of dewetting process induced by rapid thermal annealing process, 15 nm-FePt granular films possess also very good magnetic characteristics up to $\mu_0 H_c \sim 4.4$ T, $\mu_0 M_r \sim 1.3$ T, but with remaining secondary phase.

Moreover, a homemade nanoparticle generator entirely developed at IRCER and associated with the main PLD chamber allowed to fabricate ferromagnetic Co and Fe₆₅Co₃₅ nanoparticles. The diameters of NPs are well controlled in the range 2-5 nm, depending on the parameters in the nucleation cavity. All NPs are crystallized and magnetically soft.

Soft-hard magnetic nanocomposites with defined architectures and composed of FePt grains with 25% volume fraction of Fe₆₅Co₃₅ NPs, exhibit a significant increase of + 24% in remanence compared to that of conventional FePt thin film, while the coercivity remains constant at around 2 T. The challenge is about preserving simultaneously the properties of hard and soft magnetic phases, with the required high temperatures of 750°C and the associated diffusion phenomena. These results constitute an experimental evidence validating the theory about the enhancement of the magnetic properties in the composites, allowing exchange-coupling interaction between hard and soft phases. This work opens the way to micro/nanoscale architectures of model materials in order to augment their magnetic properties.

Keywords: Pulsed laser ablation, Soft-hard nanocomposites, magnetic thin films, Nanoparticles

